CONTROL OF THE PROPERTIES OF SEMICONDUCTING THIN FILMS DEPOSITED USING MAGNETRON SPUTTERING

by

Gareth William Hall

A Doctoral Thesis submitted in partial fulfilment of the requirements for the award of

Doctor of Philosophy of the Loughborough University of Technology

July 1st, 1993

"It is not enough that you should understand about applied science in order that your work may increase man's blessings.

Concern for the man himself and his fate must always form the chief interest of all endeavours; concern for the great unsolved problems of the organisation of labour and the distribution of goods in order that the creations of our mind shall be a blessing and not a curse to mankind.

Never forget this in the midst of your diagrams and equations."

- Albert Einstein (1879-1955)

Abstract

The objective of the work was to deposit semiconducting thin films with controlled properties using unbalanced reactive magnetron sputtering. It was decided to utilise this technique because it offers high deposition rate and controllable in-situ ion bombardment of the growing film, desirable attributes from both research and production perspectives. Sputtering from a metal cathode in a reactive gas atmosphere introduces process instabilities which can result in a low degree of control over the stoichiometry, optical, electrical and structural properties of the films. Whilst the focus of the study was to achieve repeatable control over semiconducting film properties, additional areas of interest associated with the reactive sputtering process were investigated as the project developed.

Improvements in magnetron design have been made to remove iron contamination from the extended poles, at the same time improving cathode utilisation. A new technique of bonding polycrystalline silicon cathodes to cooling shims has been developed using a sputtered three-metal multilayer process.

DC sputtering of silicon in the presence of oxygen, nitrogen, nitrogen and oxygen, and nitrogen and air has been used to produce films of refractive index between 2.27 and 1.45 at rates between 0.5 and 2 nms^{-1} depending on composition. Refractive index and optical transmittance of the films have been closely controlled by varying gas flow and composition, and substitution of air for oxygen increased the sensitivity so that indices of oxy-nitride films could be tailored to one decimal place.

The deposition of Indium-tin-oxide (ITO) onto glass substrates has been investigated, using a feedback control loop to control the otherwise unstable process. Use of the indium spectral emission line as a control parameter has enabled production of conducting films with resistivity 4×10^{-6} Ω.m, which were >80% transmitting in the visible. The design and deposition of antireflecting SiO_2 'sandwich' layers was used to maximise transmittance. Annealing the films in argon increased both conductivity and transmittance.

Indium doped ZnO films have been reactively sputtered with an unbalanced magnetron, the ratio of indium to zinc being controlled by varying the relative areas of the target. The addition of indium increased transparency to a maximum of 90% at 600nm. Annealing the films gave highly transmitting films with the resistivity of the doped films decreasing to around 3.4 $x10^{-3}$ Ωcm.

A new measurement technique has been devised to determine the band gap and absorption coefficient of thin film semiconductors using only three easily measured optical parameters. The energy gap, E_g, of a-Si was tailored to discrete values between 1.7 and 2.2 eV, by the addition of hydrogen during deposition. By sputtering an Sb cathode at different powers during deposition, E_g was increased further, and room temperature dark conductivity increased by a factor of 2 over a-Si without hydrogenation.

The feasibility of low-voltage, filament assisted magnetron deposition of a-Si has also been investigated, with the aim of reducing the damage caused by ion bombardment from the unbalanced magnetron.

CONTENTS

List of figures

Chapter Twelve:

List of plates

Table of Principal Symbols

Where the same symbol is shown for two meanings, the context of each symbol applies only to the chapter in which it is explained. The two meanings are entirely unrelated, and choice of symbol is, in most cases for historic reasons of consistency. Reference to this table, in the context of the chapter containing the symbol, will identify the appropriate meaning. Constants and numerical subscripts are not included here, and the explanation of the symbols used in the derivation in chapter eleven are given there.

a	Electron acceleration
A	Absorptance
A	Atomic mass of cathode
$\mathbf{B}$	Vectorial representation of magnetic field strength
d	Electrode spacing (simple glow discharge)
d	Film thickness
$\langle d \rangle$	Average grain width
d_0	Equivalent diameter of inert gas molecules
d_0	Width of plasma sheath at cathode
e	Electronic charge
E	Photon energy
$\mathbf{E}$	Vectorial representation of electric field strength
f_a	Flow of non-reactive gas
f_r	Flow of reactive gas
f_{vd}	Frequency of drift velocity component of electron travel
F_B	Force due to magnetic field
F_E	Force due to electric field
$g(\lambda)$	Fraction of emitted photons corresponding to transition $i \rightarrow j$
i_α	Current of sputtered atoms ejected at angle α to normal of target
i_0	Current of sputtered atoms ejected perpendicular to surface
I	Cathode current
I_c	Ion current
$I(x)$	Emission intensity at point x
I_0	Primary electron current at the cathode
j	Current density
J_t	Target current
k_f	Extinction coefficient of film
k_s	Extinction coefficient of substrate
m	Mass of electron
m_i	Ion mass
M	Metal atom in ground state
M^*	Metal atom in emitting state

n	Number of gas molecules per cm^3
n_a	Number of atoms ejected from cathode
n_e	Electron density
n_f	Refractive index of film
n_{gf}	Number of reactive gas molecules in film
n_{gp}	Number of reactive gas molecules entering system
n_{gpp}	Number of reactive gas molecules utilised by the process
n_i	Number of incident ions
n_{mf}	Number of metal molecules in the film
n_s	Refractive index of substrate
n_0	Refractive index of medium surrounding film/substrate
$N(x)$	Density of sputtered atoms
p	Total pressure
p_a	Partial pressure of non-reactive gas
pp	Partial pressure (in pumping speed calculation)
$P_i(x)$	Probability of exciting an electron to state i
q	Gas mass flow rate
r	Radius of circular component of electron motion
R	Reflectance
R	Resistance
R_d	Deposition rate
R_s	Sheet resistance
S	Pumping speed
$S_n(E)$	Nuclear stopping cross-section of the ion
S_y	Sputter yield
t	Duration of ion bombardment
T	Transmittance
T_{ij}	Probability of electron decaying from state i to j
T_m	Melting point of source material in °K
T_s	Temperature of substrate in °K
U_0	Heat of sublimation of target
$\mathbf{v}$	Vectorial representation of electron velocity
v_d	Electron drift velocity
V	Cathode potential
V_p	Plasma potential
ΔW	Decrease of cathode mass
α	Absorption coefficient
α	Number of ions per unit length generated by electrons
γ	Number of secondary electrons per incident ion
γ	Sputtering efficiency
ε	Ion energy per atom
ε_0	Permittivity of free space

λ	Wavelength
λ_0	Mean free path
ω_c	Cyclotron frequency
ω_p	Plasma frequency
ϕ	Work function
ρ	Resistivity
σ_B	Cross-magnetic field conductivity
Θ	Degree of oxide coverage on cathode
τ_{ij}	Lifetime of an electron excitation level

Acronyms

LCD	Liquid Crystal Display
LVS	Low Voltage Sputtering (/Sputtered)
ITO	Indium-Tin-Oxide
PEM	Plasma Emission Monitoring
SIMS	Secondary Ion Mass Spectroscopy
SZD	Structure Zone Diagram
TSD	Target-Substrate Distance
UBM	Unbalanced Magnetron
UHV	Ultra-High Vacuum

Acknowledgements

I take this opportunity to offer my gratitude to those people who have made my research at Loughborough both possible and fulfilling.

I am grateful to Prof. K. R. A. Ziebeck for allowing me to study in the Department of Physics, and to The Science and Engineering Research Council, without whose sponsorship I would not have been able to begin the project.

To all the people alongside whom I have had the pleasure of working, to the past and present members of the Thin Films Group, to those with whom discussions have been enthusiastic but always friendly, and to those who have offered support when the progress was not as rapid as one hoped, I offer my sincere thanks.

Special gratitude must be expressed to members of the Departmental Workshop, and in particular Mr. E. M. Stenlake, for the technical advice, guidance and above all, patience shown over the past three years. Without your capabilities, ideas for system modifications would have remained just that.

My final thanks to Prof. R. P. Howson, who has maintained enthusiasm for innovative research throughout the course of the work, even when at times it appeared that the light at the end of the tunnel was an oncoming train. I shall not forget your approach to the subject, and regard the application of your depth of experience as an example to us all.

To my parents, for their belief

Chapter One

Introduction

Recent years have seen rapid progress in the number of applications of thin films, particularly in the fields of optics and electronics. It is an area where there is a mutual relationship between technology and application, the spawning of a novel development in one creating a demand for advances in the other. The consumer-led acceleration in output from the world-wide semiconductor industry over the past two decades has culminated in market saturation, with products from the far-east now being little different from those available in the west. It is now arguable that the only advances that can be made to increase market share are in the development of novel materials and techniques of deposition to make existing products faster, more reliable and cheaper.

Although the work undertaken in this thesis was necessarily on a laboratory scale, a thought that was borne in mind throughout was the feasibility of scaling the process to an industrial level. One of the newest, and perhaps least appreciated deposition technologies available today is d.c. magnetron sputtering. It would seem that although the phenomena has been acknowledged for over 150 years, industrial interest and acceptance of today's technology is limited to large scale glass coating and multiple unit metallisation. The benefits offered by the

technique include high deposition rate, variable in-situ annealing with an integral ion flux and the ability to deposit metals, alloys or compounds of virtually any material in thin film form at room temperature. As with any technology, detailed knowledge of the mechanics behind what may otherwise appear to be a simple 'blasting out of atoms' is essential for advances to be made in either process control or material properties.

The objective of this thesis was to study the control of the properties of semiconducting thin films of several materials, but as with similar research, whilst it was informative and stimulating to pursue 'side-streets' which became exposed as the work developed, one was careful to avoid pursuing them too far in case they became 'blind alleys', which consume time and resources better spent on the main focus of the work. It was not the purpose of the work to study the semiconducting behaviour of the thin films in great detail; rather it was to demonstrate the control of some optical and electrical properties, investigating the different effects seen with each different compound film.

The body of the thesis has been written in twelve distinct chapters, each of which may be read in isolation, but since later chapters often exploit information accumulated from previous sections, it is perhaps more instructive to read the work in the chronological order in which it was researched and recorded. Chapter two introduces the theory of the physical sputtering process, describing its development to the present day, so that chapter three is able to expound with details of sputtering system variants, culminating with the magnetron device. Perhaps one reason for the lack of more widespread magnetron deposition by the electronics industry is the complexity of process control when reactive processing is required. Chapter four explains the challenges to reliable reactive process control introduced by reactive magnetron sputtering, so that these problems can be addressed during the development of the practical work. Chapter five gives background information concerning material properties and applications of the films which are examined in the second half of the thesis.

Chapter six describes the practical side of the work, including general experimental procedure. Since the improvements made to the existing magnetron source were considered both novel and beneficial, chapter

seven is devoted to explaining the results of the effort involved in this respect. Chapters eight to twelve each detail the controlled deposition of each of the materials, beginning with oxides, nitrides and oxy-nitrides of silicon, then indium-tin-oxide, zinc oxide and amorphous silicon. It is recognised that the silicon compounds are not strictly semiconducting thin films, but they are studied with a view to controlling the precise stoichiometries required for their applications within the semiconductor industry. Each of these experimental chapters is presented in a standard format, with any experimental requirements peculiar to the particular material being described at the outset. Following the presentation of the results and their discussion, each chapter concludes with a concise collection of the findings, in a chapter summary. The penultimate chapter introduces a variation of magnetron sputtering, low voltage sputtering of amorphous silicon, which became the object of much interest towards the culmination of this work, because of the potential advantages it is able to offer over conventional processing.

Chapter thirteen offers personal observations and concluding remarks by the author, on the basis of the results presented throughout the work for all aspects of the research. Recommendations for further study of various components of this project area are also suggested.

Chapter Two

The Physical Sputtering Process - Background Theory

2.0 Introduction

When a solid surface is bombarded with charged particles, different phenomena can occur depending on the kinetic energy of the incident particles. At incident energies below 5eV, the interactions are confined to the outermost layer of the surface, with the incoming particle either being reflected or coming into thermal equilibrium with the surface. The potential energy of the bombarding species is responsible for the ejection of secondary electrons, or in the case of compound surfaces, for the breaking or rearranging of bonds. At kinetic energies which exceed the binding energy of the surface atoms, a different effect is observed and is shown schematically in figure 2·1. Lattice atoms are pushed into new positions, giving rise to surface migration of atoms and to surface damage. At energies roughly equal to four times the heat of sublimation of the target material, dislodging of the atoms and their ejection into the gas phase becomes predominant. This is the process known as physical sputtering, and is the basis of the deposition technique throughout this work. This section will describe a brief history of the development of sputtering as a method of depositing thin films, then the theories of charged particle behaviour in vacuum, gas discharges, and

sputtering processes will be explained. The section concludes with descriptions of systems using alternative sputtering modes, including radio frequency sputtering, diode and triode sputtering, but paying particular attention to direct current magnetron sputtering.

2.1 History of the development of sputtering as a film deposition technique

The sputtering phenomenon has been recognised for over a century and a half[1,2], and sputtering was being used as a method of coating astronomical mirrors[3] as early as 1877. The quality of vacuum pumping equipment at that time was crude, vacuum evaporation was not yet feasible, and the only sputtering gas available was the residual air in the vacuum system. With the advent of improved pumps, interest in sputtering fell into decline, and was replaced by the much faster process of vacuum evaporation where even materials like Ta, W, and Al_2O_3 could be evaporated by electron beam evaporation. After a lapse of several decades, the application of sputtering to the deposition of thin films started to gain considerable importance.

During the resurgence of interest in sputtering, the first efforts at explanation of the process began to emerge. The first, proposed initially by Crookes[4] in 1891 and reinforced by von Hippel[5] in 1926, postulated that sputtering was due to the creation of very high local temperatures by the bombarding ions, leading to localised evaporation of target material. This theory predicted that sputter rate was a function of the heat of sublimation of the target, and of the kinetic energy of the impinging ions. The evaporation theory, perhaps favoured because of the advances in vacuum evaporation throughout the previous three decades, also predicted that the ejected metal atoms obeyed a cosine distribution. This was a widely accepted theory at the time because of the agreement between theory and experiment, the latter involving a simple glow discharge system between an anode and cathode operating between 0.1 and several Torr[5]. The fact that the data had been collected using a glow discharge system was the downfall of this theory. The glow discharge is not well suited for basic studies of sputtering for several reasons: (i) Ions and sputtered atoms arrive at the target with a large energy spread and undetermined angle of incidence due to their

Figure 2·1: Processes following ion impact during sputtering

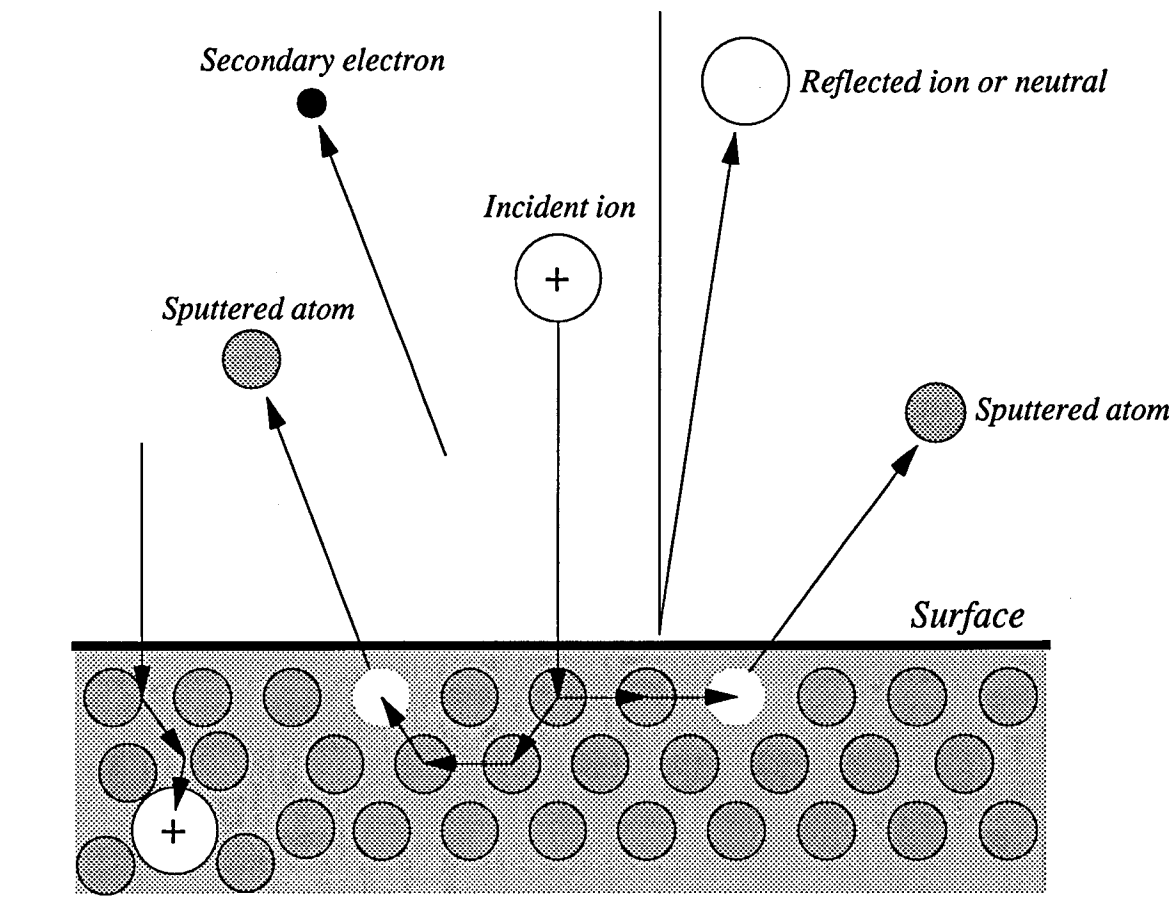

short mean free paths (see section 2.2). (ii) Some sputtered material will always diffuse back to the cathode. (iii) Bombarding-ion energy, ion current density and gas pressure are interdependent. (iv) Low bombarding ion energies cannot be accurately studied because a glow discharge cannot be maintained below a characteristic voltage.

The first attempt to collect more accurate data on sputter yields as a function of the bombarding ion energy[6,7] was made in the early 1930's. A discharge of several amperes was successfully supported between a thermionic oxide cathode and an anode below 10 mTorr. At this pressure the mean free path of ions or sputtered atoms was comparable with, or larger than the experimental apparatus dimensions. In addition, by immersing the target in the plasma so that it behaved as a third electrode, the first use of triode sputtering was recorded (see section 3.2).

The hot spot evaporation theory of von Hippel was replaced in 1909, by a more realistic theory of sputtering suggested by Stark[8]. He suggested a mechanism involving direct transfer of momentum from the incident ion to the atoms of the target. According to this collision theory, which has subsequently been further developed[9,10], the elementary event is an atomic collision cascade, where the incident ion knocks target atoms from their equilibrium positions. These atoms are caused to move in the material and to undergo further collisions, finally causing the ejection of atoms through the target surface. The consensus is that this mechanism is most dominant and is applicable to the cathode sputtering process in general. The main observations, then, are:

1. Contrary to the theory of von Hippel, the distribution of atoms sputtered from single crystal targets does not obey a cosine law, but tends to concentrate along the directions of closest packing in the crystal.

2. Sputtering yields depend on both the energy and mass of the incident ion.

3. There is a threshold energy below which sputtering does not occur.

4. At very high energies, sputter yields decrease due to the penetration of incident ions deep into the target.

5. Energies of sputtered atoms are many times higher than thermally evaporated atoms.

The experiments which yielded the above observations were carried out in high vacuum using a low pressure plasma or ion-beam bombardment, and the results are therefore not confused by the presence of a glow discharge.

Experience gained over recent years[11,12] has highlighted the advantages that sputtering offers in thin film deposition and its applications. To summarize, these are:

1. It is now possible to sputter materials such as stainless steel, Permalloy or even Pyrex glass, provided the target is kept sufficiently cool. These materials prove difficult, if not impossible to vacuum evaporate.

2. Film thickness control is comparatively simple. Once a film has been deposited with known process parameters, it is usually necessary to maintain the conditions and vary only the deposition time to achieve the desired thickness.

3. Large area targets can be employed to reduce the effect of film thickness inhomogeneity.

4. There are fewer problems with 'spitting' from the source than with vacuum evaporation.

5. Substrates can be sputter-cleaned in vacuum by ion-bombardment prior to film deposition. This feature is unique to sputtering.

6. Magnetic fields can be designed to shape the plasma for more efficient target utilization, or to improve the density of the sputter flux (see section 3.7.3).

7. If the discharge is operated at partial pressures of less than 5 mTorr, sputtered atoms arrive at the substrate with their high kinetic ejection energy, which may be beneficial to film density or adhesion

8. D.C. or R.F. sputtering of semiconductors in reactive gases can result in optimally oxidized or nitrided films.

2.2 The behaviour of charged particles in a glow discharge

Although there are several techniques available for generating the positive ions necessary for sputtering, the simplest method is by establishing a glow discharge. This is usually achieved by creating a high potential between two parallel electrodes in an inert gas atmosphere between 1 and 100 mTorr.

Several modes of gas discharge exist, and the simplest type observed between two electrodes depends on gas pressure, applied voltage, and the physical configuration of the electrodes. Figure 2·2 shows the current-voltage characteristics of a discharge running between two parallel plates in a gas with a pressure ranging between 5 and 500 mTorr. Point A is a minimum potential, where the gas breaks down abruptly, and below which there is negligible current. This region is referred to as the Townsend discharge, and here the current may be increased without a corresponding increase in voltage. Beyond the Townsend discharge, though, an increasing current creates additional charge carriers and the discharge exhibits negative resistance. As current is increased further still a second constant voltage region is reached at point B, this being known as "normal glow". Beyond point C, the potential rises with increasing current, and this region is called the "abnormal glow". It is here that most sputtering work is performed. If the current is increased beyond the abnormal glow, potential drops abruptly and the discharge becomes an arc.

Figure 2·3 is a schematic of the appearance of a glow discharge in the same pressure regime as figure 2·2, with a greatly exaggerated distance scale between the electrodes. The transport of current through a discharge occurs by the relative movement of electrons and ions under the influence of the applied electric field between the electrodes, where the total current in the system is given by the equation due to Townsend:

$$I = \frac{I_0 \exp(\alpha d)}{1 - \gamma [\exp(\alpha d) - 1]} \qquad [2\cdot1]$$

where I_0 is the primary electron current at the cathode, α is the number of ions per unit length generated by the electrons, d is the electrode spacing and γ is the number of secondary electrons per incident ion. Observing a single electron at the surface of the cathode, it is repelled

Figure 2·2: Schematic of a gas discharge

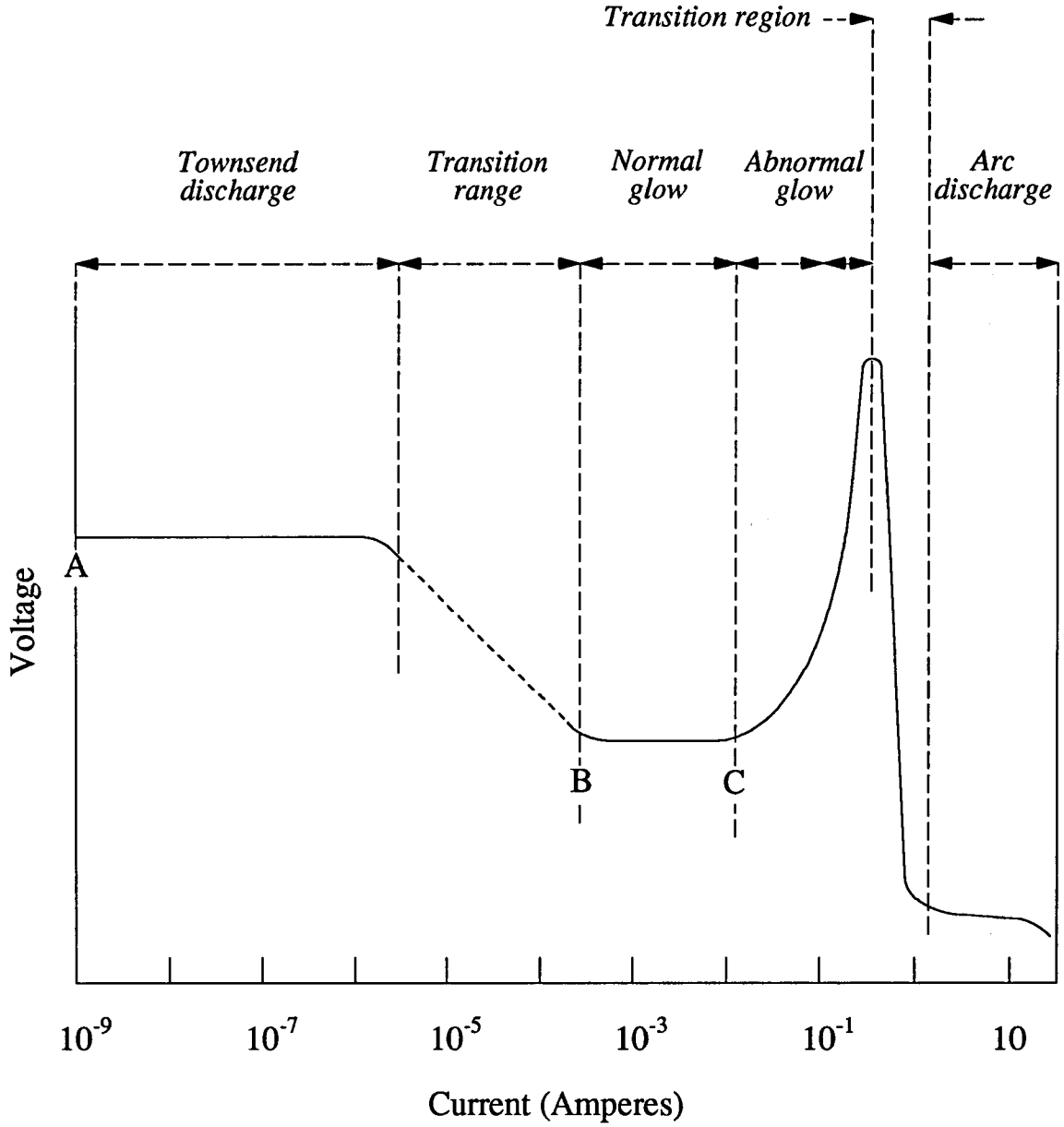

Voltage represented on a linear scale, current on a logarithmic scale

Figure 2·3: Regions of a low pressure gas discharge

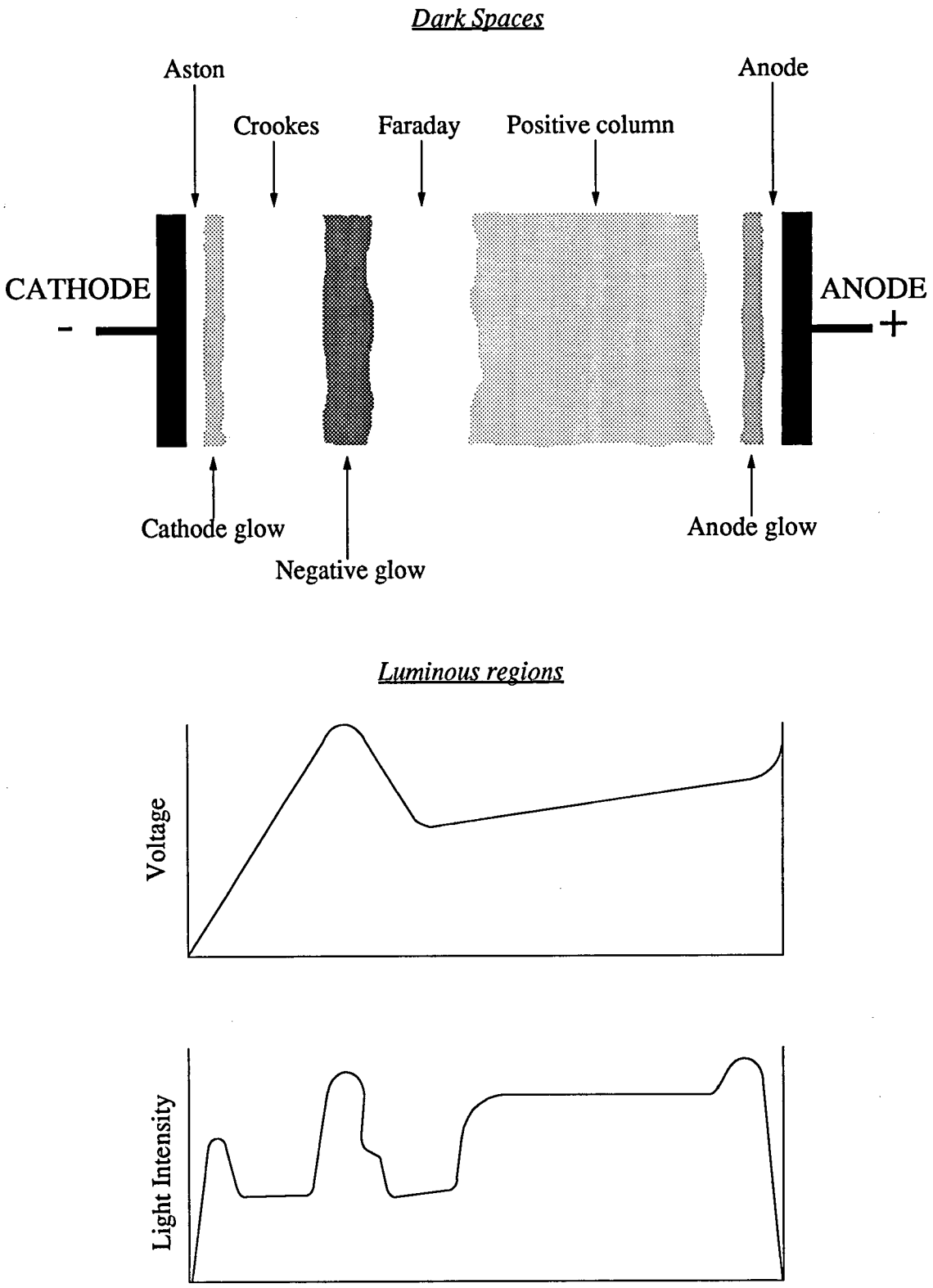

and accelerated by the strong electric field near to the cathode plate. At this stage it fails to make any ionizing collisions with the background gas because its energy of approximately 1 eV is not sufficiently above the ionization potential of the gas. This region is referred to as the "Aston dark space". As the electron moves further from the cathode, it gains sufficient energy to ionize a gas atom with which it collides. This region is the cathode glow in figure 2·2 and is the luminous region closest to the cathode. The steady state prevails when the emission of one electron from the cathode is balanced by the release of one more electron by the action of the resultant ion bombarding the cathode. At distances beyond the cathode glow, electron energies are far above that necessary for ionization, so little visible light is emitted, but most of the ionizing activity necessary to sustain the discharge occurs in the Crookes' dark space. If the anode plate is brought into the region of the Crookes' dark space, the discharge will extinguish because there are insufficient ionizing collisions to sustain the glow. The result of the large number of high energy ionizing collisions in the Crookes dark space is a large number of 'slow' electrons (that is, those which have been involved in collisions). While these do not now have sufficient energy to produce further ionization, they do have sufficient energy to cause excitation and are the cause of the negative glow.

The average distance a gas molecule has to travel before a collision is the mean free path, λ_0. The mean free path for gas molecules can be calculated using the following equation derived from kinetic theory:

$$\lambda_0 = \frac{1}{\pi \sqrt{2}\, n d_0^2} = \frac{0.225}{n d_0^2} \qquad [2\cdot2]$$

where λ_0 is the mean free path in centimetres, d_0 is the equivalent diameter of the inert gas molecules in centimetres, and n is the number of gas molecules per cm^3. The ideal gas laws enable n to be found, so that if the pressure p is in torr,

$$n = 9.656 \times 10^{18} \frac{p}{T} \qquad [2\cdot3]$$

Using a typical magnetron sputtering pressure of 3 mTorr and deposition temperature T of 25°C gives $n=9.71 \times 10^{13}$ molecules cm^{-3}. The equivalent molecular diameter of argon is 3.6×10^{-8} cm, so inserting this value and the value of n calculated above into equation [2·2] gives

the mean free path of argon ions as 1.79 cm at 3 mTorr. It can be seen from the above calculation that the distance required for an electron to travel before it has produced adequate ionization to sustain the glow is also proportional to the pressure. The thickness of the Crookes' dark space, then, increases as the pressure is decreased. At the limit, when the pressure is sufficiently low, the Crookes' dark space expands to the plane of the anode, and the glow is again extinguished. In the normal glow regime the product of dark space thickness and pressure is independent of current, and has a value of about 0.3 torr.centimetre for argon.

In the normal glow, the area of the cathode which is active in the discharge increases with increasing current such that the current density over the active portion of the target surface is constant. When the entire surface becomes active, the current can only be increased by increasing the current density, j, at the cathode. The increase in current density increases the voltage drop across the system, such that:

$$V = E + \frac{F\sqrt{j}}{p} \qquad [2\cdot4]$$

and the "abnormal" glow is reached. The voltage increase produces a higher electric field at the target, and the dark space shrinks, as shown by equation [2·5], where A, B, E and F are constants with values which depend on target material and geometry, and gas type.

$$pd = A + \frac{BF}{V - E} \qquad [2\cdot5]$$

For deposition purposes it is essential that operation is in the "abnormal" regime, to ensure complete discharge coverage of the cathode, and hence maximum target utilization and more uniform substrate coverage.

Eventually, the energy of the electrons is reduced by the series of ionizing or excitation collisions to the point where they do not have sufficient energy to sustain the ionization process. This region of the discharge is the Faraday dark space, and is found on the far side of the negative glow. The region between the Faraday dark space and the anode plate is a region of small electric field and steady supply of electrons. After diffusing through the Faraday dark space, the electrons

are accelerated towards the anode, causing further ionization in the region of normal glow; the 'positive' column. Sputtering can be achieved using the normal glow, but because the current density and voltage drop here are too low for reasonable sputtering yields to be achieved, the 'abnormal' negative column is preferred.

Finally, a fact that is seldom considered is that background gas impurities can significantly affect discharges, with consequent adverse effects seen in the quality of films deposited by the sputtering action of the discharge. Hydrogenous contaminents were discussed by Knewstubb and Tickner[13], who mention the formation of ArH^+ and H_3O^+ by the action of argon metastables on hydrogen, and water metastables on other water metastables respectively. Coburn and Kay[14] found large amounts of these species in the substrate plane of an argon dc diode sputtering system, and they reported that even trace quantities of water vapour may produce significant hydrogenous ion populations in argon discharges. Chapter eleven of this work will demonstrate the effect of hydrogen inclusion in the optical properties of semiconductor films, so the background gas impurities should clearly not be overlooked.

2.3 Sputtering processes in a glow discharge

The general properties of a glow discharge have now been discussed, but as yet little attention has been paid to the effects of the discharge on the sputtering process. This section will explain the effects of the discharge on the sputtering process, including distribution of sputtered material, the processes of sputter yield, sputter threshold and deposition rates. The section will conclude by explaining thin film formation following the sputtering of target material.

2.3.1 Distribution of sputtered material

The non-cosine behaviour of the ejected material, at least at energies which are used for modern-day sputtering, was illustrated by Wehner[15], who demonstrated the angular distribution of molybdenum atoms ejected by obliquely incident Hg^+ ions at incident energy of 250 eV. The atoms were found to be preferentially sputtered in the directions of close packing. It is thought that the ions cause chains of focused

collisions which are analogous to those created by a billiard ball striking a pack of other balls. In this instance 'focused' describes the path of an incident particle whose angle of attack is decreased by each successive impact. For the impulse to be focused, the ratio of interatomic distances in the lattice to the atomic radius must be favourable. It can be shown by simple geometry that the collision angle may grow smaller only if the interatomic distance is less than twice the collision radius, but will always grow smaller if the interatomic distance is less than $\sqrt{2}$ times the collision radius. Since the interatomic distances are smallest in the closest packed planes of a single crystal, the probability of focusing is high in these directions, and the sputter yields are also expected to be correspondingly high. For polycrystalline targets, with no preferred crystal plane orientation, the angular distribution of sputtered particles is

$$i_\alpha = i_0 \cos\alpha \qquad [2{\cdot}6]$$

where i_α is the current of sputtered atoms ejected at an angle α to the normal of the target surface, and i_0 is the current of particles ejected perpendicular to the surface. Atom ejection deposited patterns have been observed for semiconductor targets[16], and both the amount of material sputtered in a preferred direction, and the orientation of this direction depend sensitively on the angle of incidence. This would tend to suggest that contrary to the effects seen with single crystal targets, the observed preferential ejection directions for semiconductors result from near surface collision sequences rather than focusing chains. Another interesting phenomenon concerning angular distribution from semiconductor targets is the dependence on temperature. Anderson[17] discovered that preferred ejection directions are only assumed if the temperature of the target is above a characteristic temperature. At low lattice temperatures the damage caused by ion bombardment remains 'frozen-in' and results in an amorphous surface with no preferred ejection direction. Above the characteristic temperature, any surface damage is annealed out sufficiently rapidly that a subsequent impinging ion 'sees' an ordered surface, and preferentially-distributed material is sputtered. The characteristic annealing temperature depends on target type, ion mass and energy, and rate of bombardment[18], but is never

usually reached in practical deposition environments where the target has to be cooled because of the high power applied to it.

2.3.2 Sputtering yields and thresholds

Sputtering yield is defined as the number of ejected atoms per incident ion, and is the most important parameter for comparing different materials used as targets. The early work in this area used changes in the electrical resistivity of a target as a method of evaluating the removal of material, but more recent techniques include radioactive tracers, spectroscopic methods and observation of changes in the resonant frequency of a quartz crystal used as either a target or substrate. All techniques are principally calibrated against direct weight loss experiments.

As the mass of incident ions is increased, there is a general exponential increase in yield. Further increase in ion mass results in the yield increasing linearly, then less linearly, approaching a flat maximum and finally decreasing. Superposed on this general behaviour are periodic undulations which coincide with the groupings of the periodic table, and as a result of periodicities in heat of sublimation, atomic shell and crystal structure. Yield maxima are seen at the points representing the noble gases, while elements from the centre of the periodic table, such as aluminium, titanium, zirconium and the rare earths have the lowest yields.

The relationship between yield and the energy of the bombarding ion falls into three regions. Below about 50 eV little or no sputtering occurs, between 70 eV and 10 keV the yield increases with increasing voltages, and above about 30 keV a decreased yield is observed with increasing voltage. The decreased yield above 30 keV is attributed to the penetration of the high energy ions deep into the lattice, where a large proportion of their energy is lost to the bulk rather than the surface, so that at equilibrium, the sputtered species must contain sputtered atoms of the bombarding species. Nelson[19] observed that noble gas ions which were embedded at high energy congregate into microscopic noble gas bubbles, which tends to support this theory, but there is still conjecture as to whether buried ions reduce the sputter yield by a significant amount.

An important parameter in sputtering yields is the angle of incidence of the ions. With reference to the billiard ball analogy introduced in section 2.3.1 it can be predicted that sputter yields increase with more oblique incidence because the directional change of momentum for ejecting atoms in a forward direction is less. Oblique incidence, especially at higher ion energy, confines the interaction between ion and target closer to the surface, and sputtering is a more probable event than deep target penetration. Some of the earliest reliable data on yield variation with ion angle of incidence were collected by Wehner[20], who showed that for the 200 eV mercury ion bombardment of molybdenum, the yield was nearly seven times greater for 40° incidence to the normal than for 10° incidence. Wehner's results show a maximum yield for many materials, and this is generally attributed to the surface roughness of the target, which tends to decrease the yield at very oblique angles. Surface roughness affects yield even at normal incidence, where the sputtered target atoms may not be able to escape the surface and may become re-attached to the crystal on neighbouring elevations. Equation [2·7] combines the effects of decrease in target mass, ion current and duration of bombardment to formulate an expression for the yield at normal incidence:

$$\text{Yield} = \frac{n_a}{n_i} = 10^5 \frac{\Delta W}{I_c \,.\, t \,.\, A} \quad \text{(atoms/ion)} \qquad [2\cdot7]$$

where n_a is the number of atoms ejected, n_i is the number of incident ions, ΔW the decrease of target mass, I_c the ion current in amperes, t the duration of bombardment in seconds and A the atomic mass of the target.

The sputtering efficiency, γ, defined as the fraction of bombarding energy leaving the target as sputtered or backscattered particles was introduced by Sigmund[21]. He derived a value of $\gamma = 0.024$ for self-sputtering, and this value is independent of both ion energy and target material for the energy range above 1 keV. Gurmin *et al*[22] extended the calculation to obtain the following expression for the sputter yield S_y from a planar target:

$$S_y = \frac{3}{4\pi^2} \alpha \frac{4\, m_1 m_2}{(m_1 + m_2)^2} \frac{E}{U_0} = \beta V \qquad [2\cdot8]$$

where α is a function of m_2/m_1 (ion and atom masses respectively), E the ion energy, U_0 the heat of sublimation of the target, β a proportionality factor and V the cathode potential. This relationship was simplified to give:

$$S_y = \frac{\alpha S_n(E)}{16 \pi^3 a^2 U_0} \qquad [2\cdot9]$$

where $S_n(E)$ is the nuclear stopping cross-section of the ion and a = 0.219Å = the screening radius for the Born-Mayer interaction between two atoms (proposed by Andersen and Sigmund[23]). At lower ion energies, Sigmund approximated the Born-Mayer potential to obtain:

$$S_n(E) = 12 \pi a^2 \lambda_f E \qquad [2\cdot10]$$

where λ_f is a function of the ion and atom masses. From this, he obtained for the sputtering yield:

$$S_y = \frac{3 \alpha \lambda_f E}{4 \pi^2 U_0} \qquad [2\cdot11]$$

Equation [2·11] shows that the yield at low energies is proportional to the bombarding ion energy and inversely proportional to the heat of sublimation.

The early work on sputtering thresholds attempted to extrapolate yield curves to zero, but this was a difficult operation, since any measurement had to be very sensitive to detect the very small quantities of sputtered material near the origin. Results from this period[24] repeatedly cite 495 eV as the threshold sputtering potential for all gas-metal combinations. The technique of detection of a deposited film resulted in a linear appearance to the yield versus cathode potential curves, which aided the extrapolation exercise. More recent developments in plasma diagnostics, such as mass spectroscopy, optical emission spectroscopy and radioactive tracing have enabled yield measurements to be made to the order of 10^{-4} atoms per incident ion. The later measurements have shown that the yield curves are non-linear in the low potential regions, and the voltages appear to be of the order of 20 to 25 volts, rather than the 30 to 150 volts suggested previously. Thresholds appear to vary little between different ions but seem to be more characteristic for

different target materials[25]. For example, the threshold energy for copper is 17 eV for argon and neon, 16 eV for krypton and 15 eV for xenon. However, under bombardment from argon alone, aluminium has a threshold of only 13 eV, while germanium and niobium both have a threshold of 25 eV. Also reported was that the masses of the colliding species played an insignificant role, and that the threshold values are approximately equal to 4H, where H is the heat of sublimation of the target species.

2.3.3 Sputtering rate

The rate at which material deposits on a substrate is proportional to the rate at which it is removed from a cathode surface, and can be represented by:

$$R = c.I_c.S_y \qquad [2\cdot12]$$

where R is the deposition rate, c is the proportionality constant and S_y is the sputtering yield, given by equation [2·8]. From [2·8], the yield is itself a function of the cathode potential and of the ion being used. Particularly with industrial processes, it is desirable to operate a deposition system at the highest sputtering rate, and it would appear from [2·12] that the maximum possible current should be used to achieve this. While this is theoretically true, in a practical system no power supply has limitless power capability, and the only way to increase current without increasing power is to increase the pressure of the plasma. If the pressure is increased by too much, however, there is increased probability of sputtered atoms returning to the cathode by diffusion, with a consequent decreased yield. The pressure chosen on the basis of sputter rate considerations alone should therefore be the highest pressure for which the yield is still close to its maximum.

To obtain a high sputtering rate the desirable parameters are a high cathode potential, a high current density at the cathode, low sputtering gas pressure, and a heavy, inert, sputtering gas. These requirements necessitate the manipulation of the simple two-electrode discharge system, and the following chapter will explain various different approaches that have been used to increase both sputtering rate and efficiency.

2.3.4 Thin film nucleation theory

Electrical and optical properties of thin films are very often different to those of the bulk material. The difference in properties is due to the film structure, which is itself dependent on the method of film formation. The condensation of a film is initiated by the accumulation of small clusters of material through combination of several adsorbed atoms. These clusters then act as nucleation sites for further depositing atoms so that nucleation becomes film growth. Having now examined the processes occurring in a gas discharge and that of physical sputtering, this section will describe the process of film nucleation and the subsequent growth of a continuous film. The process described below is represented pictorially in figure 2·4.

When a substrate, subjected to a flux of impinging atoms, is observed using scanning electron microscopy, initial evidence of the beginning of film formation is a sudden burst of nuclei of fairly uniform size. These first nuclei have been measured between 10 and 30 Å, with a surface density of 10^{10}-10^{12} cm^{-2}. Growth is in three dimensions, but growth in the dimension normal to the substrate is less than in the two parallel dimensions, particularly in sputtering, where ion bombardment restricts growth in the normal dimension. Chopra[26] compared the saturation densities for evaporated and sputtered silver films. Initially the island density (~10^{11} cm^{-2}) was greater for the sputtered films, decreasing in both cases as deposition continued, but dependent on substrate temperature and deposition method. Coalescence is the term given to the amalgamation of neighbouring nucleation sites to form an 'island' of depositing material on the substrate. For small nuclei, this coalescence occurs in about 100 ms, and is accompanied by a reduction in the total area of all the nuclei on the substrate and an increase in their height. Nuclei which may have well defined crystallographic shapes before coalescence often become rounded following the event, although this rarely occurs with sputtering since the deposition energy and substrate temperature used do not encourage single crystal nucleation. Triangular crystallites are characteristic of the nucleation phase, while more hexagonal structures indicate that coalescence has occurred. Coalescence has been likened to the joining of two liquid droplets, with the area of the joined islands being less than the sum of the two prior to consolidation. Island height is simultaneously increased. These effects

Figure 2·4: Stages of sputtered film nucleation and growth

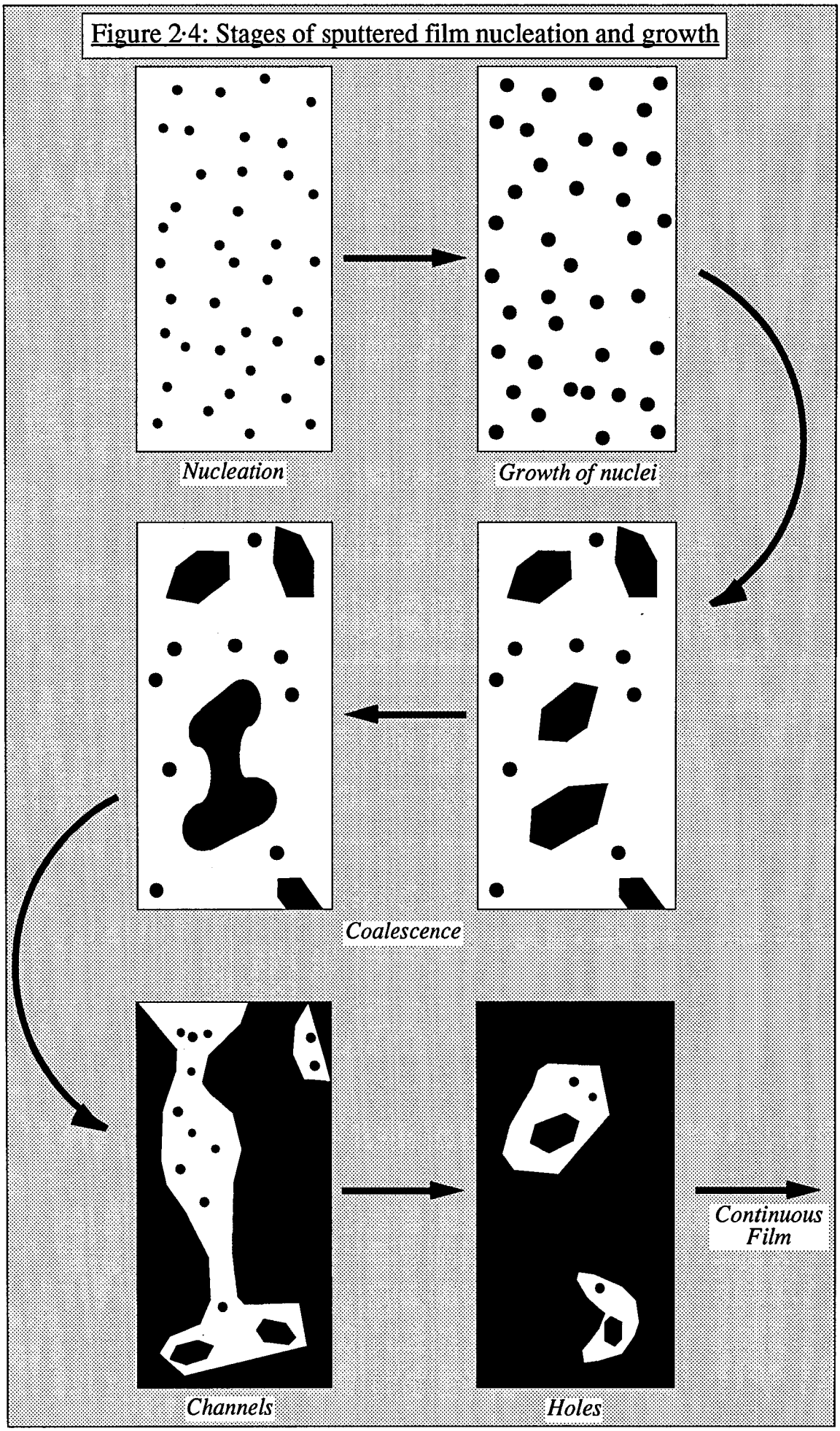

lead to the uncovered area of the substrate being greater following coalescence, allowing the secondary nucleation and growth of atoms inbetween the merged islands. The physical impetus for the liquid-like behaviour of the growing surface is reduction of surface energy, and if this were independent of crystal orientation it would act to minimize the surface area. In low energy deposition techniques such as vacuum evaporation, the reduction in surface energy results in crystallographically oriented islands, which can then be rounded by coalescence with other islands. The crystallographic islands are only seen with low power balanced magnetron sputtering (see section 3.8) and with diode sputtering, because the high energy of deposition and low substrate temperatures used with unbalanced magnetron deposition are not conducive to crystallite growth. In addition, any electrons lost from the glow may well be accelerated towards the substrate, and act to anneal any order out of the growing film.

Following nucleation and coalescence of the nucleation centres, the surface passes through the channel, then the hole stage. As islands grow, they become increasingly less rounded and eventually reach a size where they join neighbouring islands to form a continuous interwoven network structure, where the sputtered material is separated by long, narrow channels between 50 and 250 Å wide. Additional deposited material causes nucleation centres in the channels, which then grow and touch the sides, merging with the more massive regions of the film. Channels may also be bridged and filled in, again in a liquid-like manner, the process often being initiated by substrate surface irregularities, contaminents or defects. Chopra[26] found that sputtered films became continuous at much smaller thicknesses than the evaporated films, and he attributed this to the presence of electrostatic charges forcing the lateral spread of the islands.

Where a channel is bridged, the liquid-like filling of the channel is achieved by the movement of a 'front' of material down the channel at a velocity between 1 and 300 $Ås^{-1}$, depending on substrate temperature, roughness and rate of impingement of fresh material. Eventually the channels are filled in, leaving only small holes randomly spaced across the otherwise continuous film. Secondary nucleation occurs in the holes in under 100 ms, the nuclei coalescing with each other before they are incorporated into the film on one side of the hole. This leaves a series of

smaller holes, which are filled in the same manner until the substrate is covered by an uninterrupted coating.

2.3.5 Thin film morphology and structure-zone models

Once nucleation has initiated the growth process, the development of film morphology is determined by several inter-related parameters, which have been the subject of studies by two primary groups of researchers. As a conclusion to this section, thin film morphology and its determining factors will be described on the basis of the results of these 'key' models.

Movchan and Demchisin[27] were the first to categorize microstructures of vapour-phase deposited films, using what they termed a "structure-zone diagram" (SZD), in which structural features are schematically illustrated as a function of the normalised growth temperature T_s/T_m, where T_s and T_m are the substrate temperature and melting point of the source material, respectively. Their original SZD, reproduced in figure 2·5, is based on the results of the study of high rate electron-beam deposition of 0.3 - $2x10^3\mu m$ thick Ti, Ni, W, ZrO_2 and Al_2O_3 coatings, in addition to the results of other workers. They concluded that the films could be classified as a function of T_s/T_m (with temperatures in °K) in terms of three distinct zones, each with its own characteristic microstructure and physical properties. Zone 1, where $T_s/T_m<0.2$-0.3, consists of tapered crystals with domed tops, separated by voided boundaries. The internal structures of the crystals is poorly defined, although crystallite width is seen to increase with increasing T_s/T_m. Zone 2 microstructures, with T_s/T_m~0.3-0.5, consist of columnar grains separated by dense inter-crystalline boundaries. The surface topology had a visibly more matt appearance, and average grain widths, <d>, are typically less than the film thickness, and increase with increasing T_s/T_m. Zone 3 ($0.5<T_s/T_m<1$) microstructures consisted of more equiaxed grains and metallic films showed a bright, smooth surface. The transition between zones 2 and 3 is gradual, explaining the sloped demarcation of this boundary in the figure.

The simple, single-axis, two-dimensional SZD of Movchan and Demchisin became widely accepted, with the results of workers confirming that the zone structures held for film thicknesses of the order of μm, rather than mm. It was also subsequently shown[28] that the

Figure 2·5: Structure Zone Diagram of Movchan & Demchisin, reference 27

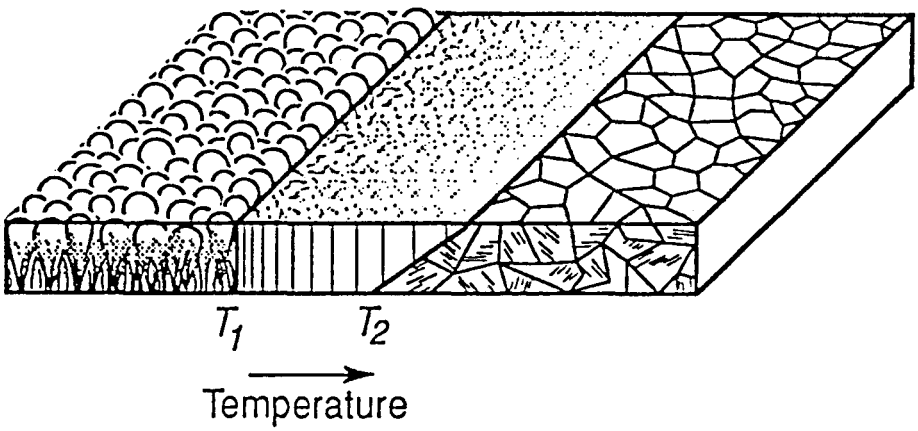

T_1 and T_2 are the growth temperatures between zones 1/2 and 2/3, respectively

Figure 2·6: Structure Zone Diagram of Thornton, reference 30

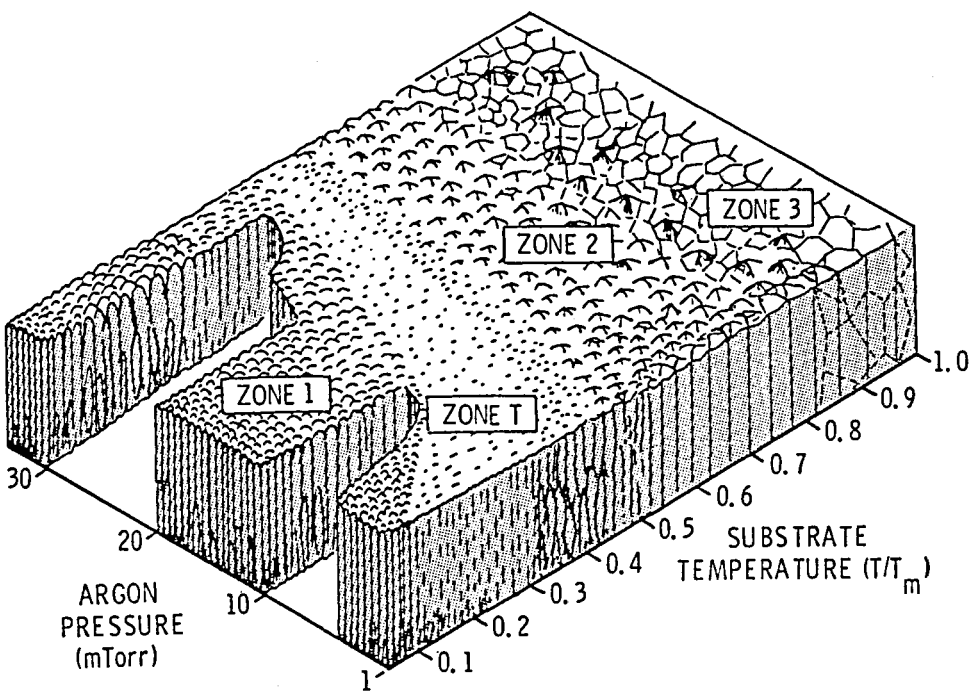

model was equally applicable to sputtered films, and to amorphous as well as polycrystalline materials[29].

In 1974, Thornton[30,31] extended the model by adding an additional axis to account for the pressure of the background gas during cylindrical post-magnetron sputtering of 25-250μm thick Ti, Cr, Fe, Cu, Mo and Al films. Figure 2·6 shows his SZD, where it is seen that increasing argon pressure increases the normalized temperatures at which zone boundaries occur. The sputtering gas pressure is not the fundamental parameter, however. Increasing the pressure to a point where the mean free path between sputtered species and the background gas is the order of the source-substrate separation increases the oblique component of the angle of incidence of the deposition flux. This results in a more open "zone 1" type structure. In addition, decreasing the pressure during sputtering will lead to more energetic particle bombardment of the film, resulting in densification. Thornton also added an additional zone to those proposed by Movchan and Demchisin, which he termed "zone T". This zone consists of a "dense array of poorly defined fibrous grains", and represents the transition between zones 1 and 2. The zone T structure was defined as the limiting form of the zone 1 structure at zero T_s/T_m. That is, the zone T fibres form the internal structure of the zone 1 crystallites.

The two previously described SZD models have now been accepted as accurate descriptions of the variation in film structure with temperature and pressure in vapour phase deposition, and are particularly applicable to sputter deposition. However, whilst the SZD provides a useful and simple method of qualitatively categorizing film microstructures, it does not offer quantitative insight into film growth mechanisms. It is important to recognise that the film growth kinetics are subject not only to T_s/T_m, but also to such variables as substrate surface roughness, contamination, and substrate material and orientation. Despite these limitations, though, the pioneering "Thornton diagram" as it has become known, has still to be bettered as a general film structure/growth model, twenty years after its inception.

Chapter Two References

1: W. R. Grove., *Phil. Trans. Roy. Soc. London*, **142**, (1842), 87

2: J. Plücker., *Pogg. Ann.*, **103**, (1858), 90

3: A. W. Wright., *Am. J. Sci.*, **13**, (1877), 49

4: W. Crookes., *Proc. Roy. Soc. London*, **50**, (1891), 88

5: A. von Hippel., *Ann. Physik*, **81**, (1926), 1043-1075

6: A. Guentherschulze & K. Meyer., *Z. Physik*, **62**, (1930), 607

7: K. Meyer & A. Guentherschulze., *Z. Physik*, **71**, (1931), 279

8: F. Stark., *Z. Electrochem.*, **15**, (1909), 509-512

9: K. H. Kingdon & I. Langmuir., *Phys. Rev.*, **22**, (1923), 148

10: F. Keywell., *Phys. Rev.*, **97**, (1955), 1611

11: P. D. Townsend, J. C. Kelley & N. E. W. Hartley, "Ion Implantation and Sputtering and Their Applications", Academic Press, (1976), Ch.6

12: R. Behrisch, Ed., *Topics in Applied Physics*, **47**, (1981), "Sputtering by Particle bombardment", Springer Verlag

13: P.F. Knewstubb & A. W. Tichner, *J. Chem. Phys.*, **36**, (1962), 684

14: J. W. Coburn & E. Kay, *Appl. Phys. Lett.*, **18**, (1971), 435

15: G. K. Wehner., *J. Appl. Phys.*, **31**, 1960, 177-179

16: G. S. Anderson & G. K. Wehner, *J. Appl. Phys.*, **31**, (1960), 2305

17: G. S. Anderson, G. K. Wehner & H. J. Olin, *J. Appl. Phys.*, **34**, (1963), 3492

18: G. S. Anderson, *J. Appl. Phys.*, **37**, (1966), 3455

19: R. S. Nelson & C. J. Beevers, *Phil. Mag.*, **9**, (1964), 343

20: G. K. Wehner, *J. Appl. Phys.*, **30**, (1959), 1762

21: P. Sigmund., *Can. J. Phys.*, **46**, (1968), 731

22: B. M. Gurmin, T. P. Martynenko & Yu. A Ryzhov, *Fiz. Tverd. Tela*, **10**, (1968), 411

23: H. H. Andersen & P. Sigmund, Danish Atomic Energy Commission, Riso Report, (1965), 103

24: V. Kohlschuetter, *Jahr. Radioaktivitaet*, **9**, (1912), 355

25: R. V. Stuart & G. K. Wehner, *J. Appl. Phys.*, **33**, (1962), 2345

26: K. L. Chopra, *J. Appl. Phys.*, **37**, (1966), 3405

27: B. A. Movchan & A. V. Demchisin, *Phys. Met. Metallogr.*, **28**, (1969), 83

28: J. A. Thornton, *Ann. Rev. Mater. Sci.*, **7**, (1976), 239

29: K. H. Guenther, *Thin Solid Films*, **77**, (1981), 239

30: J. A. Thornton, *J. Vac. Sci. Technol.*, **11**, (1974), 666

31: J. A. Thornton, *J. Vac. Sci. Technol.*, **12**, (1975), 830

Chapter Three

Sputtering System Variants

3.0 Introduction

Physical sputtering has been used as a deposition technology for an ever increasing variety of applications, and each generation of products has evolved the process to a higher level of design. This chapter will introduce five types of sputtering system, each with its own particular range of suitability, but culminating in what is widely recognised as the most efficient, controllable and high rate process available, and that which has been studied in this work.

3.1 D. C. diode glow discharge sputtering

The basic diode glow discharge sputtering configuration has been referred to when discussing physical sputtering processes. Although the technique will produce thin films of many types, the range of stoichiometries, deposition rate, film structure and density are severely limited by the low ionization and higher pressure operation characteristic of the technique. Its use is limited to research rather than industry, is suitable for contact metallization where film structure is of reduced importance, but is of little use elsewhere in the semiconductor

fabrication industry, and arguably has few advantages over vacuum evaporation. Having said this, there has been recent interest in the use of glow discharge sputtering for research applications where deposition rate is unimportant. Naoe *et al*[1] produced magnetic c-axis oriented barium ferrite thin films, and a great deal of interest has been shown in the production of four- and five-element compound superconducting films[2,3].

The basic dc diode glow discharge sputtering system is shown in figure 3·1. Voltages of the order of kilovolts are applied across the electrodes to give a current density of between 1 and 10 $mAcm^{-2}$ in the discharge, which is struck at an argon partial pressure of between 10^{-1} and 10^{-2} torr. The sputtering process is as previously described, with positive ions striking the target, ejecting neutral atoms and electrons, the latter helping to maintain the discharge. Less than 1% of the total applied power is used for the ejection of sputtered material and secondary electrons. The maximum cathode temperature attained and the rate of temperature rise is dependent on the glow discharge conditions, but the simple dc glow discharge sputtering system has very poor plasma confinement in the vicinity of the target, and the target does not usually suffer such severe heating problems as with the magnetron discharge, for example. Several cooling techniques have been reported[4,5], and this aspect will be developed in discussion of the experimental design of the magnetron in chapter seven. One of the most serious drawbacks of the self-sustained dc diode glow discharge sputtering system is the contamination of the film by the inert gas used to support the discharge. Lower pressure operation would be expected to reduce this effect, but high pressure operation is an intrinsic feature of simple glow discharge sputtering. Another disadvantage of the high pressure operating regime is the reduced adhesion of the films because of the low energy with which the neutrals impinge the substrate. For the operation of glow discharge systems at less than 20 mTorr there should be an additional source of electron injection, other than the secondary electrons emitted from the cathode. Such a modification was first made by Gawehn[6], who reported the use of a high frequency coil around the chamber to induce plasma formation. Vratny[7] used a different source of supplementary electrons, feeding the radio frequency power direct to the cathode superimposed on the dc bias. These methods offer the benefits of low

pressure operation to the glow discharge process, but there are more beneficial methods of achieving the same end.

3.2 DC Triode Sputtering

An ideal sputtering system is one in which the parameters affecting the discharge are independent and can be varied over a large range. The DC diode previously explained is an example of a non-ideal system, in that the cathodic current is voltage and pressure dependent; increase in cathodic voltage shifts the process from the normal glow to the arc region, and to maintain the discharge in the normal glow the gas pressure has to be increased. High discharge currents can be achieved only at sufficiently high pressure, but at the same time the use of high pressure causes shortening of the mean free path of particles and leads to a reduction in the deposition rate due to scattering of the sputtered flux. A development of diode sputtering which attempts to lower the working pressure while maintaining current density is triode sputtering, which involves the introduction to the system of an additional source of electrons. Electron injection into the discharge is achieved with a hot cathode, emitting electrons thermionically. The thermionic cathode is a heated tungsten filament, which can withstand ion bombardment for long periods. It is essential that the anode plate is biased positively with respect to the substrate, for if it is at substrate potential some thermionic electrons will deflect to the substrate surface, where they collect and can cause inhomogeneities in plasma density at the target.

Figure 3·2 shows a schematic of a triode sputtering system. Plasma confinement, necessary for increased plasma density, and hence lower pressure operation is achieved with a magnetic field provided by an external coil. Sputtering begins with the application of a negative potential with respect to the anode, with the familiar processes of ion mass and energy exchange occurring. The ion density in the plasma can be controlled in triode sputtering by either varying the electron emission current, or the voltage used to accelerate the electrons. Thus, a higher ionization density is maintained by supplying electrons at appropriate energies from a third electrode, with consequent operation at lower pressures ($\leq 10^{-3}$ torr) than in a conventional diode glow discharge system. The improvements offered by triode sputtering over

diode sputtering do not come without their own difficulties, however. The main limitations are the problem of non-uniform deposits from very large, flat targets, and the difficulty of controlling electron injection with sufficient accuracy for reproducible results[8].

Early work on triode sputtering concentrated on metal film deposition[9,10], which developed into alloy deposition[11], and finally successful semiconductor fabrication[12]. Sonkup[12] prepared n- and p-type GaAs films on single crystal semi-insulating substrates and studied the electrical properties of the films. Doping was achieved by co-sputtering a silicon or magnesium target of semiconductor grade purity, at a rate controlled by an applied pulsed voltage.

3.3 Getter Sputtering

The purity of a growing film is endangered by admixtures of active gases in the inert gas used. To reduce the concentration of active gas contaminents, use is made of the 'getter' effect. A depositing film is an active 'getter' of impurities, that is, it chemisorbs or forms compounds with residual gas molecules and the gas impurities which they carry. Molecules such as O_2, H_2, H_2O, N_2 and CO interact strongly with a number of metals, particularly aluminium, tantalum and titanium[13]. The getter effect can also reduce the process pressure, in the manner of a titanium sublimation pump in UHV systems, giving the associated benefits of lower pressure operation.

In a sputtering system consisting of a very large cathode and an equally large substrate holder, material that is deposited at the centre of the assembly will be free from impurities present in the sputtering gas, or those outgassed from the chamber walls. This is because the impurity atoms make many collisions with the sputtered material before reaching the central region, and have a high probability of being gettered before reaching that area. However, the technique is unable to remove gaseous impurities that were present in the cathode. Practical system dimensions are finite, and a reasonably gas-tight active volume has to be created within the system. With such an arrangement a positive pressure of sputtering gas is maintained within the chamber, and the tendency of contaminents such as oil vapours from the pumping system to enter the

Figure 3·1: DC Diode sputtering apparatus

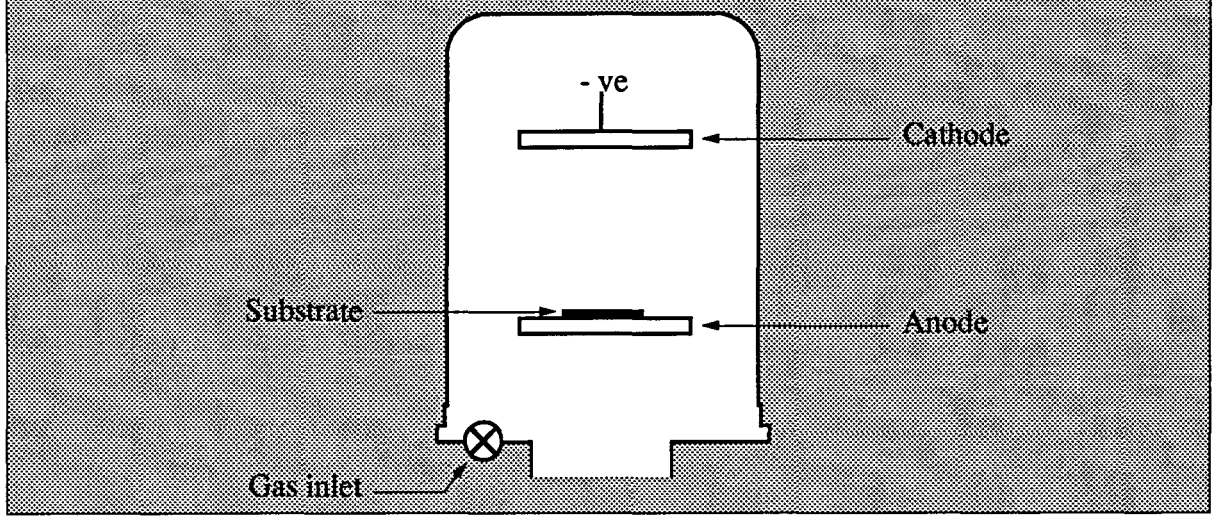

Figure 3·2: DC Triode sputtering apparatus

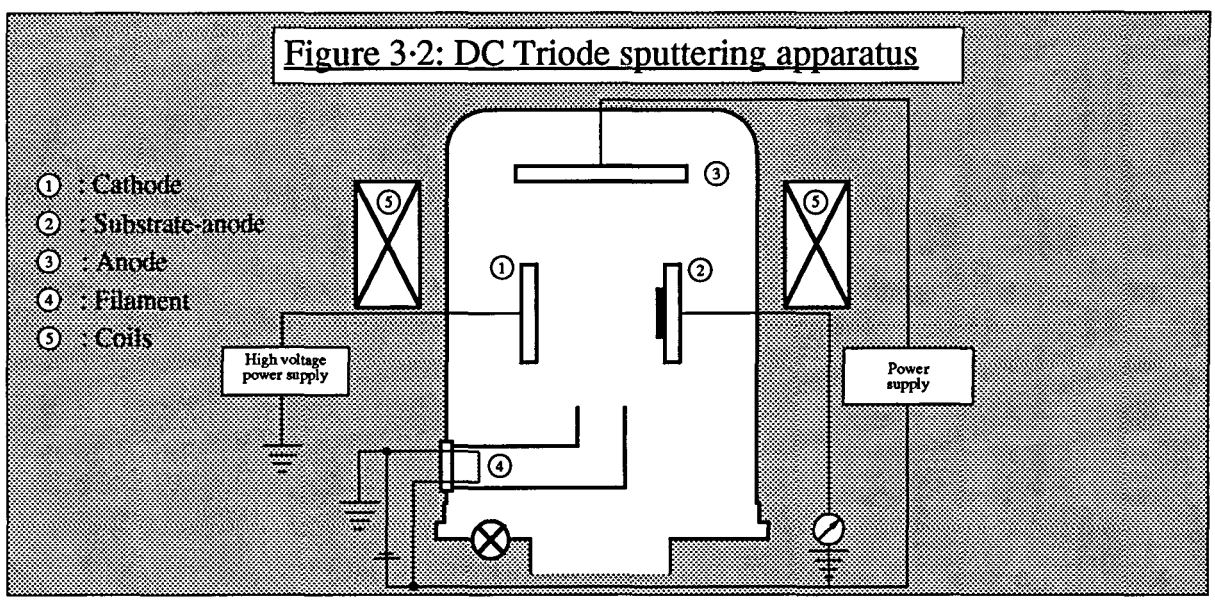

Figure 3·3: Getter sputtering apparatus

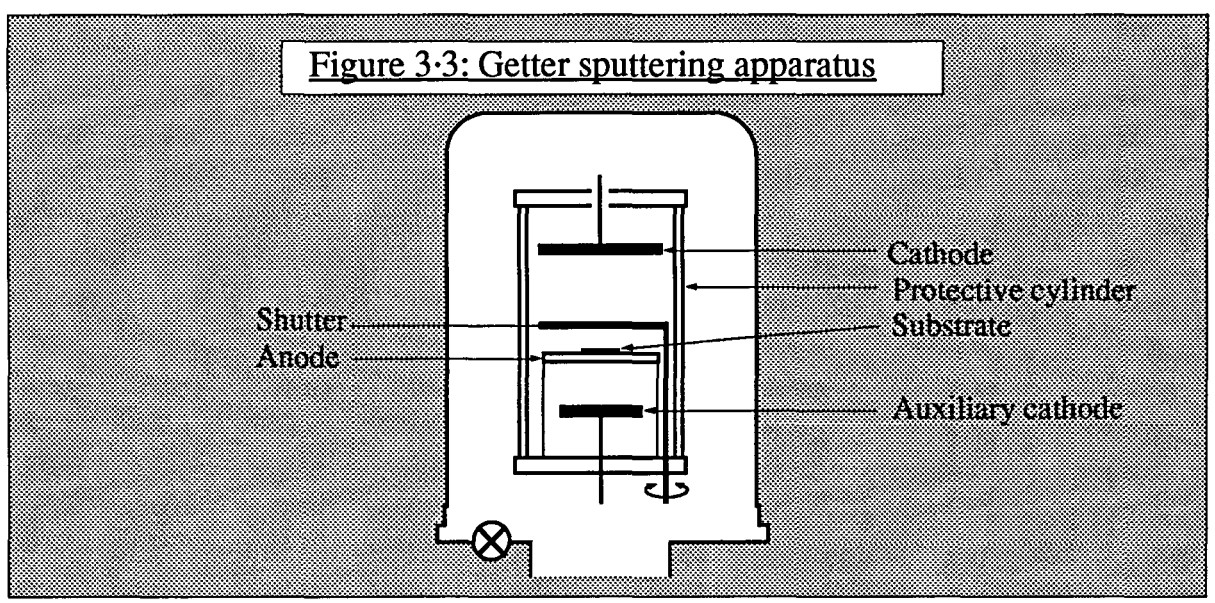

sputtering environment is reduced. Also, providing the enclosed volume is reasonably gas-tight, the pressure differential maintained between it and the main chamber volume can prevent backstreaming of pump oil vapour. A simple getter sputtering system is shown in figure 3·3, where two cathodes of the same material are located symmetrically with respect to a close fitting cylindrical volume inside the main chamber. The system is divided into two parts, the gettering region and the working region, in such a way that the gas which enters the working region has had to pass through the gettering region and is thus deprived of admixtures. The gases enter the vessel at the bottom, and maximum gettering of impurities occurs at the lower cathode, with additional gettering by the burial of impurities in the continuously depositing material on the cylinder walls. After sufficient purification has taken place, the pressure will have lowered and the shutter is opened to allow deposition from the top cathode onto the substrate.

The preparation of films by getter sputtering has not been extensively reported since the early work[14], perhaps because it is a technique which can be applied to other more commercially viable systems, such as magnetron sputtering. Hong *et al*[15] have reported successful deposition of GdCo alloys using getter sputtering, the argon content of the films being less than 1.0 atomic percent, and uniformly distributed.

3.4 Radiofrequency (rf) sputtering

The sputtering techniques described previously assume that the target should be conducting, so that it can act as the cathode plate, and will attract inert gas ions to perpetuate the process. In conventional dc sputter systems, the substitution of an insulating target material would result in an immediate accumulation of surface positive charge on the front face of the target, preventing any further ion bombardment.

The charge accumulation can be prevented by bombarding the insulator with both ion beam and electron beam particles simultaneously[16], but the most practical scheme for sputtering insulators was first suggested by Anderson *et al*[17]. If a low frequency alternating current is applied between the electrodes, the system behaves as if there were two cathodes, with a dark space being present in front of each. Such a

system is a succession of short lived dc discharges and, as in the case of conventional dc systems, relies on the generation of secondary electrons from one or both electrodes to sustain the discharge. As the frequency of applied potential is increased, the minimum operating pressure of the discharge is decreased, with the effect noticeable above about 50kHz and levelling off above several megahertz. In this situation the discharge is not being sustained by secondary electrons from the electrodes, but by those generated by the high frequency of the supply potential. Electrons in an rf field gain energy from the field as they oscillate within it by repeated collisions with gas atoms, so that the ordered simple harmonic motion of the electrons changes to a random motion. The electrons increase the random component of motion until they have sufficient energy to ionize a gas atom with which they collide. Thus, the high voltage necessary with dc sputtering to maintain the discharge, is not needed by the rf glow. Since the electrons have higher mobilities than ions, many more electrons reach the surface of the dielectric target in the positive half-cycle than ions will during the negative half, and the target develops a negative self-bias. The negative dc bias on the target surface repels electrons and creates an ion-rich sheath in front of the target, analogous to the Crooke's dark space in dc sputtering. The ions present there are accelerated to the target and consequent ejection of sputtered material occurs. The ion sheath does not appear below 10 kHz, and 13.56 MHz is usually the preferred operating frequency. Because the rf discharge is confined between the two electrodes, any electron which is randomly scattered out of this region no longer oscillates in the field, does not attain sufficient ionizing energy and is lost to the glow. The use of magnetic fields to trap the otherwise lost electrons is thus more necessary for rf than for dc sputtering. It is also essential to site an earthed plate behind the metal electrode on which the target is located. This prevents any discharge behind the target and contamination from metal sputtered from the plate.

Perhaps the most important difference between dc and rf sputtering systems is the need to provide an impedance matching network between power supply and chamber for the latter. It is also necessary to ensure adequate grounding of the substrate platform with rf sputtering, since a short circuit under dc conditions may exhibit considerable rf impedance, and if left uncorrected, can lead to undesirable induced rf voltages on the substrate surface. Adequate environmental shielding

must also be undertaken to protect against the interference of the 13.56 MHz radiation with communications equipment.

Several of the compounds produced in the experimental part of this work have been deposited using rf sputtering elsewhere. Radiofrequency sputtering of ITO[18], ZnO[19,20], SiO_2[21] and a-Si:H[22] have all been reported, but these all suffer two significant disadvantages inherent in the rf sputtering process. Because the target material is in pressed powder form of well-known stoichiometry, the deposited film is limited to the same stoichiometry, and has a lower deposition rate (a mere 0.3 $Å s^{-1}$ for the cited case of ZnO[19]) than dc sputtering at the same power. Chapter 4 will describe how dc reactive sputtering can be used with a single elemental target to deposit compound oxide and semiconductor films at higher rates than rf sputtering from an oxide target, and with continuously variable stoichiometries.

3.5 The dc planar magnetron source

The sputtering techniques previously explained, using dc diode, triode and radiofrequency, have the common disadvantage of slow deposition rate, and are consequently of little commercial feasibility. They are also high power consuming processes in relation to the amount of material transported. Magnetron sputtering encompasses a family of sources which achieve high deposition rates at lower pressures than standard sources, by employing a particularly oriented magnetic field in tandem with the electric field. Following an account of the development of the technique to date, the physics of the electron confinement and magnetic field design which distinguish the magnetron from conventional diode sputtering will be discussed.

3.6 The development to date of magnetron sputtering as a deposition technology

The basic principle of all magnetically enhanced sputtering techniques was indirectly discovered by Frans Penning[23], who patented a device for copper sputtering in 1939. In the Penning magnetron, the magnetic field was parallel to the length of a hollow cylinder, where the sheath of the

cylinder was used as an anode and an axially oriented cylinder of smaller diameter the cathode. Electrons within the cylinder are forced to travel small cycloidal paths on large circles concentric with the axis of the cylinder. An electron continues on this path until collisions are made with the gas, whereupon it moves closer to the anode at the centre of the cylinder. Because the electrons must undergo ionizing collisions before they can escape from the ends of the cylinder, the discharge can be sustained at very low pressures, and very high current densities can be achieved. The principle of the Penning magnetron was incorporated into a pressure gauge still used in high vacuum deposition today, where the potential difference between the electrodes is usually about 2kV and the magnetic field strength about 400 gauss.

The configuration of the Penning magnetron, and the similar developments of hollow[24]- and post-cathodes[25] demonstrate the confinement of primary and secondary electrons in a plasma utilising crossed electric and magnetic fields. For practical deposition purposes, however, the cylindrical systems have two main disadvantages. They are necessarily cylindrical to attain radial electric field and so are not well suited to large area substrates which have to be sited inside the 'tube'. Perhaps more important are the electron end-losses from the tube which reduce the efficiency of secondary electron generation, and hence both decrease plasma density and increase the minimum operating pressure. The resultant lack of substrate plasma bombardment has in the past been used to advantage in the coating of thermally sensitive substrates[26] but a magnetron sputter source without end losses is generally the preferred system today from the consideration of sputter rate, operating pressure and simplicity of target replacement. Such a system is the planar magnetron, introduced in 1974 by Chapin[27], although the basic principle had been demonstrated in 1959 by Kesser and Pashkova[28]. The general case of the planar magnetron is explained below, leaving specific design improvements developed during the course of this work to be described in chapter seven.

With linear drift velocities of the order of 10^7 ms^{-1}, electron end losses from cylindrical magnetrons are considerable, but the planar magnetron eliminates such losses whilst maintaining the desirable low pressure operation and high plasma density characteristic of the technique. To prevent electron loss, the drift path must conform to a closed loop. One

simple geometry is a disk shaped cathode having a toroidal plasma ring facing and parallel to a fixed substrate holder, which acts as the anode[29]. An alternative design is a rectangular or oval cathode, where the substrates are moved past the depositing flux to aid uniformity[30], and is extensively used in the large area glass coating industry. These two designs are the most popular, and the easiest to manufacture, but more intricate designs have been reported for coating of unique substrates[31]. Magnet arrangements can vary considerably from one design to another, the only constraint being that there must be at least one closed path where the magnetic field lines are parallel to the target surface. Figure 3·4 depicts a common rectangular magnetron where the re-entrant magnetic field is parallel to the target surface midway between the entry and exit points of the magnetic flux line. Also shown in the figure is the erosion zone created by such a domed magnetic field configuration. It is the desired closed loop designed to eliminate end losses, and has become known as the 'race track' because of its appearance. Away from the central region the field lines are at some angle α to the target, so that as the electrons accelerate across the dark space they gain a component of velocity $v'=v \sin\alpha$ parallel to the B field. This velocity carries the electrons along the magnetic field line, across the dome and down towards the target surface once more. Electrons originated by ion impacts on the target at a point where B is parallel to the target surface will have a small velocity v' across the dome. Those created or reflected from a point on the target where $\alpha \neq 0$ will move across the dome through the region where B is parallel to the target, so the highest electron density will be in this region. Ion creation rate is consequently highest here, and assuming the ions do not move far from their point of creation because of their greater mass, maximum sputtering of the target will occur beneath this region. A disadvantage of planar magnetron sputtering in this respect is that target erosion only occurs in the transverse magnetic field region. Unless efforts are made to widen this region, the incident ions are focussed into an increasingly narrow zone as erosion proceeds, leading to the characteristic V-shaped erosion profile. The target lifetime is reached when the groove reaches the back surface, and reported target utilizations at this point range from 26%[32] to 50%[33]. A figure of 90% has been quoted[34] for a design where a tubular target rotates around fixed magnets, giving the effect of a narrow planar magnetron with a continuously refreshed target

surface. The effects of maximum erosion in a region parallel to field lines is demonstrated in chapter seven when the erosion of non-target material resulted in film contamination and made it necessary to modify the magnetic design in order to both widen and move the maximum erosion zone.

Cathode cooling is imperative in magnetron sputtering because of the high power dissipation at the cathode. Indeed, an estimated 55%-70% of the power delivered to the cathode is dissipated in the coolant[35]. The primary limiting factor is the amount of power that can be safely applied to the cathode without it melting, cracking or warping. The design of the coolant supply system, its pressure and flow rate behind the cathode, the structural stability of the cathode and its thermal conductivity are important considerations which have to be addressed when building a new device. Such considerations have had to be made during the modification to the magnetrons used in this work.

The magnetic array behind the target is usually held in a non magnetic metal former, the body, which assumes cathode potential during operation. To prevent sputtering from the sides of the magnetron body, an earth shield is employed. This is a metallic non-magnetic 'shell' which surrounds the sides of the magnetron and is held at ground potential. It is essential that the distance between the magnetron body and earth shield be less than the mean free path for electrons at the particular process pressure used. If it were not, the electrons would attain enough ionizing potential before reaching the shield and a discharge would preferentially strike between the body and earth shield as if the latter were an anode, leading to arcing, rapid heating of the shield and zero sputtering from the intended source. For most planar magnetrons the earth shield is no more than 2 or 3mm from the body, compared with a mean free path of 1.79cm at 3 mTorr for argon. The rear of the magnetron body has to be similarly protected by an earth shield, which is normally part of the one around the sides, the whole shield assembly being physically and electrically isolated from the body by a polymeric insulator.

Figure 3·4: The erosion zone of a planar magnetron defined by crossed v and B fields

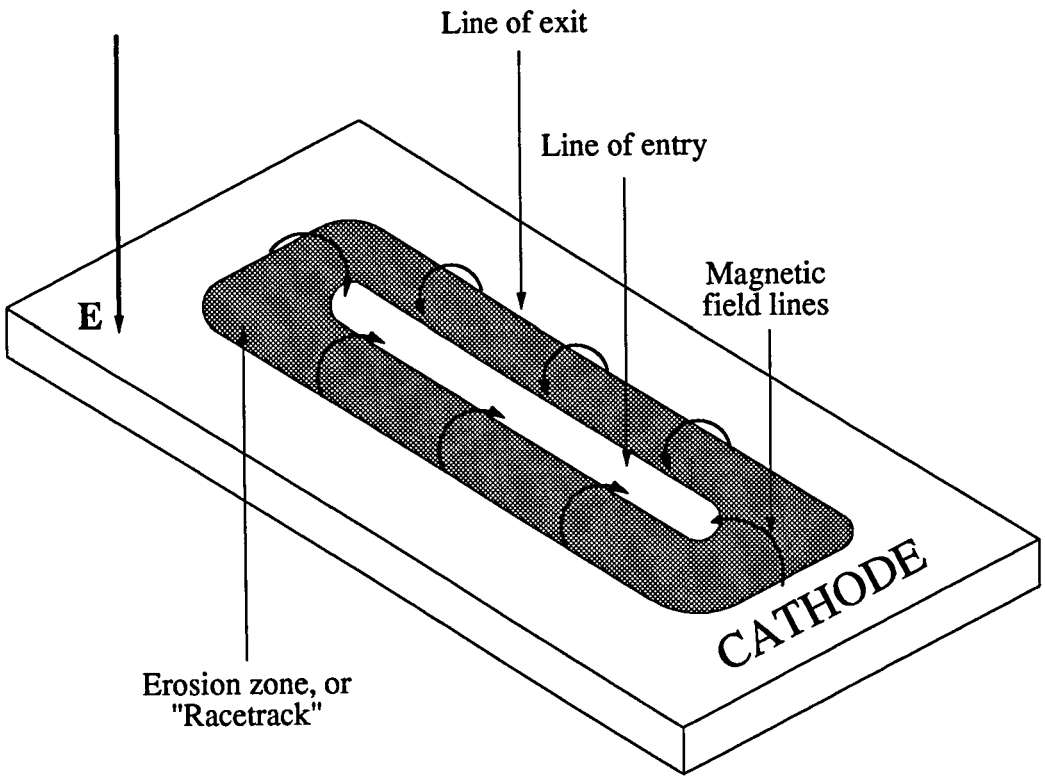

3.7 Physics of electron confinement and effects on operating characteristics

3.7.1 Behaviour of a moving electron in a magnetic field

Consider the motion of an electron with mass m, moving with velocity **v**, under the action of the force e(**v** x **B**) in a uniform **B** field. Force and acceleration are always perpendicular to both **v** and **B**, so any component of **v** parallel to **B** remains unchanged. Assuming the electron is initially moving with its velocity perpendicular to **B**, as in figure 3·5, the force is Bev in magnitude and acts at 90° to **v**. It can only alter the direction of v, not its magnitude, so the electron moves in the circular path shown. If we let the radius of the path be r_2, the acceleration towards the centre is v^2/r. Classical mechanics gives the force $Bev=mv^2/r_2$, or:

$$r_2 = \frac{m v}{e B} \qquad [3\cdot1]$$

3.7.2 Behaviour of an electron in electric and magnetic fields.

Now suppose that a stationary positive charge Q placed at any point in a region experiences a force $\mathbf{F}_E$. There is an electric field in the region whose strength **E** at the point is given by the force per unit positive charge:

$$\mathbf{E} = \mathbf{F}_E/Q \qquad [3\cdot2]$$

Now assume that the charge is an electron e, so that the force acts in the opposite direction to that experienced by the positive charge above. In this case the force on the electron is given by $\mathbf{F}_E = e\mathbf{E}$. If the charge is moving with a velocity **v** in a magnetic field of strength **B**, it will experience a force $\mathbf{F}_B$, given vectorially by:

$$\mathbf{F}_B = e\ \mathbf{v} \times \mathbf{B} \qquad [3\cdot3]$$

The Lorentz force law states that when both **E** and **B** exist at a point, the total force **F** on the electron e moving with velocity **v** is given by

$$\mathbf{F} = e\,(\mathbf{E} + \mathbf{v} \times \mathbf{B}) \qquad [3\cdot4]$$

The Lorentz force enables the trajectories of electrons free to move under the action of **E** and **B** to be calculated.

Using the notation of figure 3·6, it can be seen that any z-component of velocity will remain unchanged because no force acts along this axis (out of the page). Hence, any motion beginning in the xy-plane will remain there. Given any initial velocity, the general trajectory can be obtained by solving the equations of motion.

$$F_y = m\ddot{y} = e(E - v_x B) \qquad [3\cdot5]$$

$$F_x = m\dot{x} = e v_y B \qquad [3\cdot6]$$

If, however, the initial velocity v_y is zero and v_x = E/B, then both F_x and F_y are zero and remain so. Of all the particles entering the fields with a velocity perpendicular to both, only those with v = E/B are undeflected. It is clear that an electron moving with v = E/B experiences no force in the y-direction and is effectively in a zero y-field. A non zero y-field will only come into effect when v_x differs from E/B.

Let $vx = ux$ + E/B, and the equations of motion become

$$F_y = e\,u_x B \qquad [3\cdot7]$$

$$F_x = e\,v_y B \qquad [3\cdot8]$$

If the system was viewed from an origin moving with an x-velocity of E/B, equations [3·7] and [3·8] would be the equations of motion.

The resultant motion from a fixed origin is thus a combination of a uniform linear drift velocity and a uniform circular motion in the same plane, the latter being generated by the influence of B being

Figure 3·5: Forces on an electron under v x B, no E field

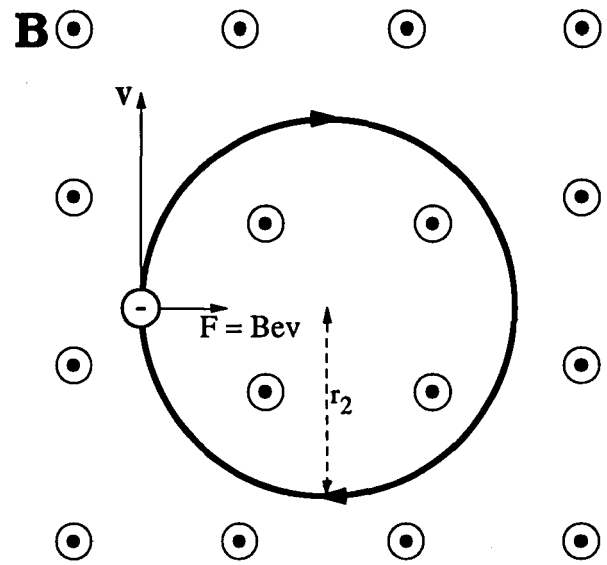

Figure 3·6: Forces on an electron under E x B

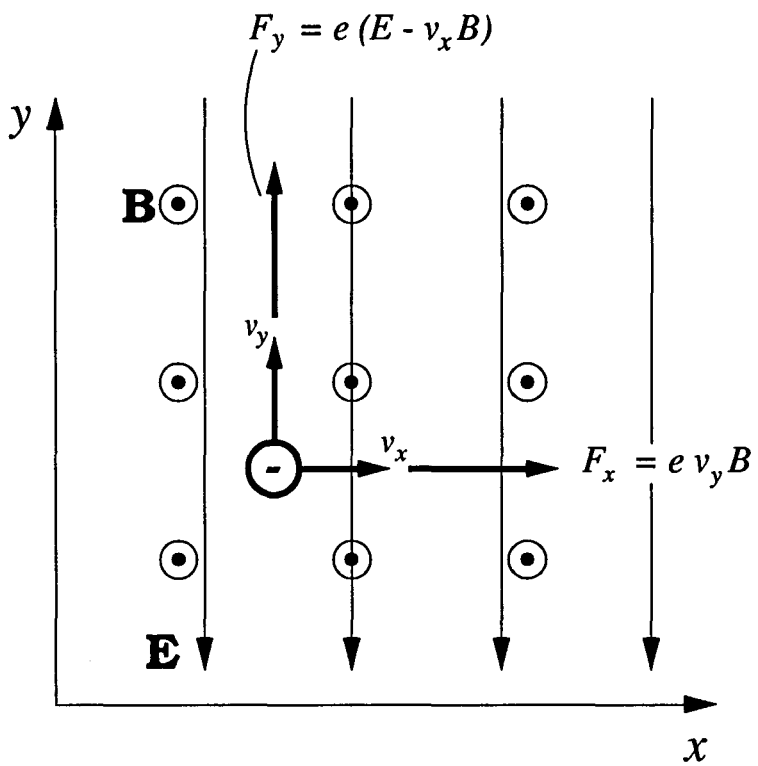

perpendicular to the initial direction of the electron. The angular acceleration is mv^2/r, and is equal to the magnetic force evB, so the radius of the circular motion $r = mv/eB$, with v having components u_x and v_y. The drift velocity can be written as $v = E/B$, in which case

$$r = \frac{E \,.\, m}{B^2 . e} \qquad [3\cdot9]$$

3.7.3 Implications for electron travel above a magnetron cathode

An effect similar to the creation of the dark space seen in diode sputtering, where a space-charge region is formed in front of the cathode, is seen with the magnetron. The magnetron 'dark space' is difficult to model and is generally assumed to have a thickness of ~0.5mm. It is across this region only that the electric field acts, with the plasma beyond remaining essentially neutral.

Assuming a 'typical' planar magnetron, the magnetic field will be ~500 Gauss (0.05 Tesla), the operating potential around 500 V, and the dark space at typical sputtering pressures 0.5mm. These conditions give an electric field strength of the order of 10^6 Vm^{-1}, which results in the radius of the circular component of **E x B** cycloid motion attaining a value between of ~2.5 mm in the dark space and the drift velocity E/B of the order of 10^7 ms^{-1}. Figure 3·7 depicts the electron travel in the **E x B** fields with magnitudes as above, and shows the radius r = 2.5mm of the circular component. Also shown to scale is the dark space of 0.5mm thickness. There is zero **E** field above the line 'A'-'B' so the only motion applicable to the **E x B** model in a magnetron is that below the line. Reference is seldom made to this in the literature, much of it assuming that the **E x B** field alone is responsible for the electron trapping close to the cathode surface[36,37], when it is seen from the above discussion that this field only gives the electron an acceleration with a small angle deflection across the dark space.

Figure 3·8 shows the net motion above the cathode. Beginning with its ejection from the cathode surface, the electron is subject to the E x B force, but *only in the dark space region.* This force gives it a component of velocity at a small angle to the normal, but the magnitude of the E field overpowers the B field to such an extent that the ejection direction is essentially normal to the cathode surface across the full width of the

Figure 3·7: Motion of an electron with E x B oriented as figure 3·6

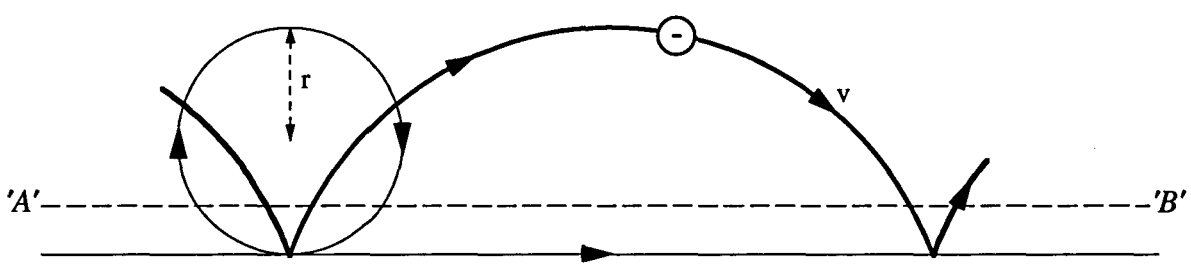

Circular motion + linear motion = cycloid

Line 'A'-'B' is the projected limit of magnetron dark space, shown only as a reference level to aid understanding of figure 3·8.
The dark space concept has no meaning in the above figure.

Vertical dimensions illustrated are not to scale

Figure 3·8: An approximation to the electron path above the cathode of a planar magnetron

Vertical dimension not to scale

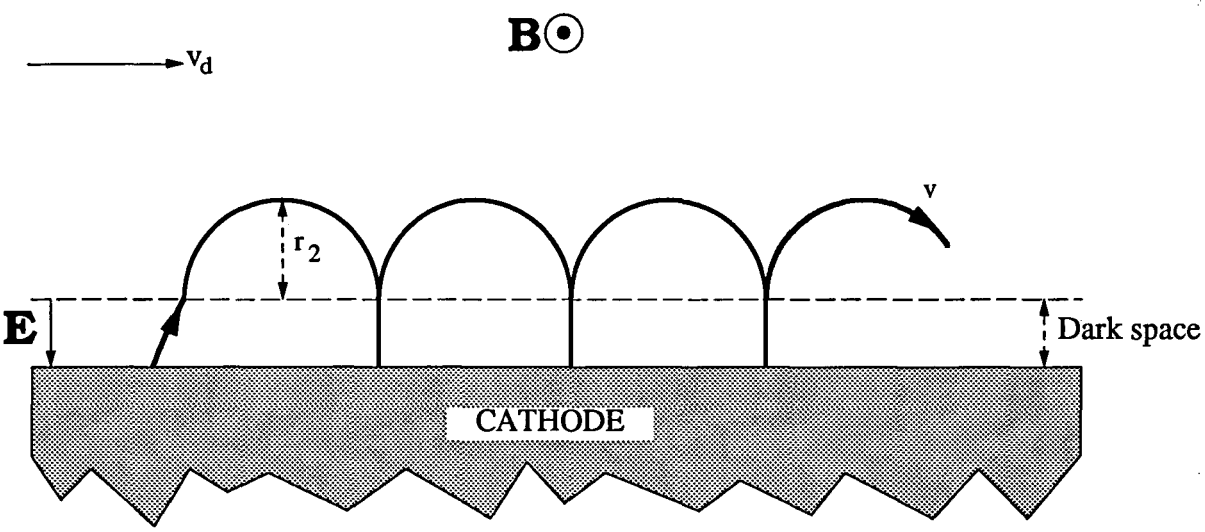

Under typical magnetron operation:

Argon pressure = 3 mTorr
$v = 1.3 \times 10^7$ m/s
$r_2 = 1.5$mm
Dark space ~0.5mm
$v_d \sim 8.4 \times 10^6$ m/s

dark space. Upon entering the plasma region with velocity v, obtained from its acceleration through the dark space, the electron undergoes the circular deflection due to the **v x B** field (equation [3·1]). After completing a half cycle it encounters the dark space once more. The electrons involved in this semicircular motion have mean free paths of the order of ~1m, so it is reasonable to assume the electron has velocity equal to that with which it left the **E** field, and that it will penetrate the dark space to the cathode, where it will be repelled and ejected normal to that surface. This repeated ejection from, and return to, the **E** field results in the electron travelling in a series of semicircular 'hoops' precessing around the erosion zone of the cathode.

3.7.4 RF frequencies induced in the plasma.

The movement of charged particles described above gives rise to oscillation frequencies which have been observed[38], and can affect the power supply to the magnetron if it is not suitably protected. These frequencies are now quantified for each motion, assuming a magnetron with a magnetic field of 500 Gauss (0.05 Tesla) and an operating voltage of 500V operating in 3 mTorr of argon. The erosion zone is assumed to be 25mm wide, with a radius at its centre of 5cm, so that its length ~30cm.

(i) The ejection velocity from the dark space is calculated by equating the acceleration energy to the kinetic energy:

$$eV = \frac{1}{2} mv^2 \qquad [3\cdot10]$$

Hence v = 1.3 x10^7 ms^{-1}. Combining the radius of curvature above the dark space (equation [3·1]) with the velocity[33] gives an estimate of the drift velocity v_d as:

$$v_d = \frac{2v}{\pi} \qquad [3\cdot11]$$

So v_d ~ 8.4 x10^6 ms^{-1}. The drift velocity period around the 0.3m long erosion zone is then 3.5 x10^{-8} s, and the frequency of the drift velocity component, f_{vd} = 28 MHz.

(ii) Using the 'typical' magnetron parameters once more, equation [3·1] gives the radius of curvature in the plasma to be 1.5mm, and the

time taken to traverse the semicircle is 3.6 $x10^{-10}$ s. The deceleration, a, across the dark space is calculated by equating the forces:

$$-ma = eE \qquad [3\cdot12]$$

Hence a = -1.75 $x10^{17}$ ms^{-2}. This gives the time to decelerate as 7.5 x 10^{-11} s. The electron crosses the dark space twice before it completes one cycle, so the total time in dark space is 1.5 x 10^{-10} s. The time for one period is then 5 x 10^{-10} s and the frequency of 'hopping' is 1.9 GHz.

(iii) Rossnagel and Kaufman[39] reported a proportional relationship between the **v x B** drift current and magnetron current, with the drift current generally a factor of 3 to 9 higher. There was also a dependence of the drift current on gas pressure, with lower pressures leading to higher drift currents. They proposed that the magnitude of the drift current implied that the dominant mechanism for electron conduction across magnetic field lines was Bohm diffusion[40], characterized as a turbulent collective behaviour of the electrons. The electron collision frequency is increased by several orders of magnitude by the turbulent, collective motion of the electrons. Following such turbulence, some electrons will be scattered onto nearby magnetic field lines, around which they rotate, but are also subject to a drift velocity along the lines. This results in a helical path, whose cyclotron frequency ω_c is given by:

$$\omega_c = \frac{eB}{m} \qquad [3\cdot13]$$

The 'typical' magnetron values give ω_c = 8.8 GHz.

(iv) The plasma frequency is given by:

$$\omega_p^2 = \frac{e^2 n_e}{m \varepsilon_0} \qquad [3\cdot14]$$

Taking the electron density n_e = 2 $x10^{15}$ m^{-3} for a magnetron[41], gives ω_p = 2.5 GHz.

Table 3.7 summarises the calculated rf frequencies induced by magnetron operation.

Table 3.7 Origins and magnitudes of induced frequencies

Origin of induced frequency	Induced frequency
Electron drift velocity	28 MHz
Electron 'hopping'	1.9 GHz
Cyclotron	8.8 GHz
Plasma	2.5 GHz

It has been shown above that by arranging the electric and magnetic fields in which an electron is located such that they are normal to each other, it can be made to travel in a cycloid path. Its motion is affected so that the distance it travels between two points is many times the linear distance between the points. With regard to gas discharge processes, the consequent reduction in collision cross-section has the joint effect of increasing plasma density and of confining the plasma close to the target surface.

3.7.5 The current-voltage relationship

The functional relationship between operating current I and voltage V for a planar magnetron is given empirically by

$$I = kV^n \qquad [3{\cdot}15]$$

where k and n are constants, the exponent n generally in the range of 5 to 15. Both constants depend strongly on gas-target combination, magnetron design, magnetic field and configuration and other experimental parameters. When n assumes a high value in the range, the voltage change is slow for large changes in discharge current and can, in most experiments, be ignored.

Ordinarily, the electron temperature within the plasma will be of the order of a few eV, whilst the ion temperatures can be hundreds of degrees centigrade. Although essentially neutral, the plasma potential

becomes slightly positive with respect to the anode, and the plasma is bordered by space-charge regions. In the plasma sheath at the magnetron cathode (analogous to the Crookes dark space of diode sputtering) the potential difference is large compared with the electron temperature. The ion current density through this sheath is given by Child's law[42]:

$$j = \left(\frac{4\varepsilon_0}{9}\right)^2 \left(\frac{e}{m}\right)^{0.5} \left(\frac{V^{1.5}}{d_0^2}\right) \qquad [3\cdot16]$$

where j is the dominant charge carrier density (ions at the target), ε_0 the permittivity of free space, e/m the charge to mass ratio for the ion species, and d_0 the width of the sheath.

It may be intuitively assumed that the magnetron plasma is bounded by positive space-charge sheaths, and that the relation between discharge voltage and current would follow Child's law, equation [3·16]. However, the voltage dependency of equations [3·15] and [3·16] are visibly dissimilar. Measurements of the dependence of sheath thickness on operating potential[43] have shown a relation of the form:

$$d = cV^m \qquad [3\cdot17]$$

where c is a constant and m a negative number between -3 and -6 for the cited case of a copper target sputtering in argon. Combination of equations [3·17] and [3·16] gives a result similar to the empirical result given by equation [3·15], confirming that the sheath is indeed a simple, positive space-charge sheath.

3.7.6 Magnetron generated modifications of gas density

Local perturbations in gas density in the cathode region of a magnetron were reported by Hoffman[44]. A strong "sputtering wind" was found in near-cathode regions, driven by the kinetic energy of sputtered atoms and a component of reflected neutrals from the cathode surface. The net density change in the cathode region as a result of sputtering has been more recently studied by Rossnagel[45]. By inserting sampling tubes, connected to a capacitance manometer, into the plasma he found that the local gas density in the cathode region dropped significantly as the

current to the cathode increased. Reductions of up to 85% of the original gas density were found at 3kW, using Cu sputtered in Ar. The density reduction was even greater for high sputter yield cathodes, and for high-mass gas atoms such as Ar and Kr. Two possible reactions were suggested to account for the gas rarefaction; the transfer of kinetic energy from the sputtered atoms to the gas ions, and the heating by reflection and neutralization of ions following target bombardment. Experimental results were inconsistent with the latter mechanism, showing that the strongest gas density reduction occurred with heavy gas atoms, which would be expected to have a very low reflection probability. The significance of the rarefaction of gas close to the cathode is that it will change the impedance of the plasma, and hence the voltage as a function of discharge current. The discharge voltage is the product of the discharge current and plasma impedance at that current. Discharge current is given by the current density times the *effective* area of the cathode, the latter being the area of the racetrack. Current density, j, for weak magnetic fields was derived by Chapman[46]:

$$j = 0.6n_e (kT_e/m_i)^{0.5} \qquad [3\cdot18]$$

where n_e is the electron density, T_e the electron temperature and m_i the ion mass. The plasma impedance is a function of the discharge current and can be calculated from the cross-magnetic field conductivity σ_b, based on Bohm diffusion:

$$\sigma_B = en_e/16B \qquad [3\cdot19]$$

Impedance is related inversely to the conductivity given by equation [3·19]. The voltage, then, is the product of plasma impedance and discharge current, and when combining these terms the electron densities cancel, leaving only a functional dependence on electron temperature:

$$V = \alpha (kT_e)^{0.5} \qquad [3\cdot20]$$

where α is a constant for a given gas-target combination, magnetic field and system geometry.

The discharge voltage has been shown above to be a function of local gas density in the cathode region, which is caused by the heating of gas atoms by sputtered target material. As discharge current increases, the sputter flux density increases and the gas density is reduced due to the sputtered atoms, with the result that the plasma impedance, and hence magnetron voltage, increase. In the empirical relationship of equation [3·15], systems with proportionally high gas rarefaction will be characterized by a small value of n. In cases with very little, or no sputtering, such as He gas with W cathodes, no gas density changes will occur and the voltage is almost constant with exponents of 25 to 75 or more.

3.8 'Balanced' and 'Unbalanced' magnetrons

Effects of ion-assisted deposition have been studied extensively in recent years, but only during the last six or seven years has the potential to use magnetron sputtering as a source of beneficial ion bombardment been realised. In conventional planar magnetrons, the discharge is confined by the magnetic field to a region close to the cathode surface, with the result that bombardment of the growing film with particles other than the depositing film material is minimized. There have, however been many cited examples of improved thin film properties obtained by bombarding the growing film with ions[47-49]. It is generally recognised that the ion bombardment process during film growth will change the film nucleation process, film morphology, stoichiometry, adhesion, stress, degree of crystallinity, and optical and electrical properties. These changes are attributed to the re-sputtering of condensed species, modification by in-situ annealing and to increased adatom mobility[50]. Ion assistance has proven particularly useful for hard protective coatings[51] and for wear resistant metallurgical coatings[52]. Since the planar magnetron has a ready supply of ionized particles available whilst it is in operation, the technique can be adapted to direct a proportion of these ions towards the substrate during deposition to enhance the film properties without significantly affecting the sputter rate. Published work on ion fluxes from magnetic discharges is still

minimal, despite the significant advantages provided by the technique. Schiller *et al*[53] reported that for most dc magnetrons the ion fluxes are usually 5-10% of the deposition flux. Fraser & Cook[54] were perhaps the first to recognise the potential of the technique, and to discuss the use of "aiding" or "opposing" magnet configurations behind the substrate to affect the ion flux to the substrate. The pioneering work on ion-assisted magnetron deposition was undertaken by B. Window & N. Savvides, whose three papers[55-57] from 1986 initiated interest in ion modification using magnetrons, and quantitatively categorized the two states of magnetic field which they termed "balanced" and "unbalanced".

The basic magnetic geometries showing the extremes of unbalance are shown in figure 3·9, for a planar magnetron with a central cylindrical magnet and a concentric annular magnet to complete the necessary closed field. Type I is one extreme, where all the magnetic field lines originate from the central magnet, with some not passing into the annular magnet. In the other extreme, type II has all field lines originating on the annulus with some not passing to the centre. The intermediate type shows the balanced special case where all field lines pass from the centre to the annular pole. It is rarely appreciated that the balanced magnetron cannot be practically achieved, because it requires equal strength for inner and outer poles. The planar magnetron design precludes this because its geometry dictates that there is a greater volume of magnetic material around the outer pole, so that balance is rarely achieved even by using magnetic materials of different strengths in outer and inner poles.

Type II designs are easily identifiable by observation of the plasma confinement they provide. Viewed from the side, such designs show a 'plume' of discharge extending toward the substrate from the centre of the target, caused by the concentration of secondary electrons around the field lines in the centre, which they meet first on scattering or 'leaking' from the racetrack. Some electrons accelerate away from the cathode and scatter out of the closed field, taking ions with them by electrostatic forces. The substrate is usually isolated, but can be biased if the substrate or film are conducting. Because of the relative masses of electrons and ions in the plasma, the substrate is subject to a greater flux of the former and an isolated substrate will charge negatively with respect to the plasma until the two fluxes are equal. This is the self-bias

Figure 3·9: Three degrees of magnetron balance

From reference 55

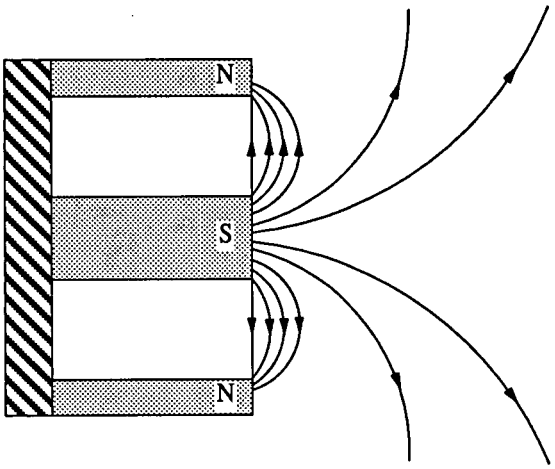

TYPE I

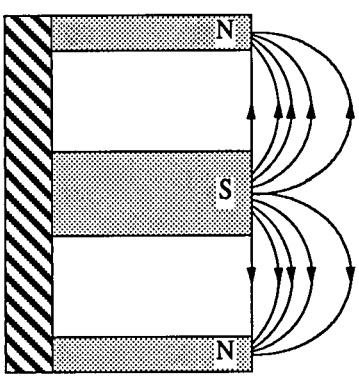

INTERMEDIATE

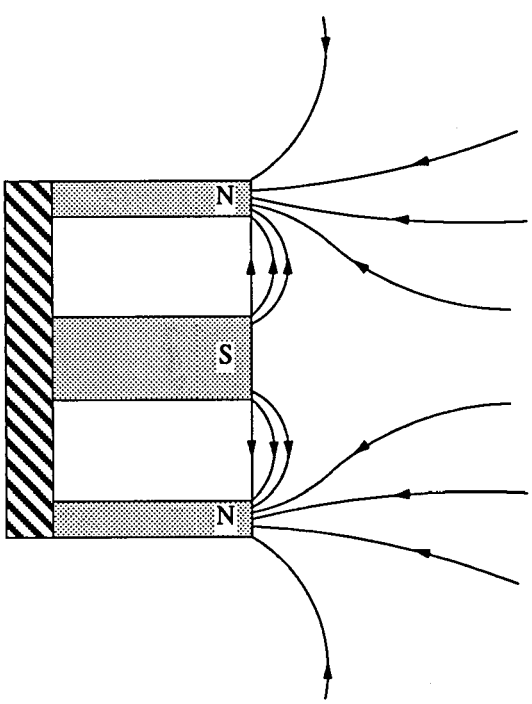

TYPE II

Plate 3·1
The unbalanced magnetron plasma extending towards the substrate

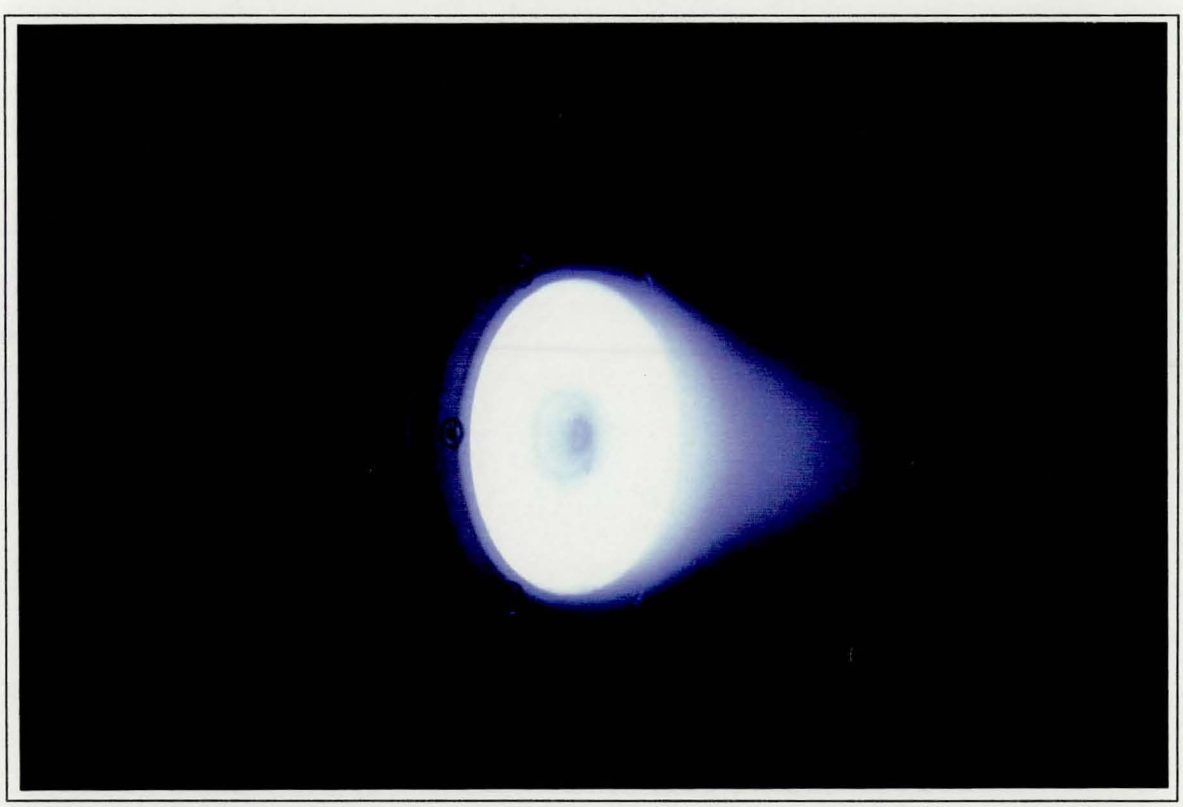

potential of the substrate and is the potential which insulated substrates will assume. It is this potential which accelerates ions towards the substrate to give bombardment of the film. In general, unbalanced planar magnetrons are quoted as imparting self-biases of around 30V[58-60], changing only slowly with magnetron operating power. The practical upper limit to ion current density is determined by re-sputtering, when the substrate or film undergo a bombardment in excess of the sputter threshold. Such re-sputtering is routinely used in the ophthalmic and large area glass coating industries, for pre-deposition discharge cleaning of the substrate using oxygen ions. An example of a type II discharge, from the work on silicon oxide undertaken in this study, is shown in plate 3·1, with the characteristic 'plume' clearly visible.

The unbalanced magnetron provides a comparatively simple, low cost solution for ion-assisted vacuum deposition. Not only does the source supply a deposition flux, but also a flux of ions and electrons coincident upon the substrate, the magnitude of which can be varied at will by the use of auxiliary magnets or substrate biasing potentials. For insulated substrates, the equalisation of ion and electron currents allows the substrate to develop a self-bias of around -30V with respect to the plasma, with a incident ion current density of around 5 $mAcm^{-2}$, dependent on deposited species.

3.9 A new development: Low-voltage magnetron deposition

The sputter yield, as defined in chapter two, has been compiled for a collection of cathode materials as a function of incident ion energy by Bunshah[61]. The results for silicon are reproduced in figure 3·10, and show that the highest yields are obtained with higher energy ions. At the cathode voltages of around 700V used for the conventional unbalanced magnetron deposition of a-Si in the previous chapter, the yield per ion is 0.55. If the yield in atoms/ion is converted to atoms per unit current, and then divided by the operating potential of the magnetron at each ion energy, a figure for sputter flux per unit power is obtained. The additional curve in figure 3·10 shows the calculated sputter flux per unit power as a function of ion energy, obtained from the original data of Bunshah. Since the multiplier to convert ions to unit current is a

Figure 3·10
Variation of silicon sputter yield with ion energy (reference 61)
and resulting calculated sputtering efficiency curve

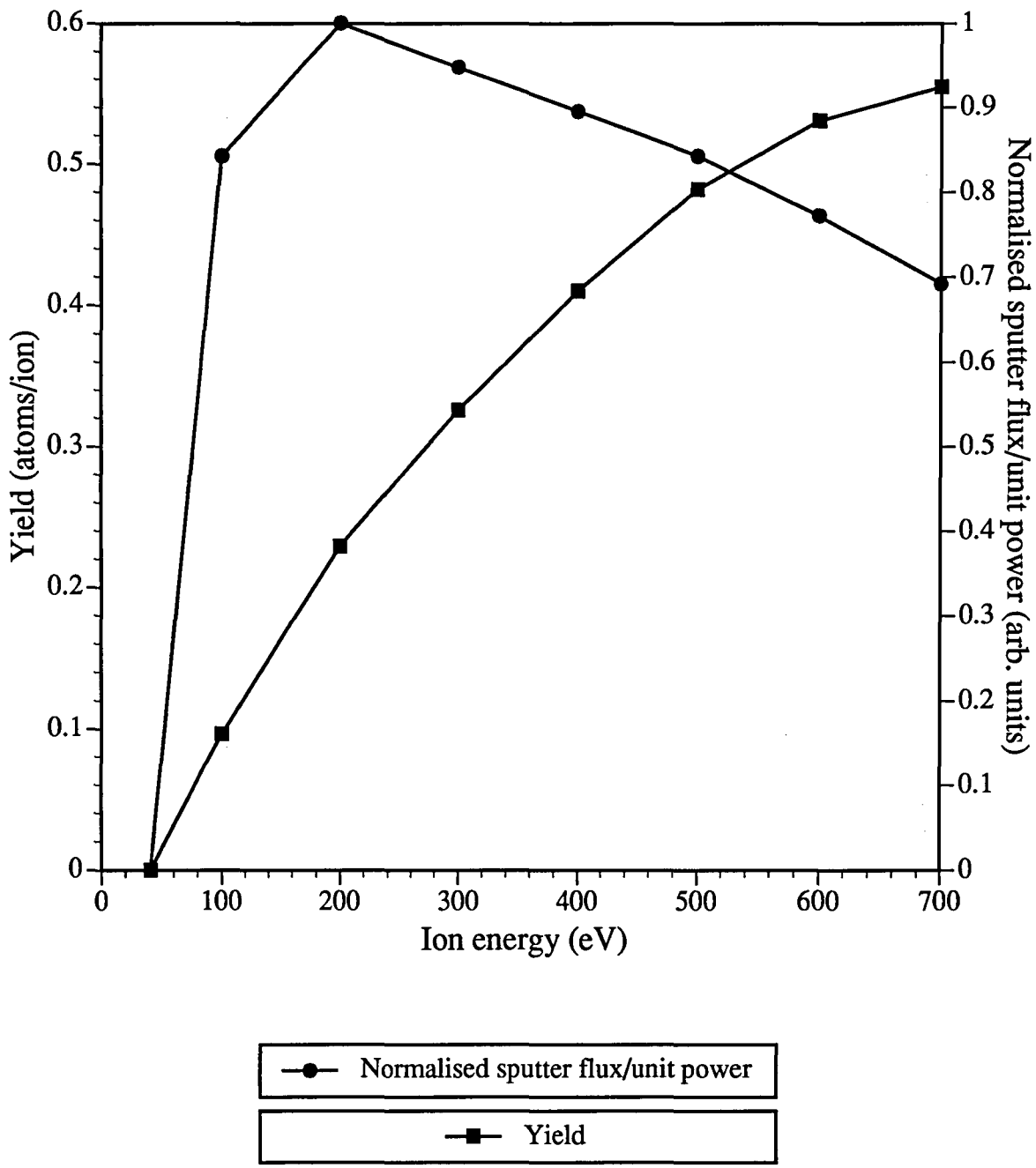

constant, the normalised unit power figure has been calculated by dividing the yield (atoms/ion) directly by the magnetron voltage. This calculation shows that the highest sputter flux per unit power does not occur at a magnetron potential of 700V, where the yield is highest, but at 200V. An additional advantage gained by operating at such a low voltage is the much reduced ion damage to the film. Although the initial energy of the ions will be ~200eV, traversal across the dark space will reduce this energy to ~100eV, and it was anticipated that this low bombardment energy would result in the band gaps of deposited films moving more towards that of the crystalline structure. Despite the lower sputter yield, then, the advantages of low voltage sputtering (LVS) are twofold; (i) reduced ion damage to the film, and (ii) a more efficient sputtering process.

The application of low-voltage magnetron deposition is a new discipline, and has only been reported recently. Having introduced the advantages of the technique with respect to film properties and sputtering efficiency here, chapter five will present an example of the technique applied to the deposition of indium oxide films. Chapter twelve will describe in detail the design requirements necessary for the development of the low voltage magnetron source used in this Thesis.

Chapter Three References

1: M. Naoe, S. Hasunuma, Y. Hoshi & S. Yamanaka., *IEEE Trans. Magn.*, **17**, (1981), 3184

2: M. Hong, J. Kwo, C. H. Chen, A. R. Kortan & M. Okada, AIP Conf. Proc. (USA), **182**, (1988), 127

3: J. Schubert, U.Poppe & W. Sybertz, *J. Less Common Met.*, **151**, (1989), 277

4: L. I. Maissel & J. H. Vaughn, *Vacuum*, **13**, (1963), 421

5: L. I. Maissel, U.S. Patent 3294661, (December 1966).

6: H. Gawehn, *A. Agnew Phys.*, **14**, (1962), 458

7: F. Vratny, *J. Electrochem Soc.*, **114**, (1967), 505

8: S. Maniv, *Vacuum*, **33**, (1983), 215

9: J. Edgecumbe, L. G. Rosner, and D. E. Anderson., *J. Appl. Phys*, **35**, (1964), 2198

10: R. C. Sun, T. C. Tisone & P. D. Cruzan., *J. Apl. Phys.*, **44**, (1973), 1009

11: R. O. Adams, C. W. Nordin & K. D. Masterton., *Thin Solid Films*, **72**, (1980), 335

12: D. M. Mosher & R. J. Sonkup, *Thin Solid Films*, **98**, (1982), 215

13: R. A. Swady, "Development of vacuum technologies for the preparation of high purity thin films in simple systems", PhD Thesis, Loughborough University of Technology, U.K., (1992)

14: H. C. Thuerer & J. J. Hauser, *J. Appl. Phy.*, **40**, (1969), 2994

15: M. Hong, E. M. Gyorgy & D. D. Gacon, *Appl. Phys. Lett.*, **44**, (1984), 706

16: R. L. Hines & R. Wallor, *J. Appl. Phys.*, **32**, (1961), 202

17: G. S. Anderson, W. N. Mayer & G. K. Wehner, *J. Appl. Phys.*, **33**, (1962), 2991

18: C. V. R. V. Kumar & A. Mansing, *J. Appl. Phys.*, **65**, (1989), 1270

19 A. Valentini, A. Quirini & L. Vasanelli, *Thin Solid Films*, **176**, (1989), L167

20: A. Krzesinski., *Thin Solid Films*, **138**, (1986), 111

21: J. Santamaria, F. Sanchez-Quesada, G. Gonzalez-Diaz, E. Iborra & M. Rodrguez-Vidal, *Thin Solid Films*, **125**, (1985), 299

22: G. S. Sunatori & A. a. Benezin., *J. Appl. Phys.*, **55**, (1984), 3125

23: F. M. Penning., *U.S. Patent 2146025,* (1939)

24: W. D. Gill & E. Kay., *Rev. Sci. Instrum.*, **36**, (1965), 277

25: F. A. Green & B. N. Chapman., *J. Vac. Sci. Technol.*, **13**, (1976), 165

26: D. Bohm, E. H. S. Burhop & H. S. W. Massey., "Characteristics of Electrical Discharges in Magnetic Fields", McGraw-Hill, (1949)

27: J. S. Chapin., *Res./Dev.*, **25(1)**, (1974), 37

28: I. G. Kesser & V. V. Pashkova., *Sov. Phys. Tech. Phys.*, **4**, (1959), 254

29: S. Schiller, U. Heisig & K. Goedicke, *Thin Solid Films*, **40**, (1977), 327

30: R. L. Cormia, P. S. McLeod & N. K. Tsujimoto., *6th Int. Conf. on Electron & Ion Beam Tech.*, San Francisco, (1974), page 248

31: S. Schiller, U. Heisig & K. Goedicke., *7th Int. Conf. on Vac. Met.*, Tokyo, Japan, November 1982

32: J. S. Chapin., *Res. Develop.*, **25(1)**, (1974), 37

33: A. G. Spencer, C. A. Bishop & R. P. Howson., *Vacuum*, **37(3/4)**, (1987), 363-366

34: M. Wright & T. Beardow, *J. Vac. Sci. Tech. A* , **4(3)**, (1986), 388-392

35: D. J. Ball., *J. Appl. Phys.*, **43**, (1972), 3047

36: J. S. Chapin., *Res. & Dev.*, January 1974, p.37-40

37: W. D. Munz, in "Wear and Corrosion resistant coating by CVD and PVD", ed. H. K. Pulker, Wiley (1989)

38: A. G. Spencer & R. P. Howson, *Vacuum*, **38**, (1988), 497-498

39: S. M. Rossnagel & H. R. Kaufman, *J. Vac. Sci. Technol. A*, **4**, (1987), 88

40: D. Bohm., "The Characteristics of Electrical Discharges in Magnetic Fields", ed. by A. Guthrie & R. K. Wakerling, McGraw-Hill, (1949)

41: S. M. Rossnagel & H. R. Kaufman, *J. Vac. Sci. Technol. A*, **4**, (1986), 1822

42: K. S. Fancey & A. Matthews, *Surface & Coatings Technol.*, **33**, (1987), 19

43: S. M. Rossnagel & H. R. Kaufman, *J. Vac Sci. Tech A*, **5**, (1987), 2276

44: D. W. Hoffman., *J. Vac. Sci. Technol. A*, **3**, (1985), 561

45: S. M. Rossnagel.,*J. Vac. Sci. Technol. A*, **6**, (1988), 19

46: B. Chapman.,"Glow Discharge Processes", Wiley, New York(1980)

47: M. Marinov, *Thin Solid Films*, **46**, (1977), 267

48: J. E. Greene., *CRC Crit. Rev. Solid State Mat. Sci.*, **11**, (1983), 47

49: W. P. Sproul., *Thin Solid Films*, **107**, (1983), 141

50: J. A. Thornton & A. S. Penfold., "Thin Film Processes", ed. J. L. Vossen & W. Kern, Academic Press, (1978), p.75

51: D. G. Teer & K. C. Laing, Proc. 8th Int. Conf. on Ion & Plasma Ass. Tech., Brussels, (1991), p. 202

52: W. D. Munz, D. Hofman & K. Hartig, *Thin Solid Films*, **96**, (1982), 79

53: S. Schiller, V. Heisig & K. Goedicke., *Thin Solid Films*, **40**, (1977), 327

54: D. B. Fraser & H. D. Cook, *J. Vac. Sci. Technol.*, **14**, (1977), 147

55: B. Window & N. Savvides, *J. Vac. Sci. Technol. A*, **4(2)**, (1986), 196

56: B. Window & N. Savvides, *J. Vac. Sci. Technol. A*, **4(3)**, (1986), 453

57: B. Window & N. Savvides, *J. Vac. Sci. Technol. A*, **4(3)**, (1986), 504

58: S. L. Rohde, I. Petrov, W. D. Sproul, S. A. Barnett, P. J. Rudnik & M. E. Graham, Proc. 17th Int. Conf. on Metall. Coatings & 8th Int. Conf. on Thin. Films., San-Diego, (1990)

59: R. P. Howson, H. A. Ja'fer & A. G. Spencer, *Vacuum*, **44(3/4)**, (1993), 191-195

60: K. Oka., "Plasma activated growth of reactively sputtered optical thin films", PhD Thesis, Loughborough University of Technology, U.K., (1988)

61: R. F. Bunshah, "Deposition Technologies for Films and Coatings", Noyes Publications, U.S.A. (1982), 179

Chapter Four

Reactive magnetron sputtering and its control

4.0 Introduction

Reactive sputtering is a powerful technique for the deposition of a large number of compound thin films, many of which can only produced with difficulty using competing technologies. The films are usually reactively sputtered at temperatures less than 300°C, although crystalline films demand much higher temperatures. Despite its apparent simplicity as an extension of elemental magnetron sputtering, reactive sputtering is a complex process, involving interactions between the physics of the sputtering process, plasma discharges, growth kinetics, and the chemistry that occurs at both cathode and substrate surfaces.

This section will concentrate on dc reactive magnetron sputtering, describing the concept of the two states of target coverage induced by the reactive gas and the resultant hysteresis effect. It will discuss various methods employed to control the system when a reactive gas is used to deposit compound films, with particular reference to the technique employed throughout this work.

4.1 Target poisoning and the resultant process instability

There are numerous advantages to reactive magnetron sputtering compared with sputtering compound targets. Metal targets can be more easily purified, machined and bonded than compound targets, and since the former are usually conductive, dc power supplies can be used, avoiding the complexity and expense of rf systems. On the other hand, the added complexity of a second (reactive) gas to the system necessitates tighter process control. Not only does attention have to be paid to total process pressure, substrate temperature and bias, particular attention must also be paid to gas flow rate and gas distribution.

The key concept in reactive dc magnetron sputtering is controlling the state of the target surface. Of major concern is the abrupt transition between 'metal' mode, where the target surface is free of reactive gas species, and 'poisoned' mode, where the surface is partially or totally coated with such species, the latter being characterised by a much reduced deposition rate and sometimes severe arcing. It was identified by Schiller *et al*[1] that owing to the inhomogeneous discharge density of magnetrons due to the erosion zone, the sputter rate and oxidation rate are not constant over the target surface and show a pronounced site dependence. As a result, the degree of oxide coverage Θ on the target must also be site dependent. This leads to the possibility of three states existing simultaneously on the target surface; fully poisoned, fully metal, or partially poisoned. Their diagram is reproduced in figure 4·1, and shows the variation in Θ across a target cross-section surface with x being the distance from the centre. A peak is seen in the metal sputtering rate at the centre of the erosion zone, whilst the poisoning rate is fairly uniform. A consequence of this is that the centre of the erosion zone stays metallic and the periphery becomes poisoned with reaction products. This is a widely recognised feature of reactively sputtered targets, and has been used as a diagnostic aid for determining the plasma discharge characteristics of planar magnetrons[2].

The metallic mode is characterized by a high deposition rate, and therefore a high capacity for consumption of reactive gas, and by a low partial pressure of reactive gas due to the gettering effect of surfaces which surround the discharge. Conversely, the poisoned mode gives rise to a low sputter rate and low reactive gas consumption. The classic

Figure 4·1: Differential magnetron cathode poisoning (Reference 1)

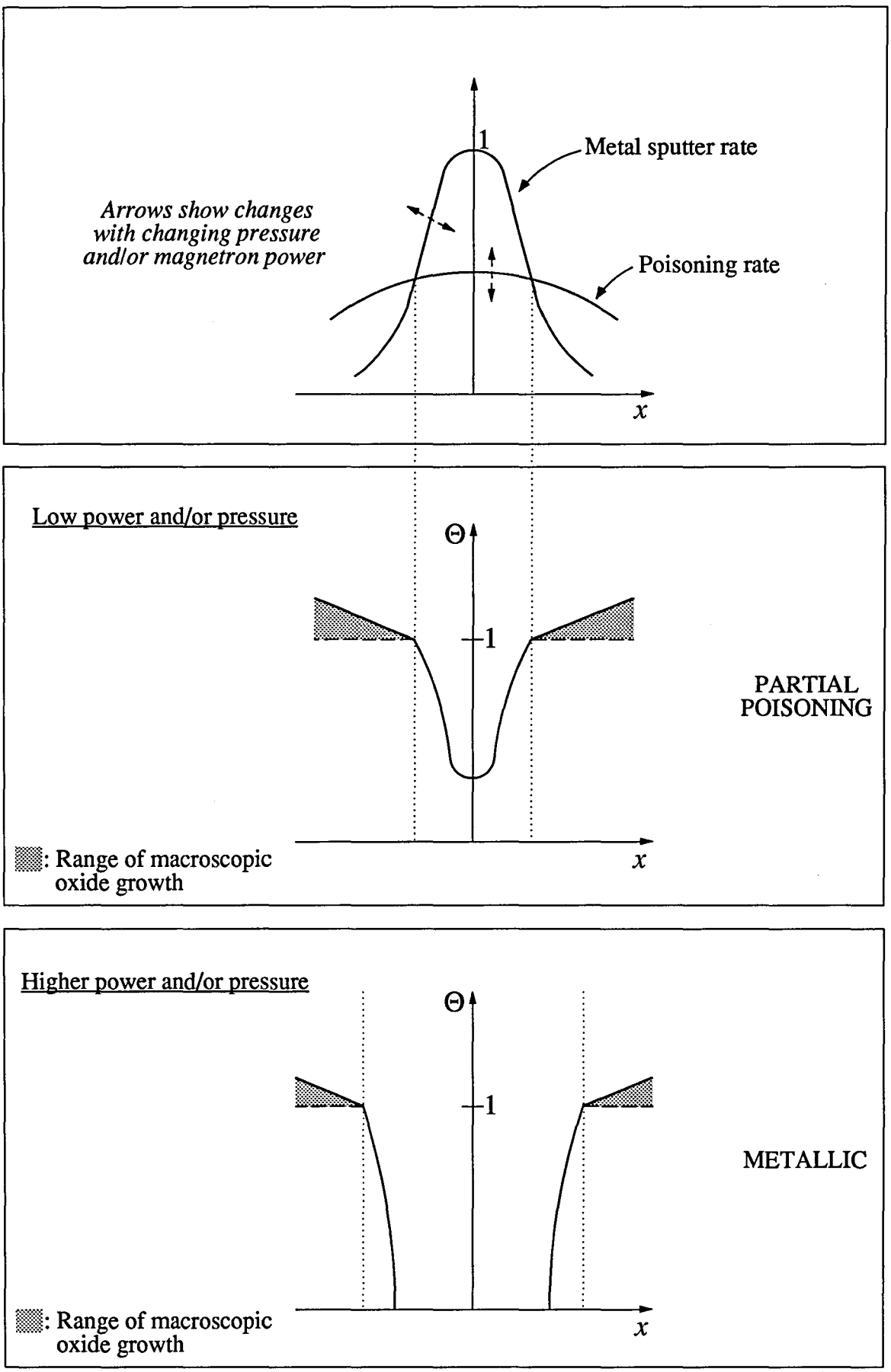

model of the effects of the two states upon system pressure are shown in figure 4·2, which could apply to the sputtering of In in an Ar/O_2 mixture. A constant pressure p_a is maintained by the flow of non-reactive gas f_a into the continually pumped system. Thus p_a is the pressure at which the In target could be used to deposit an In film. The dashed line represents the linear increase in total system pressure that would be expected from increasing f_a alone. However, the total pressure does not increase in this way because the gas reacts with the metal. As shown by the solid line, the system pressure p remains constant at its initial value p_a, until a flow rate f_{r1}, when it rises to a new value p_1. If no sputtering took place the value of p at this total flow rate would be p_0, so that $\Delta p = p_0 - p_1$ is the reduction in system pressure due to the reactive sputtering. Once the equilibrium value of p has been established changes in f_r cause p to change linearly, the value of Δp between the system pressure with and without reactive sputtering being constant at each value of f_r. If f_r is reduced to f_{r2}, though, Δp increases and the system pressure decreases from p_2 to the initial value p_a. Generally, the transition between the two target modes occurs abruptly at f_{r2} and f_{r1}, and as a result depends on the direction of the transition.

Sproul[3] describes the hysteresis effect more qualitatively, and his explanatory hysteresis loops for both pressure versus flow and for deposition rate of TiN_x versus flow are reproduced in figures 4·3(a) and 4·3(b). There is no initial change in nitrogen partial pressure n_{pp} because all reactive gas combines with the sputtered metal. When the flow reaches point B the n_{pp} suddenly rises because sufficient nitrogen is present to cause a compound to form on the target surface. As a consequence, the titanium sputter rate falls off, and the amount of nitrogen consumed by the process also drops. Hence there is a large increase in n_{pp}, and any further increase in nitrogen flow beyond this will result in a linear increase in n_{pp} above point C. The n_{pp} does not decrease along the same path if nitrogen flow is now decreased. The n_{pp} stays high until the nitrided target surface is broken through and metal is sputtered once more. At this point, D, the nitrogen consumption increases rapidly, with a corresponding drop in n_{pp} to the original level.

Referring once again to Schiller's model and figure 4·2, the magnitude of the critical reactive gas flow f_{r2} is a measure of the basic stability of the system. The higher the value of f_{r2} at which the corresponding

Figure 4-2: Stable operating modes (——) for a magnetron discharge with constant reactive gas flow

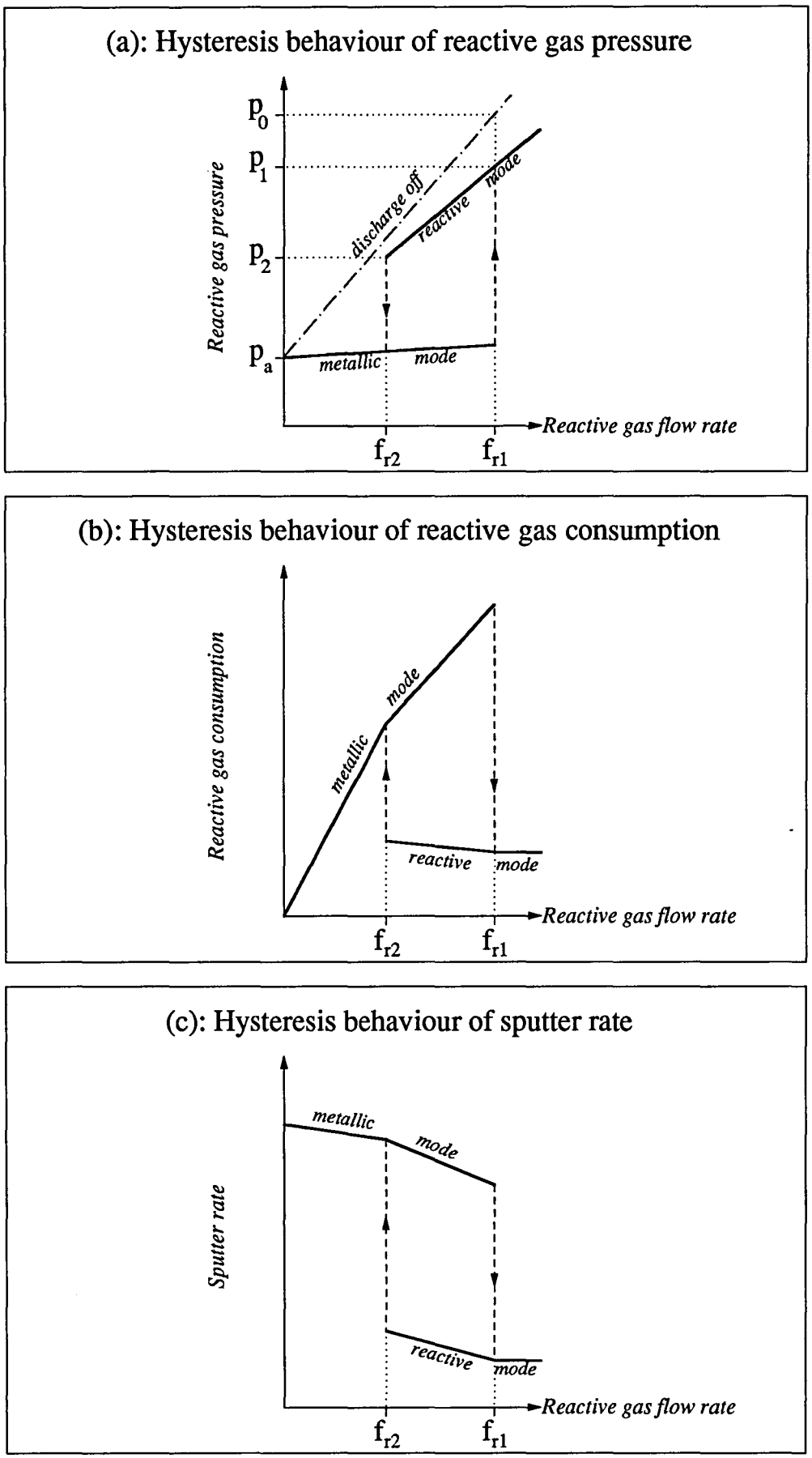

stability can be maintained, the greater the degree of reaction between the metal and reactive species. In order to obtain compound species at the substrate, at the desired degree of reaction, it is necessary to obtain a high degree of stability. Methods of process control within the otherwise unstable system shown by the hysteresis of figure 4·3(a) will now be described.

One method employed to reduce the hysteresis effect is to never allow the target to become irretrievably poisoned. Sproul[3] and Aronson *et al*[4,5] have reported using a pulsed reactive gas flow to successfully deposit TiN from a target continuously operating between the two modes, and Howson *et al*[6] have deposited TiO_2 in a similar manner. Aronson found that by using two independent timers to control the 'on' and 'off' pulsing states of the piezoelectric valves controlling nitrogen flow, the process could be maintained around the knee of the hysteresis. With the valve open, the target moved toward the poisoned mode, depositing a nitride film. If the valve was closed immediately prior to the onset of the fully poisoned mode, the operating point dropped back down the same curve. If flow was again turned on before the curve reached the baseline, the process oscillated between the two states controllably. The deposition rates were found[5] to be typically between 50% and 70% of the metal sputtering rate and even with relatively long duration pulse times, the films were found to be of constant stoichiometry throughout their thicknesses, without any detectable layering. The main disadvantage of the pulse technique is the large amount of process optimization which has to be undertaken before films with the desired stoichiometry of compound can be repeatably produced. Also, the deposition rate was still too low, and the control system too complex for an industrial scale operation.

It has been seen that target poisoning is the initiating mechanism for the hysteresis effects characteristic of dc reactive magnetron sputtering. Maniv *et al*[7] reasoned that if the reactive gas flow to the target could at least be reduced, the probability of a poisoned target and hysteresis instability would also reduce. They introduced a baffle between the target and substrate, with the reactive gas entering on the substrate side. The oxygen flux to the target was indeed reduced by the baffle; oxygen reacts with the metal deposited on the walls of the apertures of the baffle. Results obtained for sputtering a Cd_2Sn alloy target showed that

Figure 4·3(a): Nitrogen partial pressure vs. flow hysteresis loop for reactive sputtering of TiN_x with target power of 10kW (From reference 3)

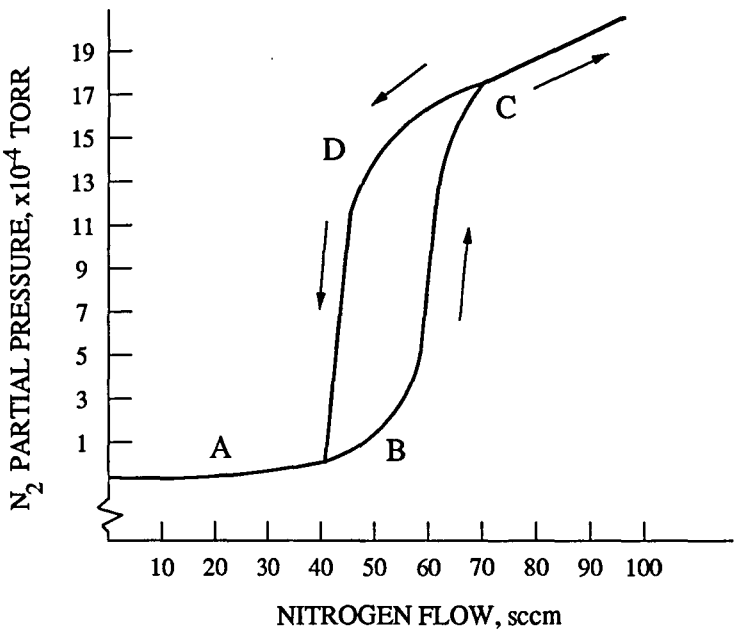

Figure 4·3(b): Deposition rate hysteresis loop under deposition conditions of figure 4·3(a)

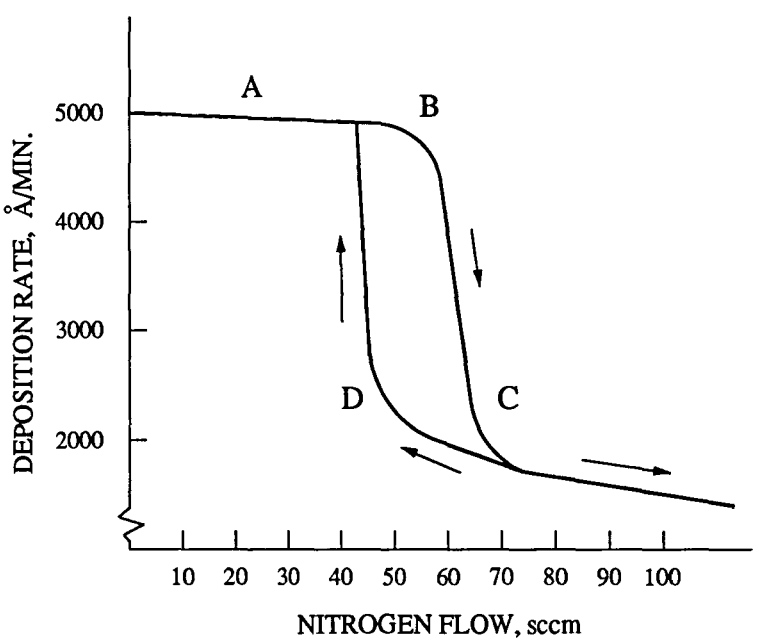

by using the baffle and coupling 100W rf to the substrate they were able to achieve stoichiometric conducting transparent oxides with 95% transmittance and resistivity of 4.5 x10^{-4} Ωcm. Successful use of the baffle technique has also been reported by Brett *et al*[8] for ZnO, Este and Westwood[9,10] for Al_2O_3 and AlN, and Scherer and Wirtz[11] for Al_2O_3, SiO_2, SnO_2 and Ta_2O_5.

In 1984 Schiller *et al*[12] published a paper detailing important aspects of the stable control of the deposition process between the two target modes. For a system in which titanium was sputtered in a partial pressure of oxygen, p_{O2}, the target to substrate distance (TSD) was found to influence the stoichiometry of the deposited TiO_x. At small TSDs a high p_{O2} is necessary to complete compound formation with the higher flux density of titanium present there. As a result of the high p_{O2}, the target surface quickly reverted to poisoned mode, with a low sputter rate of over stoichiometric TiO_x, with reported x values as high as 2.4. As the TSD was increased, the titanium flux density decreased due to the cosine distribution and so a lower p_{O2} was needed for full compound formation at the substrate. Since target poisoning is more likely for high oxygen partial pressures, Schiller concludes that by increasing target to substrate distance, stoichiometric films of TiO_2 are formed with lower reactive gas partial pressures and there is a reduced probability of complete target poisoning. The variation of plasma emission intensity with reactive gas flow is described in the same paper, and is shown to exhibit the familiar hysteresis effect, similar in form to the reactive gas pressure versus flow curve of figure 4·3(a). Figure 4·4 is a reproduction of the plasma emission variation with reactive gas flow rate for the deposition of both TiN and TiO_2. The similar hysteresis loops shown by both plasma emission and reactive gas pressure variations with flow prompted the idea of the use of plasma emission to control the process within the otherwise unstable operating regime This is briefly alluded to, but the idea is not elaborated on until later papers by the same author.

In 1988, Spencer *et al*[13] developed a conceptual model to quantify the pressure instability causing the hysteresis effects in the parameters previously identified. They did this by isolating the effects of increasing reactive gas partial pressure at target and substrate separately, then combining the two effects to give the reactive gas consumption model.

Figure 4·4: Hysteresis in plasma emission intensity between 460 and 470nm with variation in reactive gas flow
(From reference 12)

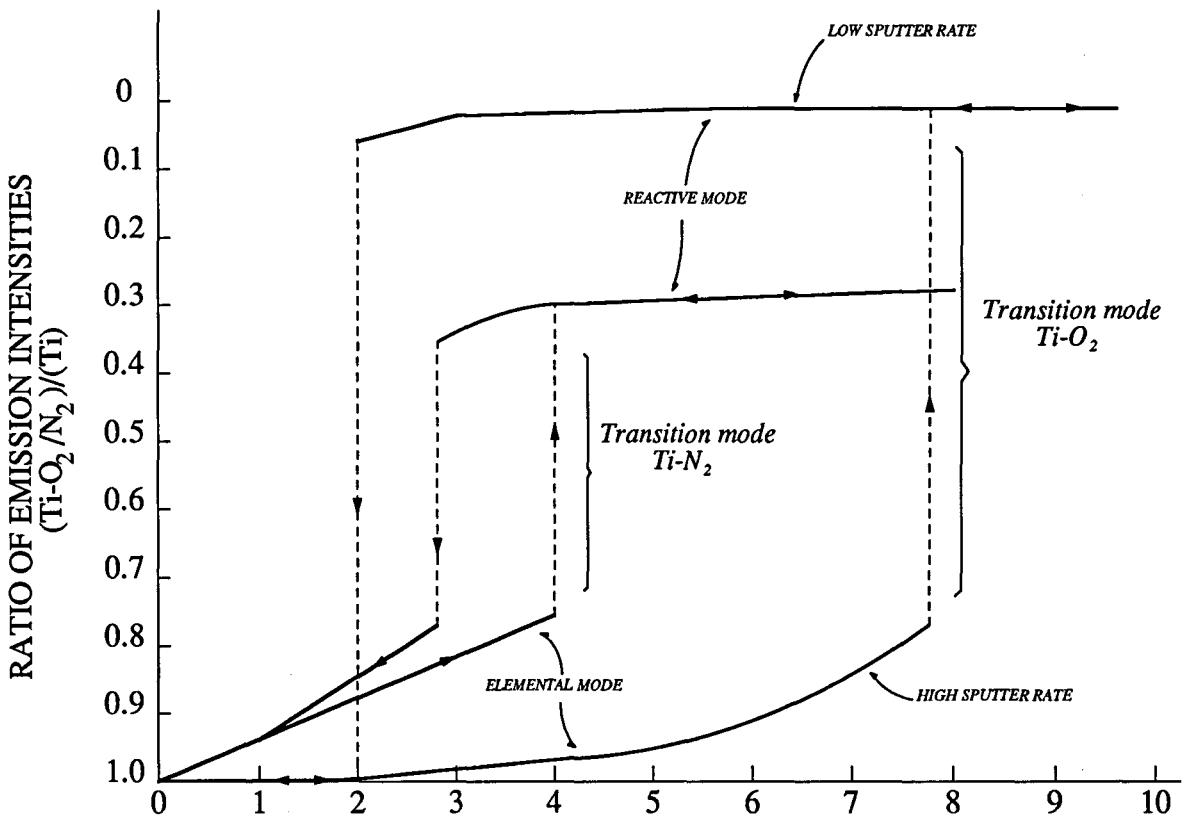

Figure 4·5: Origins of reactive gas consumption by the film (From reference 13)

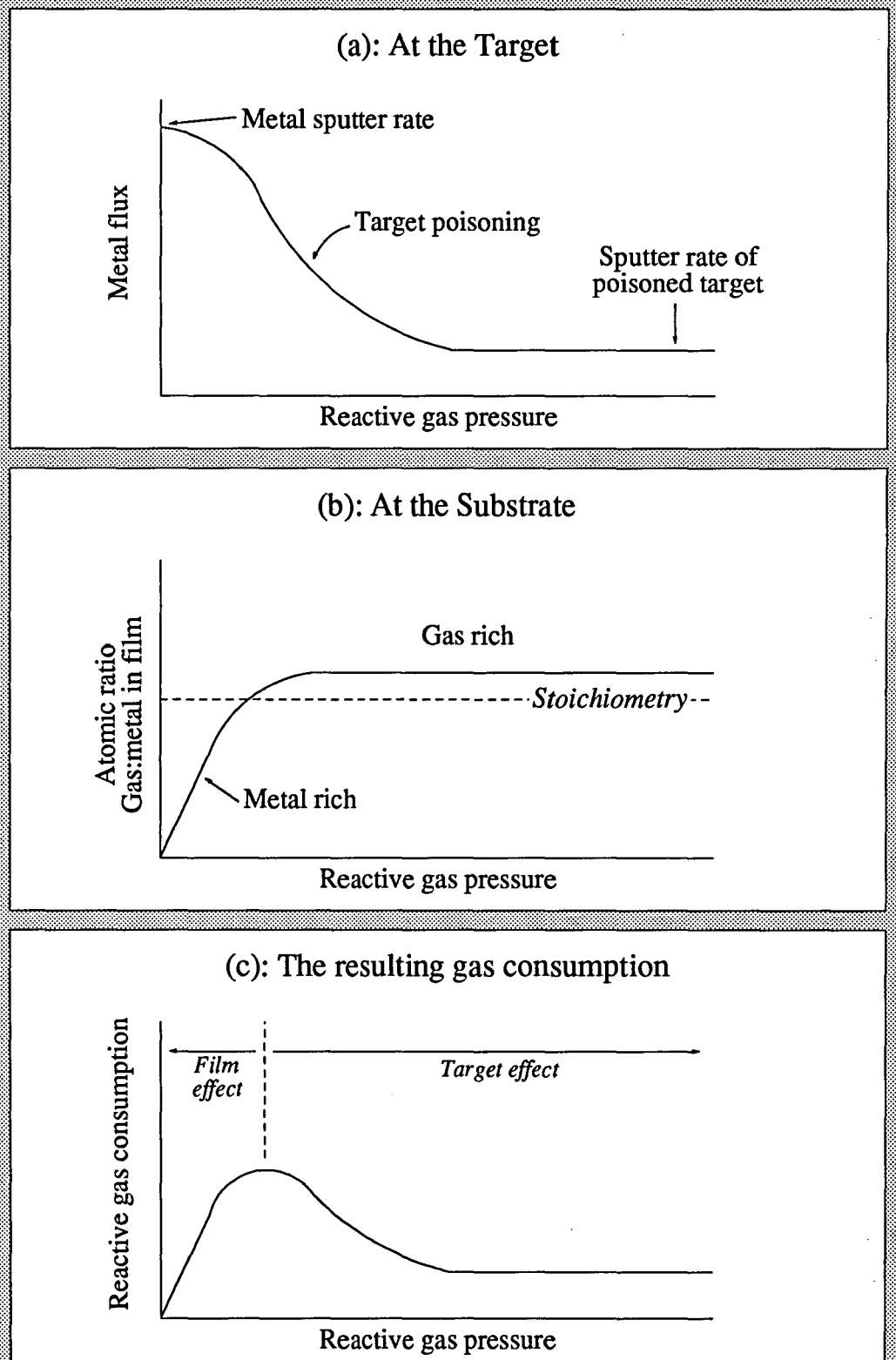

Figure 4·6: Oxygen consumption curve for Titanium
(From reference 14)

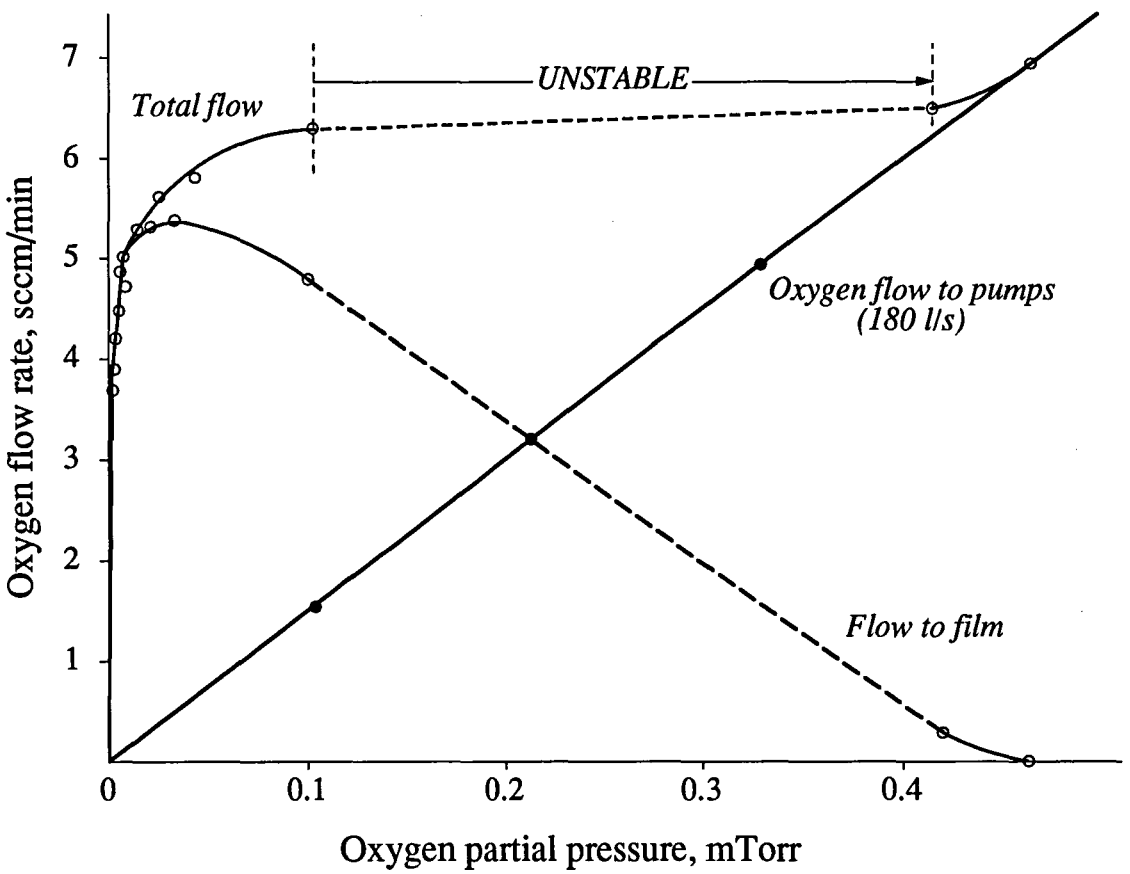

In the following discussion reference is made to figure 4·5. The target surface is continuously poisoning and then sputtering clean. Where the poisoning rate exceeds the cleaning rate a partially poisoned state exists and increasing the reactive gas pressure will increase the proportion of the target area that is poisoned. The resulting decrease in metal flux and sputter rate continues until the target is completely poisoned when the metal flux remains essentially constant, figure 4·5(a). With low reactive gas pressures, the rate of formation of the compound film at the substrate is limited by the arrival rate of the metal flux and by the utilization of the reactive gas, and so a metal film is initially formed. As the reactive gas pressure is increased the deposited film becomes less metallic, eventually saturating in an over-stoichiometric state, figure 4·5(b). The processes at the target and substrate combine to give the complete reactive gas consumption curve of figure 4·5(c). Spencer[14] confirmed the results of the model with experimental data for the oxygen consumption of titanium; his result is reproduced in figure 4·6 and shows the unstable region in which the process is uncontrollable using manual pressure control alone.

4.2 Control within the instability

It is clear that the switching between poisoned and metal target modes is an inherent feature of reactive sputtering, so rather than try to remove the resultant hysteresis, a technique had to be found to maintain the process in the unstable region between modes. The pulsed technique of reactive gas flow previously discussed had been effective but required continuous operator monitoring and adjustment of pulse status times to maintain the desired set-point. What was needed was an automatic control system which used a process parameter indicative of the target state as the feedback signal in a control loop. Such a system was that alluded to by Schiller in his early paper[12] where the control parameters were spectral emission lines from the plasma.

4.2.1 Light emission from a dc magnetron plasma

Observations of light emission from discharges, and their use as a diagnostic tool is not new. Von Hippel[15] first observed emission spectra of sputtered atoms in 1926, and Stuart and Wehner[16] later showed that

the emission intensity in the plasma was proportional to sputter yield of the particular target being used. Sawatsky and Kay[17] showed that the emission intensity from a polycrystalline copper target could be used as an indicator of sputter yield, and Stirling and Westwood[18] have used emission and absorption spectroscopy to study the sputtered species from an aluminium target.

The emission of light in the positive column of a dc plasma results from electron transitions between two energy levels, with the line spectrum being characteristic of their atomic species. Enjouji *et al*[19] assumed excitation to be caused by electron-inelastic neutral atom collisions, so that the excitation and emission process of metal atoms could be expressed as follows:

$$M + e \rightarrow M^* + e \qquad [4\cdot1]$$

$$M^* \rightarrow M + h\nu \qquad [4\cdot2]$$

where M represents the metal atom in the ground state and M* the metal atom in the emitting state.

Assuming excitation due to inelastic electron collisions, the emission intensity at a point x in the discharge, corresponding to the transition between energy levels i and j is given by:

$$I(x) = N(x)\, P_i(x)\, T_{ij}\, g(\lambda) \qquad [4\cdot3]$$

where $N(x)$ is the density of sputtered atoms, $P_i(x)$ is the probability of exciting an electron to state i, T_{ij} is the probability that the electron will decay back to state j, and $g(\lambda)$ is the fraction of emitted photons corresponding to this transition that are collected. Schiller *et al*[20] stated that the intensity of a chosen spectral line at any point in the discharge is proportional to the number of level transitions from j to i per unit time and unit volume:

$$I_{ij} = \frac{n_k^*}{\tau_{ij}} \approx 10^8 . n_k^* \ s^{-1} \qquad [4\cdot4]$$

where n_k^* is the number of atoms per unit volume having an excitation level j, and τ_{ij} is the lifetime of the excitation level, usually[21] of the order of 1-10 ns. Greene[22] showed that the total number of excitation collisions per second per atom is given by:

$$P_i(x) = \int n_e(x,v_e)\sigma_{exc}(v_e)dv_e \qquad [4\cdot5]$$

$$= \frac{1}{(2m_e)^{1/2}} \int E_e^{-1/2}\, \sigma(E_e)\, n(x,E_e)\, dE_e \qquad [4\cdot6]$$

where n_e, m_e and E_e are the electron population density, mass and kinetic energy, respectively. σ_{exc} is the excitation cross-section.

As an extension of equations [4·1] and [4·2], Enjouji *et al*[19] obtained the following linear relationship between deposition rate R_d, emission intensity I and target current J_t:

$$R_d \propto \frac{I}{J_t} \qquad [4\cdot7]$$

It has been found experimentally[23] that the relationship between the intensity of the tantalum emission line at 481nm and the discharge current and power is linear when operating in the metal mode, in the pressure range 0.1 to 1 Pa. This linearity is also found between intensity and deposition rate. At operating pressures below 0.1 Pa, however, the linearity is only found within a restricted power range. With a discharge power of 3kW the intensity increased by a factor of 2.4 when the pressure was increased from 0.1 to 1 Pa. The corresponding increase in deposition rate over the same pressure range was only 1.3. These results have been confirmed by work done by Greene *et al*[24] and Enjouji *et al*[19], and are reproduced in figures 4·7(a) and (b).

Spectroscopic studies of high rate reactive sputtering of tantalum[23] in Ar-O_2 show a pronounced non-linear fall in emission intensity even at low oxygen partial pressures due to the increasing oxygen coverage of

Figure 4·7(a): Intensity of Ta emission line (481nm) v. discharge current for metal sputtering. (From reference 23)

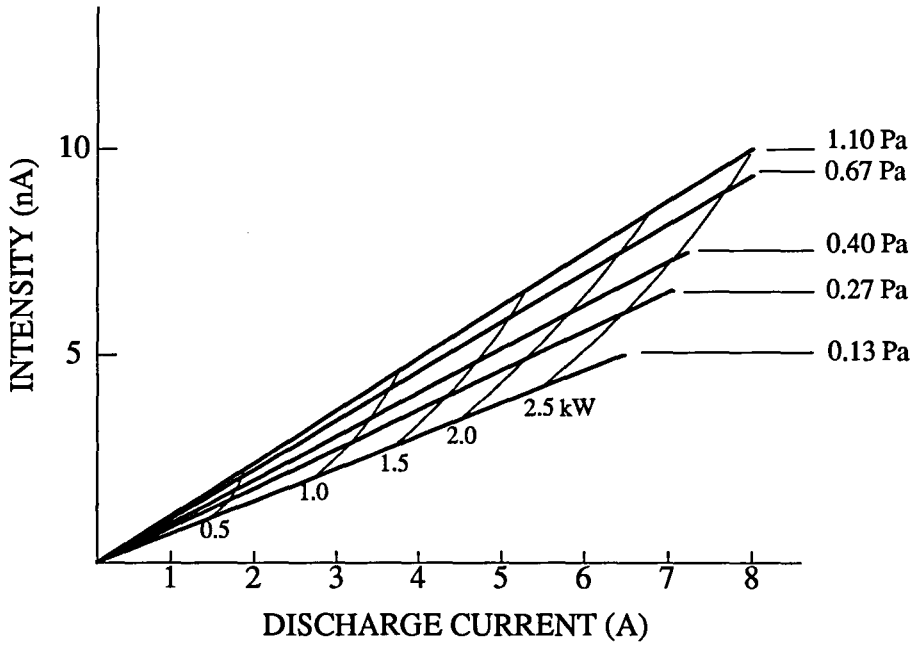

Figure 4·7(b): Intensity of Ta emission line (481nm) v. discharge power for metal sputtering. (From reference 23)

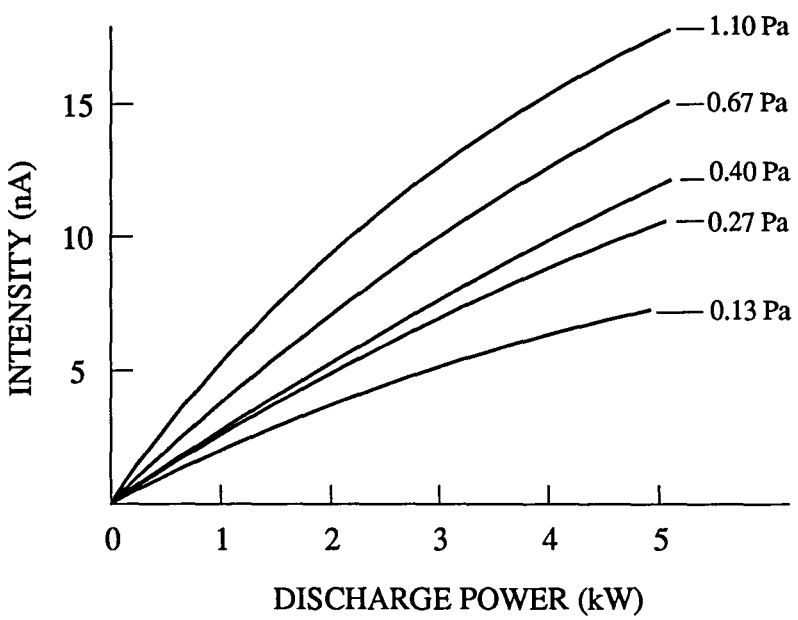

Figure 4·8: Intensity of Ta emission line (481nm) v. pressure ratio for reactive sputtering in argon-oxygen. (From reference 23)

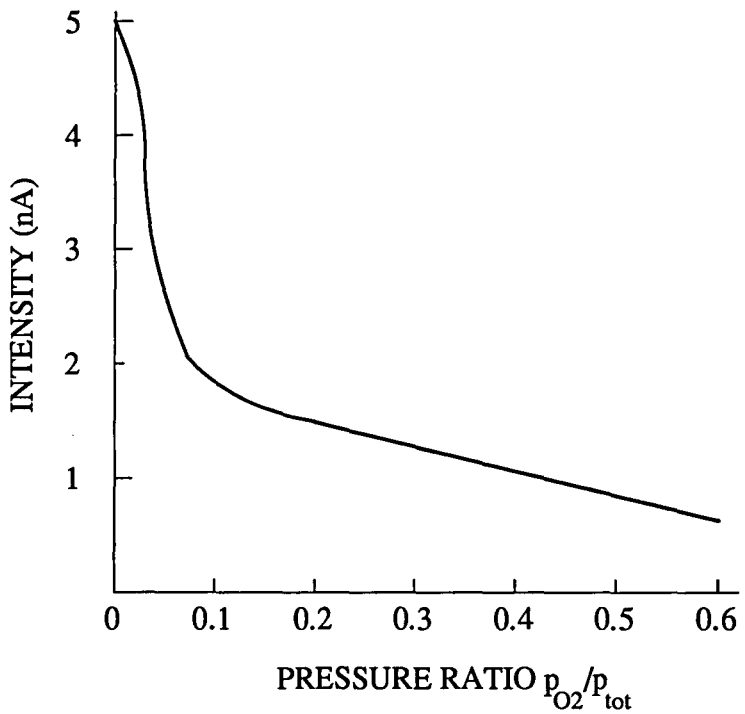

Figure 4·9: Intensity of Ta emission line (481nm) v. deposition rate for metal sputtering (From reference 23)

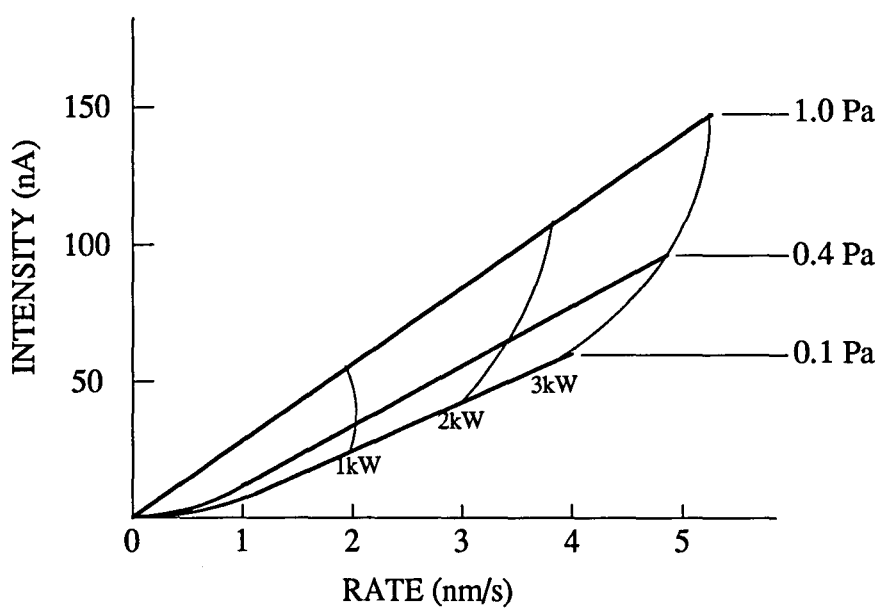

the target, figure 4·8. This coverage follows a reduction in ion current to the target which, in turn, causes a reduction in the metal sputter rate, figure 4·9.

To summarise, there is a linear correlation between the intensity of light emission from a discharge due to electron energy level relaxations and the magnetron parameters of current, power and deposition rate. These relationships, combined with the strong pressure dependence, enable the emission intensity to be used either as a diagnostic tool for determination of target or plasma status, or as a control parameter in reactive sputter deposition.

4.2.2 A solution to the problem of control - Plasma Emission Monitoring

In section 4·1 examples were cited of the causal mechanisms for the pressure instability inherent in conventional reactive magnetron deposition. The deposition of films for systems of low basic stability is possible only in the transition mode, that is between the extremes of 'poisoned' and 'metal' modes, and a discharge in this mode requires a means by which to stabilize the process. Adopting this approach necessitates the acquisition of measurands that characterize the state of the process at any instant. Indirectly measured parameters such as sputter rate are too inaccurate, reactive gas partial pressure is not suitable due to the time delay in signal acquisition caused by remote gauging, and the plasma density at the substrate cannot be quantified without affecting the deposition process. However, as has been shown in the previous section, the plasma emission intensity of a spectral line is directly related to several indicators of target status, and as such is a very suitable measurand for control loops. In 1987, Schiller *et al*[20] detailed a control system which he had first alluded to in a previous paper[12]. The technique was termed Optical Emission Monitoring (OEM) or Plasma Emission Monitoring (PEM), and is arguably the most reliable reactive process control instrument in use at present, on both laboratory and industrial scale.

Conventional methods of process control aim to de-couple the events occurring at target and substrate to increase the basic stability of a system. The technique of pulsing reactive gas previously described is one such method. PEM opposes conventional principles, by taking

advantage of the coupling, rather than attempting to remove it. Hence, target to substrate distance is kept low, reactive gas admission is near the target, and a plasma shield formation toward the chamber is encouraged. These measures increase the excitation of reactants at the substrate and result in the required degree of reaction at a lower reactive gas flow rate. With reference to figure 4·2, another result is that f_{r2} and f_{r1} are moved closer together, so that the basic stability of the system is reduced considerably. The above measures taken to couple target and substrate effects give the process such a degree of instability that the process would be unusable without PEM control.

The PEM equipment and parameters specific to the system used throughout this work will be described in the results and discussion chapters later, but the general principle is given here. The usual format of a PEM control loop is illustrated in figure 4·10. The process is initiated when the target is in metal mode, so that a 100% reference signal can be identified. An optical fibre views the plasma across the target surface diameter to maximize the light intensity received by the controller. Care has to be taken to ensure that the end of the fibre bundle does not become coated with sputtered material, which would reduce the magnitude of the transmitted signal, and that the fibre 'sees' a full cathode diameter to avoid false indications of target mode, which may occur if the fibre is directed at the periphery where oxide tends to accumulate. In addition to the emission lines corresponding to the target there will be emission lines present in the discharge resulting from electron transitions for Ar, the reactive gas, carbon compounds from contamination sources and H_2 and O from water vapour dissociation. To filter out the background and unwanted line emissions, a monochromator is used to select only the desired line emission of the target. The wavelength of the monochromator is chosen so that the signal it passes is unaffected from nearby argon or reactive gas emission lines, which could interfere with the metal signal. From the monochromator the signal is fed to a photomultiplier to convert it to a potential, which then passes to the controller. The controller compares the incoming signal with an operator-selected 'set-point' of emission intensity. Should the set point be lower than the incoming signal, the controller automatically opens a piezoelectric control valve to admit a flow of reactive gas to the system. The addition of reactive gas causes a change in target mode, so that a smaller area of its surface sputters

Figure 4·10: Plasma Emission Monitoring (PEM) control loop

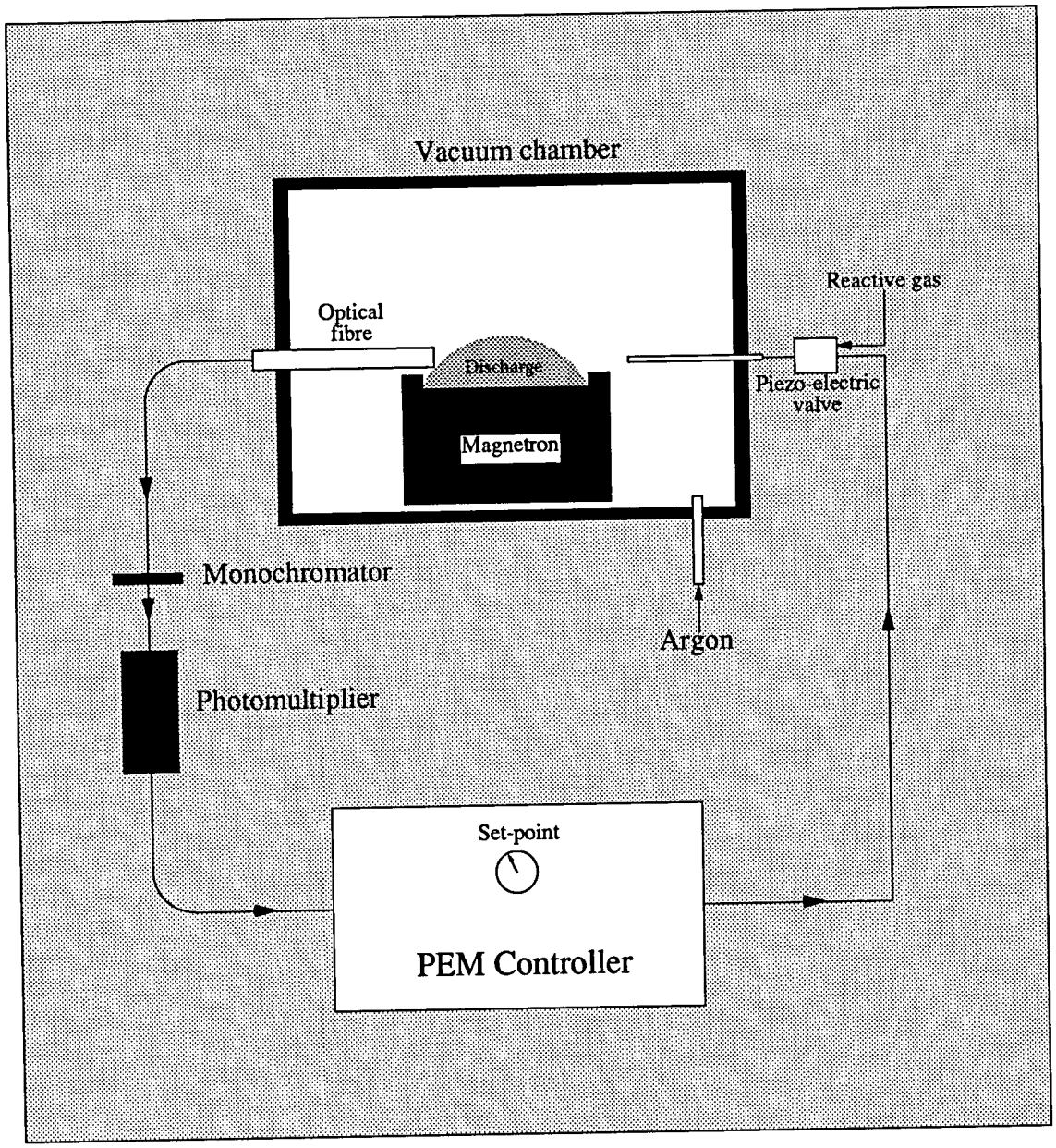

metal, and the emission signal falls to a new level indicative of the target state. Automatic adjustment of the valve continues until the magnitudes of the set-point and input signal are equal, at which point the controller holds the process stable. Piezoelectric valves are used because of their quick response, so providing the time constant of the control loop is not too long and the gas admission not too remote from the plasma, the system will react to the onset of a poisoned target by reducing reactive gas flow to move the process back towards the knee of the hysteresis loop of figure 4·3(a).

Chapter Four References

1: S. Schiller, U. Heisig & K. Goedicke, *Thin Solid Films*, **64**, (1979), 455-467

2: T. Fukami & F. Shintani, *Thin Solid Films*, **151**, (1987), 373-381

3: W. Sproul., U.S. Patent 4428812.

4: A. J. Aronson., *Microelec. Manuf. & Test.*, January 1988, 25-26

5: A. J. Aronson, D. Chen & W. H. Class, *Thin Solid Films*, **72**, (1980), 535-540

6: R. P. Howson, K. Suzuki, C. A. Bishop & M. I. Ridge, *Vacuum*, **34 (1-2)**, (1984), 291-294

7: S. Maniv, C. Miner & W. D. Westwood, *J. Vac. Sci. Technol.*, **18**, (1981), 195

8: M. J. Brett, R. W. McMahon, J. Affinito & R. R. Parsons, *J. Vac. Sci. Technol.*, **A1**, (1983), 352

9: G. Este & W. D. Westwood, *J. Vac. Sci. Technol.*, **A2**, (1984), 1238

10: G. Este & W. D. Westwood, *J. Vac. Sci. Technol.*, **A5**, (1987), 1892

11: M. Scherer & P. Wirtz, *Thin Solid Films*, **119**, (1984), 203

12: S. Schiller, G. Beister & W. Sieber, *Thin Solid Films*, **111**, (1984), 259-268

13: A. G. Spencer, R. P. Howson and R. W. Lewin, *Thin Solid Films*, **158**, (1988), 141-149

14: A. G. Spencer.,"High rate reactive magnetron sputtering", PhD Thesis, Loughborough University of Technology, U.K., (1988)

15: A. von Hippel., *Ann. Phys. (Leipz)*, **80**, (1926), 672

16: R. V. Stuart & G. K. Wehner, *J. Appl. Phys.*, **33**, (1962), 2345

17: E. Sawatzky & E. Kay, *Rev. Sci. Instrum.*, **37**, (1966), 1324

18: A. J. Stirling & W. D. Westwood, *J. Appl. Phys.*, **41**, (1970), 742

19: K. Enjouji, K. Murata & S. Nishikawa, *Thin Solid Films*, **108**, (1983), 1-7

20: S. Schiller, U. Heisig, K. Steinfelder, J. Strümpfel, A. Friedrich & R. Fricke, Proc. Int. Conf. on Ion Plating & All.Techn., Brighton, (1987), p. 223-30.

21: G. Herzberg., "Atomic Spectra & Atomic Structure",Dover, NewYork (1945)

22: J. E. Greene., *J. Vac. Sci. Technol.*, **15(5)**, (1978), 1718-1729

23: S. Schiller, U. Heisig, K. Steinfelder & J. Strümpfel, *Thin Solid Films*, **96**, (1982), 235-240

24: J. E. Greene & F. Sequeda-Osorio, *J. Vac. Sci. Technol.*, **10**, (1982), 235

Chapter Five

Semiconducting and related thin film materials - An introduction

5.0 Introduction

The purpose of this section is to introduce the materials prepared in this work, before their controlled properties are presented in chapters seven to eleven. In addition, a short compilation of some current applications and competing deposition techniques is given here for each material.

5.1 Silicon oxides, nitrides and oxy-nitrides

Films of silicon oxides, usually silicon dioxide, are used extensively in the microelectronics industry as passivation and barrier layers. Their reported preparation techniques have included those suited to large area coating; pyrolitic decomposition of silanes, reduction of silicon and oxygen-containing compounds, plasma oxidation and anodisation[1]. Having said this, the applications of SiO_2 are limited because the material is structurally porous[2]; the high permeability to impurities and the migration of impurity ions being undesirable in electronic devices. The ion migration effect has been shown to be negligible in silicon nitride films, however, even at high temperatures, and the ability to

mask against alkali ions, oxygen and water vapour[3] is one of the most important advantages the nitride has over the oxide. In addition, the former has good thermal shock resistance and extreme hardness, making it equally applicable as a barrier coating in the aerospace industry. Silicon oxy-nitrides have a similar range of applications as both oxides and nitrides of silicon, but combine the higher visible transparency of the former with the higher density of the latter. Comparable techniques of deposition have been used[4] for applications such as insulation, passivation and masking and layers for integration in photovoltaics.

The advantage of reactive sputtering applied to the deposition of the three variations of silicon compound film above, is that it can be used to coat thermally sensitive substrates of small to medium area with accuracy, without the use of toxic gas. Reactive magnetron sputtering was considered well suited for deposition of controlled stoichiometries of each compound, whilst observation was made of the effects of the process parameters on film refractive index and optical transparency.

5.2 Indium oxide

Indium oxide, In_2O_3, is a non-stoichiometric compound under various conditions, with an In:O ratio greater than 2:3. This non-stoichiometry results in an n-type degenerate semiconductor or even semi-metal at high electron concentrations, with low resistivity, the magnitude varying with deposition technology but usually between $\sim 10^{-2}$ and 10^{-4} Ωcm. It has a band gap of between 3.7 and 4.4 eV, and hence has high transparency in the visible. Conclusive evidence is still lacking as to the conduction mechanism in doped In_2O_3, but the consensus appears to be that high conductivity may be achieved either by the creation of oxygen vacancies or by incorporation of donor carriers. During film formation, a large number of native donors are produced because of oxygen vacancies. Such a deficiency can also be created by post-deposition heating in a slightly reducing atmosphere, but this process is reversible and the carriers so created may be easily removed on exposure to warm air. When small amounts of Sn are added to In_2O_3, the Sn enters substitutionally in the cation sublattice so that Sn^{4+} replaces In^{3+}, and creates n-type donors. The substitution reaction predominates

any oxygen vacancy doping when the Sn concentration exceeds 10% mol. Another effect of Sn inclusion is reported by Fan and Goodenough[5], where Sn^{3+} ions are thermally excited to Sn^{4+} with liberation of a conduction electron. Bosnell and Waghorne[6] have discussed the possibility that the Sn can exist as lower oxides such as Sn_3O_4, creating an oxygen vacancy.

In recent years it has been demonstrated that the injection of electrons into the racetrack of an unbalanced magnetron, independent of the so-called 'secondary' electrons created by the sputtering process at the cathode, can result in a much lower operating potential, enabling operation at lower pressures[7,8]. Towards the conclusion of the experimental work for this Thesis, a paper[9] was published which developed the concept of *low voltage* magnetron deposition, and cited remarkable effects on the resistivity of ITO films. Although the inclusion of experimental detail was carefully avoided by the paper, the results showed a halving of ITO resistivity by reducing the operating potential to just over half of its normal magnitude. Operation at -250V gave a resistivity of 1.9 $x10^{-4}$ Ωcm for substrates at 200°C, and at -110V this fell to 1.2 $x10^{-4}$ Ωcm. The dramatically enhanced properties of the ITO were attributed to the much reduced ion bombardment of the growing film resulting from the lower energies imparted by the reduced cathode potentials. The bombardment energy was not reduced to zero however; sufficient energy was retained to provide the benefits of film densification and optimum oxygen dopant level incorporation.

Some applications of In_2O_3:Sn, ITO, include spectrally selective heat reflecting films[10], contact and antireflection layers in heterojunction photovoltaics[11], protective coatings[12], active and passive aircraft transparency coatings, transmitting electrodes for optoelectronics[13], laser-resistant coatings[14] and antistatic coatings for satellites[15].

5.3 Zinc oxide

Zinc oxide is similar to ITO in the respect that it is also a wide band gap (~3.3eV) n-type semiconductor, where band gap states are introduced either by addition of foreign dopants, or by oxygen vacancies evolving interstitial zinc atoms[16]. Any impurities introduced in the host material

are ionized, and the associated electrons occupy the bottom of the conduction band in the form of an electron gas.

Because of its amenability to defect or impurity doping, its low cost and non-toxicity[17],it has attracted interest for use in applications such as window coatings[18], LCDs and solar cells[19]. Various doped oxide semiconductors have different applications such as In_2O_3:Sn or CdO:Sn with low resistivities, and SnO_2:F with high durability. ZnO:Al coatings[18-20] have attracted less interest, and ZnO:In even less[21].

Transparent conducting zinc oxide films have been prepared by rf sputtering of pure ZnO targets, ZnO contaminated with dopant material, or by co-sputtering ZnO and metal dopants[22-24]. A smaller volume of work has been carried out using dc reactive sputtering[25,26], with careful control of the oxygen partial pressure[27] to achieve the necessary stoichiometry.

5.4 Amorphous silicon

Pure amorphous silicon, a-Si, is a highly defective material because of the high density of dangling bonds which appear as electronic states in the band gap. The addition of hydrogen passivates these states, and the low density of defect states enables n- and p-type doping of the hydrogenated material.

Amorphous silicon is an important semiconducting material, with applications as diverse as photoreceptors[28,29], image sensors[30], and, because it has an absorption coefficient more than one order of magnitude higher[31] than that of single crystal silicon at 500nm, photovoltaics. Amorphous silicon photovoltaics are almost exclusively thin film, and hold the greatest promise for inexpensive cells at present. Following Research into a-Si photovoltaics begun[32] in the late 1960's, the first devices were produced in 1974[33], by the glow discharge decomposition of silane (see below). These films contained hydrogen as a result of the decomposition, which acts to saturate dangling bonds at the microvoids and at other defects in the silicon film.

The majority of previous work with the material has been with plasma assisted chemical vapour deposition, where the source gas, such as silane

(SiH_4) is decomposed by electron impact into a mixture of radical and ion species. These react in the gas phase and at the substrate to form the solid film. Other techniques have been microwave dissociation[34], triode sputtering[35] of silane, and reactive evaporation of silicon[36]. Reactive sputtering of a-Si has been reported[37-39] to a lesser extent, but it has been recognised[40] that sputtering techniques provide more direct control of hydrogen incorporation than is possible with glow discharge film growth. With this preparation technique, hydrogen is used as the reactive gas in the controlled sputtering of an elemental silicon cathode. Silicon hydrides are formed at the target surface, which, along with neutral hydrogen and any gaseous or solid source dopants, arrive at the substrate and react to form the a-Si:H film. The hydrogen content in the film is thus controlled by substrate temperature and partial pressure of injected hydrogen during the process. It has also been reported[41] that high density films are formed under moderate ion bombardment, and that the bombardment results in an increased hydrogen content. The small amount of work on dc reactive magnetron sputtering of doped a-Si:H, compared with silane decomposition found in the literature, and the advantages provided by the former, suggested that the material would be well suited to investigation with the unbalanced magnetron system.

Chapter Five References

1: T. L. Chu., *SCP & Solid State Tech.*, May, 1967, 36

2: T. L. Chu, J. R. Szedon, *J. Electrochem. Soc.*, **115(3)**, (1968), 318-321

3: S. M. Hu, *J. Electrochem. Soc.*, **113**, (1966), 693

4: C. -E. Morosanu, *Thin Solid Films*, **65**, (1980), 171

5: J. C. C. Fan & J. B. Goodenough, *J. Appl. Phys.*, **48**, (1977), 3524

6: I. R. Bosnell & R. Waghorne, *Thin Solid Films*, **15**, (1973), 141

7: J. J. Cuomo & S. M. Rossnagel, *J. Vac. Sci. Technol A*, **4**, (1986), 393

8: K. Steenbeck, E. Steinbess, G. Schmidt & G. Bruchlos, *Vacuum*, **42**, (1991), 39

9: S. Ishibashi, Y. Higuchi, H. Nakamura, T. Komatsu, Y. Ota & K. Nakamura, *Proc. 1st Int'l Symp. on ISSP*, Tokyo (1991), 153-158

10: G. Frank, E. Kauer & H. Köstlin, *Thin Solid Films*, **77**, (1981), 107-117

11: J. B. Dubow & D. E. Burk, *Appl. Phys. Lett.*, **29**, (1976), 494

12: R. Puyane (ed.), Proc. Battele Seminar on Coatings on Glass, *Thin Solid Films*, **77**, (1981)

13: J. P. Fillard & J. C. Manifacier, *Jp. J. Appl. Phys.*, **9**, (1970), 1012

14: W. T. Pawlewicz, I. B. Mann & W. H. Lowdermilk, *Appl. Phys. Lett*, **34**, (1979), 196

15: K. Ito & T. Nakazawa, *Surf. Sci.*, **86**, (1979), 492

16: L. Vasanelli, A. Valentini & A. Losacco, *Sol. Energy Mat.*, **16**, (1987), 91

17: K. L. Chopra, S. Major & D. K. Pandya, *Thin Solid Films*, **102**, (1983), 1

18: Z. C. Zin and C. G. Granqvist, SPIE Vol. 823 *Optical Materials Technology for Efficiency and Solar Energy Conversion VI* (1987), 28-35

19: S. Maniv, C. J. Miner and W. D. Westwood, *J. Vac. Sci. Technol. A*, **1 (3)**, (1983), 1370-1375

20: T. Minami, K. Oohashi, S. Takata, T. Mouri and N. Ogawa, *Thin Solid Films*, **193/194**, (1990), 721-729

21: G. L. Harding, B. Window and E. C. Horrigan, *Solar Energy Materials*, **22**, (1991), 69-91

22: P. S. Nayar & A. Catalano, *Appl. Phys. Lett.*, **39**, (1981), 105

23: Z-C Zin, I. Hamberg & C. C. Granqvist., *Appl. Phys. Lett.*, **51**, (1987), 149

24: L. Vasanelli, A. Valentini & A. Losacco., *Sol. Energy. Mater.*, **16**, (1987), 91

25: M. J. Brett, R. W. Mcmahon, J. Affinito & R. R. Parsons, *J. Vac. Sci. Technol. A*, **1**, (1983), 352

26: M. J. Brett & R. R. Parsons, *Can. J. Phys.*, **63**, (1985), 819

27: R. Lewin, R. P. Howson, C. A. Bishop & M. I. Ridge, *Vacuum*, **36**, (1986), 95

28: I. Shimizu, S. Sirai & E. Inoue, *J. Appl. Phys.*, **52**(4), (1981), 2776

29: M. Ondris, G. Van der Voort & W. den Boer, *Journal of Non Crystalline Solids*, **59**, **60**, (1983), 1243

30: F. Okumaura, S. Kaneko & H. Uchida, Extended Abstracts of 5th Conf. on Solid State Devices & Materials, (1983), 201-204

31: Y. Hamakawa., *Appl. of Surf. Sci.*, **22/23**, (1985), 859-878

32: H. F. Sterling, R. C. G. Swann, *Solid State Electron.*, **8**, (1965), 653

33: D. E. Carlson., US Patent 4,065,521, (1977)

34: S. J. Hudgens, A. G. Johncock & S. R. Ovshinsky, *J. Non-Cryst. Solids*, **77/78**, (1985), 809-812

35: K. Ando, M. Aozasa & R. G. Pyon, *Appl. Phys. Lett.*, **44(4)**, (1984), 413-415

36: R. V. Kruzelecky, D. Racansky, S. Zukotynski, F. Gaspari, C. I. Ukah & J. M. Perz, *J. Non-Cryst. Solids*, **108**, (1989), 115-127

37: M. Pinarbasi, N. Maley, A.Myers & J. R. Abelson, *Thin Solid Films*, **171**, (1989), 217-233

38: G. N. Parsons, C. Wang & G. Lucovsky, *Thin Solid Films*, **193/194**, (1990), 557-587

39: T. D. Moustakas & W. Paul, *Phys. Rev. B*, **15**, (1977), 1564

40: R. A. Rudder, J. W. Cook Jr. & G. Lucovsky, *Appl. Phys. Lett.*, **45(8)**, (1984), 887-889

41: B. Drevillon, C. Senemaud, C. Cardinaud, M. D. Khodja & C. Codet, *Phil. Mag. B*, **54(5)**, (1986), 335-342

Chapter Six

Experimental -
The deposition system and film analyses

6.0 The vacuum system

6.0.1 Vacuum pumps

The system had originally been an Edwards evaporation chamber, but had been converted for use as an air-to-air sputtering unit, as shown in Figure 6·1. Rough evacuation of the chamber was achieved with a 660 litres/minute double-belt driven rotary pump, which typically reduced the pressure from atmospheric to 150 mTorr in under 10 minutes. At this pressure a hydraulic actuator opened the centrally oriented high vacuum valve to the water cooled diffusion pump, which had a specified pumping speed of 3100 litres/minute, but gave approximately 250 litres/minute at the chamber. The diffusion pump had no cold trap, and the lack of viewports precluded the addition of Meissner cooling coils. Even with these limitations a base pressure of $3x10^{-6}$ Torr was achievable by pumping overnight.

6.0.2 Chamber construction and pressure measurement

The deposition chamber was a 60cm diameter stainless steel bell jar, with 25mm leadthroughs located around the circumference of the base

plate to allow access for water, gas, electrical and optical fibre connections. A copper tube had been attached to the external surface of the chamber in a spiral arrangement, so that cold mains water at 50 psi could flow through and cool the walls. In addition to preventing the walls from heating and outgassing during long deposition times with high magnetron operating powers, or when using the halogen lamp heating station used in chapter eleven, the cold water flow through the jacket was found to decrease the base pressure of the system by $1x10^{-6}$ Torr from the pressure achievable at room temperature with the flow off. The system, in use, is shown in plate 6·1.

Total and partial pressure measurement was continually monitored throughout deposition runs, using the three gauges shown in figure 6·1. To outline the purpose and operation of the gauging arrangement, the pumpout procedure from atmosphere is briefly described. All vacuum pumps were run continuously to maintain the sealing oil (rotary) and the working oil (diffusion) at the desired operating temperatures, and all valves remained closed whilst the system was not in use. Having lowered the chamber so that the integral 'o'-ring seal was in contact with the base plate, the roughing valve was opened, allowing the roughing pump to evacuate the chamber to 40 mTorr. This roughing pressure is monitored on the CVC pirani gauge, labelled '2' in the figure. The pirani gauge head contains a metal envelope enclosing a tungsten filament. For a given voltage across the filament, its temperature, and hence its resistance, depend on the rate of heat conduction away from it by the surrounding gas. Since the conductivity of the gas depends on its pressure in the molecular flow regime, the resistance of the filament also depends on the gas pressure. Modern pirani meters contain solid state equivalents of Wheatstone bridge networks in which the filament forms one arm, and the pressure is read directly. At a roughing pressure of 150 mTorr, the roughing valve shuts, and both backing and high vacuum valves are fully opened. The diffusion pump throat is now open to the chamber and the continuous cycle of evaporating, then condensing jets of oil pull residual air molecules from the chamber, reducing the pressure below the operating domain of the pirani gauge.

For pressures lower than millitorr order the Edwards penning gauge was used. Also known as the cold cathode ionisation gauge, the penning

Figure 6·1: The deposition system and vacuum pumping equipment

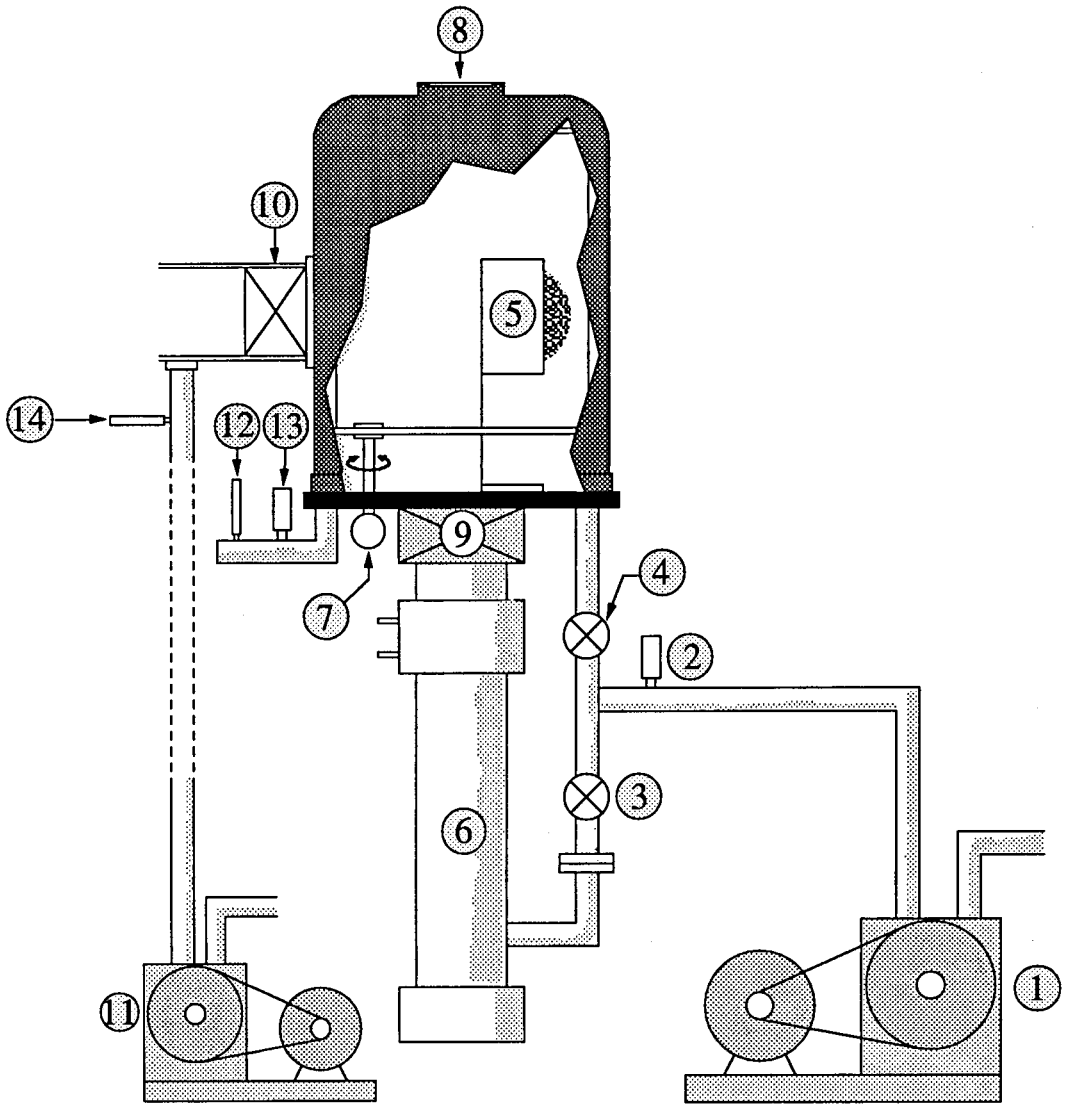

1: 660 litres/minute rotary pump
2: Pirani gauge - backing pressure
3: Backing valve
4: Roughing valve
5: Magnetron
6: 3100 litres/minute oil diffusion pump - (~250 litres/minute at chamber)
7: Stepper motor
8: Window
9: High vacuum valve
10: Load lock gate valve
11: 47 litres/minute rotary pump
12: Penning gauge - base pressure
13: Pirani gauge - process pressure
14: Pirani gauge - airlock volume pressure

Plate 6·1
The deposition system - external

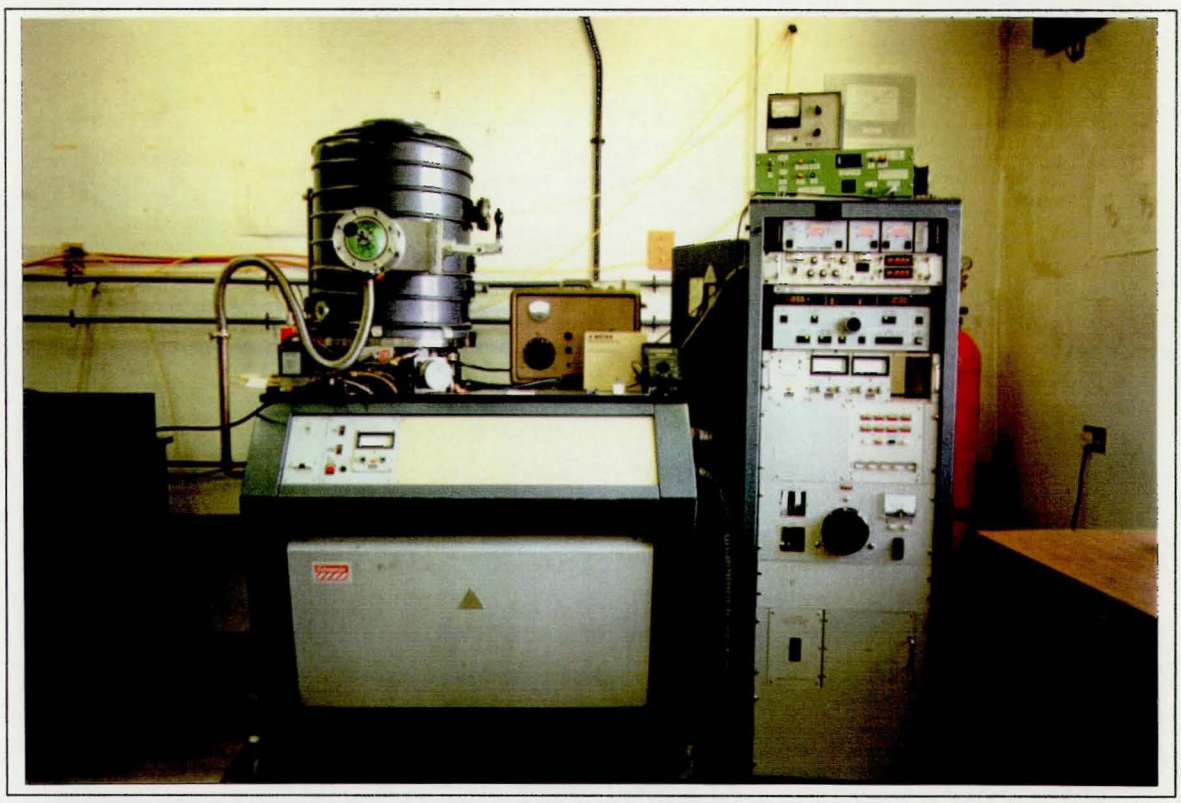

type makes use of perpendicular magnetic and electric fields of 600 Gauss and 2kV respectively. Labelled '12' in the figure, the potential is applied between two electrodes in an open ended glass envelope, and at suitable system pressures a discharge is struck. Electrons in the discharge oscillate and spiral around the field lines so that the ion current produced by their bombardment of gas molecules can be measured by a 0-100μA moving coil meter. The penning gauge was never used above $5x10^{-4}$ Torr because of the risk of sputtering from the electrodes.

Once the desired base pressure was achieved, a constant flow of argon was admitted to the chamber as an inert backfill for the magnetron discharge to strike. The order of magnitude of pressure for magnetron operation is mTorr, so an additional pirani gauge head '13' was used to measure the process pressure inside the chamber. Sensitivity of the pirani gauge head varies with gas type, so calibration was necessary for film depositions where the sensitivity of the gauge to the reactive and inert gases was markedly different. Accurate calibration was particularly important when hydrogen was used for the deposition of a-Si:H, because of the wide range in sensitivity of the Pirani gauge to Ar and H.

The two chamber pressure gauge heads, '12' and '13' should ideally be located in the deposition volume, but because of the reactive nature of many of the film depositions, both were sited along a copper tube to one side of the chamber. The tube had a large internal diameter of 40mm, so that its conductance would not give false pressure readings, and was of sufficient length to ensure that the heads were remote from any activated oxygen or depositing films, which could coat the warm metal elements inside both heads, again inhibiting accurate pressure measurement.

For experiments at argon partial pressures of 10mTorr and above, a modification was made to the hydraulic piston which opened the high vacuum valve. An adjustable stop was added to the end of the piston arm to limit its travel so that the degree of movement of the high vacuum valve could be selected to give slower pumping speed, and correspondingly higher chamber pressure for a given flow of argon. This modification was also particularly useful for quick switching

between high pressure (150 mTorr) Ar/O_2 plasma cleaning conditions and low pressure (3mTorr) film deposition.

6.1 Gas admission and flow measurement

For precise control of reactive sputtering using an inert gas and at least one reactive gas, advanced instrumentation must be used to quantify the gas flows giving rise to the partial pressures measured using the gauging described above.

Of the many types of gas admission valves available, the piezo-electric valve was chosen for use throughout this work. It is particularly suited to fast switching of gas, such as that necessary in the control of a reactive process using PEM control, and has a continually variable aperture with a response time of only 2ms. Flow through the piezo-valves was measured using electronic mass flow sensors. Gas enters the device through a contaminent screen, before passing through a stainless steel element which converts the turbulent flow from the storage bottle into a laminar flow. A small part of this flow is then diverted through a glass sensing tube, in which two heated resistance thermometers are located. At zero flow the two thermometers are at the same temperature, but as gas flow across the tube increases, heat is extracted from them, and since the gas extracts heat from the first thermometer in line, it is unable to extract as much from the second. The resulting temperature imbalance between the two thermometers is converted to a dc voltage output which is linearly proportional to the mass flow rate through the flow meter.

Specific detail of the design requirements of the reactive gas admission manifold will be given in chapter eight, when introducing the deposition of silicon compounds.

6.2 The Airlock and Substrate Loading Mechanism.

An important modification to the system was the addition of a separately pumped airlock, labelled '10' in figure 6·1. The airlock has an internal diameter of 100mm, and a depth of 130mm external to the main

chamber. At the interface between the airlock volume and the main chamber is a manually operated gate valve, manufactured by VAT Ltd., so that the airlock volume can be differentially pumped out prior to opening the gate valve to give access to the chamber.

Inside the main chamber are three sprung wheels in a horizontal plane, one of which is driven by a stepper motor external to the vacuum system, via a rotary leadthrough. The drive wheel can be seen in figure 6·1 attached to the stepper motor, labelled '7'. A ring fits around all three sprung wheels, and on top of this is located a 'cage' to hold up to five substrates in a vertical plane. Each substrate is placed in the airlock volume, attached to the end of a vacuum tight rod. The end of the airlock is sealed with a perspex disc against an 'o'-ring and the volume evacuated using the rotary pump labelled '11', which has a rating of 47 litres/minute, and could typically pump the airlock from atmosphere to 40 mTorr in 2 minutes. When this pressure had been identified on the pirani gauge '14', the airlock pump was switched off to prevent the possibility of backstreaming of diffusion pump oil into the chamber on the opening of the gate valve. The pressure in the airlock was sufficiently low at 40 mTorr to have negligible effect on chamber pressure when the gate valve was opened, to permit the loading of the substrate onto the cage. Following the loading operation, the arm was retracted and the gate valve closed once more to ensure the integrity of the high vacuum was not solely dependent on the perspex/rubber 'o'-ring interface. The stepper motor driver was programmable in that the number of steps could be pre-selected to permit rotation of the cage (and substrate) to the deposition zone and back to the airlock port. The step angle was only 1.8° and the speed of rotation continually variable from 0.25 revolutions/minute to 2.5 revolutions/minute, which gave reliable, reproducible, and semi-automatic control of substrate location control in the chamber without the need for visual verification. Plate 6·2 shows a glass slide, mounted in the holder in the deposition zone during the deposition of silicon nitride. The ring between source and substrate is the reactive gas distribution manifold.

Plate 6·2
A substrate in the deposition zone during silicon nitride production, with the 'pink' plasma characteristic of nitrogen clearly observed

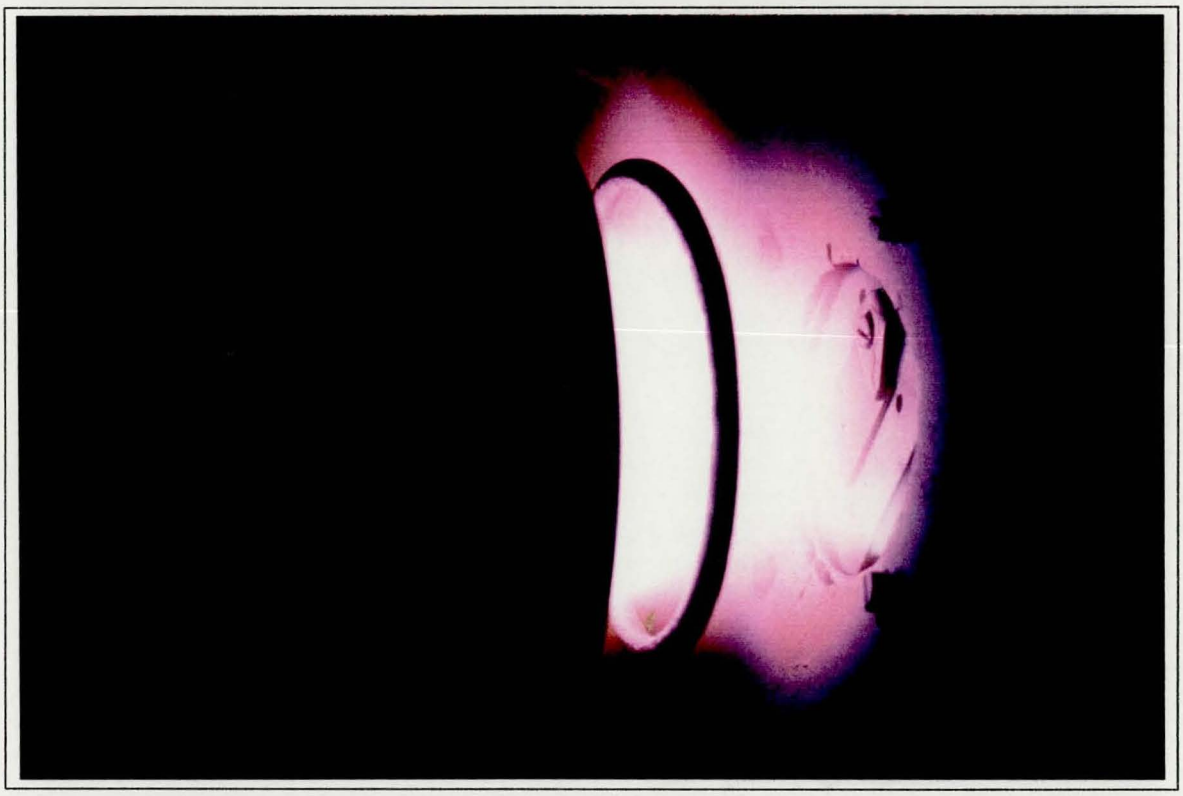

Plate 6·3
The plasma probe immersed in the plasma during silicon oxide deposition

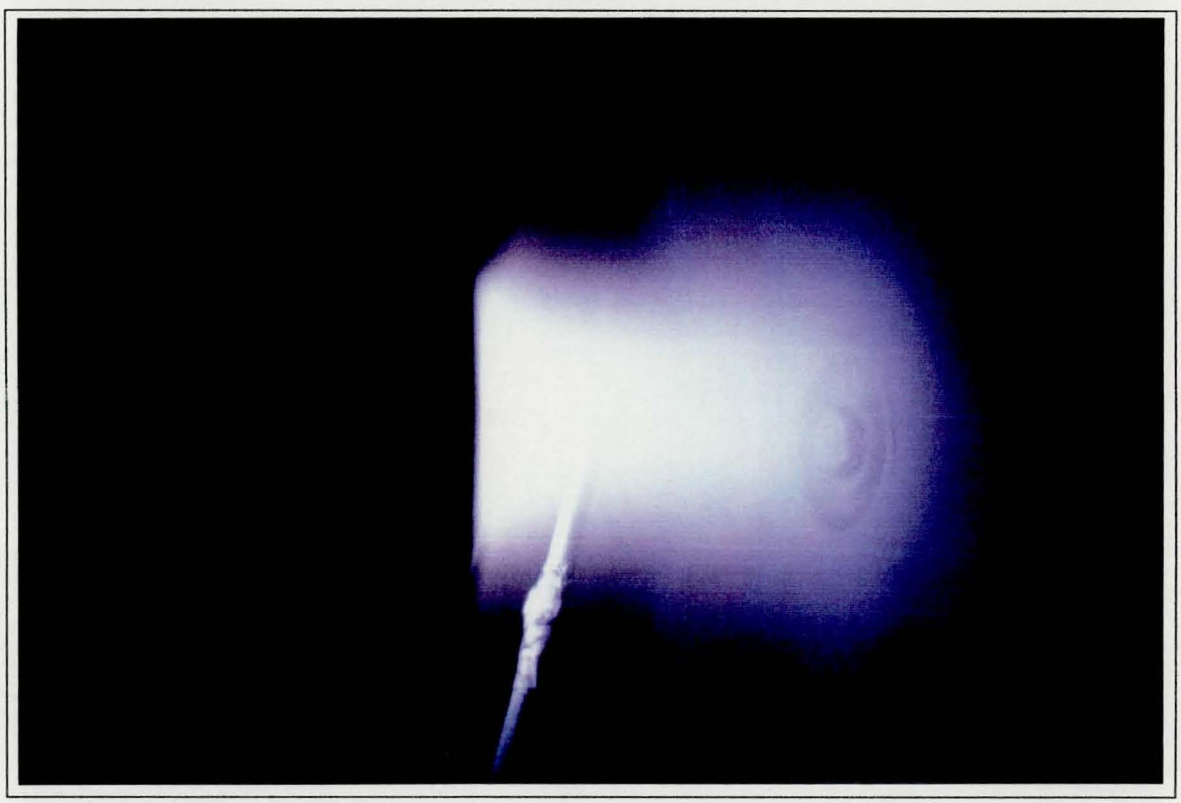

6.3 Magnetron Power Supply

It has already been shown why a magnetron device does not have the requirement for the high dc voltage necessary for dc diode sputtering. A power supply for dc magnetron sputtering must give a voltage ranging no higher than -1kV, and at such voltages the corresponding current capacity will only be limited by the maximum power density at the cathode, and by the stability of the electronic circuitry. It is not too great a problem to design a dc power supply with the above specification, but magnetron operation with its associated high current density at the cathode poses additional difficulties with often uncontrollable arcing.

Arcs are high power density short circuits which have the effect of miniature explosions. When they occur on the target surface they can cause localised heating and even melting. The material is ejected in the form of microdroplets, with resultant damage to the material being processed, and degradation of the target structure. There are two causes of arcs in sputtering, mechanical sources and sources due to electric field aberrations. The former are primarily flakes of target material which short various parts of the structure, commonly target to chamber, by bridging the dark space or by touching the shield. This cause occurs with greater frequency as the deposition time and sputter rate are increased, when material accumulates and fragments as compressive stress overcomes adhesion. Local variations in the electric field at the target surface are the other cause of arcing, and can be created by gas pockets, voids, dielectric clumps, grain boundaries and surface blemishes. An operating target will reach a set of equilibrium conditions including power distribution and heat load, and if sudden changes in power are made either by design or by poor regulation of the power supply, arcing can occur until equilibrium is re-established. Arcing is also seen with 'new' targets or those which have been exposed to air, and these have to be 'run-in' with a slowly increasing power density to avoid arcs originating from accumulated oxides or water adsorption. Even with efficient target cooling, the surface is always at a higher temperature than the bulk, and if the temperature difference is enhanced by poor target bonding or by the use of thick targets, localised 'hot-spots' may occur. These areas are one of the principal causes of arcs, either because they produce thermal electrons or because they are much

closer to doing so. These thermal electrons increase the power density by adding to the production of secondary ions, with resultant melting or sublimation of small areas of target.

It can be seen from the above discussion that the power supply feeding the system is the ultimate cause of arcing, particularly in the reactive processing carried out in this work where partial coverage of the target with dielectric compounds is unavoidable. The MDX range of power supplies, produced by Advanced Energy Industries Inc., do not prevent arcs from occurring, but extinguish them before any damage is done. It has been found experimentally[1] that an area where an arc has occurred takes approximately 5ms to return to equilibrium upon the removal of the discharge current. Circuitry within the MDX supplies senses the onset of the large current spike due to an arc, and cuts the power to the load for the order of 5 to 10ms, reducing the energy discharged into the arc by several orders of magnitude, before automatic re-ignition of the discharge.

The MDX power supply will give full power to a magnetron cathode from 500 to 1000V, controlled within any of the three regulation modes. The unit can be set to deliver constant current, voltage or power, and in most of the work the latter was selected. A programmable ramp enables the ramp up to a power set-point which was useful for the run-in of targets particularly prone to arcing, such as indium-tin. Connection to the magnetron was made with a coaxial UHF cable, the inner core carrying the negative potential and the sheath providing earth protection.

6.4 Plasma Diagnostics

6.4.1 Assessment of ion bombardment at the substrate

In order to evaluate the degree of unbalance of the magnetrons used throughout this work, and to determine the damage to the films due to ion impingement, use was regularly made of a probe, placed in the plane of the substrate. Two parameters of interest will be referred to in several of the sections to come; the ion current density impinging the

substrate plane and the floating potential or bias that a conducting film would acquire due to this ion flux.

The theory of probes in plasmas, particularly when a magnetic field is present, is complex[2,3] and the detail is unnecessary here. The use of a Langmuir probe[4,5] allows the determination of several plasma parameters, including ion current density, plasma potential, floating potential and electron temperature. Langmuir probe experiments, however, will only yield meaningful results if a large number of effects[6] on the probe due to the plasma are considered, which prevent the measured I-V characteristics from being a true measure of the plasma parameters.

It was decided not to use a Langmuir probe throughout this work, because of the difficulties in obtaining accurate results with such a technique. A stainless steel plate, 1cm^2 and 0.5mm thick was spot-welded to a hollow glass arm, through which electrical leads ran to and from the plate. Since the plate was the active area of the device, it is henceforth referred to as the probe head. Because ion current and floating potential are of most interest at the substrate, the probe directly replaced the substrate for measurement of these parameters, facing the magnetron target. Surrounding the probe head was a disc of stainless steel, 7cm in diameter and containing a cut-out region to allow the central location of the probe. The 7cm disc reduced edge effects from the smaller probe head when the device was immersed in the plasma, where the ion flux passing around the head would otherwise show behaviour analogous to inserting a small flat plate normal to a current of liquid. The head was biased using a Philips power supply external to the system, and the I-V data for the probe could be collected under different plasma operating conditions. Plate 6·3 shows the probe head immersed in an unbalanced plasma during the preparation of silicon oxide samples.

A simplified plasma probe I-V characteristic is shown in figure 6·2, with the measured plasma parameter points marked. Point 1 is the current at -100V probe bias. At this point the current is largely due to the flux of ions diffusing to the probe from the plasma region, which typically floats between +2V and +20V above the anode potential[7]. The bias of -100V is regularly used for this measurement, because whilst it

Figure 6·2: Typical simplified probe characteristic with important plasma parameters marked

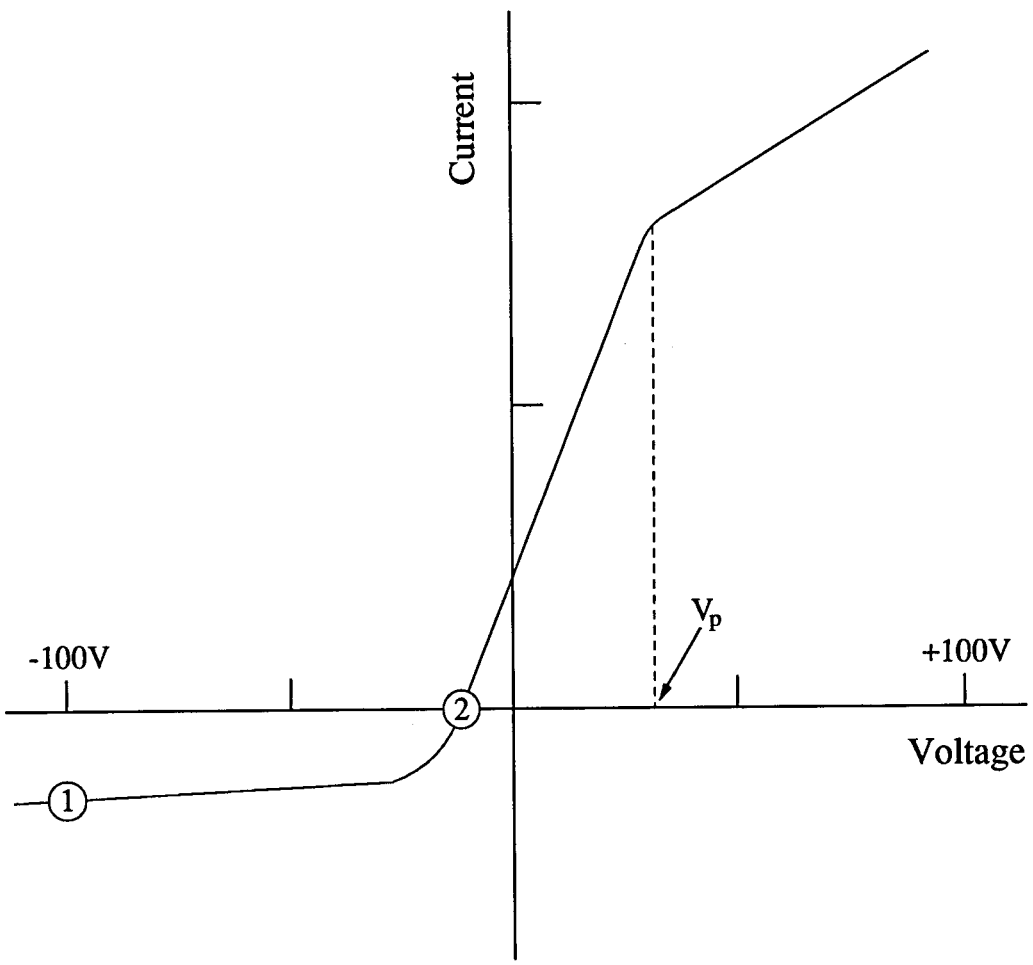

① : Ion current density (mA/cm^2)

② : Floating potenial (V)

is sufficiently negative to repel electrons in the plasma, for most designs of magnetron it is not so negative that ions are accelerated to energies where they would produce significant secondary electrons and sputter the probe head. For the purpose of this work, it did not matter if the probe head suffered from secondary electron emission, because it was not the plasma that was under inspection, rather the *effect of the plasma* on a substrate, and so any effects seen on the probe would be those seen by a substrate in the same plane. The ion current density is approximately constant up to the plasma potential V_p, with the ions dissipating their energy close to the surface of the film, modifying film growth as a result. Because the probe was constructed to have an area of 1 cm^2, the ion current density was always directly measured in $mAcm^{-2}$.

Graphically, the floating potential is defined as the point of intersection of the I-V curve with the voltage axis. The electron and ion currents to the probe must clearly be equal at this point, but due to their greater velocity the electrons arrive at the probe faster than ions. Excess electrons unable to recombine on the surface of the probe form a negative electric field there, which repels further electrons and attracts ions until the two currents are equal. This mechanism is referred to as ambipolar diffusion. Due to this mechanism the substrate is said to have acquired a self-bias, or floating potential at point 2. The film is at this point bombarded by ions having energy equal to their charge multiplied by the difference between the floating potential and the plasma potential, and an equal flux of electrons. The floating potential is also important because it gives the potential reached by an insulating substrate, as the majority of samples in this work were.

6.4.2 Quantification of related process components.

It is useful to calculate the magnitudes of several additional components of the reactive plasma deposition process, so that quantitative comparisons can be made between deposited materials, and between the techniques by which they are prepared. The calculated parameters, neglected by many workers, are the ratio of number of argon ions to metal atoms at the substrate n_i/n_m, the ion energy per metal atom ε, the ratio of gas input to that utilised for film growth n_{gp}/n_{gf}, and the minimum necessary reactive gas partial pressure for stoichiometry. The calculations are achieved using the following assumptions:

(i): The sputter flux is uniform in all directions.

(ii): Neutrals are neglected from the calculation involving material and ion transport to the substrate.

(iii): The sputtered metal atoms react with the reactive gas only at the substrate.

(iv): All compounds are fully stoichiometric; In_2O_3, SiO_2, ZnO, etc., and no consideration is made for dopant concentration in the transparent semiconductors.

(v): The density of the film is assumed to be equivalent to that of the bulk material.

An example of the necessary calculations is given for SiO_2 here, with the results for the other compounds simply presented at the end of the appropriate chapter.

The ion current was measured using the previously described technique, and has units of $mAcm^{-2}$, dimensionally equivalent to Coulombs per square centimetre per second. The ion current, I_c, is simply divided by the charge carried by a single negative ion as it accelerates away from the cathode, to give the number density of ions per square centimetre per second, n_i:

$$n_i = \frac{I_c}{1.602 \times 10^{-19}} \ cm^{-2}.s^{-1} \qquad [6\cdot1]$$

For SiO_2, the ion current density of 2.50 $mAcm^{-2}$ gives $n_i = 1.6 \times 10^{16}$ ions.

To calculate the number of compound molecules present in the film after 1 second, n_c, assume a substrate area of $1cm^2$, so that from the deposition rate of 0.8 nms^{-1}, the volume of the film is calculated. From this figure and the molecular weight of SiO_2, the film contains 2.11×10^{15} SiO_2 molecules. Since each stoichiometric compound molecule in the film contains one molecule of each of the constituent elements, half of this figure are silicon metal molecules, n_{mf}, and half are oxygen molecules, n_{gf}. If it is assumed that the impinging ion has an energy of ~30eV upon reaching the substrate, the ion energy per silicon atom is $30 \times n_i/n_m$, about 455eV, and hence provides more than the necessary

bombardment energy of tens of electron-volts to complete chemical bonds and densify the film. The remaining energy is dissipated as heat at the substrate.

Details of the reactive gas consumption are calculated from the inert and reactive gas flows and pressures, and from the pumping speed. The experimental oxygen flow rate for the stoichiometric film was 7.5 sccm, i.e. 0.125 sccs. The number of O_2 molecules entering the process per cm^3 per second, n_{gp}, is calculated from O_2 density and the above volume of 0.125 sccs, and is found to be 3.37×10^{21} molecules.cm^{-3}.s^{-1}. The number of reactive gas molecules involved in the plasma process, n_{gpp}, is calculated by assuming the "process" reaction occurs over the surface area of a hemispherical discharge in front of the magnetron cathode, having the same diameter as the target. For this work, the diameter of the target was 9.5cm, giving a hemispherical area of 567 cm^2. The number of reactive gas molecules over $1cm^2$, n_{gf}, has already been calculated from the experimental results, so the number on the surface of the hemisphere is obtained from a simple multiplier.

For SiO_2, the ratio of reactive gas molecules entering the system to those utilised by the plasma process, n_{gp}/n_{gpp}, is 5×10^3.

One might have expected the consumption of reactive gas by the process to have been higher than that shown by the calculation, and experience with 50cm rectangular magnetron cathodes has indeed shown that consumption by the process can be dominant. The experimental configuration used for SiO_2 incorporated a much smaller racetrack area, lower sputtering powers and lower gas flow rates than those necessary for large scale operation. These differences, combined with the errors introduced by the assumption that reactions occur only over the surface of the discharge hemisphere, account for the calculated results.

For a given gas type, the pumping speed S is related to the mass flow rate q, and the partial pressure pp by:

$$q = S.pp \qquad [6\cdot2]$$

where q is in $Pa.l.s^{-1}$, Q is in ls^{-1} and pp is in Pa. For the purpose of this exercise, assume that the pumping speed for argon and oxygen is the same. The argon flow rate and partial pressure were 90 sccm and 3 mTorr respectively for SiO_2. Conversion factors for q and pp are as follows[8]:

$$1 \text{ sccm} = 1.684 \text{ Pa.l.s}^{-1} \qquad [6\cdot3]$$

$$1\text{mTorr} = 0.133 \text{ Pa} \qquad [6\cdot4]$$

Using the above figures, $S_{argon} = 380 \text{ l.s}^{-1}$. The oxygen flow needed for stoichiometry was 7.5 sccm, so converting units and using equation 6·2 with $S = 380 \text{ l.s}^{-1}$ gives the minimum necessary oxygen partial pressure for reactive deposition as 0.25 mTorr, a magnitude not measurable with standard Pirani gauge heads. We believe the above estimate of the reactive gas utilisation, combined with the recognition from PEM theory that reactive gas content is determined by the utilisation by pumps, surfaces and growing film, provides a more accurate quantification of the reactive gas content in the sputtering atmosphere than that proposed by Petrov *et al*[9]., who use the expression:

$$n_{gp} = \frac{F_{rg}}{F_{Ar} + F_{rg}} \text{x}100\% \qquad [6\cdot5]$$

where F_{rg} and F_{Ar} are the flow rates of reactive gas and argon respectively. This equation does not take into consideration the effects of reactive gas utilisation by the pumps, chamber surfaces, target or film.

Having demonstrated the technique at length for the example of SiO_2, only the results are given at the end of the appropriate results and discussion chapter for each compound film type. Other compounds, such as In_2O_3, require the introduction of appropriate proportional multipliers to calculate n_{gf} and n_{mf}, in order to balance molecular equations.

6.5 Determination of optical parameters of the deposited films

In device applications, knowledge of the absorptance and surface reflectance of deposited films is fundamental. The photovoltaic, LED display, microelectronic, opthalmic and optoelectronic industries rely on accurate assessment of these optical variables in order to consistently guarantee the performance of devices. Optical transmittance and reflectance were two parameters necessary in quantifying the transparency and antireflection aspects of the indium-tin-oxide films, and were essential in the determination of band gap and absorption coefficient of the amorphous silicon films using the novel derivation introduced in chapter eleven. To be able to compare the films deposited in this study with work in competing technology elsewhere, the precise evaluation of reflectance and transmittance had to be undertaken.

6.5.1 The dual-beam spectrophotometer

To measure the transmittance, reflectance and absorption spectra of the semiconductor and oxide films, a dual beam spectrophotometer was used. Figure 6·3 shows a schematic of the Hitachi 323 UV-VIS-NIR recording spectrophotometer used throughout this study, which has a spectral range of 185 to 2500nm, and a photometric accuracy of better than 0.5% of full scale in transmittance mode. The description of the optical path through the instrument is for the transmittance mode of measurement. The apparatus is set to switch between two light sources depending on the spectral region being examined. A tungsten source is used for visible and near infrared ranges, and a deuterium source for ultraviolet measurements. Light of the appropriate wavelength is focussed on the entrance slit by the source selector mirror and an angled flat mirror. On leaving the slit, it is directed to the quartz prism by the collimating mirror, and the light dispersed by the prism is directed to the exit slit by the collimating mirror once more. The light beam emerging from the exit slit enters the photometer and is split into two by the rotating sector mirror, which allows the beam to pass and then reflects it, alternately. One beam passes through the sample and the other beam through an uncoated substrate, to recombine into an alternating pulse signal at another sector mirror. Depending on the wavelength of incident light, the pulse is converted into a current

Figure 6·3:

Optical Layout of Hitachi 323 UV-Visible-IR Spectrophotometer

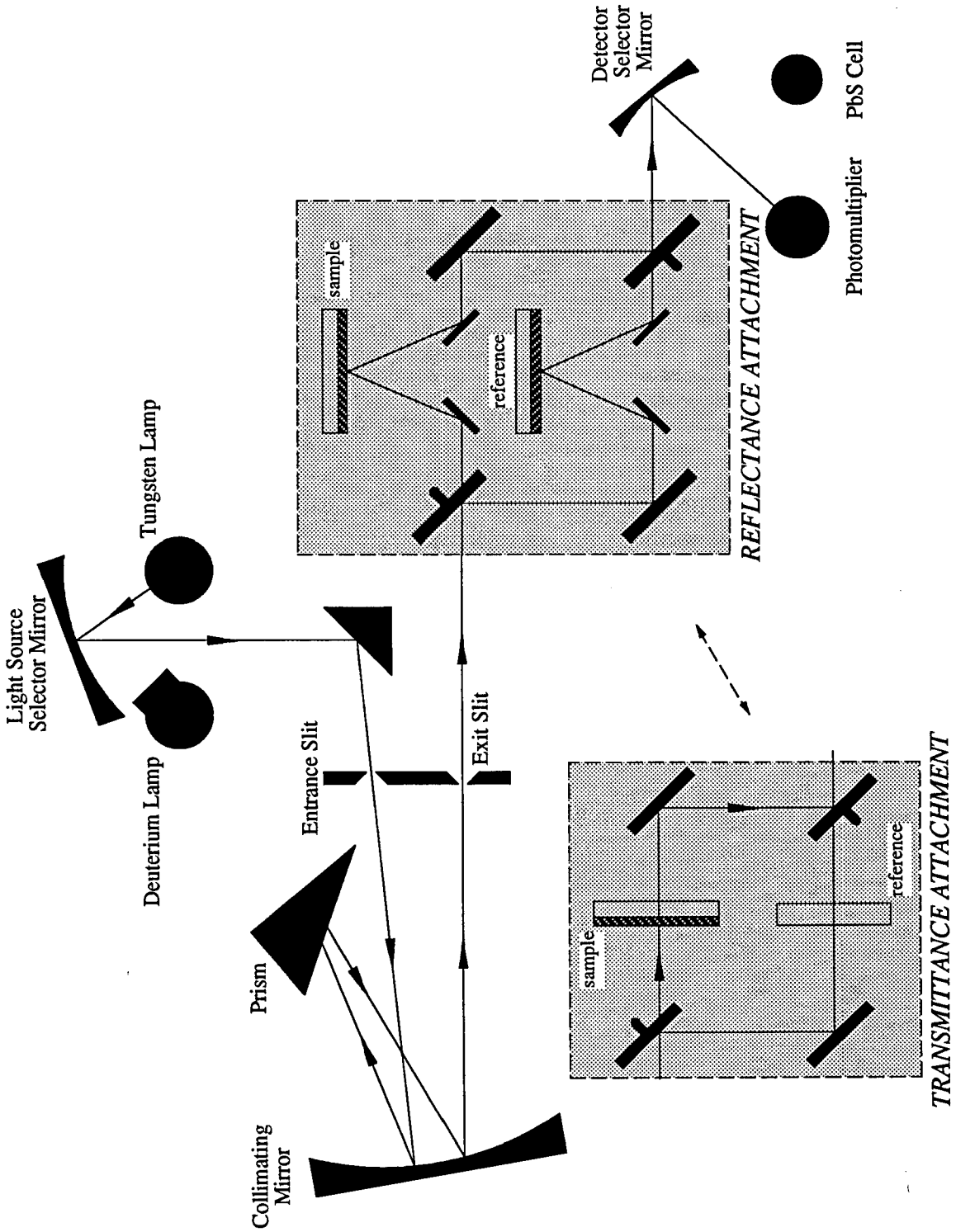

signal by either a PbS cell or photomultiplier tube, and passes through an amplifier network to convert it to a voltage signal. This voltage signal is split into three components; the reference, sample and zero signals, and each is changed to D.C. voltage by a corresponding hold circuit. The output from the reference hold circuit is applied to the motor controlling the slit width, and the slit width is automatically varied between 5μm and 2mm by a servo circuit to control the energy of light incident on the detector so that the reference hold voltage is a constant 3 volts. A divider circuit accepts amplified reference and sample hold voltages, and generates a signal proportional to the transmittance of the sample.

Transmittance calculations were begun by calibrating the 100% and zero% lines across the wavelength of interest. The instrument does not initially indicate a flat 100% transmittance over the entire range, due to 100% line bending caused by a reduction in reflection efficiency of the mirrors. Calibration involved inserting two identical substrates over the reference and sample windows, and coarsely adjusting the position of the recorder pen to the 100% line at 500nm, the centre of the visible. Finer adjustment could then be achieved by moving through the wavelength range from 300 to 700nm, adjusting the 100% line compensation knobs, which are tunable at 310, 340, 355, 400, 500, 600 and 700nm in the visible, and at 1050, 1700, 2300 and 2600nm in the infrared. The zero line is calibrated by moving through the spectrum with the slit closed. Evaluation of the transmittance spectrum of a sample film is then achieved by placing the film+substrate combination over the sample window of the instrument with the uncoated substrate over the reference window, and scanning through the spectral range. Since the reference is an uncoated substrate and not air, the resulting output will be the difference between the transmittance of the coated and uncoated substrates.

Figure 6·3 also shows the reflectance attachment which replaces the transmittance attachment. The optical path is longer, but the operation is similar. Two aluminium coatings were sputter deposited simultaneously to give identical reflectances, and their absolute reflectivity is quantified using the 'V-W' apparatus described in the following section. If the absolute reflectivity is not suitably close to the theoretical reflectance of pure aluminium at 633nm, a new pair are deposited with different

thickness to the first pair. When the absolute reflectance was close to theoretical, the two mirrors could be used over the spectrophotometer windows to calibrate the 100% line, ensuring that the reduction in reflectance of aluminium towards the blue end was taken into account. Sample measurement is then made, relative to the reference, by scanning through the spectrum as in the transmittance mode.

For many of the single layer films produced in this work, optical absorptance was calculated using the simple relationship between reflectance R, transmittance T and absorptance A:

$$100\% = A\%+R\%+T\% \qquad [6\cdot6]$$

This relationship was found insufficient for the amorphous silicon systems, however, and section 11.1 will describe a novel technique involving the spectrophotometer, enabling absorptance and absorption coefficient to be accurately derived.

6.5.2 Absolute reflectivity

The reference mirrors used in the spectrophotometer were, wherever possible, freshly sputter-deposited aluminium films on glass substrates. As an aid to cross-calibration of the spectrophotometer in reflectance mode it was necessary to appraise the absolute reflectivity of the reference mirror. In addition, the technique was useful as a spot reflectivity measurement at a single wavelength for any of the film types produced.

Figure 6·4 shows the apparatus used for absolute reflectivity measurement. Initially, the apparatus is used to evaluate two reference mirrors, which are two nominally identical coatings deposited simultaneously, and mounted parallel to each other with the coatings facing. Here 'reference' is used as a means of identification and does not have the same context as the reference mirror used in the spectrophotometer. Light at 633nm from the laser strikes an angled mirror, deflecting the beam onto one of these mirrors with a reflection coefficient R1. It then deflects to the second reference mirror with a reflection coefficient R2, but because the two mirrors are nominally identical R2 = R1. The reflection from this surface diverts the beam

Figure 6·4

Absolute reflectivity by the VW technique

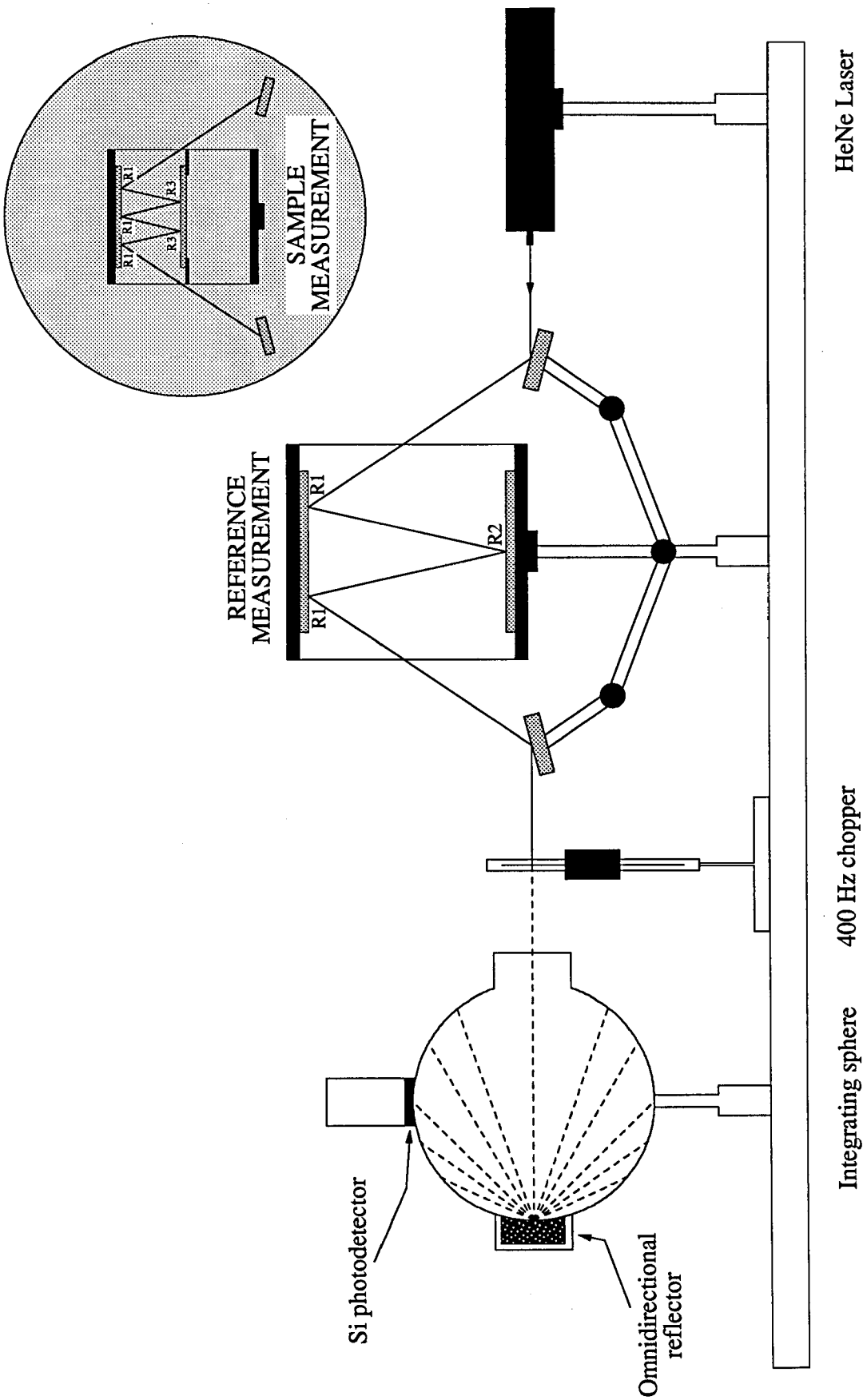

back to the first mirror, with a reflection coefficient R1 once more. On its exit, the beam has suffered three reflections, with a compound reflection coefficient of $R1^3$. To quantify the effect of the reflections on the beam, it is then axially directed into an integrating sphere, through a chopper. The omnidirectional reflector scatters the light equally over all angles, so that the photodetector can convert the photon energy collected from the internal surface of the sphere into an electrical signal. A lock-in amplifier is used to display the signal as a dc signal by using the frequency of the chopper (400Hz) as a reference input, and the signal from the photocell as the other input. The voltage output from the amplifier then corresponds to $R1^3$.

Measurement of the spectrophotometer mirror (for the purposes of absolute reflectivity now referred to as the 'sample') is similar, except that the geometry of the apparatus is such that the 'sample' is situated film-side up, mid-way between the two reference mirrors, and parallel to both. With this geometry, the beam undergoes three reflections from the top reference mirror and two from the sample mirror, giving a compound reflection coefficient of

$$R1^3 . R2^2$$

Once this reflection coefficient has been converted into a dc signal, a simple quotient reveals

$$\frac{\text{Sample reflection coefficient}}{\text{Reference reflection coefficient}} = \frac{R1^3 . R2^2}{R1^3} \qquad [6\cdot7]$$

The reflection coefficients from the reference mirrors cancel, so the absolute reflectivity of the sample is simply the square root of the ratio of the voltages from the amplifier. It must be stated that this is only valid at the wavelength of the incident light, and so cross-calibration of the spectrophotometer could only be achieved at 633nm.

The 'V-W' technique, so-called because of the arrangement of the reflected beam in figure 6·4, is a simple, little known technique for spot measurement of absolute reflectivity. Its sensitivity relies on the two reference mirrors having identical reflection coefficients, and on the sensitivity of the amplifier, which in this case was of the order of microvolts.

6.6 Electrical characterization.

Of all the properties of the films that were measured, electrical characteristics were the least investigated. Of greater interest for dielectric and semiconductor films alike were their optical properties, and these were found to be more sensitive to small changes in deposition parameters and dopant levels than film resistivity. In the case of the dielectric films, electrical characterization was an unnecessary exercise. However, the following technique was particularly useful for the quantification of electrical resistivity of the conducting oxides.

6.6.1 Quantification of sheet resistance

With reference to figure 6·5, the resistance of a rectangular shaped film, measured in a direction parallel to the film surface, is given by

$$R = \frac{\rho.L}{d.b} \qquad [6.8]$$

If the film is assumed to be square, L=b and equation [6.8] becomes

$$R = \frac{\rho}{d} = R_s \qquad [6.9]$$

Hence the resistance R_s of one nominal square of film is independent of the edge dimension of the square, depending only on resistivity and thickness. The parameter R_s is termed the sheet resistance of the film and has dimensions of ohms per square ($\Omega/\square$). It is a particularly useful parameter in a production environment where samples are being removed from the vacuum chamber in rapid succession. Such was the situation for films deposited throughout this work, and the evaluation of sheet resistance described below revealed not only whether the film was electrically better or worse than the previous sample, but by how much.

Once sheet resistance had been quantified, sample thicknesses were measured using the techniques to be described in section 6·7 and the resistivity, ρ, calculated using

$$\rho = d.R_s \qquad [6.10]$$

Figure 6·5:

The film dimensions used for derivation of sheet resistance, and of the four-point probe

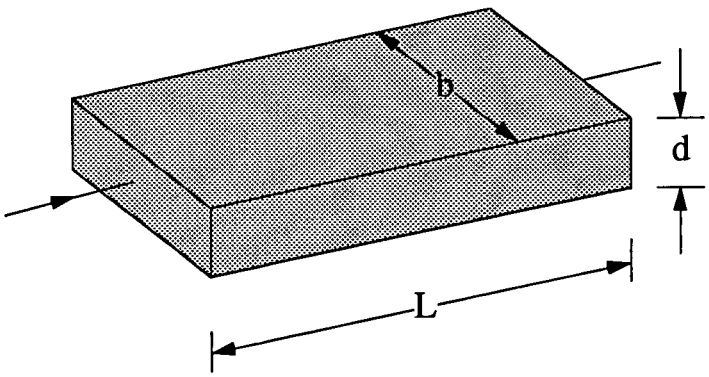

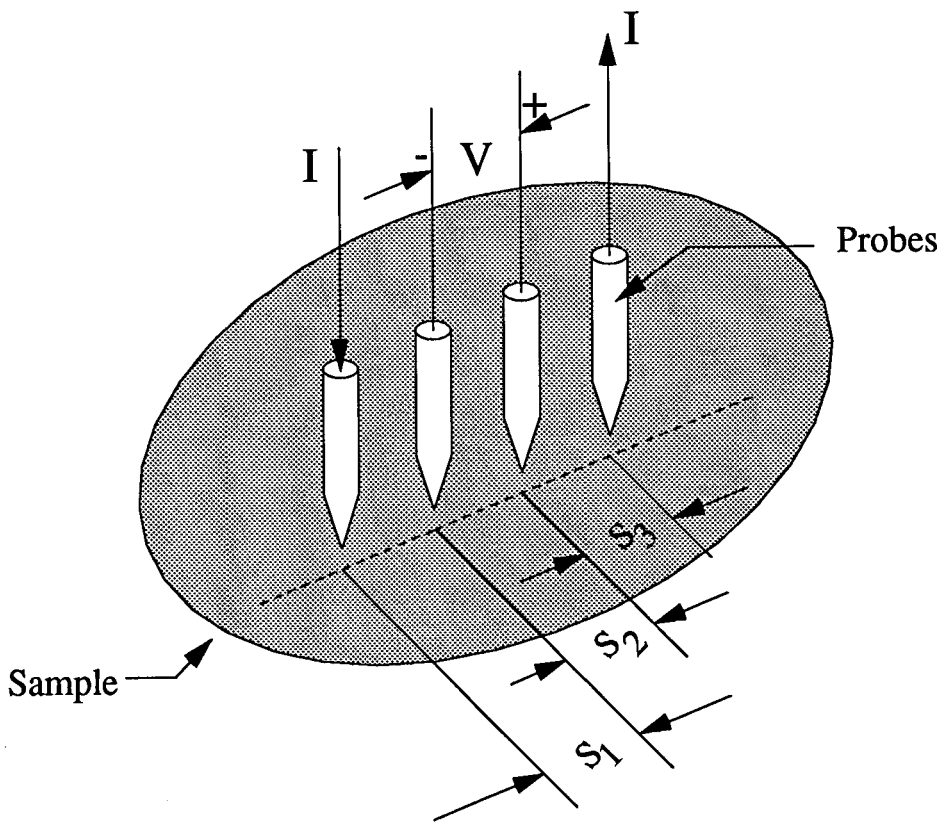

The calculations resulting in this equation suggest that the most direct method of measuring R_s is to prepare a rectangular film, measure its resistance, and divide by the number of squares between the two end contacts. While direct measurement of the number of squares is the simplest method, it is not practical for instant evaluation during a deposition run, and a technique which does not rely on specially prepared samples for each measurement is preferred. Further, because resistivity is dependent on film thickness, it is usually necessary to determine the sheet resistance at more than one point on the sample to compensate for non-uniform thickness, and this requirement renders the production of many rectangular samples unfeasible.

The most common solution is the use of the in-line four-point probe, shown schematically in figure 6·5. The in-line configuration was considered by Valdes[10], who demonstrated that when the probes are placed on a film of semi-infinite volume, the resistivity of the material is given by

$$\rho = \frac{V}{I} \frac{2\pi}{1/S_1 + 1/S_3 + 1/(S_1+S_2) - 1/(S_2+S_3)} \qquad [6.11]$$

When the probes are equidistant, $S_1=S_2=S_3$, and so

$$\rho = \frac{V}{I} . 2\pi S \qquad [6.12]$$

Valdes showed that if the material is an infinitely thin slice resting on an insulating support, equation [6.12] becomes

$$\rho = \frac{V\, d\pi}{I \log_e 2} \qquad [6.13]$$

or

$$\frac{\rho}{d} = R_s = 4.532 \frac{V}{I} \qquad [6.14]$$

The practical device was constructed from four spring loaded precision pins, 15mm long, 1.7mm in diameter, and the intra pin spacing was 2.5mm at the needle tips. The pins were mounted in a PVC holder, designed to provide equal contact pressure to the film when the pins were in contact with the film. A 'Datastore' microprocessor voltmeter (Schlumberger/Solartron Limited) was connected to the probes, and was programmed to measure resistance by supplying a potential difference

to the inner two pins, and dividing this by the current flowing between the outer pins. The meter was auto-ranging, and was sensitive to 1μV. Also written into the program was a multiplication factor of 4.532 so that the display automatically showed sheet resistance in ohms per square. The arrangement proved a successful method of attaining instant sheet resistance information, but it is was found that care had to be taken to prevent the pins penetrating soft films such as In_2O_3. Only the initial measurement could reliably be accepted in these cases because subsequent applications of the pins resulted in a higher sheet resistance due to the voids in the film caused by the penetration.

6.7 Film thickness determination

Thickness is one of the fundamental parameters of interest throughout the study. Many of the calculations of semiconductor properties such as resistivity and absorption coefficient rely on an accurate determination of this parameter. In a production environment it is essential to have instant feedback concerning the thickness of deposited films so that changes in process parameters can be made to maintain efficiency and consistent film properties. The coater used in this work was an air-to-air machine (see section 6.0.2) and did not require the in-situ thickness monitoring characteristic of batch processing, so all thicknesses were assessed on removal from the coater. Measurement techniques are as diverse as the coatings they measure, so only the techniques actually used in the work are described below. The two most natural ways of assessing the thickness of any component are by eye and fingernail. Optical techniques are the successor to the eye, and stylus techniques are the successors to the fingernail, and both of these successors were successfully used for thickness determination of the semiconductor films produced throughout the work.

6.7.1 Thickness determination using the stylus technique

The stylus technique is a post-deposition contact measurement of film thickness and is somewhat destructive, although over only a small area of the film surface. It can also be used to determine surface texture, although this application is more limited and is better suited to techniques such as atomic force microscopy.

A diamond tipped stylus, of conical radius 12.5μm, is dragged across the film surface over a linear distance of 1mm, with a force between 10μN and 30μN depending on the film hardness. The instrument measures the vertical displacement of the stylus as it traverses the film/substrate boundary, with this magnitude converted to electrical signals by a transducer. The signal is then amplified and filtered if necessary, before being recorded on a paper strip or CRT display. The stylus instrument used throughout this work was a *Talystep* produced by Rank Taylor Hobson Limited. Vertical amplification is between $5x10^3$ and $2x10^6$ in nine steps, with a resolution of 5nm.

With all stylus instruments the tip should cross a film/substrate interface at least once during its traverse, and the definition of this interface is the key to successful use of the technique. Several methods have been devised to ensure a sharp demarcation between the two surfaces. The deposition of a spot of TiO_2 powder dissolved in isopropanol over part of the substrate prior to deposition, has been successful[11] in producing a sharp step. The substrate is coated, and the spot removed with de-ionised water to leave a sharp boundary between surfaces. Softer, less dense films pose a problem for evaluation by the stylus technique in that the stylus will scribe into the surface during the traversal, even at the lowest applied pressure. A solution to this was found by Silver and Chow[12], who deposited a hard, thick layer of silicon monoxide over the area of the step, enabling measurement of thicknesses in the range 300-3000Å to be made with uncertainties of 100-200Å.

For the semiconducting films described later in this chapter, whose thicknesses were evaluated using the Talystep, substrate/film interface steps created in either of two ways. The first method involves dragging a razor blade across the film, through to the substrate. This results in the appearance of a 'valley' on the recorder trace, the depth corresponding to film thickness. Care had to be observed with this technique to avoid (i) multiple scratches, with the possibility of overlapping 'valleys', (ii) film debris collecting at the 'valley' floor disguising the true depth and (iii) scratching the substrate in addition to the film, again giving incorrect film thickness. The technique preferred throughout the work has been the masking of the substrate. In-contact masks, generally, are to be avoided in step formation because of the shadowing caused by the leading edge. This was most clearly seen in

initial trials when using cover slips or adhesive tape as a mask, where the step was seen as a long shallow curve, often containing plateau, and an accumulation of deposit formed on the film side of the mask. Figure 6·6 shows the solution designed to cure the shadowing problem. A razor blade was clamped at an angle of 30° to the substrate, which was itself clamped to the backplate. When exposed to the deposition flux, the finely tapered leading edge of the blade, with an edge thickness of 79μm created a sharp 'shoulder', with no shadowing and insignificant accumulation of deposit. Thin adhesive tape masks and cover slips are 120 μm and 215μm thick respectively, and neither have a tapered contact edge. Unlike the razor blade, neither makes good surface contact with the film. An actual Talystep trace taken for hydrogenated silicon is shown in figure 6·7. The step can be clearly seen, and the film thickness measured as 295nm at a vertical magnification of $1x10^5$.

6.7.2 Thickness determination using ellipsometry

Ellipsometry is a powerful, non-contact, non-destructive diagnostic tool, and does not even require a film edge. Its sensitivity is such that changes in film thickness of 0.07Å have been observed using this technique[13], and it has the advantage of revealing film refractive index in the same measurement of thickness.

Even though the method dates back to Drude[14] in 1889, ellipsometry has recently attracted considerable attention because of a wide variety of applications in modern solid state optics, particularly in the physics of surfaces, interfaces and thin films[15,16]. Drude derived a formula relating the amplitude ratio of, and phase difference between the parallel and perpendicular components of light incident upon a film. Also incorporated into the formula are the amplitudes of total reflection and Fresnel coefficients at the interfaces of the system. This multicomponent formula is used in computer calculations to determine n_f and k_f for opaque films, and n_f, k_f and d for transparent films.

Ellipsometry is based on the change in state of polarization of light reflected from a substrate. On reflection from a surface, the ratio of the parallel and perpendicular components of radiation, p_p/p_s and the phase difference between these components, $\Delta p_p - \Delta p_s$, undergo changes dependant on the optical constants of the substrate, n_s and k_s, the angle of incidence θ, the optical constants of the film n_f and k_f, and the film

Figure 6·6: Technique devised to create film step edge

Vertical scale exaggerated for clarity

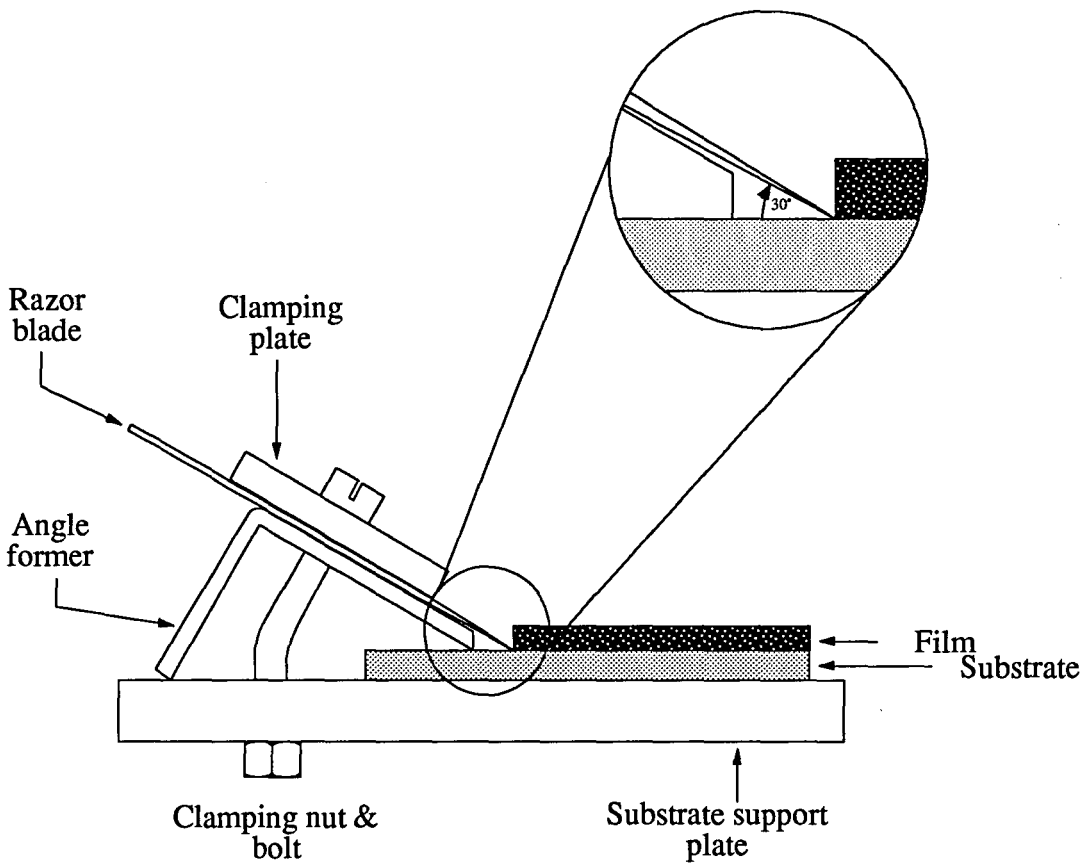

Figure 6·7: Talystep output

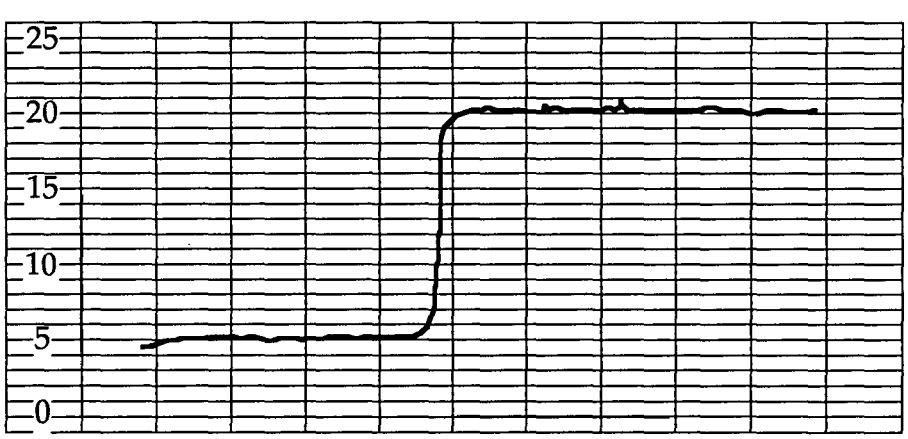

Film height = 295nm

thickness d. Providing the optical constants of the substrate are known and the film is non-absorbing (such that $k_f = 0$), the only unknowns in the equations describing the state of polarization are the refractive index n_f and the thickness d of the transparent film.

The ellipsometer used in this work was a Gaertner L117, and its schematic is shown in figure 6·8. Throughout the work the angle of incidence θ was kept constant at 50°. The coherent light at 633nm from a HeNe laser is linearly polarized by the polarizer before impinging the film surface with a power of no more than 1mW. After reflection the light is transmitted through a quarter wave plate compensator, which compensates the change of polarization of a light beam due to reflection. It then passes through a second polarizer termed the analyzer, and finally through a filter to remove extraneous background light. Beyond the analyzer is a photomultiplier, the output of which is displayed on a variable gain extinction meter. In practice the polarizer and analyzer are rotated until extinction of the beam is achieved, at which point the ellipticity caused by the polarizer-analyzer combination is the exact opposite of that produced by the film. Although there are 32 combinations of polarizer and analyzer which will result in extinction, only four of these are mutually exclusive. Knowing n_s and k_s in addition to these four positions, the computer program is used to determine n_f and k_f for opaque and transparent films. The technique is most accurate for film/substrate combinations with a large difference in refractive indices.

Where glass substrates were used, values of $n_s = 1.5$ and $k_s = -0.005$ were assumed. In such a situation, both film and substrate were transparent, and the reflections from each of the interfaces were not sufficiently separate. One solution is to blacken the back surface of the substrate, but the preferred method was to mount the substrate onto a 10mm thick glass plate, with a drop of immersion oil between the two. The oil had a refractive index of 1.5 and optically matched the two glasses, giving the effect of a very thick substrate and separated the two reflected beams. Where silicon substrates were used, a different program was necessary to calculate n and k prior to deposition. These parameters could then be inserted into the other routine in addition to the polarizer and analyzer positions, to determine optical constants of transparent films subsequently deposited.

Figure 6·8
The Gaertner L117 Ellipsometer - schematic

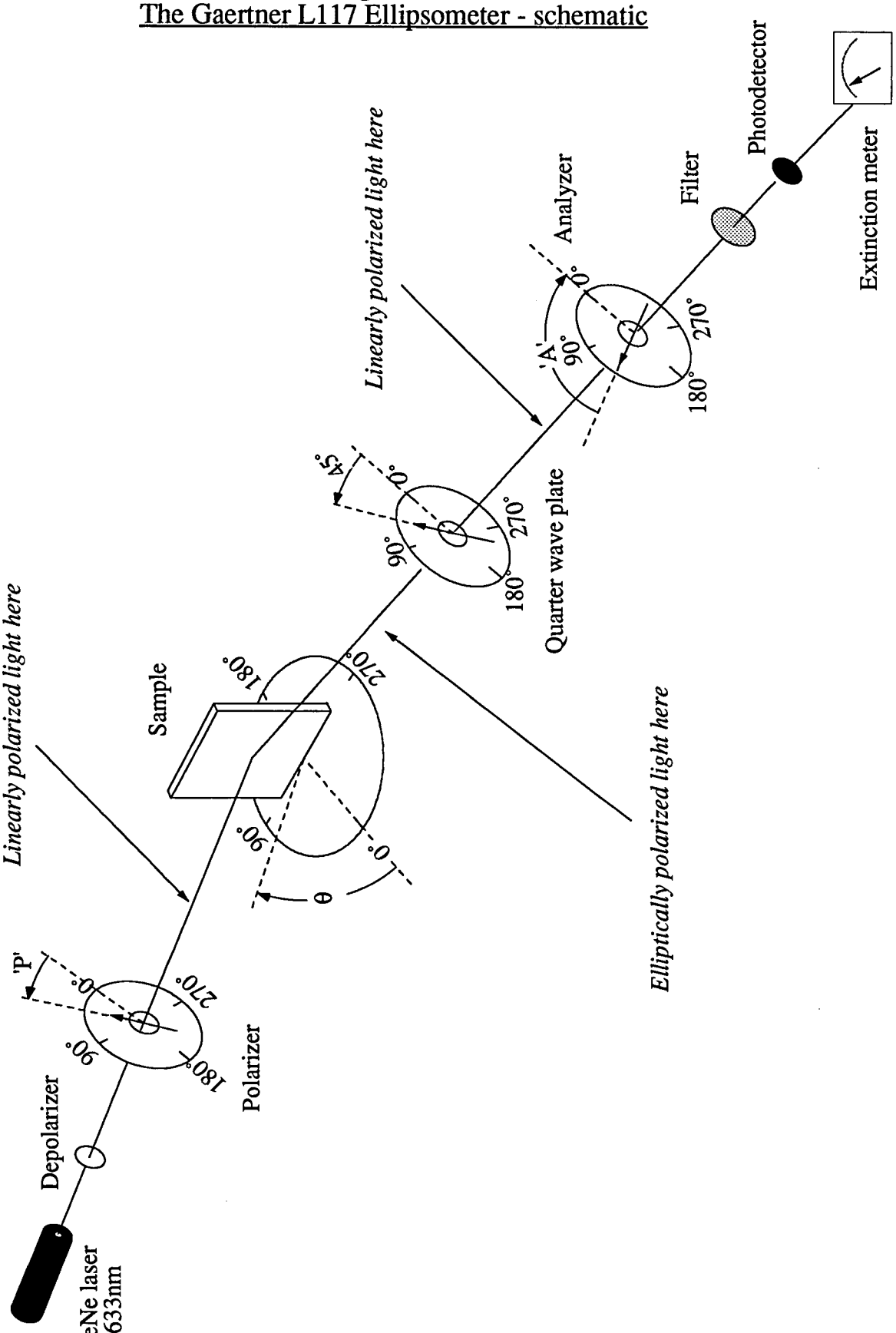

6.8 Surface analysis

Doping levels in semiconductors can easily be quantified using surface analysis techniques. Similarly, contaminent concentrations in films may only be revealed using instrumentation with sensitivity of parts per million or billion. For these reasons, two techniques were employed during the work, and the fundamentals of each are described below.

6.8.1 Auger electron spectroscopy (AES)

The technique of AES has emerged as one of the most widely used analytical techniques for obtaining the chemical composition of solid surfaces. A high sensitivity for analysis in the 5-20Å region near the surface, rapid acquisition speed, composition depth profiling and the ability to detect all elements from lithium to uranium are the basic advantages of this technique.

The Auger effect was discovered by Pierre Auger[17] in 1925 while working with X-rays. The technique of using electron excited Auger electrons to identify surface impurities was suggested by Lander[18] in 1953, but the high sensitivity of the technique was not realised until 1968, when Harris[19] demonstrated the use of differentiation of the energy distribution N(E) vs. E curves to obtain the Auger spectra in their present form.

In its simplest form, the Auger process is understood by considering the ionization of an isolated atom under electron bombardment. When an incident electron with sufficient primary energy E_P ionizes a core level, the vacancy is immediately filled by another electron from, for example, level L1. The energy (E_P-E_L) from this transition can either be released in the form of characteristic X-rays, or be transferred to another electron, in the L2 level, for example. This is ejected from the surface as an Auger electron. The measured energy of the electron is approximately equal to

$$E_K - E_{L1} - E_{L2} - \phi_A \qquad [6\cdot15]$$

where ϕ_A is the work function of the analyzer material. The Auger electron energies are characteristic of the target material and independent of the incident beam energy.

The apparatus used was a Varian 10kV Auger electron spectrometer[20]. Normal operating conditions were ~1.1μA, $3x10^3$ eV primary beam energy in a 100μm diameter spot. Argon was used in a static back-filled ion gun having a current density of 75 $x10^{-6}$ Acm^{-2}, and the base pressure of the system was 5 x 10^{-9} Torr.

6.8.2 Secondary ion mass spectrometry (SIMS)

The importance of the SIMS technique lies in its remarkable sensitivity. It is capable of detecting most elements in the ppm to ppb range, and was ideally suited for detection of dopant and contaminant concentrations in the semiconductor films deposited in this work.

The interaction of energetic ions with a solid results in the ejection, or sputtering, of substrate atoms and molecules in both neutral and charged states. The theory of the sputtering process was described in depth in chapter two, and is equally applicable for the SIMS process. This moderately efficient production of secondary ions coupled with very high sensitivity mass spectrometric techniques forms the basis of SIMS. The first experiments dealing with SIMS were performed in the late 1930's as part of a general study of negative ion formation resulting from ion bombardment of metal surfaces[21]. A sputtering ion source for mass spectrometers was described[22] in 1949, and by the mid 1960's a number of other workers[23,24] had contributed to the field. It was also during this period that the first SIMS instruments were developed[25] and investigations illustrating particular practical applications were reported[26].

The SIMS system used was a Cameca Ims 3f, and incorporated a unique ion-optical system, enabling the instrument to be used as an ion microscope. The diameter of the primary ion beam was between 25μm and 100μm for the work in this study, and the corresponding ion current density was usually <100 $mA.cm^{-2}$, with sub-micron spatial resolution. Mass analysis is achieved with a high transmission, high resolution magnetic sector mass spectrometer (resolution adjustable between 200 and 10000). The trace sensitivity of SIMS made it an ideal

technique for the analysis of the dopants in silicon films produced, with detection limits for elements in silicon in the range of 10^{13} to 10^{16} atoms.cm^{-3}.

Chapter Six References

1: D. Schatz., "The MDX as a strategic tool in reducing arcing", *Application Notes*, Advanced Energy Industries, Inc., 1983.

2: J. A. Thornton., *J. Vac. Sci. Technol.*, **15**, (1978), 188

3: L. Holland & G. Samuel, *Vacuum*, **30**, (1980), 267

4: L. Schott., in "Plasma Diagnostics", ed. W. L. Hotgreuen, North Holland Publishers (1968), p. 668

5: D. M. Manos., *J. Vac. Sci. Technol. A*, **3(3)**, (1985), 1059

6: P. A. Chatterton, J. A. Rees & C. J. Wu, 8th Int. Conf. on Ion & Plasma Ass. Tech., Brussels, (1991), p. 018.

7: B. Chapman., "Glow Discharge Processing", Wiley, (1980).

8: "Ultraflow mass flow sensor & controller manual", Vacuum General Inc., Jan. 1986.

9: I. Petrov, V. Orlinov & A. Misiuk, *Thin Solid Films*, **120**, (1984), 55-67

10: L. B. Valdes., *Proc. I.R.E.*, **42**, (1954), 420

11: A. Piegari & E. Masetti., *Thin Solid Films*, **124**, (1985), 249-257

12: M. D. Silver & E. T-K Chow., *J. Vac. Sc. Tech.*, **2**, (1965), 203

13: R. J. Archer & G. W. Gobeli., *J. Phys. Chem. Solids*, **26**, (1965), 343

14: P. Drude., *Ann. Phy. Chem.*, **36**, (1889), 532

15: R. M. A. Azzam & N. M. Bashara.,"Ellipsometry & Polarised Light", North Holland Publishers, (1971)

16: H. Yokota, M. Nishibori & K. Kinosita., *Surface Sci.*, **16**, (1969), 275-287

17: P. Auger., *J. Phys.Radium*, **6**, (1925), 205

18: J. J. Lander., *Phys. Rev.*, **91**, (1953), 1382

19: L. A Harris., *J. Appl. Phys*, **39**, (1968), 1419

20: G. Critchlow., Personal Communication, Surface Analysis Group, Loughborough Consultants Ltd., November 1991

21: R. H. Sloane & R. Press., *Proc. Roy. Soc. Ser. A*, **168**, (1938), 284

22: R. F. K. Herzog & F. P. Viehböck., *Phys. Rev.*, **76**, (1949), 855

23: R. C. Bradley., *Phys. Rev.*, **117**, (1960), 235

24: A. J. Smith & L. A. Cambey & D. J. Marshall, *J. Appl. Phys.*, **33**, (1962), 2915

25: H. J. Liebl & R. F. K. Herzog., *J. Appl. Phys.*, **34**, (1963), 2893

26: J. A. McHugh & J. C. Sheffield., *Anal. Chem.*, **39**, (1967), 377

Chapter Seven

Results and discussion - Improvements to the magnetron source

7.0 Contamination problems with the existing source

In the early stages of the work on silicon sputtering it was noticed that the silicon films were visually fully absorbing above a thickness of approximately 150nm, whereas literature figures for similar work state that silicon films are opaque to around 750nm. When analysed with ellipsometry, it was found that the 150nm thick films had refractive indices of 4.40 and extinction coefficients of -1.81, compared with theoretical bulk values of 3.50 and -0.20 respectively. Although there is always a difference between bulk and thin film values of these optical constants, such a disparity indicated the presence of unacceptable levels of contamination in the film. Before any further deposition work could continue, the contamination source had to be identified and modifications made to eliminate it. This section describes the construction of the magnetron at the outset, the disadvantages it possessed, and the series of remedies employed to correct both the contamination it caused and the resultant improvements in target utilisation.

7.0.1 The preceding magnetron design history, and improvements made

Preceding work had used magnetrons constructed using AlNiCo magnets, chosen because of the smaller range of magnetic alloys available at that time. For a given demagnetisation factor, AlNiCo alloy magnets have a larger physical volume compared with rare earth magnets currently on the market, to compensate for the weaker magnetic field strength which they provide. The original design was a simple, nearly balanced magnetron which was deep in order to accommodate the longer AlNiCo magnets, and resulted in maximum target erosion mid-way between inner and outer poles, with no erosion from the pole pieces.

The next progression was to bonded NeFeB magnets, which offer a high energy product combined with exceptional resistance to demagnetisation, typically five times that of AlNiCo. The latter type were forsaken for the higher field strength and more compact NeFeB in both inner and outer regions of the circular magnetron, and this was the design provided at the outset of this work. A single ring of magnets was located in the magnetron body around the edge of the face, with a smaller opposed ring in the centre to complete the magnetic trap. In addition, concentric mild steel pole pieces were attached above the magnetic rings to pull more field out in front of the target to increase the flux parallel to the surface. The maximum flux density at the cathode was 380 Gauss with this design, which exceeded the strength of the Alcomax design, at the same time being a more compact unit.

It was soon noticed during the silicon deposition work with the NeFeB magnetron that a 5mm wide ring on the face of the outer pole, and another on the inside edge, remained uncoated by the deposition flux and it was proposed that some part of the magnetic circuit was parallel to the pole over this region, causing it to sputter. If this was so, Fe would be detectable in the deposited films from the mild steel pole piece, which would account for the unusually high extinction coefficient of the silicon films. Auger analysis of the first sets of films indeed showed there to be an extremely high iron concentration of 11% in the silicon, which was clearly not acceptable and would undoubtedly give inaccurate optical and electrical results in the other semiconducting films to be investigated. Having decided that the source of the

contamination was outer pole piece erosion, see figure 7·1(a), a water cooled 'cap' was constructed and fitted onto the magnetron earth shield in order to mask any sputtered iron from reaching the substrate. The cap, shown in figure 7·1(b), covered the outer pole face, so that only the silicon target could be seen when viewed from in front of the magnetron. It was isolated from both cathode potential, and from the earth shield to which it was physically attached, to prevent it acting as an electron drain for the plasma. Ellipsometry was again used and showed a reduction in both refractive index and extinction coefficient to 3.48 and -0.58 at the thinnest absorbing film thickness which was now 850nm. To determine whether the iron contamination had been completely masked from the substrate, Auger analysis of the film was used, but showed there still to be a 6.4% concentration, despite the reduction in optical constants. An extension piece was machined for the cap, and fitted as shown in figure 7·1(c), but although it may have been more efficient in masking the pole sputter flux, and despite it being isolated, it drew a high electron current from the discharge, which would only strike at 900V, 0.03A. The masking experiments showed that whilst it was possible to reduce iron content in the films, the shielding necessary to remove it would result in extinguishing the plasma. Rather than continue to try to treat the symptom of contamination, the possible cause was targetted.

It has already been stated that the original 'Alcomax' magnets were longer than the newer NeFeB type, in order to maintain the strength of the magnetic field at the target. The latter were only 40% of the length of the original type, and the additional benefit of the associated compact design was considered a bonus. When the magnetic field lines for each design were studied, though, the cause of the pole erosion became apparent. Figure 7·2 compares the magnetic field lines for each design, and for the longer AlNiCo magnets the paths are the intended loops between poles, with the parallel component giving maximum target erosion in the centre of the racetrack. When the shorter, stronger NeFeB magnet design is considered, the path length between outer pole and base-plate is comparable to, or less than that between poles. As a result, some magnetic field lines are attracted to the base-plate near the outer pole, and there is then a component parallel to the edge of the outer pole. This corresponds directly to the uncoated area seen on the pole piece face, and the position of the erosion zone at the periphery of

Figure 7·1: Configurations of earth shield masking of outer pole pieces, Original magnetron design

(a): No masking of outer pole erosion

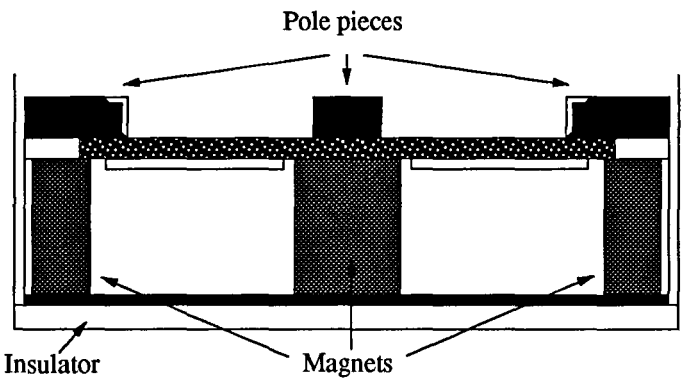

Fe concentration in film: 11%

(b): Partial pole masking

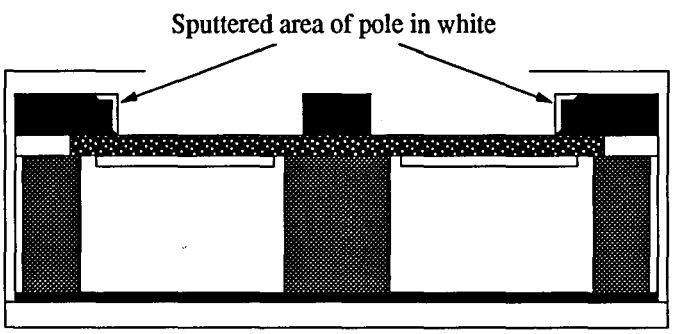

Fe concentration in film: 6.4%

(c): Full pole masking

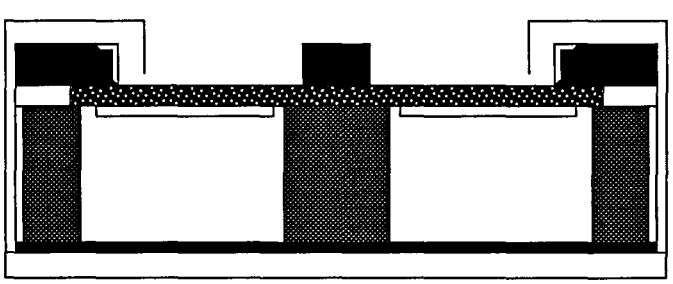

Discharge will only strike at 900V, 0.03A

Figure 7·2: Effect of magnet type on target erosion, and on pole sputtering

Original design using AlNiCo magnets.
Uniform erosion of target, with no pole sputtering.

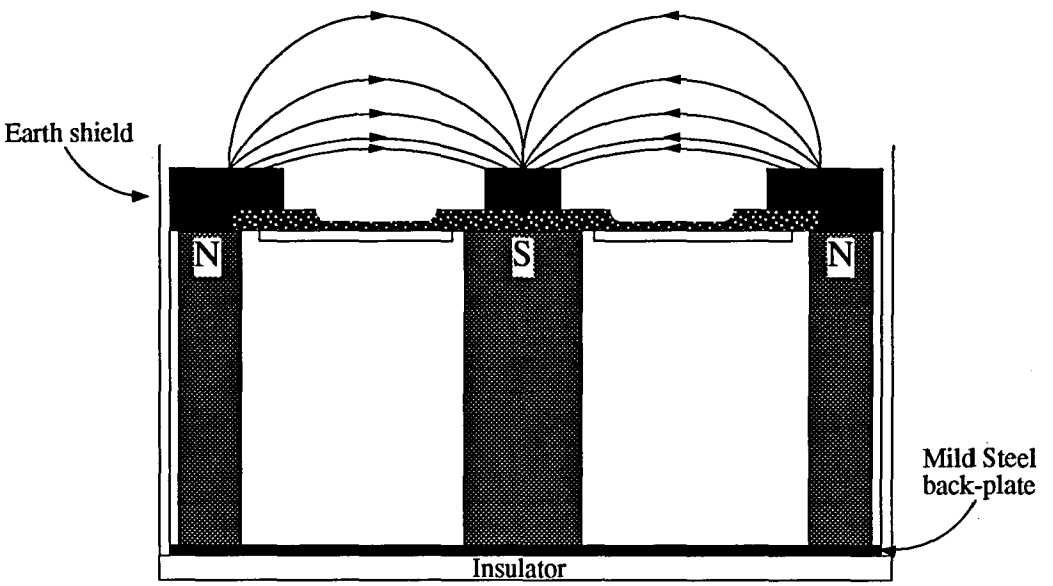

KEY TO MATERIALS: : Magnets : Pole pieces : Target, showing erosion

NeFeB magnets in succeeding design.
Target erosion zone pushed out, and sputtering of outer poles due to parallel component of magnetic field as shown.

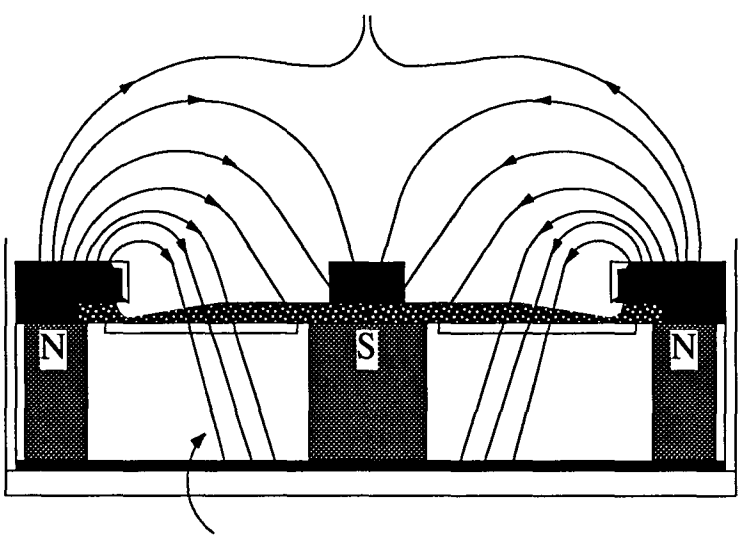

the silicon target shown in plate 7·1 is additional proof of this component of magnetic field.

Figure 7·3(a) shows the magnetic field lines in the design available at the start of the work, built using NeFeB. The field strength of 360-380 Gauss between the poles is above the necessary threshold for plasma initiation, but the familiar 'domed' field shape of the archetypal magnetron is not seen. Many field lines 'dip' towards the back of the magnetron because of the short distance from outer pole to base-plate, and are parallel to the outer edge of the target and the pole piece shortly after leaving the pole. Section 3.6 explained the reason for maximum sputter erosion where magnetic field lines are parallel to the target, and this effect is demonstrated here, with maximum erosion of the target at its outer edge, and erosion of the inside edge and face of the pole.

It was clear that to cure the problem would be largely an empirical exercise, undertaking different magnet configurations until the 'dipping', or 're-entrant' field lines were seen to be pushed out towards the centre of the magnetron to give maximum erosion midway between the poles. The next process was to remove the central pole piece to see the effect on re-entrant field lines and on the magnitude of field strength at the target. The effect is shown in figure 7·3(b), where the field strength fell to 270 Gauss and the field lines dipped to a greater extent, causing the pole erosion seen in white in the figure. Such a low field strength was considered too close to the operating threshold, especially when using a thick, low conductivity target such as silicon, so it was decided to maintain the use of the central pole piece.

The circular geometry of the magnetron, and the annular arrangement of the magnetic circuit resulted in a greater volume of magnetic material around the perimeter of the magnetron. Because of this, it was decided to increase the volume of the material in the central region, anticipating that this would result in a greater field strength above the centre pole. If this proved to be correct, it would be expected that the field lines would be preferentially pulled towards the central pole rather than the base-plate, forming the traditional closed domed field. A test magnetron body was built containing 126 holes at varying concentric locations, so that experiments could be made by inserting magnets at different locations and with different orientations until the field shape

Plate 7·1

Erosion profile is concentrated at the periphery of a silicon target, caused by the re-entrant magnetic field seen with the 'standard' NeFeB magnetron

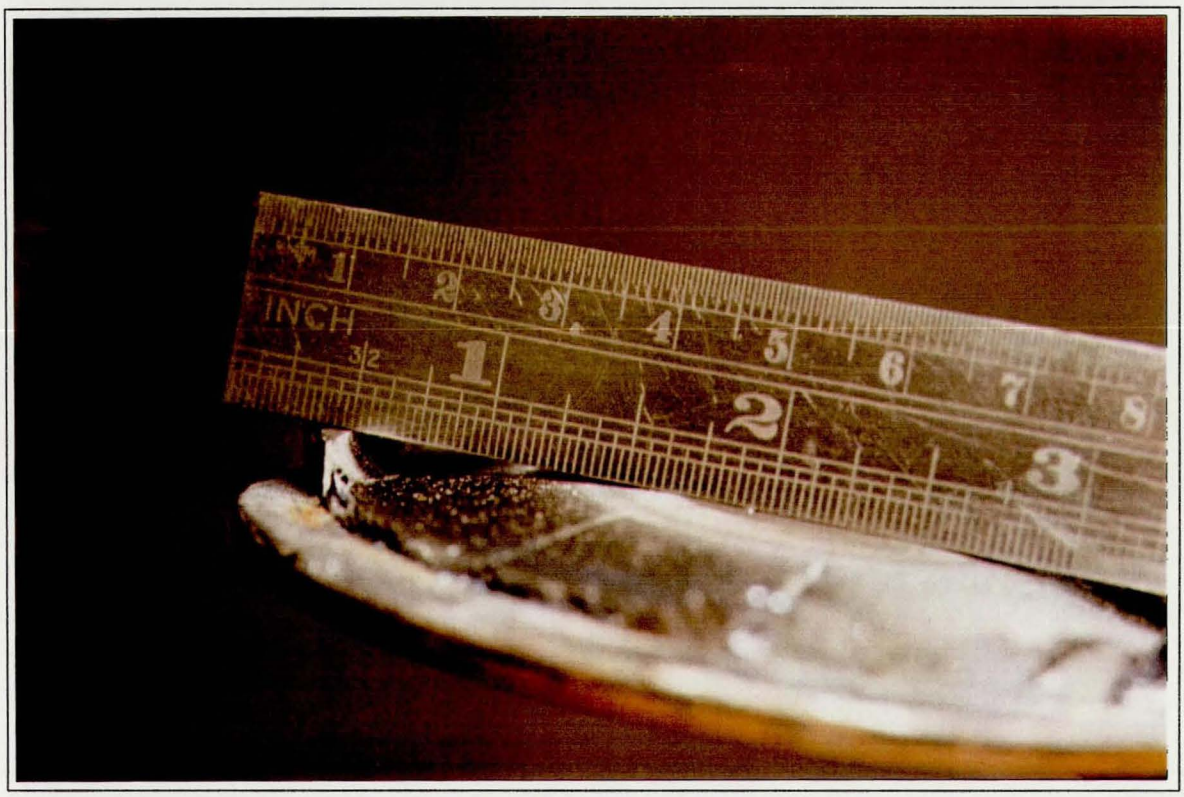

Plate 7·2

The magnetic confinement provided by the introduction of intermediate magnets in order to repel the re-entrant magnetic field

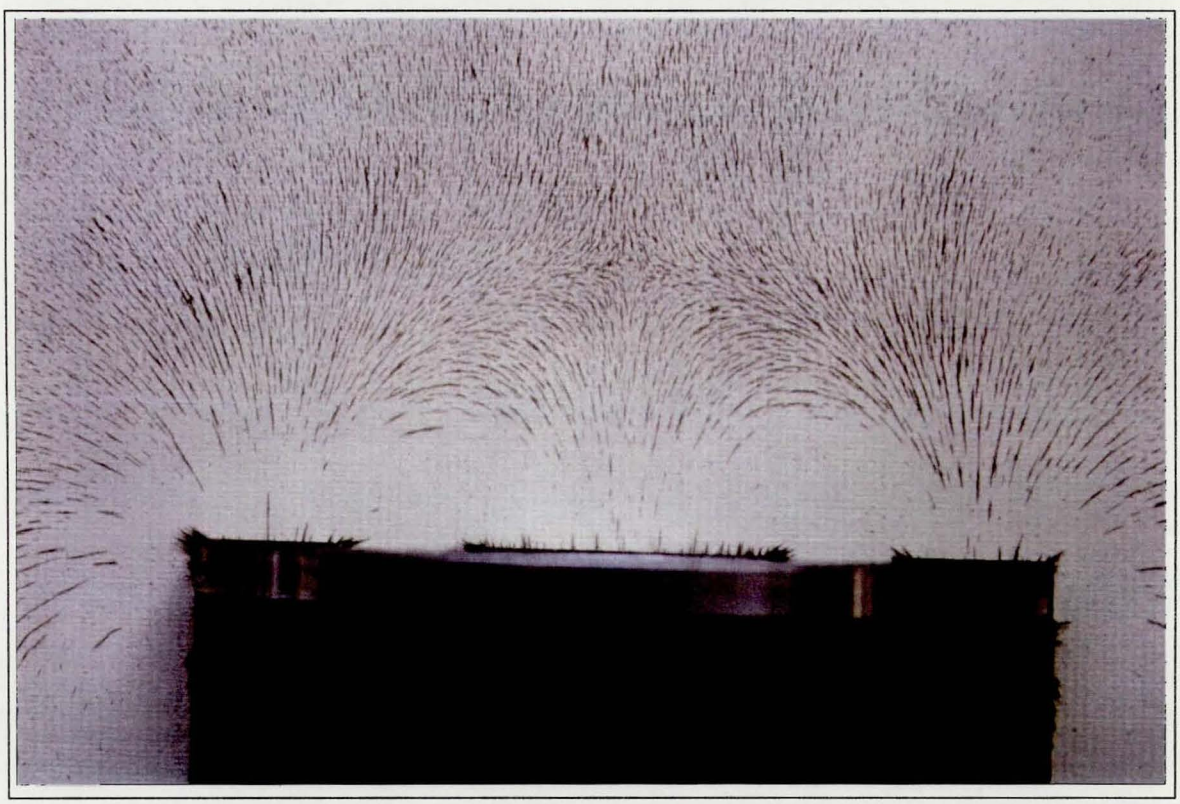

Figure 7·3: Progression towards optimum magnetic circuit design for 100mm magnetron, using NeFeB magnets

(a): Modification 1

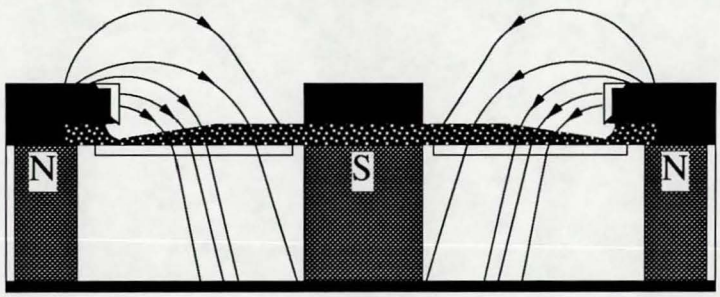

Magnetic field strength at target, midway between poles

360-380 Gauss

(b): Modification 2

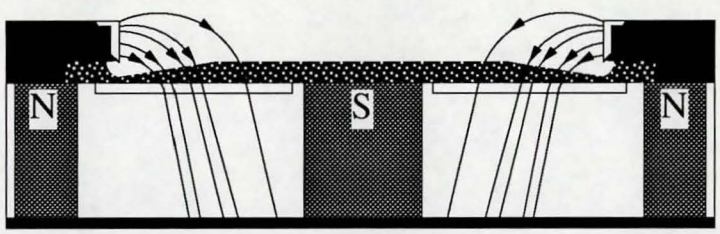

Magnetic field strength at target, midway between poles

270 Gauss

(c): Modification 3

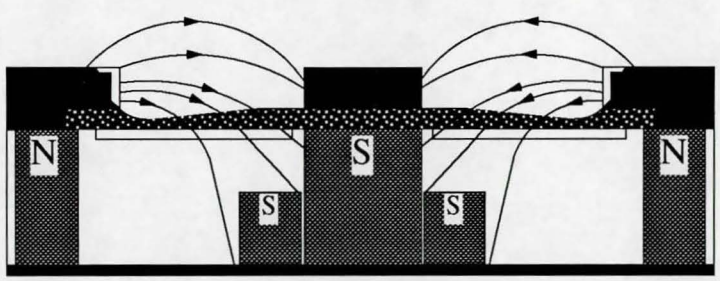

Magnetic field strength at target, midway between poles

Centre pole in: 530 Gauss.
No centre pole: 460 Gauss.

(d): Modification 4

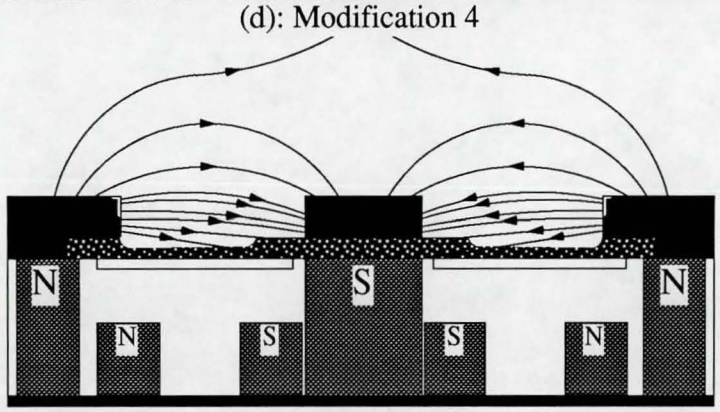

Magnetic field strength at target, midway between poles

Centre pole in: 680 Gauss.
No centre pole: 600 Gauss.

was correct. The depth and location of the cooling water channel precluded adding magnets of the same length as the annular magnets, so a ring of half-length, like-orientated magnets was inserted around the central magnet. Figure 7·3(c) shows the effect of the additional centre magnets, with a slight reduction in parallel field at the periphery due to more field lines being pulled towards the centre, flattening out the profile and reducing the magnitude of the re-entrant component. Although the erosion problem visibly remained, it was noticed that the central pole piece was not necessary to the operation of the magnetron now that a greater volume of magnetic material was used in the centre. A field strength of 530 Gauss without the pole piece was still well above the lower operating threshold, so the removal of this pole piece in future also removed another source of possible film contamination.

Despite the benefits of an increased magnetic field strength at the cathode, the re-entrant field and the deleterious pole sputtering and poor target utilisation associated with it, still persisted. The previous trial involved *attracting* the field towards the centre of the magnetron, so the next strategy was to assist this process by *repelling* any re-entrant field before reaching the base-plate. This consisted of a ring of magnets under the inside edge of the outer pole, of the same orientation as the outer annulus, and the effect is shown in figure 7·3(d). The resultant magnetic field strength was 680 Gauss with the centre pole, and 600 Gauss without, so the addition of repelling magnets opposed to those of the outer annulus increased the field strength by 150 Gauss. As seen in plate 7·2, the field lines formed a dome, peaked over the centre of the desired racetrack, and many formerly re-entrant lines were pushed up by the opposed ring so that they were almost parallel to the target surface. Although pole sputtering was still evident, it had been reduced to a 2mm ring, from the original 5mm. This encouraging result suggested that the only way to remove the re-entrant field lines, given that the centre and outer magnetic volumes were fixed, was to add more opposed magnets to push the field out towards the front of the magnetron.

The final design, incorporating two like-oriented rows of magnets close to the outer annulus to repel the re-entrant field and one near the centre to attract it, is illustrated by figure 7·4. This addition effectively brought the outer pole closer to the centre, or alternatively increased

the strength of the outer pole, making the device more unbalanced. This was confirmed during testing of the design for 3kWh with a silicon target. After this time, the target erosion had been moved towards the centre, the inner edge of the pole piece had coated with silicon and there was a much smaller area of erosion on the corner, as shown in the figure. The region 'A'-'B' is the erosion area, where the field lines are parallel to the target, explaining why the edge of the pole coats with silicon, rather than sputtering. Comparison of plates 7·3 and 7·4 shows the immediate improvement in magnetic field shaping provided by the additional rows of intermediate magnets, with the re-entrant field clearly removed in the latter plate. It is also instructive to compare plate 7·1 with plate 7·5, where the erosion zone of the latter has been moved away from the outer pole by the improved magnetic design. Auger analysis of 500nm thick films showed the Fe contamination to be approximately 2% with this design, which was a considerable improvement from the original 11% level, but still of sufficient significance to affect the qualities of the semiconductor films. Having removed the majority of Fe contamination with magnetic field manipulation, it was decided to remove the remainder by manipulation of the electric field.

Returning to basics, the pole piece was sputtering over the small area shown in white in figure 7·4 due to the combined effects of magnetic and electric fields, the latter arising from the pole piece being at cathode potential during use. Ideally, it should be made of an insulator, to prevent ion bombardment, but also magnetic to maintain the high magnetic field strength of the design. Since no readily available materials possess both these qualities, a method of isolating the pole piece was sought. Various options for isolating the pole piece were examined. The first was to insert a PTFE ring between the pole and target, but this would only be successful until it coated with sputtered material, when it would become conducting, enabling the pole to acquire cathode potential, with the onset of erosion once more. An insulating coating for the pole was the next consideration, with the prior exclusion of self amalgamating PVC, PTFE or vinyl sprays and plastic dip coatings because of their low heat tolerances when exposed to a plasma.

Figure 7·4: Optimum magnetic circuit design for reduction of contamination from poles in the NeFeB magnetron, showing resultant field lines

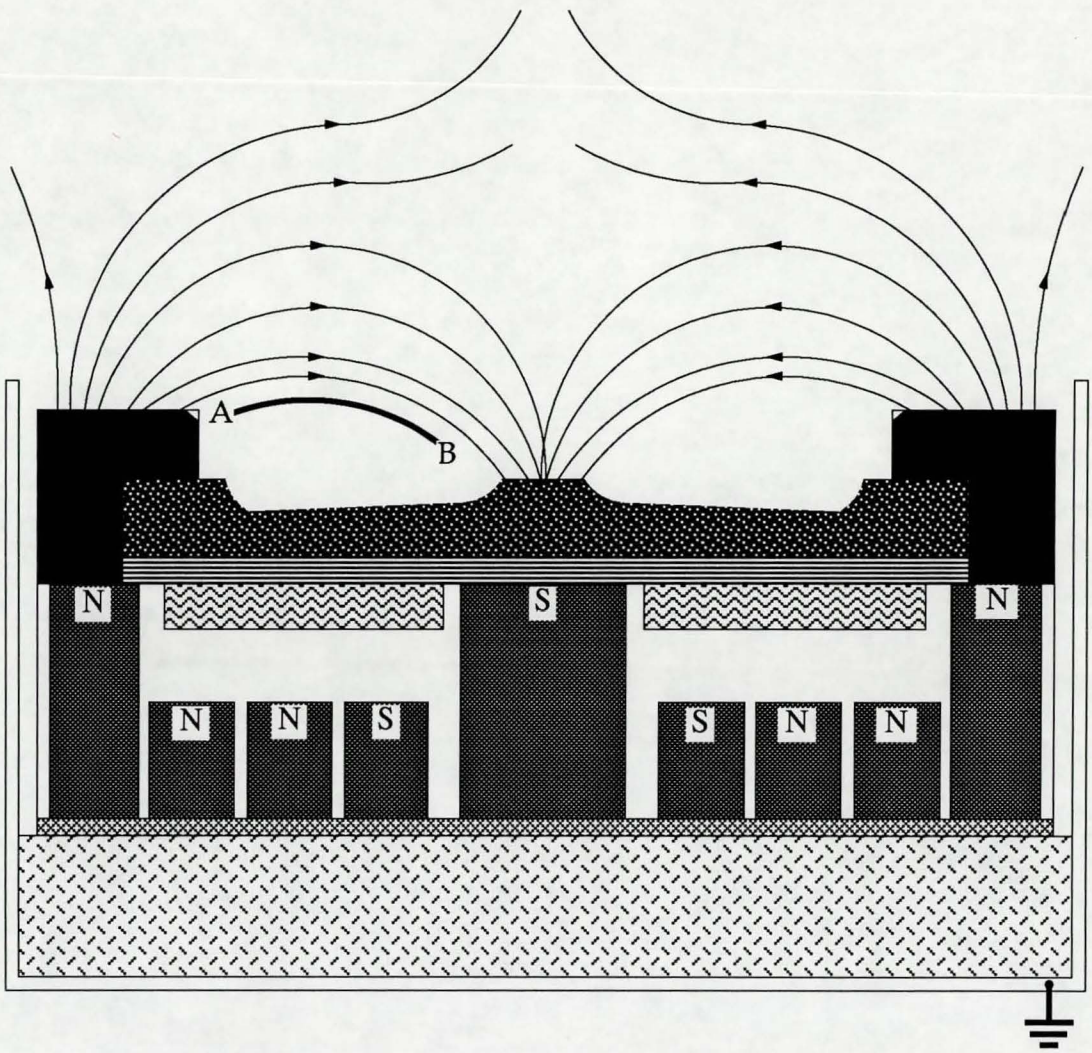

Plate 7·3
The re-entrant field at the outer pole of the 'standard' NeFeB magnetron

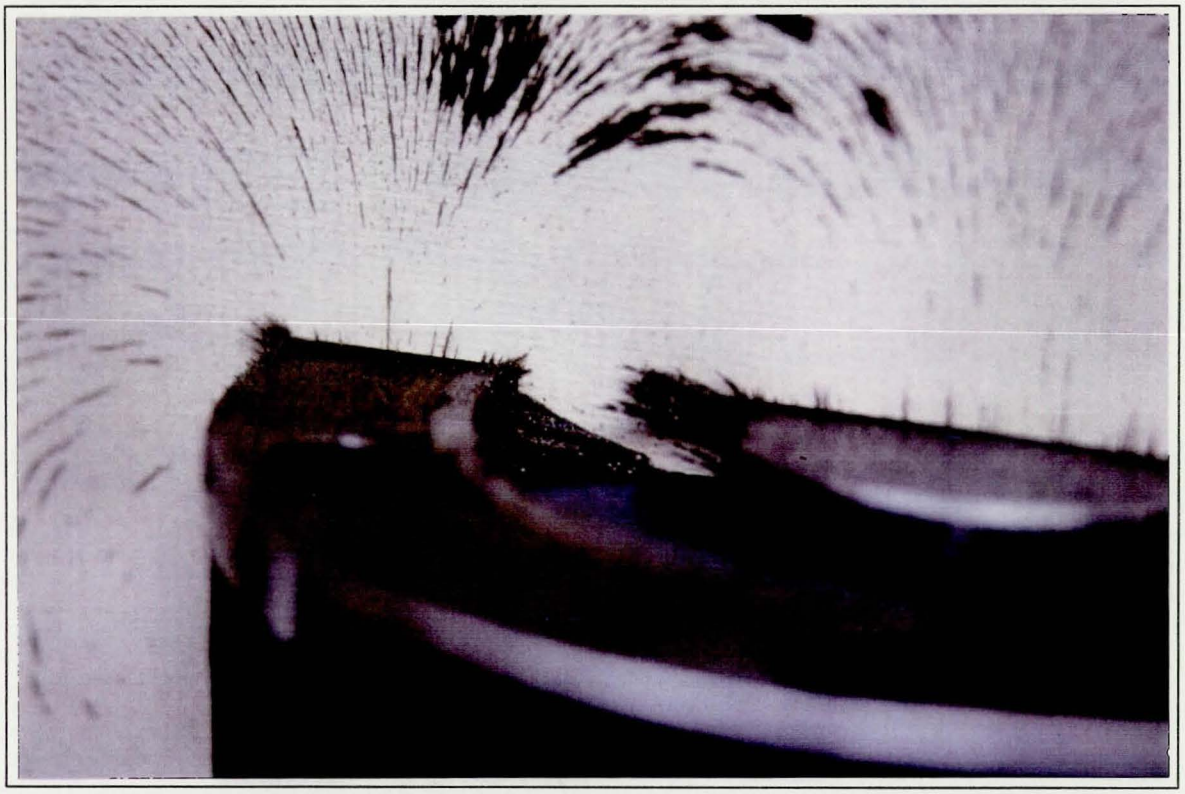

Plate 7·4
The effect of intermediate magnets upon the re-entrant field

Plate 7·5
A silicon target after 2kWh use, showing the location of the centre of the erosion zone when intermediate magnets are introduced to the 'standard' magnetron

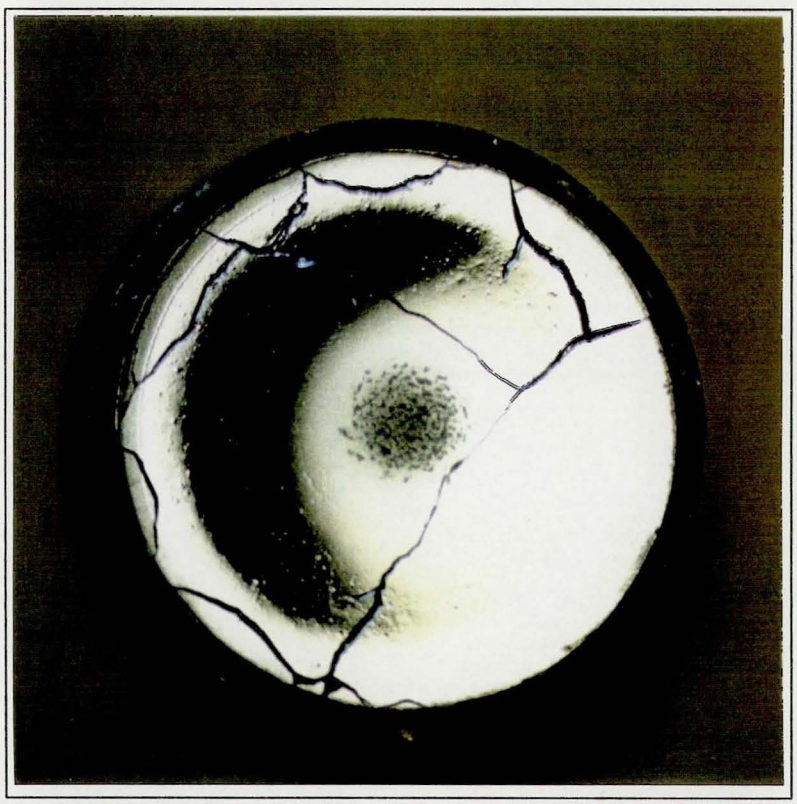

The solution was to use a modified silicone conformal coating, applied to the pole piece as a spray, in three coats, with each layer baked at 100°C for two hours as recommended. This material was high-vacuum compatible, would withstand 350°C and was insulating to 90kVmm^{-1}. With this technique, the pole retains its magnetic properties for optimum field shaping and when it becomes coated in sputtered target material it attains a conducting surface, assumes cathode potential and undergoes ion bombardment which sputters the target material from it. When the target material has been sputtered from its surface, the silicone insulator is revealed once more and ion bombardment of the pole ceases. This cycle of deposition on the pole, conducting layer formation and removal of the deposit to reveal the insulator continued without damage to the silicone coating, erosion of the pole, or Fe contamination of the films for the duration of the work.

Visual examination of the pole piece showed that it was covered by sputtered target material with no penetration of the insulating coating, and Auger evaluation showed no detectable Fe in 700nm thick sputtered silicon films. Ellipsometry of the same films gave their refractive index and extinction coefficient to be 3.82 and -0.43 respectively, confirmation that the original values of 4.40 and -1.81 were due to the Fe contamination. An additional benefit of the new magnetic design and pole insulation was that the erosion zone was moved closer to the centre of the target, giving higher utilisation.

7.0.2 Operating characteristics of the improved design

The assembled magnetron is shown in plate 7·6, using a silicon cathode whose construction will be detailed in the following section. Although the new magnetic field configuration had been measured as 680 Gauss, the bounds of operation would not be known until an assessment had been made of the operating characteristic of the device. The limits of operation are determined by factors such as efficient rate of heat removal from the cathode, mechanical and thermal stress in the cathode and regulation limitations of the power supply. A common technique for determining the safe operating limits of a particular magnetron source design is the study of its current-voltage relationship.

Figure 7·5 shows the variation of current with applied voltage for both zinc and silicon cathodes over an applied power range up to 1.3 kW, at

Plate 7·6
The fully assembled, free standing magnetron

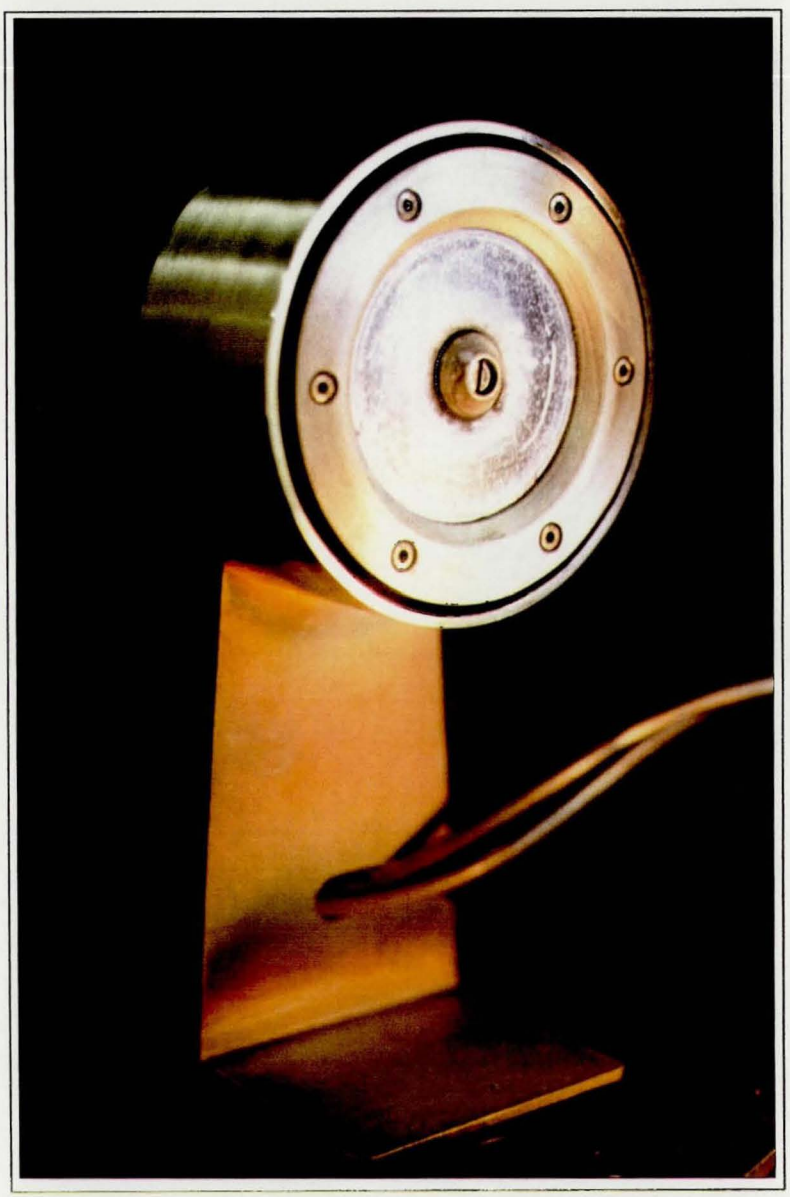

Figure 7·5
Operating characteristic of improved magnetron
for zinc and silicon cathodes

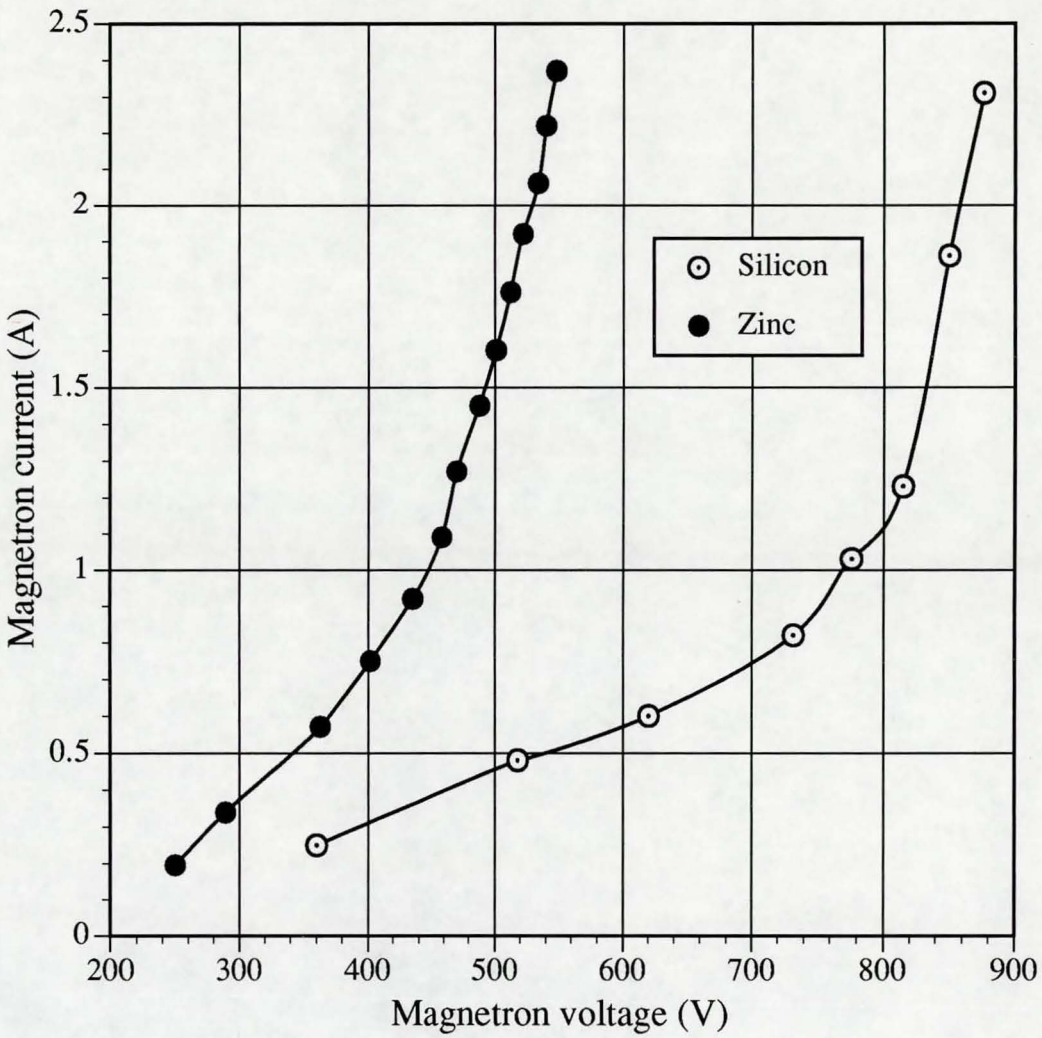

the typical argon partial pressure for sputtering of 3 mTorr. Both curves follow the general relationship given by equation [3·15], with increasing gradients with voltage due to the effect of the exponent n. Following plasma ignition, the current rises approximately linearly with voltage to 450V for zinc and 740V for silicon, where the linearity breaks down. There is a steeper rise in current above these voltages, indicating either (i) a reduction in efficacy of magnetic confinement due to heating of the magnets so that their temperature approached the Curie point, or (ii) inability of the water flow to remove the thermal load on the cathode, causing a change in its conductivity. Operation in this range is to be avoided because relatively small voltage increases result in large current increments, giving a higher mean deposition rate, but the gradient is such that small fluctuations in voltage due to transient arcs would lead to variable current density, deposition rate, film structure and density. In addition, the silicon characteristic approaches the maximum potential of 1023V delivered by the MDX supply, and would leave little room for the voltage rise expected from the addition of most reactive gases.

From the evaluation of the operating characteristics it was concluded that the new source design could only be operated reliably below 750 V with a silicon cathode, the least conducting of all targets used, to avoid the problems associated with the anomalies introduced by the upper 'tail' of the characteristic. The high conductivity of zinc resulted in a similar curve to that of silicon, but also enabled the cathode to be operated over a wider current range because of the lower operating voltages, with the associated advantage of higher deposition rates. It was concluded from the operating characteristic of figure 7·5 that the magnetron design was suitable for deposition work to proceed.

7.1 Magnetron target construction

7.1.1 Metallic and alloy targets

All reactive sputtering undertaken in this work was either from a metal target or from an alloy of two or more metals. None of the targets were in direct contact with the cooling water because of the risk of (i) flooding the vacuum chamber with water should the target wear

through, (ii) accumulation of calcium deposits from the water on the rear of the target causing poor 'o'-ring sealing and deterioration of the surface finish and (iii) damage to the 'o'-rings with repeated breaking of the water channel/target interface when changing target type. A 0.25mm thick stainless steel shim clamped between the water channel and rear of target to prevent the above risks, whilst maintaining good thermal and electrical contact. The water channel was less than 4mm deep to ensure high pressure flow through the device, and the inlet and outlet were set at the bottom and top of the channel respectively to prevent the collection of air pockets at the bottom of the target which would otherwise cause localised overheating and even melting.

Some of the existing targets had a bolt hole through the centre magnet so that the pole piece could act as a centre clamp. This was rendered unnecessary by the higher magnetic field provided by the optimised design explained in section 7.0.1, but the central hole was retained for expensive targets until they wore through, when they were replaced by a solid target.

7.1.2 The In:Sn target

Indium-tin oxide sputtering was from an alloy target of In:Sn10%wt, cast into an aluminium backing plate. This composition was chosen from the findings of work which had identified this proportion of tin as giving the best compromise between transparency across the visible and low resistivity[1]. The two metals alloy at a lower temperature than the melting point of indium alone, so the backing plate was placed on a thermostatic hot plate at 145°C, so that the metals could melt into each other. Some mechanical abrading of the backing plate was necessary to ensure 'wetting' was accomplished, rather than simple melting, which would not necessarily make a good electrical, mechanical or thermal bond.

7.1.3 The silicon target.

A polycrystalline silicon target was the preferred choice of target material for the oxide, nitride, oxy-nitride and hydrogenated films produced. Single crystal silicon, although purer, did not possess the thickness or mechanical resistance to surface temperature differentials experienced by a magnetron cathode. Polycrystalline silicon slices,

100mm square, 8mm thick and having typical crystal sizes of the order of 15mm were acquired from Wacker Chemitronic. One such square is shown face-on, at a scale of 1:1 in plate 7·7, courtesy of the supplier. The square was cut to a 100mm diameter circle using a diamond saw, and it was during this process that the brittle nature of the silicon was observed. Prior to the optimisation of the magnetic design, all targets were bolted through the centre, so a hole was bored through the silicon using a spark eroder under kerosene. Since the material was so brittle under tension, mechanical strength had to be provided by a combined shim/backing plate fixed to the rear surface of the target to provide support and good electrical contact.

A copper backing piece was used, but some difficulty was experienced in soldering the two materials together, with Pb/Sn alloy solder de-wetting from the silicon surface. An extensive set of trials was conducted, using combinations of different surface treatments, multilayer materials and thicknesses in order to bond the two materials, and only the final successful combination is reported here. To prepare a clean silicon surface on which to deposit the multilayer, the face was coarsely abraded to provide a key, then washed in hot isopropanol, concentrated HCL and de-ionised water before admission to the vacuum chamber. Prior to the first coat, the silicon was exposed to a 150 mTorr oxygen discharge from a pair of aluminium electrodes to remove any organic surface contaminents which may have remained. The first coating was a 200nm thick Al film, used as an electrical contact to the silicon. Since the surface of Al is easily oxidised and difficult to solder by Pb/Sn alloy, a 100nm layer of Cr was immediately deposited on top. The Cr was introduced as a 'glue' layer to promote adhesion, and to prevent the solder from de-wetting. The surface of the Cr needed protection against corrosion and oxidation during the hot bonding process, so a 100nm layer of Au was introduced as surface passivation, and because it reacts rapidly with both Pb and Sn.

The three layer structure was necessary to fulfil functions of electrical contact, adhesion, soldering and passivation, and whilst seeming a clumsy technique, it provided a bond which lasted for the lifetime of the target. Once the multilayer was complete, the silicon was heated to 160°C and coated with molten indium rather than solder, because of the bulk which the former provided. The copper backing plate was

Plate 7·7
Polycrystalline silicon cathode material, shown actual size

Photograph courtesy of Wacker-Chemitronic GmbH

similarly covered with a 1mm layer of molten indium, before the two were pressed together. Excess indium was squeezed out from between the two materials as pressure was applied to the silicon, ensuring complete coverage of both facing surfaces and eliminating air pockets which could cause delamination during use. When the indium had cooled and solidified, the polycrystalline silicon and copper backing plate were an integral unit, able to mounted in the magnetron. After several tens of hours of use, the silicon targets were seen to crack, due to compounded thermal and mechanical clamping stress, but because of the strong indium bond, they still remained usable.

Chapter Seven References

1: R. Lewin, R. P. Howson, C. A. Bishop & M. I. Ridge, *Vacuum*, **36(1-3)**, (1986), 95-98

Chapter Eight

Results and discussion - Oxides, Nitrides and Oxy-nitrides of Silicon

8.0 Experimental particulars

The deposition system and substrate handling technique have already been covered in chapter six, which describes general experimental procedure common to the preparation of all materials included in this study. The preparation of each different material required slight modification to the general experimental procedure, and a short description is included at the beginning of each of chapters eight to twelve for this purpose.

Reactive gas admission was designed to promote compound formation at the substrate, not at the cathode, to reduce the probability of poisoning. The manifold design was a circular looped tube, containing a series of equidistant 1mm diameter holes, which were offset to direct the gas toward the substrate. The design, shown in plate 8·1, ensured that the path from gas feedthrough and admission was short, so that a long time constant was not introduced into the PEM control loop. The substrate to source distance for these compounds, as for all others produced in this work was 65mm. The optimum distance for uniform coatings has been quoted[1] as approximately 0.4 times the active target diameter, but

Plate 8·1
The reactive gas admission manifold and PEM sight tube

Note that gas admission holes are angled towards substrate, not target

restrictions of chamber geometry, gas admission line location and necessity to reduce substrate heating from the unbalanced plasma resulted in this factor approaching 0.7 for this work. The reactively sputtered silicon compounds produced in this section were studied for their optical properties, with the objective of achieving precisely tailored refractive indices and thicknesses with high visible transparency. As several of the optimised compounds were expected to have refractive indices close to that of the glass slides usually used as substrates, ellipsometry would not have yielded accurate data. For this reason, two samples were prepared simultaneously for all materials in this section. One substrate was a glass slide, which was subsequently used for spectrophotometric evaluation, and the other was a slide pre-sputtered with an absorbing layer of approximately 1μm of silicon. Ellipsometry determined n and k for the silicon prior to the reactive deposition, after which the silicon compound coverage would be evident due to interference effects. Knowing n and k for the substrate enabled thickness and refractive index of the compound film to be accurately determined because of the large difference in n for the substrate and for the film.

8.1 Silicon and its oxides

A simple but necessary experiment was undertaken to confirm the linearity between deposition rate and applied power for the newly bonded polycrystalline silicon cathode in the improved magnetron source. Figure 8·1 verifies the linearity, and shows that the behaviour of the source and cathode is as expected.

Figure 8·2 shows the variation of sheet resistance and silicon film thickness with deposition time for the cathode operated at a constant power of 400W in 3 mTorr argon. Evidence of a linear relationship between silicon thickness and deposition time at constant power highlights an advantage which sputtering offers over competing technologies. Reliable estimates of different film thicknesses can be made simply by varying deposition time and extrapolating a figure such as 8·2, within reasonable limits. Neither thermal evaporation nor electron beam evaporation have such a simple dependence. The demonstration of the thickness/time dependence aided the rapid

Figure 8·1
Confirmation of linear dependence of deposition rate on magnetron power, using polycrystalline silicon cathode.

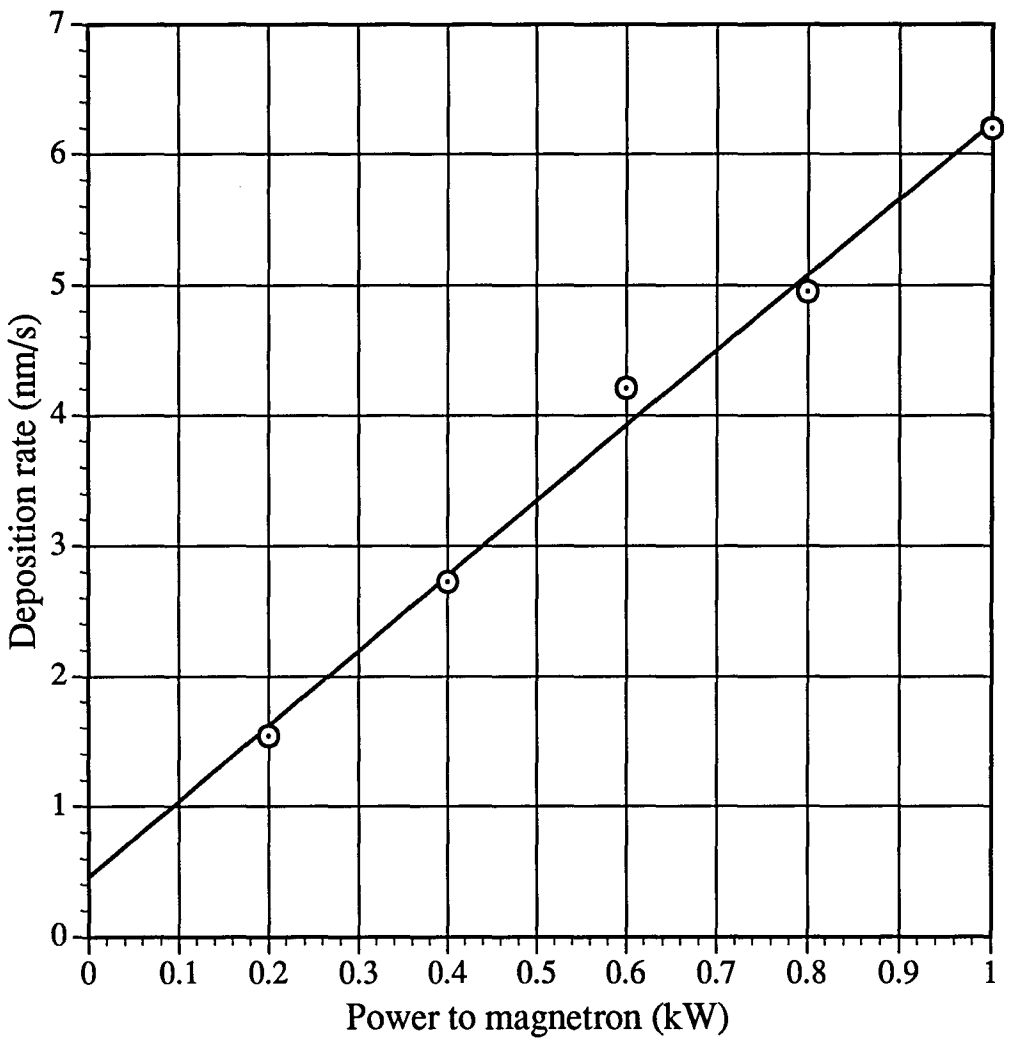

Figure 8·2
Variation of sheet resistance and film thickness with deposition time, using a silicon cathode at constant power of 400W

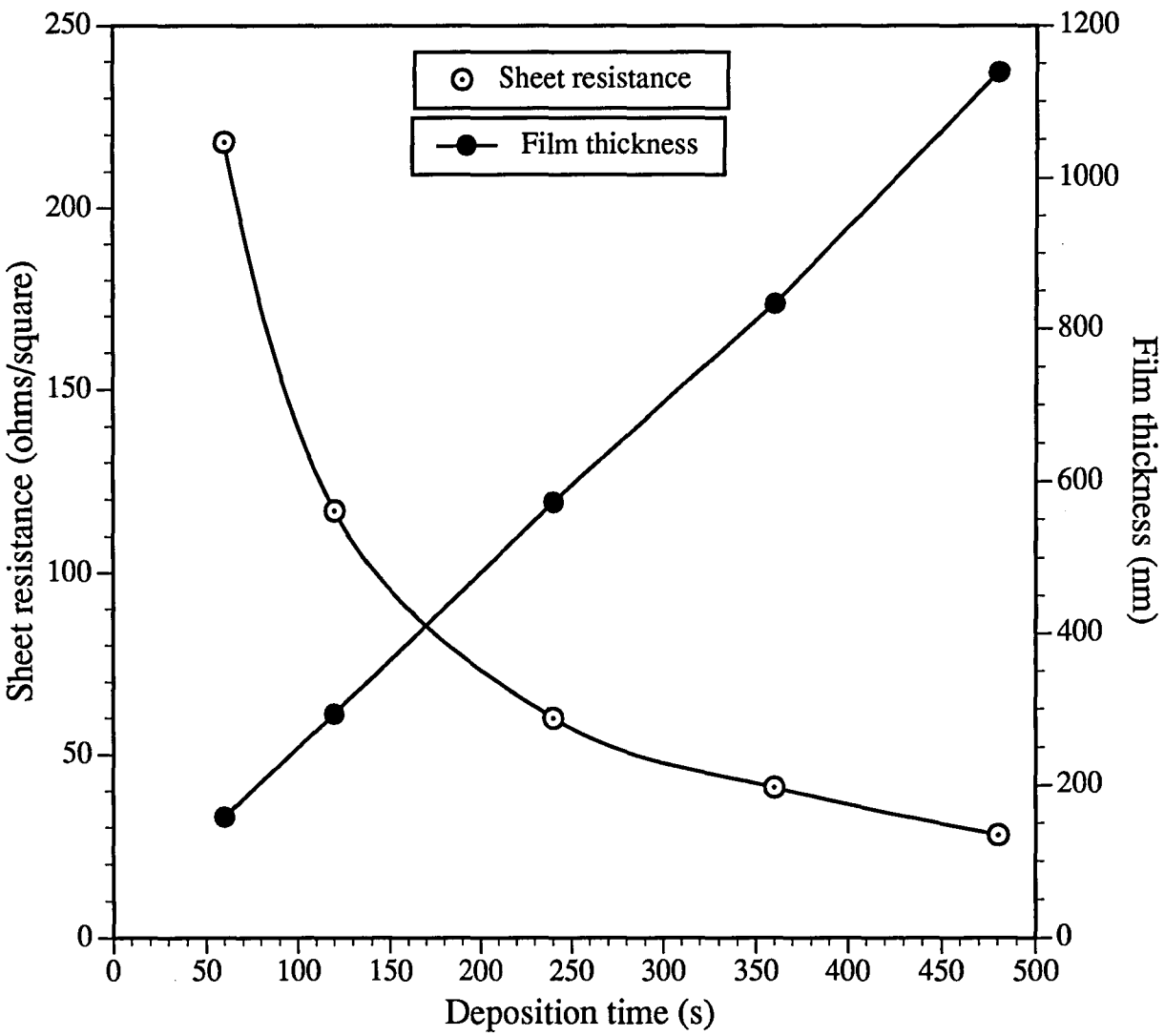

production of film series throughout the work, as it was later also found to hold for compound films. As a point of interest, by combining R_s and t from the silicon series shown, the resistivity of sputtered polycrystalline films was found to be $3.4x10^{-5}$ Ω.m, and constant across the range of thicknesses.

Figure 8·3 shows the refractive index of the oxides as a function of oxygen flow rate. Below a flow rate of 4 sccm the films are primarily silicon with very little oxygen incorporation, and it is assumed that the oxygen consumption at such low flow rates is by the pumping system rather than by the film or target. Consequently, the refractive index in this region assumes values close to that of bulk silicon. As the flow rate is increased, the transition between silicon monoxide and dioxide occurs, and the change in n from 2 to 1.5 indicates the formation of the stoichiometric dioxide at a flow rate of 7.5 sccm. At flow rates higher than this, over-stoichiometric films are deposited with refractive indices less than 1.5. Film thickness, also shown in this figure, rises to a maximum at 6 sccm of oxygen, only to fall as oxygen flow is increased further. The initial increase in thickness between flow rates of 4 and 6 sccm was assumed to be due to the majority of oxygen consumption by the growing film, with less consumed by the target and pumps. Above 6 sccm the film consumes a small proportion of the available reactive gas enabling the fully stoichiometric monoxide and dioxides to be approached, with the majority now consumed by the target surface. This results in partial poisoning and consequently lower sputter rate, explaining the lower film thicknesses. Deposition rates of monoxide and dioxide were approximately $2nms^{-1}$ and 0.8 nms^{-1} respectively, with plasma bombardment effects at the substrate as shown in Table 8·1 below.

Table 8.1: Unbalanced plasma parameters at the substrate

n	Substrate bias (V)	Ion current ($mAcm^{-2}$)
2.00	26.9	1.80
1.45	23.2	2.50

An observation which became common to all reactively sputtered silicon compounds was the similarity in form of the film thickness and cathode

Figure 8·3
Refractive indices and film thicknesses of silicon oxides
as a function of oxygen flow.
Deposition time 60s at 400W

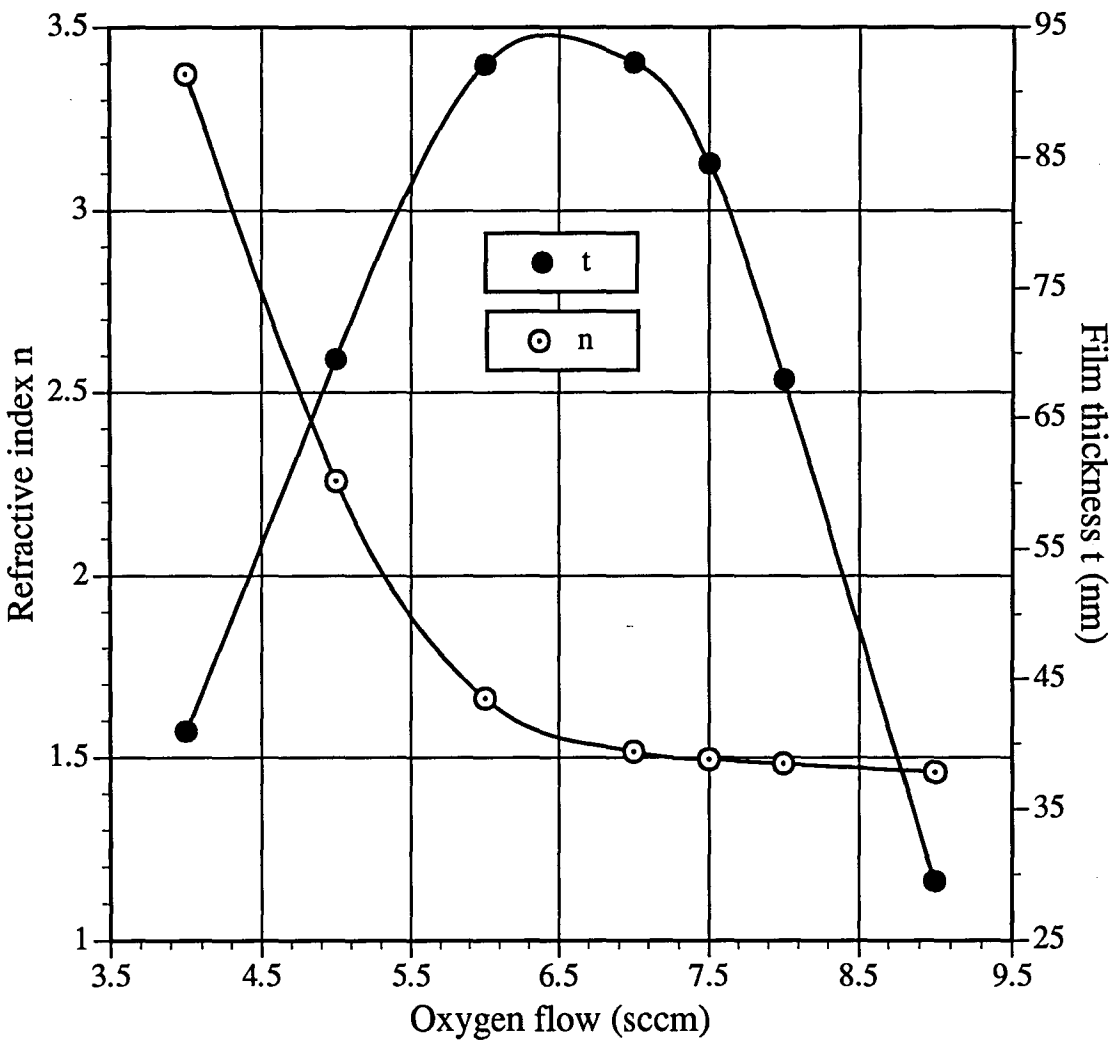

voltage relationships with reactive gas flow. The effect is demonstrated for silicon oxide production in figure 8·4. Cathode voltage rises only by 20V up to an oxygen flow rate of 6 sccm, the small rise attributed to the rate of 'cleaning' of the target being greater than the rate of poisoning. Such low flow rates are insufficient to cause any significant oxidation of the target, which would be accompanied by a more dramatic voltage change. Over the same range of oxygen flow, silicon oxide thickness also increases. Assuming a constant silicon sputter rate due to the nearly constant voltage, the substrate is subjected to a constant flux of silicon, but an increasing flow of oxygen. With sputter flux constant and oxygen flow increasing throughout a series of films, the film thickness increases. Beyond the peak in thickness and voltage at approximately 6.5 sccm oxygen, more oxygen is consumed by the target than by the process and the target surface becomes partially poisoned. The process remains stable due to the control provided by the PEM loop, despite the partial poisoning of the cathode. Increased poisoning causes the target surface to become less conducting, with the associated fall in cathode voltage. The lower sputter rate of the partially oxidised target causes a reduced sputter flux, which combined with the higher oxygen flow rates causes the observed reduction in film thickness.

Optical transmittance is an important property of silicon oxide coatings particularly when they are used in anti-reflection stacks, where the number of layers can exceed 100. Stoichiometric silicon dioxide with a fully characterised refractive index of 1.45 and known thickness is of little practical use if it contains significant optical absorption. Figure 8·5 shows the optical transmittance of the oxides identified by the refractive index data points of figure 8·3. Absorption occurred in the blue region of the spectrum for those with the highest indices, but as the dioxide was reached at an index of 1.46 the blue absorption had been removed to give a transmittance of ~96% in the visible.

From the collated refractive index, film thickness and optical transmittance data it was shown that reactive deposition of silicon dioxide films could be realised, giving a close degree of control of n and t. Iteration along the refractive index/oxygen flow figure enabled precise selection of the film index to be made to one decimal place, with process stability maintained by the PEM control loop.

Figure 8·4
Thicknesses of silicon oxides and corresponding cathode potentials as a function of oxygen flow.
Deposition time 60s at 400W.

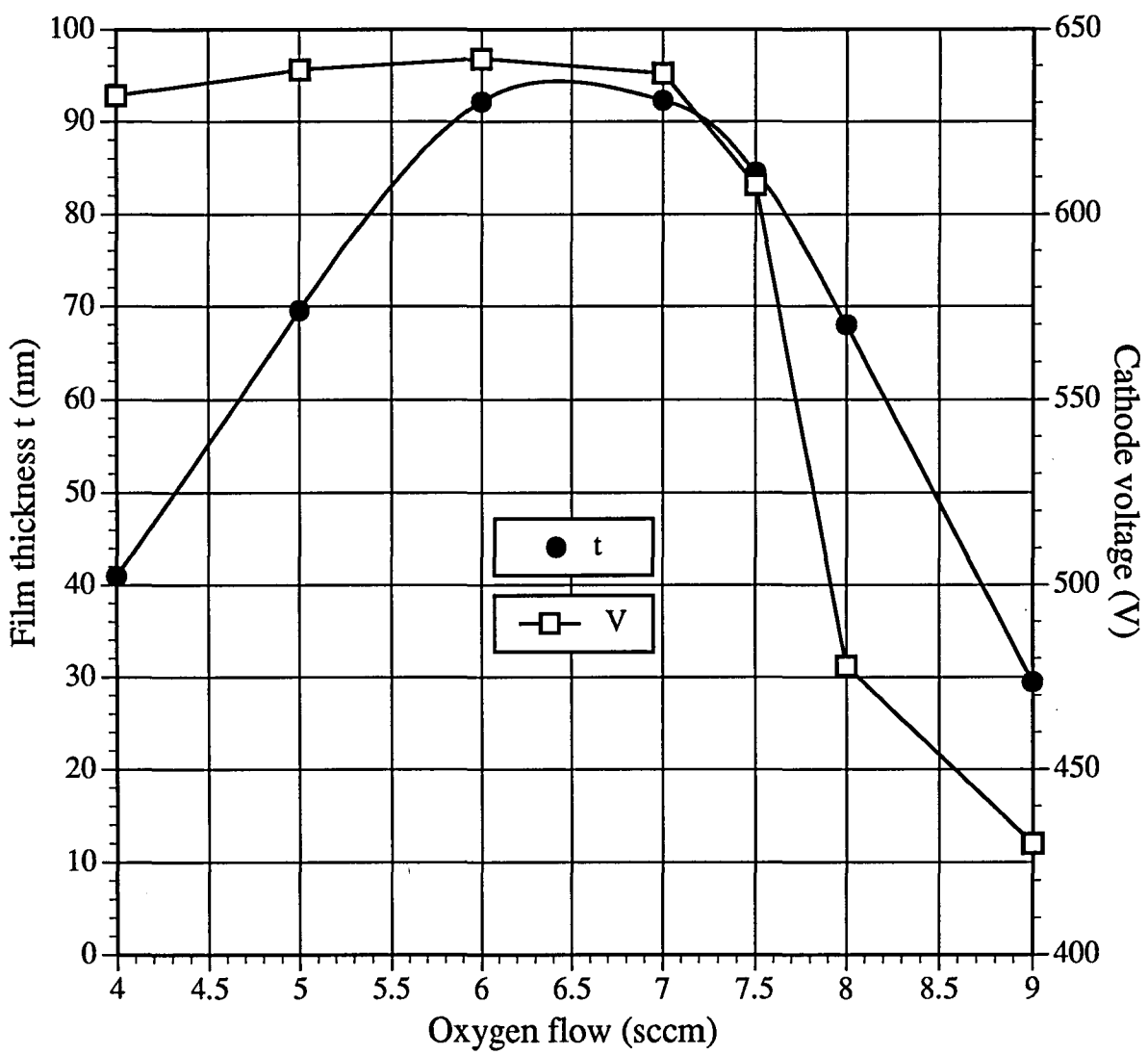

Figure 8·5
Optical transmittance of silicon oxides

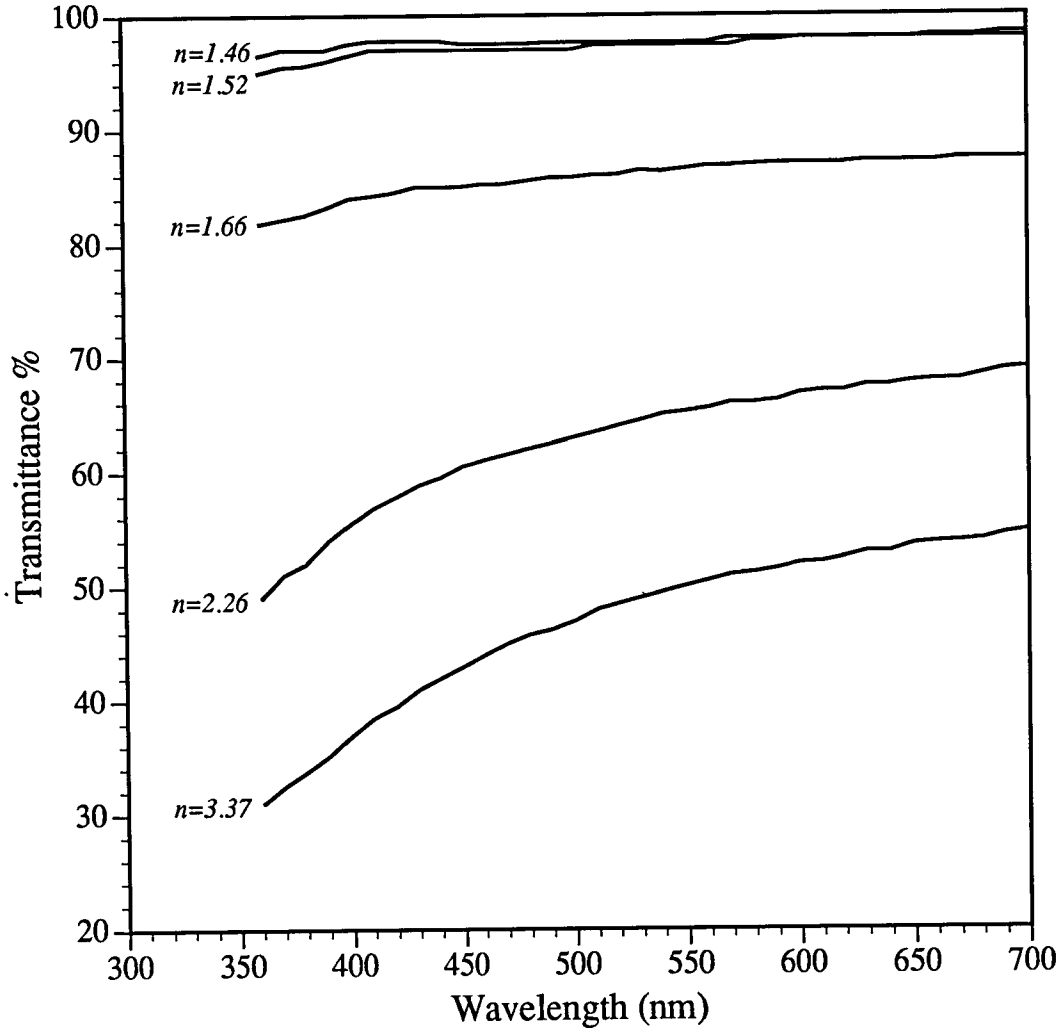

N.B. It is recognised that the transmittances of ~96% for the n=1.46 and n=1.52 samples are inaccurate, since they are apparently higher than the transmittance of the uncoated glass substrate, which has a reflectance of 4% from each face, giving it a transmittance of 92% at best.

8.2 Silicon nitride films

The refractive indices and thicknesses for silicon nitrides are shown in figure 8·6 as a function of nitrogen flow. Reactive gas flow rates necessary to produce nitrides were approximately five times those necessary for oxide deposition, presumably because nitrogen is less reactive than oxygen.

Refractive index follows a smooth progression from bulk silicon, at nitrogen flows of less than approximately 10 sccm, through sub-stoichiometric nitrides to silicon nitride with an index of 2.27. This index was attributed to the stoichiometric nitride because it combined the highest index with maximum transparency, despite the expected absorption in the blue seen in figure 8·7. The deposition rate at this index was 0.5 nms^{-1}, the substrate bias was 24.4V and the ion current was 2.4 $mAcm^{-2}$. Over-stoichiometric nitrides were then produced such that a flow of 48 sccm gave an index of 2.09. As an optical material, the silicon nitride with refractive index of 2.27 would have had limited application because of the 19% absorption shown at 500nm in the figure. Its use would have been limited to an application such as a passivation layer for integrated circuits, where its greater wear resistance would be an advantage over SiO_2.

In a similar manner to the preparation of SiO_2, then, silicon nitride was deposited with a precise refractive index, using an iterative progression through the series of data points shown in figure 8·7. Once n had been optimised, the system could be held stable to deposit the required refractive index whilst deposition time was linearly varied to create films of desired thickness.

8.3 Silicon oxy-nitrides

As an exercise in the control of a reactive process using two reactive gases, information accrued from the preparation of SiO_2 and Si_3N_4 was used to deposit silicon oxy-nitrides from the silicon cathode in a fixed nitrogen flow and variable oxygen flow. The 'base-line' for the composition of the compound was the silicon nitride identified in the

Figure 8·6
Refractive indices and film thicknesses of silicon nitrides as a function of nitrogen flow.
Deposition for 60s at 400W

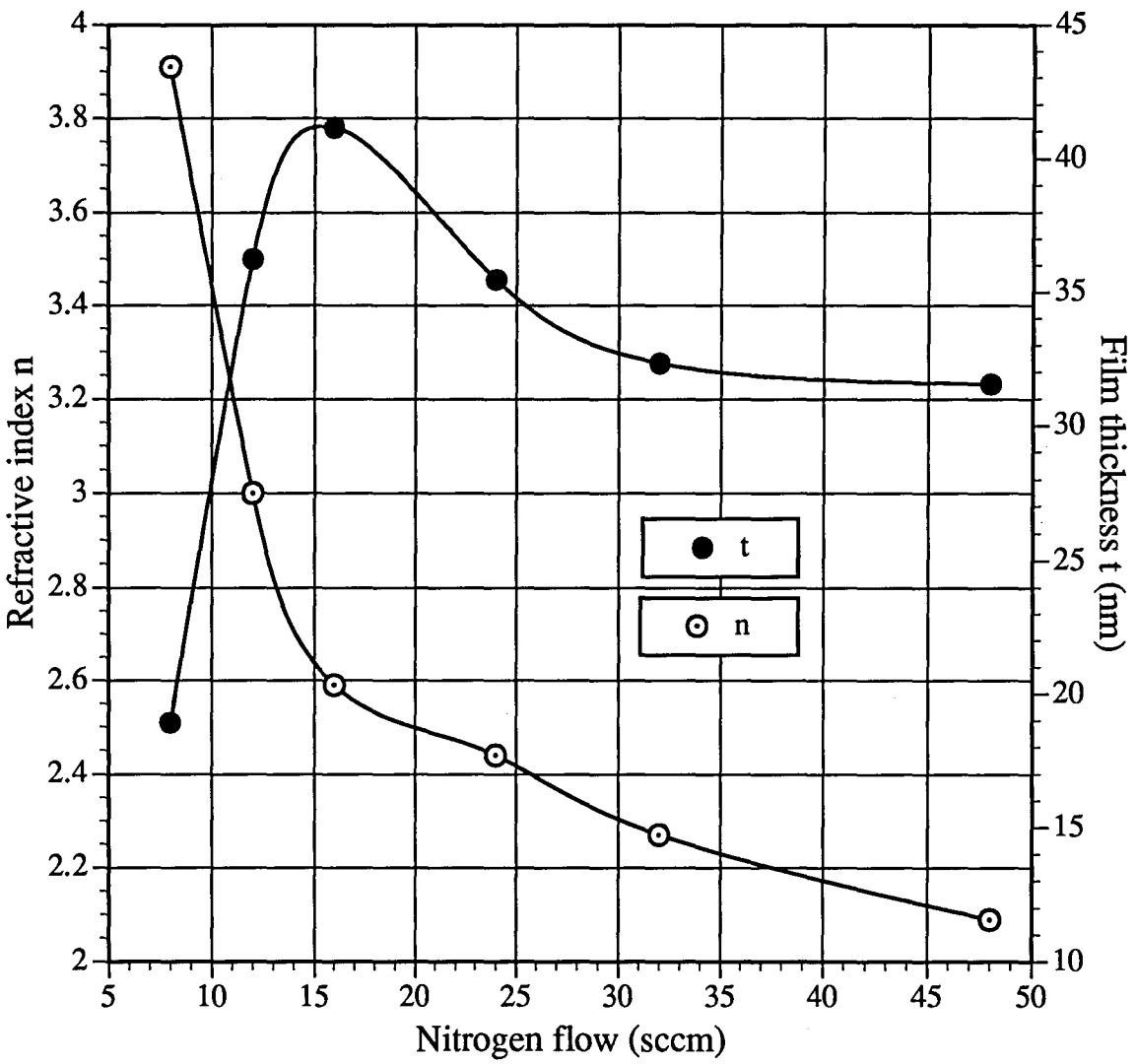

Figure 8·7
Optical transmittance, reflectance and absorptance
for optimised silicon nitride, with n=2.27

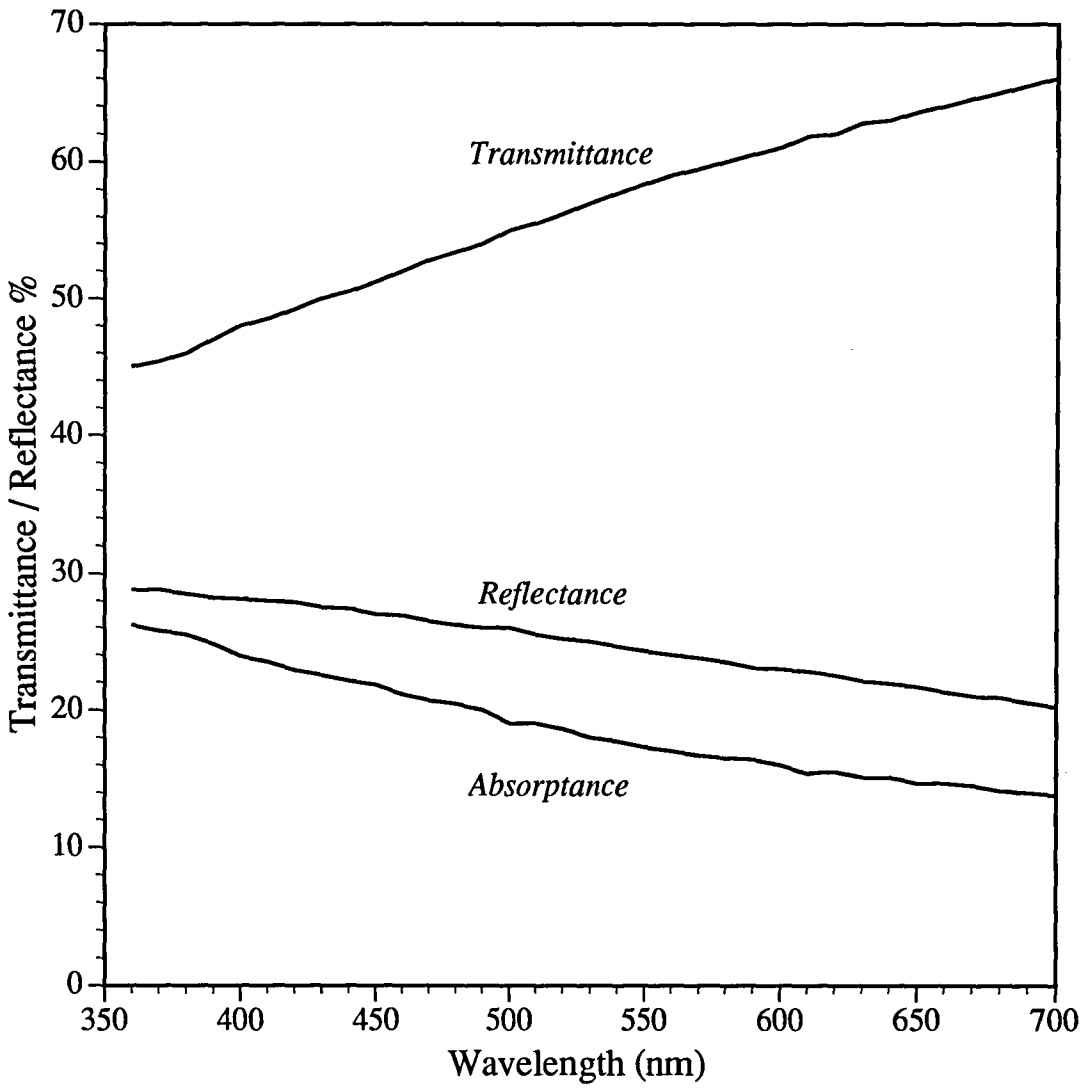

preceding section, prepared using a nitrogen flow rate of 32sccm, which gave a refractive index of 2.27.

Figure 8·8 shows the effect of increasing oxygen flow rate on refractive index, with the familiar decrease in the latter property. Refractive indices were obtained which ranged from 2.36 to 1.39, the former index within 0.09 of the nitride deposited at the same flow in the Si_3N_4 experiments, illustrating the reproducibilty of results. Films with $n<1.58$, produced at oxygen flow rates higher than 4 sccm, were attributed to oxide films where the oxygen flow rate is high enough for sputtered silicon atoms combine with the more reactive gas component in preference to nitrogen[2]. The optical transmittance of the series with $1.45 \leq n \leq 2.36$ is shown in figure 8·9. Taken as a whole, the series fall between the transmittance of the oxides and nitrides produced in previous experiments, which is perhaps to be expected due to the utilisation of the reactive gas combination. Such a yellowish appearance in silicon oxy-nitrides has also been observed by Eriksson[3] and Heitmann[4].

Those coatings with $1.58 < n < 2.36$ were termed 'oxy-nitrides' using the criterion that their refractive indices fell between those of optimum dioxide and nitride previously defined. Such oxy-nitrides had optical transmittances at 500nm ranging from 53% to 84% respectively. This investigation showed no significant difference in the degree of substrate ion-bombardment for the oxides, nitrides or oxy-nitrides. The sample at the mid-point of the oxy-nitride region, with n=1.66, acquired a substrate bias of 26.6V, induced by an ion current of 2.5 $mAcm^{-2}$.

Figure 8·8 demonstrated that the oxy-nitride films are formed in a narrow range of oxygen flow rates between 0 sccm and 2 sccm. It was decided to examine the narrow range in greater detail, but it was felt that the gas flow meters could not be depended on to admit fractions of one sccm reliably, and so an alternative means of admitting such small flow rates was devised. The proportions of nitrogen and oxygen in air are 78.08% and 20.95% respectively[5], so if the same air flow is used as that of oxygen in the previous oxy-nitride experiment, and the total nitrogen flow is constant, the abscissa of figure 8·8 will attain a five-fold increase in sensitivity whilst the reliability of the flow meters is maintained by operating them in their intended range. Nitrogen

Figure 8·8
Refractive indices and film thicknesses of silicon oxy-nitrides as a function of oxygen flow in a constant nitrogen flow of 32 sccm. Deposition for 60s at 400W.

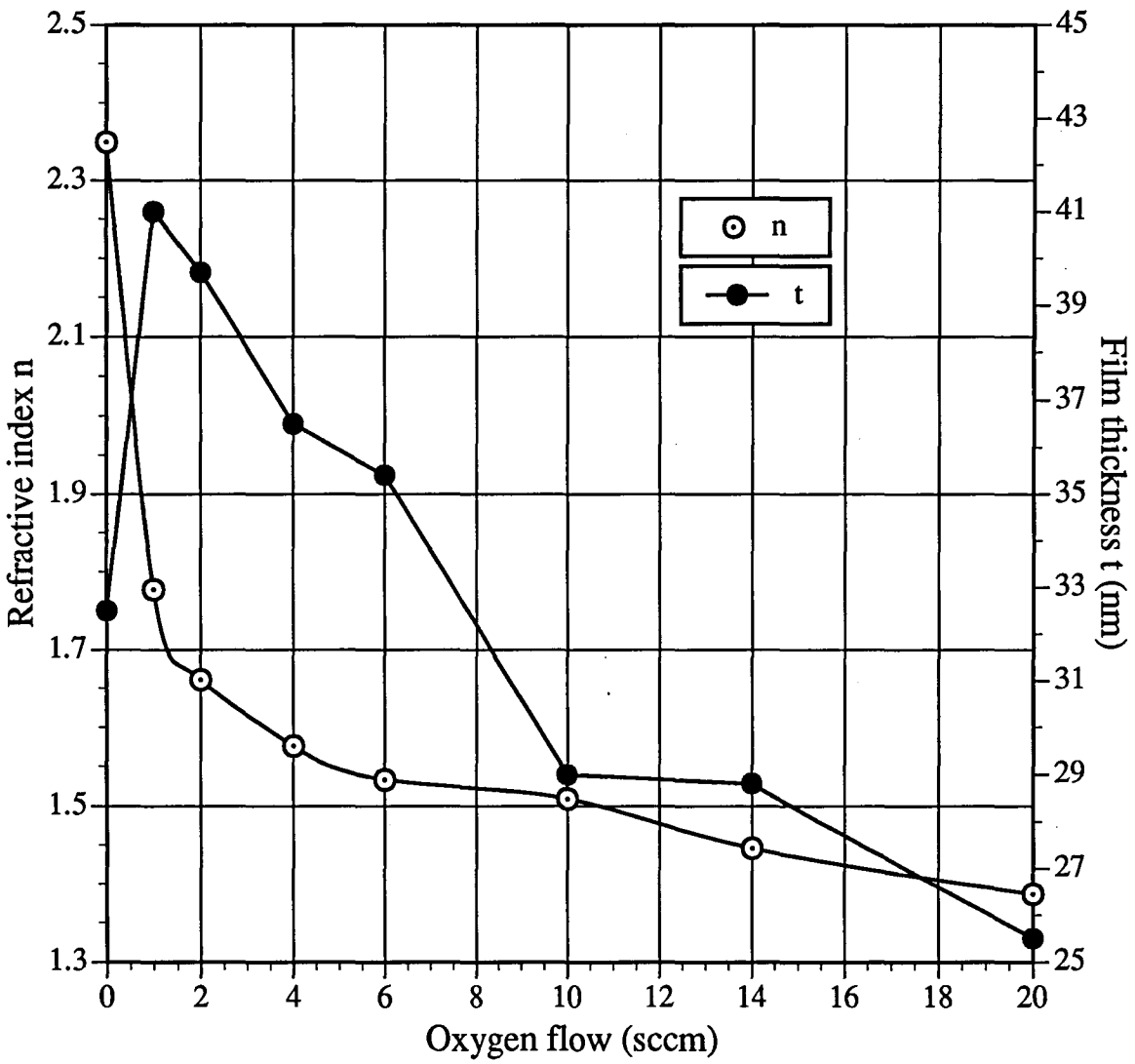

Figure 8·9
Optical transmittance of silicon oxy-nitrides using oxygen as the reactive gas and a constant nitrogen flow of 32 sccm

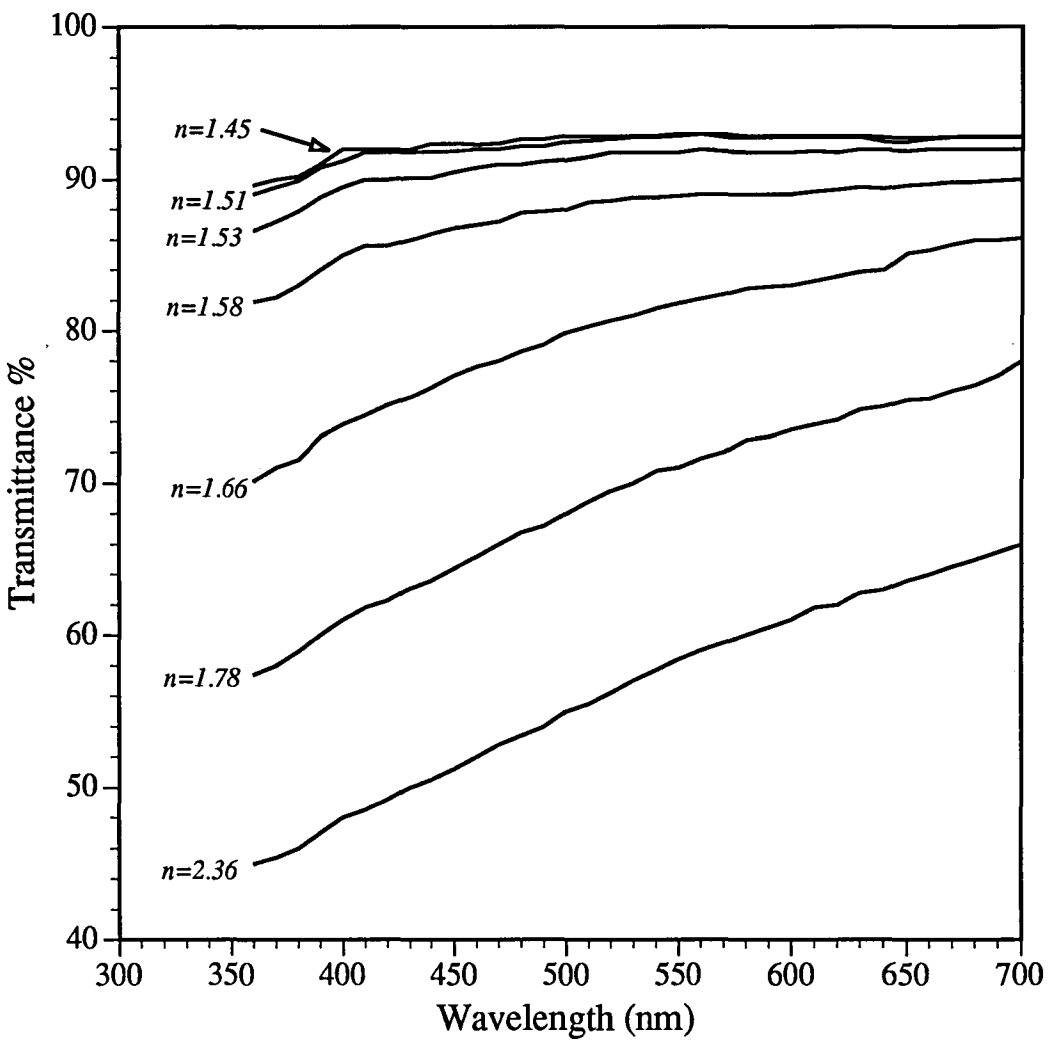

admission was adjusted for each sample so that the flow rate from the nitrogen line plus the effective nitrogen flow rate from the air line was maintained at 32 sccm as before, to give a 'base-line'. Before each increase in air flow rate the system pressure was left to stabilise, so that the water vapour in the air could be pumped away. Figure 8·10 shows the effects of oxygen flow rates between 0 and 3 sccm, corresponding to between 0% and 9.16% of nitrogen flow. Even after the adjustment of the nitrogen line flow rate to maintain the total flow, the refractive index of the sample produced at zero oxygen flow was within only 0.06 of the original silicon nitride sample produced using 32 sccm nitrogen. Silicon oxy-nitrides deposited using air as the additional reactive gas were variable from n=2.33 to n=1.60, with a greater sensitivity within that range.

8.4 Reactive gas and deposition flux calculations

Table 8.2: Reactive gas and deposition flux transport parameters

Film	$\frac{n_i}{n_m}$	ε	$\frac{n_{gp}}{n_{gpp}}$	Necessary reactive gas partial pressure (mTorr)
SiO_2	14.8	443	5×10^3	0.25
Si_3N_4	33	991	8×10^4	1.06

No data is presented for silicon oxy-nitrides in table 8.2, because their stoichiometry was not known. An interesting comparison between oxide and nitride formation is highlighted in the table from the ratio of numbers of ion to metal atoms, n_i/n_m. The nitride has more than twice the ratio of silicon dioxide, and as a result its energy per atom is correspondingly greater. The ratio of reactive gas molecules in the process to those utilised by film growth is an order of magnitude greater for nitrides than oxides, attributed to the lower reactivity of nitrogen. In addition, it is suggested that the four-fold increase in reactive gas flow needed to produce stoichiometric nitride, reflected by the higher necessary partial pressure shown in table 8.2, restricted the path to the substrate for the depositing metal atom flux, whilst the higher energy ions had a higher probability of arrival.

Figure 8·10
Refractive indices and film thicknesses of silicon oxy-nitrides as a function of effective oxygen flow, obtained using air as the reactive gas in a constant nitrogen flow of 32 sccm. Deposition for 60s at 400W.

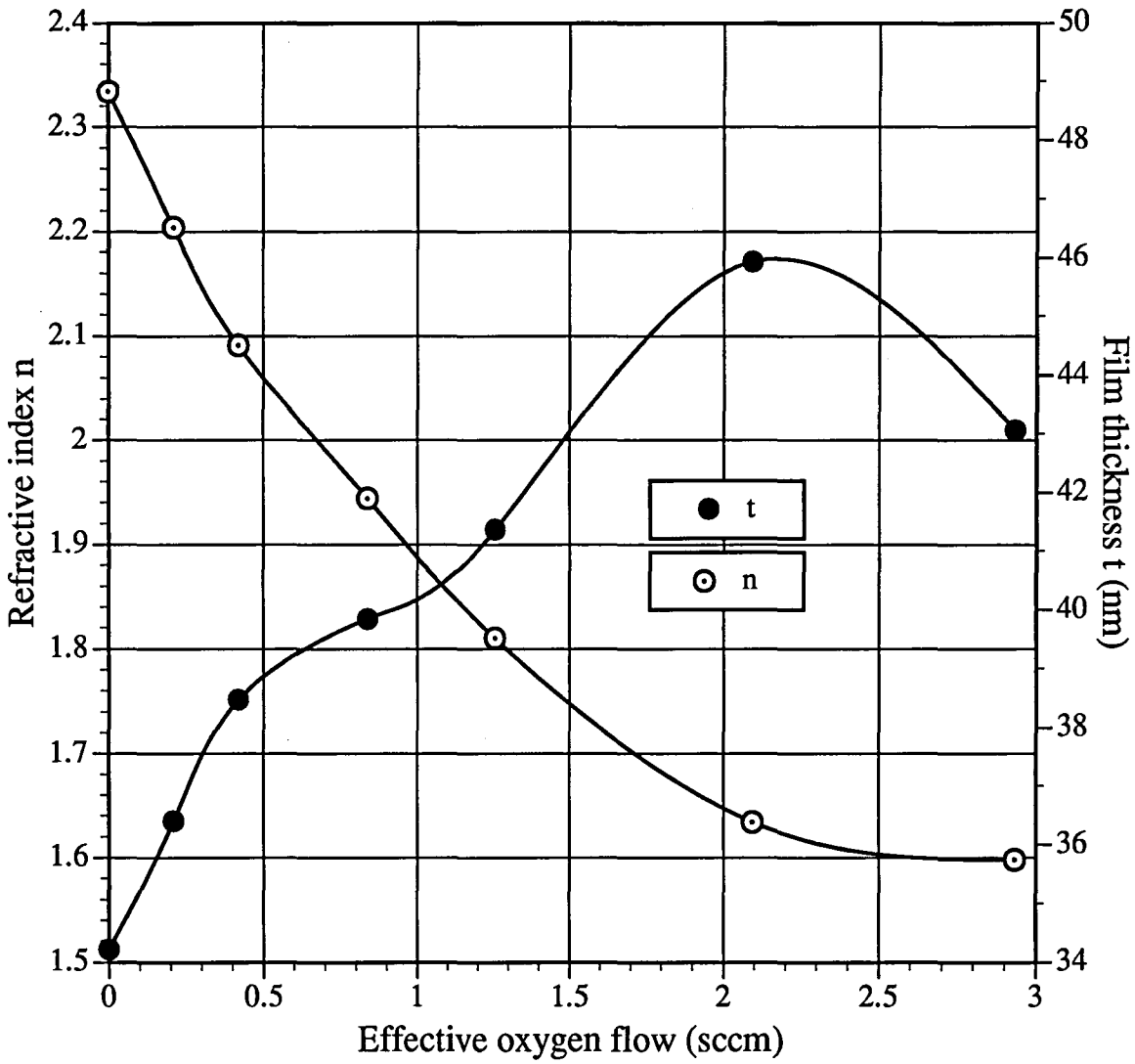

8.5 Chapter summary

1: By using the PEM control loop, refractive indices of silicon oxides, nitrides and oxy-nitrides have been tailored to one decimal place, iterating towards the desired figure.

2: Optical transmittance of silicon dioxide was over 96% across the visible, at thicknesses of 125nm.

3: Silicon monoxides and sub-stoichiometric monoxides had lower transmittances, with increasing blue absorptance with refractive index.

4: Silicon nitrides had greater absorptance than either SiO or SiO_2,

5: The careful admission of different oxygen flows in addition to the appropriate constant nitrogen flow needed for Si_3N_4 enabled silicon oxy-nitrides to be deposited.

6: By using air as an alternative reactive gas to oxygen, the sensitivity to oxygen flow was increased by a factor of five, enabling the refractive index of silicon oxy-nitrides to be controlled with even greater accuracy.

Chapter Eight References

1: S. Swann., *Vacuum*, **38**, (1988), 791-794

2: P. J. Burkhardt & L. V. Gregor, Extended Abstract, *14th Nat. Vac. Syposium.*, (1967), 31

3: T. S. Eriksson & C. G. Granqvist, *Appl. Optics*, **22(20)**, (1983), 3204-3206

4: W. Heitmann., *Appl. Optics*, **10**, (1971), 2690

5: R. C. Weast & M. J. Astle, "CRC Handbook of Chemistry and Physics", CRC Press Inc., (1982), F-172

Chapter Nine

Results and discussion - Indium-Tin-Oxide

9.0 Introduction

The aim of this section was to deposit thin films of ITO onto glass using the PEM control system. A verification of the pressure instability was to be made for the deposition system, followed by determination of the effect of substrate bias on the resistivities of the films. Once the resistivity range of room-temperature-deposited ITO had been identified, the experience gained from chapter eight with tailoring of silicon oxides was to be used to design and deposit a transparent conducting stack with reduced reflection across the visible.

9.1 Experimental particulars

There were no variations from the general experimental procedure previously discussed. PEM control was used throughout, tuned to the indium emission line at 451 nm, and reactive gas distribution was through a circular manifold 2cm in front of the target. Plate 9·1 shows the apparatus arranged for ITO deposition. The cage and substrate holder are shown, the former enclosing the magnetron to the right of

Plate 9·1
The deposition chamber - internal

Also shown are the monochromator/photomultiplier (front, right), stepper motor (front, centre), and flow meters/valves (front, left)

the system. The piezo-electric gas admission valves and flow meters are to the left of the plate, whilst the stepper motor, optical fibre (blue) and monochromator/photomultiplier are to the bottom right.

The experiment to determine the effect of substrate bias on film properties was carried out with the help of H. Barankova, of the Institute of Chemical Technology, Prague. This part of the work was undertaken in parallel in a $1m^3$ vacuum system, having a different pumping characteristic to the Edwards system previously described.

9.2 Indium line emission as a control parameter for PEM feedback control

Chapter four described in detail the reasons for, and the principles behind the PEM control system for control of the reactive sputtering process. The deposition of ITO is more demanding of process stability than most reactively sputtered compounds in that the region of stoichiometric oxides which are both optically transparent and electrically conducting is very narrow, attributed to presence of the dopant by Mukherjee[9]. In addition, the narrow process window falls directly in the pressure instability described in chapter four. The requirement of PEM is thus twofold, (i) to maintain the system within the pressure instability, and (ii) hold the process sufficiently stable for conducting, transparent ITO to be repeatably deposited over a reasonable timescale. Verification of the pressure instability was the purpose of the initial experiment of this section, and entailed increasing the oxygen flow while the process was running and observing the effect on the oxygen partial pressure. If the expected pressure instability was not in evidence, it was anticipated that the combination of system geometry and magnetron design was such that the PEM would not be necessary. Figure 9·1, however, confirms the usual non-linearity of the two parameters, and is similar in form to the results[2] shown in figure 4·6. The conclusion was that PEM would, as predicted, be necessary for any consistent ITO deposition.

A peculiar phenomenon became apparent during the controlled ITO process which was not observed with any of the other compound films produced during this work, and has not been reported in references to

Figure 9·1
Oxygen flow rate / partial pressure characteristic for ITO deposition.
Target power 600W with 3mTorr argon backfill

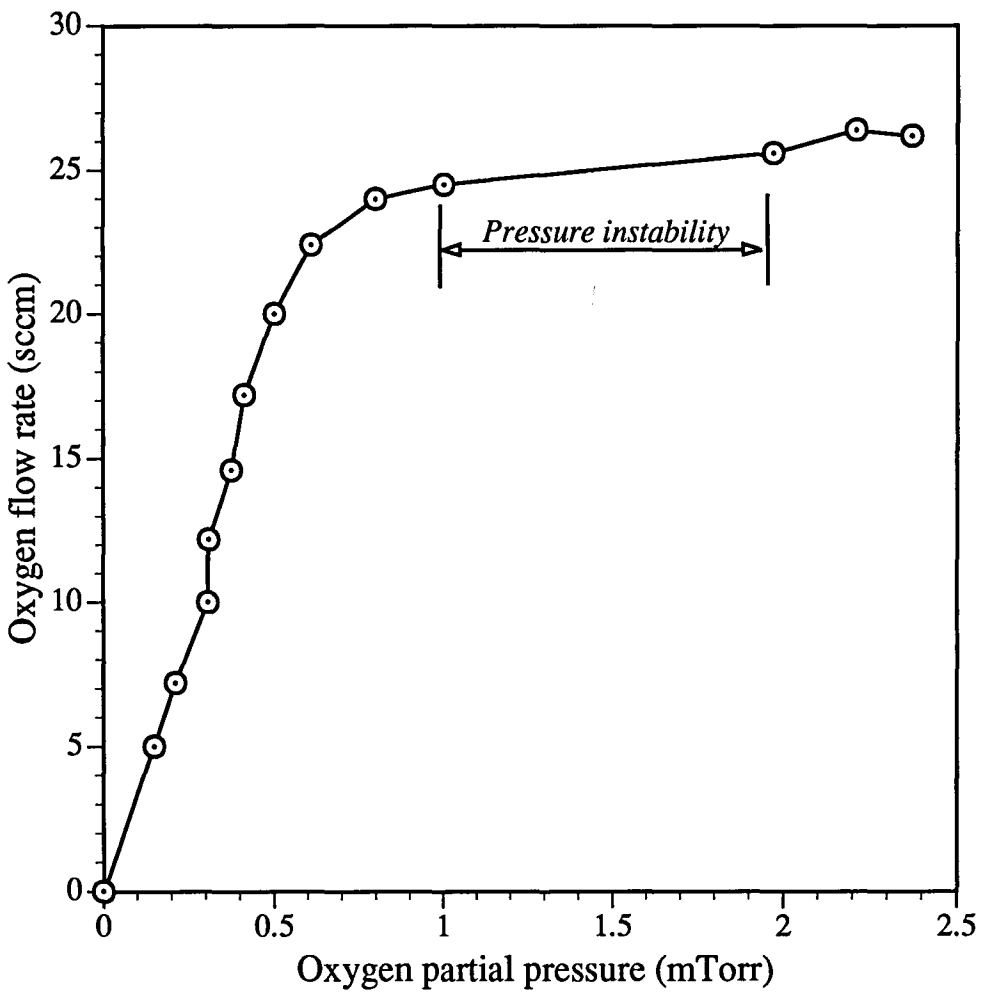

PEM or to sputtered ITO films to date. Starting from a 'clean' In:Sn metal target, the PEM set-point is reduced to admit a higher flow rate of oxygen to the process. The intensity of indium emission should, then, be inversely proportional to oxygen flow (or partial pressure) throughout the range of ITO stoichiometries. When PEM was initially used to control the ITO process, the unconventional behaviour of emission intensity shown in figure 9·2 resulted. At flow rates less than 12 sccm the intensity behaved as expected, reducing as the reactive gas flow increased, but above 12 sccm the emission actually increased with higher oxygen flows. Such a contradictory result, where the indium signal apparently *rose* with increasing target poisoning was so aberrant from the logic of PEM theory that the effect was attributed to faulty components of the control loop. No faults were found with the electronics, the optical fibre was not coated, there were no relevant overlapping emission lines near to the 451nm to which the monochromator was tuned, and replacing the target had no effect on the behaviour of the signal, so efforts were made to confirm these indications that the effect was indeed real.

Again starting from a target in metal mode, an emission intensity was obtained, and observed over a period of 45 minutes following the manual admission of a *constant* flow of oxygen through the manifold. The expected result would have been that the emission intensity would have fallen as the constant reactive gas flow, uncontrolled by PEM, fully oxidised the target so that the In flux was effectively reduced to zero. Figure 9·3, however, shows the result of the experiment, which is contrary to this conventional theory. The signal did drop initially for the first 2 minutes after oxygen admission, but increased rapidly over the next 25 minutes so that 45 minutes after admission of the reactive gas, when one would have expected the target to have poisoned, the signal had risen to three times the initial value. The decrease in cathode voltage over the same time period, also shown in the figure, indicated that the target had oxidised, at least partially, whilst the apparent relative magnitude of indium in the plasma had trebled.

This result, although interesting from the theoretical standpoint, indicated that control of the ITO process was perhaps not to be possible, so an attempt was made to iterate towards a resistance minimum using

Figure 9·2
Unorthodox behaviour of indium emission intensity under PEM control showing oxygen 'chasing' emission signal

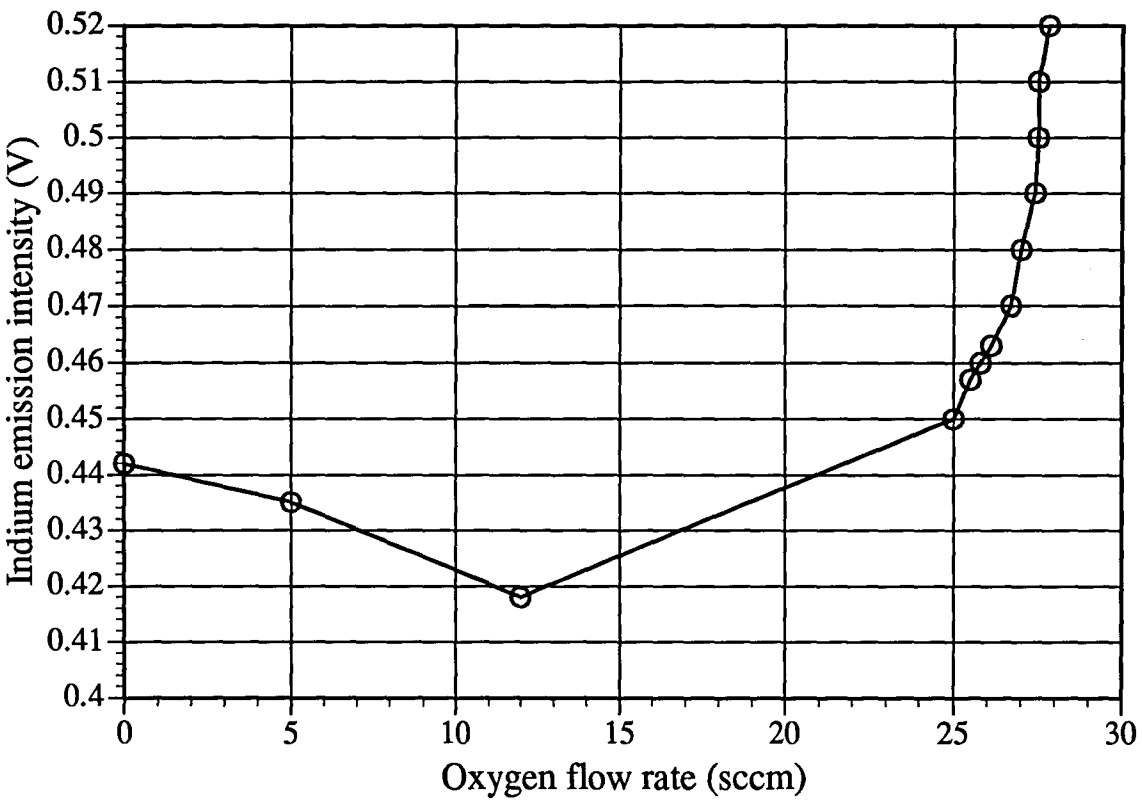

Figure 9·3
Unorthodox variation of indium emission intensity with time following the admission of a constant flow of 10 sccm oxygen

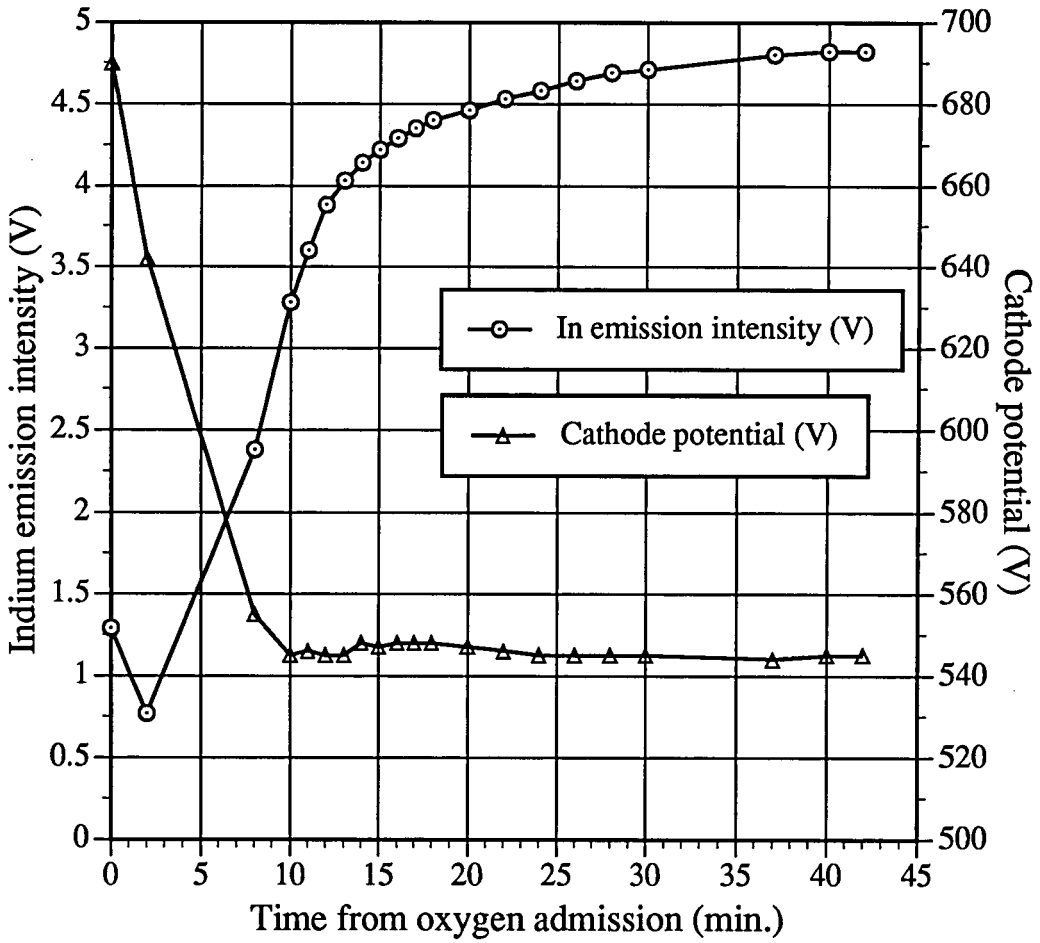

the control. The normal pattern for ITO resistance begins with metal films at low reactive gas flows, through absorbing cermets, to conducting oxides at the resistance minimum, and finally to transparent insulators. The resistance minimum R_s min will usually occur at approximately 40% of the initial indium emission intensity. Figure 9·4 shows the first attempt to locate R_s min by using PEM to control the oxygen admittance, and it was immediately obvious during the experiment that the process was uncontrollable, with the sheet resistance increasing as shown, and no conducting oxides being produced. It was realised that the increase in indium signal with oxygen admission was causing the PEM control feedback loop to admit more oxygen in order to decrease the signal to the set-point. Hence, the phenomenon of increasing indium signal resulted in positive feedback in the PEM loop.

From the earlier results of figure 9·3, it was seen that the process approaches a steady state 45 minutes following the admission of a constant oxygen flow, so a final attempt was made to achieve the expected sheet resistance curve. Rather than try to control the process from a metal target, 10 sccm of oxygen was admitted to the process and when the indium signal intensity had stabilised at the higher level, PEM was switched on with the set-point at that level. This technique enabled stable process control, and although the iteration did not begin from metal films, it was possible to find R_s min and use PEM to hold the system at that point. Figure 9·5 shows the familiar variation of sheet resistance with oxygen flow rate for ITO films produced at a power of 600W. The resistance minimum was particularly sharp, located between 23 and 25 sccm of oxygen, and the inset shows that the process needs to be held stable to within 0.2 sccm to enable the deposition of the films with lowest resistance. The resistance minimum for this figure was 37Ω/□, giving a deposition rate of 2.4nms^{-1} and film resistivity of 3 x10^{-6} Ωm.

Having now successfully adapted to the problem of increasing indium emission with oxygen flow, some thought was applied to a possible explanation. It is possible that the conducting coatings on the substrates were causing changes in plasma density, and hence changes in the region of plasma which the optical fibre was viewing. This suggestion would only apply in the region of figure 9·5 where conducting films occurred, and it has been shown that the phenomenon was in evidence across the

Figure 9·4
Variation of ITO sheet resistance with oxygen flow for an increasing indium emission intensity with flow. Films produced at 1kW, 60s.

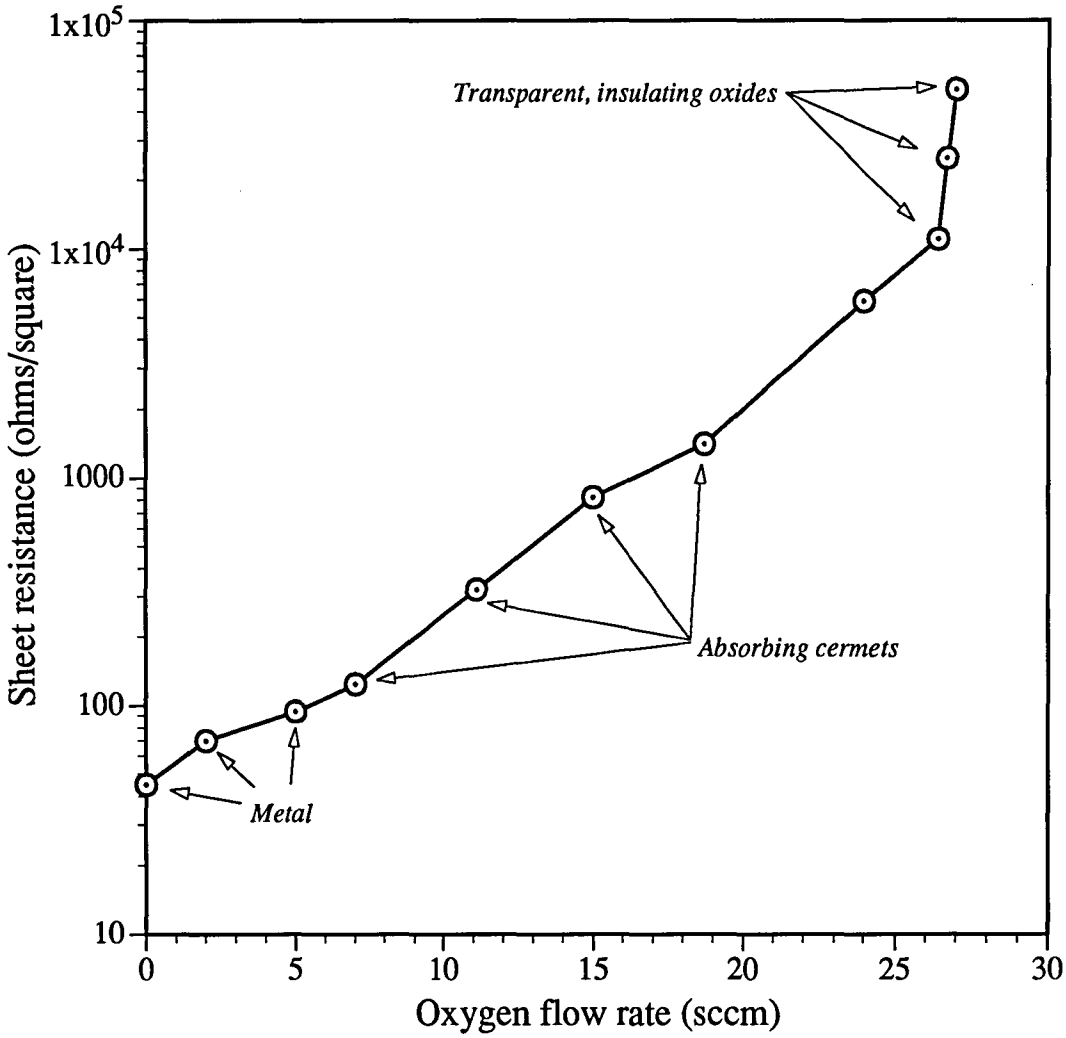

Figure 9·5
Sheet resistance of controlled ITO films as a function of oxygen flow, with inset showing narrow region in which R_s min is found.

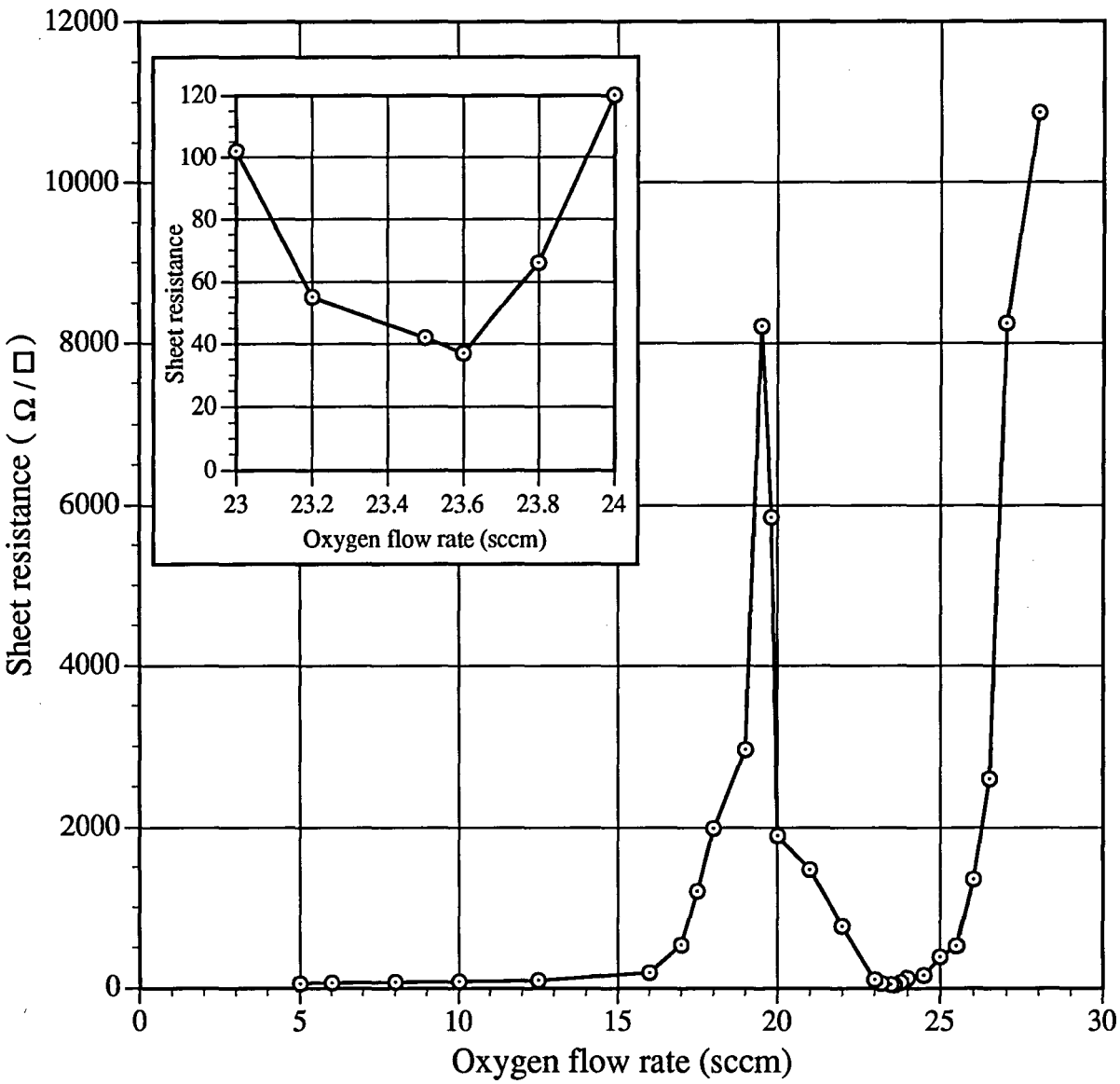

range of oxygen flows used. Another suggestion is that In-O_2 species present in the plasma may have emission lines close to the 451nm indium line, and were picked up by the monochromator as the indium signal was quenched by the oxygen, although no data has yet been found to support this theory. The most plausible theory to date is that the addition of reactive gas, in this system geometry, with the newly designed unbalanced magnetron, creates micro-pressure instabilities in the region where the end of the optical fibre is located. This theory is in line with that described in section 3.7.6, where Hoffman[3] and Rossnagel[4] reported local gas density perturbations in the cathode region and plasma density changes, respectively.

9.3 Resistivity variation with substrate bias

Successful PEM control having now been established, work could progress into decreasing electrical resistivity and increasing optical transparency, two areas of paramount importance in the industrial uses of ITO. The first experiment, undertaken with the assistance of H. Barankova, aimed to improve on the room temperature deposited resistivity of 3 x10^{-6} Ωm obtained above.

Previous work in the same vacuum system[5] with rf biases applied to the substrate had not shown any improvement in film resistivity, but it was thought, however, that an increase in deposition rate might be obtained by increasing oxygen reactivity created in the plasma. The benefits of a lower oxygen partial pressure, and of operating the cathode in a more metal state resulted in a higher sputtering rate. Controlled deposition of optimum conducting films was made at two different dc substrate biases of -5.73V and -30.4V. The preparation of optimum conducting films at lower partial pressures of oxygen was observed and the properties obtained, together with the rates of reactive gas flow, are shown in figures 9·6(a) and (b). It is seen from figure 9·6(a) that higher substrate bias enabled the resistivity minimum to be achieved at lower oxygen partial pressure, but despite this, and the greater oxygen activation, the deposition rate remained about the same. As a result, the dc bias gave the same result of the previous work with rf bias; no reduction in film resistivity from that obtained by using an isolated substrate. It was concluded that the higher surface bombardment provided by the

Figure 9·6

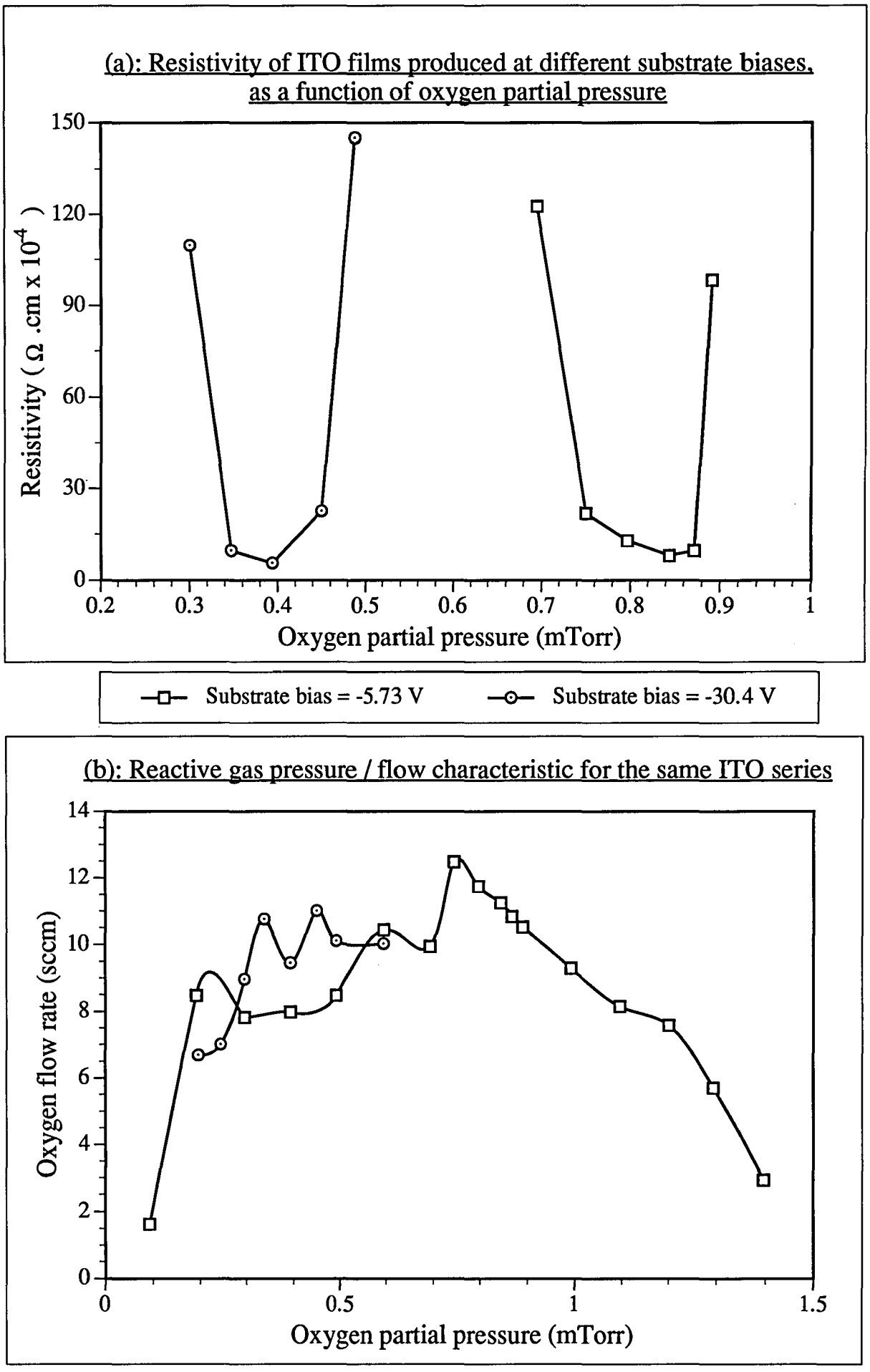
(a): Resistivity of ITO films produced at different substrate biases, as a function of oxygen partial pressure
Resistivity (Ω .cm x 10⁻⁴)
150
120
90
60
30
0
0.2
0.3
0.4
0.5
0.6
0.7
0.8
0.9
1
Oxygen partial pressure (mTorr)
Substrate bias = -5.73 V
Substrate bias = -30.4 V
(b): Reactive gas pressure / flow characteristic for the same ITO series
Oxygen flow rate (sccm)
14
12
10
8
6
4
2
0
0
0.5
1
1.5
Oxygen partial pressure (mTorr)

negative substrate bias and unbalanced magnetron reduced the sticking coefficient, or that the energy of the impinging plasma flux was sufficient to induce re-sputtering. Results also showed that the partial pressure of oxygen at which optimum ITO films are made in figure 9·6(a) correspond with the peaks in the flow versus pressure characteristic of figure 9·6(b), for both substrate biases. This showed that the optimum films were obtained under conditions where the gas flow consumed by the growing film was a maximum, corresponding with the same observation by work in the preparation of conducting tin oxide films[6].

Having observed the effects of substrate bias on electrical resistivity and reactive gas consumption by the ITO film, the next aim was to improve both electrical and optical properties using an exercise which would combine the experience gained with tailored silicon oxides with fine PEM control of ITO to produce a coating with technological application.

9.4 Improving the optical properties of ITO

The medical, aerospace, automotive, defence and other industries have requirements for highly transparent, conducting coatings onto glass, acrylic and polymer substrate materials. It was decided to prepare ITO with the controlled technique, and then improve its visible transparency by overcoating with a silicon oxide layer.

The standard technique of designing antireflection (AR) coatings in the ophthalmic and glass coating industries is to optically match successive film layers so that their optical thicknesses are such that the beams reflected from the upper and lower surfaces differ in phase by π. For a single layer antireflecting at wavelength λ, this optical thickness is $\lambda/4$, and it can be shown[7] that the required refractive index n_f of a film coating glass with refractive index n_s is given by:

$$n_f = (n_0.n_s)^{0.5} \qquad [9\cdot1]$$

where n_0 is the refractive index of the surrounding medium, usually air. For n_s=1.50 the required n_f is 1.22, and no known optical materials are available with such a refractive index. The single layer coating, then, cannot achieve zero reflectance even at the minimum because of the absence of suitable low-index materials. One method used is to deposit the first layer with known refractive index at a quarter wave thickness, so that the wavelengths at which it will cause reflectance minima can be estimated. Successive layers are then optically matched to this film so that their reflectance minima coincide with the reflectance maxima of the underlying film combination. Another technique makes use of the broadening effect of a $\lambda/2$ layer to give an improvement over single layer performance. A $\lambda/2$ layer of higher index than the substrate (such as ITO) is inserted between the substrate and a $\lambda/4$ layer of low index (such as SiO).

The theory behind AR coatings is considerably more complex than alluded to above, and the field of antireflection coatings would comprise a comprehensive study alone. It was not the purpose of this work to design and deposit an AR coat, rather to show a positive improvement in the transparency of ITO films, using as-deposited resistivity and refractive index as fixed parameters determining the first layer thickness.

The intention was to make two sets of films, glass/ITO and glass/ITO/SiO_2, with the aim of reducing the reflectance peaks (hence increasing the transmittance) present in the glass/ITO combination. Another set of films were also to be made, with a glass/SiO_2/ITO/SiO_2 structure, in order to see the effect of using SiO_2 as a matching layer into the glass substrate. No improvement in optical transparency was to be expected with the latter design, as the refractive indices of glass and SiO_2 were nominally equal.

The previous experiments had established that optimum ITO film resistivity of 3.6-3.8 x 10^{-6} Ωm was achievable with a refractive index of around 2, and that the use of PEM enabled reliable, repeatable operation of the system to give a stable resistance minimum of 30Ω/□. The thickness of ITO required for these parameters was ~125nm, so this established the starting point; 125nm of ITO would be deposited onto 'KG3' glass, which gives a reflectance minimum at a wavelength of

500nm, close to the centre of the visible. The SiO_2 layer of a half wave optical thickness, and lower index than the ITO, should then cause reflected beams to differ successively in phase by π, reducing the reflectance maxima created by the ITO alone. It was expected that it would be necessary to vary the SiO_2 thickness from the theoretical $\lambda/2$, to shift the position of the reflectance minima in relation to the maxima shown by the ITO.

Figure 9·7 shows the spectrophotometer output for the quarter wave layer of ITO. The KG3 glass shows a higher reflectance than standard crown glass; approximately 6% per side compared with the usual 4%. Reflectance minima from a single layer coating of higher refractive index than the substrate will only reach the reflectance of uncoated substrate, as shown in the figure. The predicted reflectance minimum at ~500nm is also seen, along with periodic minima either side of λ. The coatings showed a pronounced blue reflectance at low incidence, attributed to the 37% reflectance peak at 450nm, and shown in plate 9·2. It is interesting to observe that the peak transmittance of 82% corresponds with the reflectance minimum at 500nm, and those transmittance peaks of 66% and 72% correspond with reflectance minima at 460nm and 640nm respectively. This single ITO coating would not be useful in a practical situation because of its low, single peaked transmittance and periodic reflectance minima. It was hoped that the SiO_2 overlayer design would raise and flatten the transmittance, at the same time reducing the reflectance below that of the uncoated substrate.

Figure 9·8 shows the spectra for the glass/ITO/SiO_2, comprising 125nm of ITO and 85nm of SiO_2, the latter having a refractive index of 1.50. The additional layer on top of the ITO, once optimised for thickness, reduced the reflectance maxima shown in figure 9·7 so that the combined reflectance of the layers gives a reflectance less than the uncoated substrate over a large proportion of the visible. Reflectance peaks at 540nm and 700nm gave the films a yellow/orange appearance. Although peak transmittance showed no improvement over the single layer design, the 'smoothing' and reduction of the reflectance similarly smoothed the transmittance output, so that it exceeded 80% for over half of the visible wavelengths, compared with only 6% of the same spectral region coverage for the single layer. The design aimed to use

Figure 9·7
Optical reflectance and transmittance of 125nm ITO on KG3, compared with the uncoated substrate.

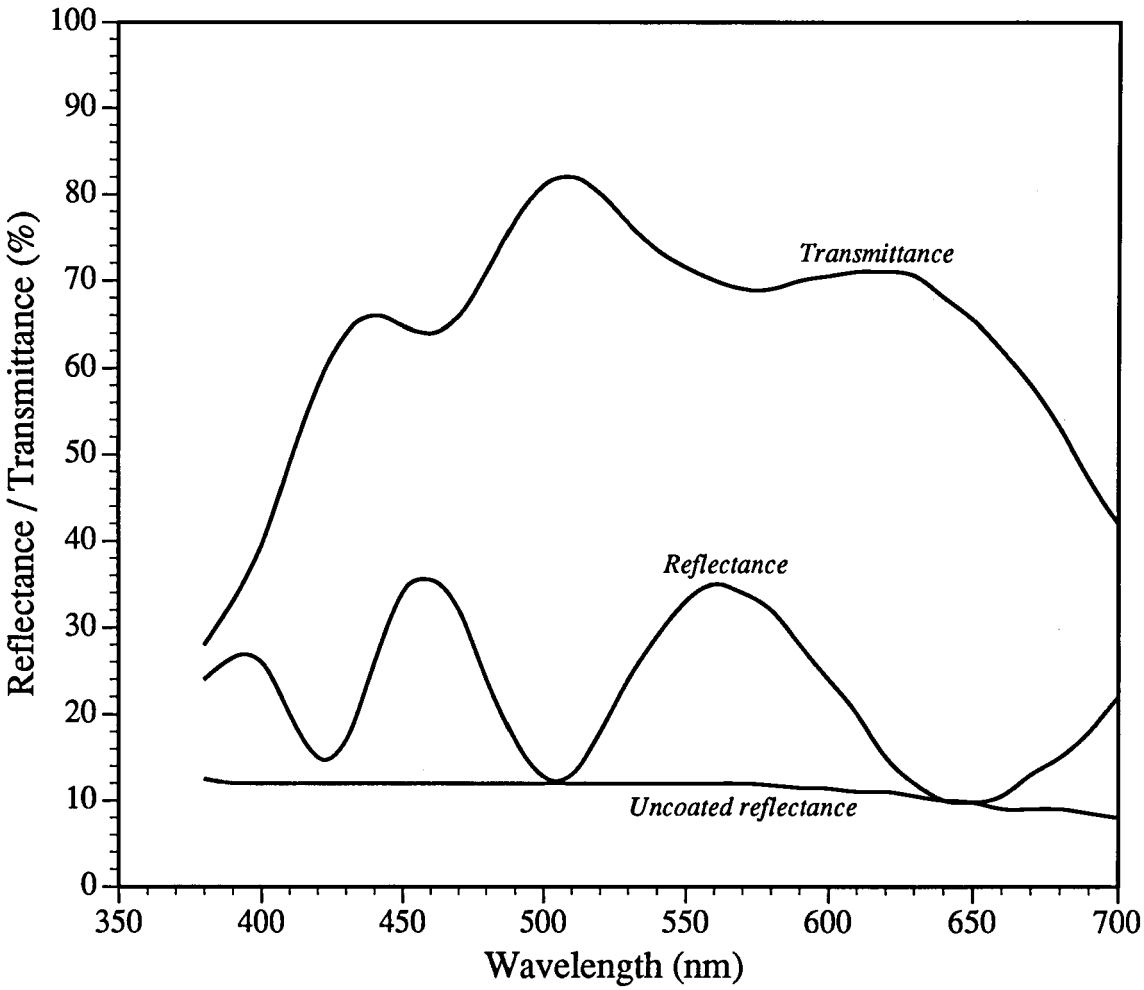

Plate 9·2
ITO film of figure 9·7 seen in reflectance

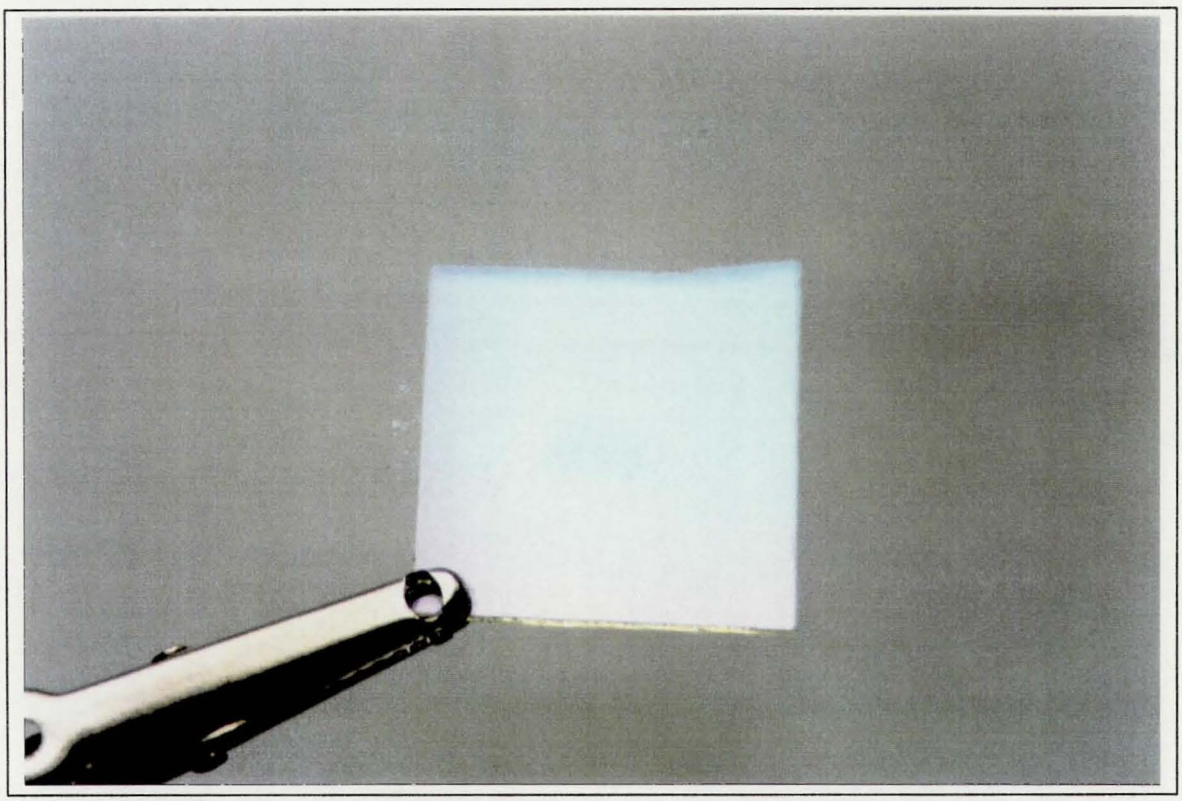

the overlayer to create reflectance minima in the centre of the visible, and the effect is clearly seen from the figure, where the minima at 480nm and 610nm correspond well with the maxima in transmittance at the same wavelengths.

The final design was glass/SiO_2/ITO/SiO_2, with the thicknesses for the two film materials maintained at those values giving the improvements in the previous design. There should have been no optical advantage gained with this design over the glass/ITO/SiO_2 structure, because the SiO_2 in contact with the substrate was an optical match with a refractive index of 1.45-1.50. The initial purpose of this three layer design was to examine the effect of 'keying' the substrate surface with an optically matched material, to promote adhesion of the ITO, but as seen from the spectra in figure 9·9 an unexpected benefit was gained. Reflectance remained lower than the uncoated substrate up to 610nm, with the greatest reduction between 530 and 560nm, where the uncoated reflectance was reduced by a third. Peak transmittance was higher than either of the previous two designs, 93% at 550nm, and the transmittance exceeds 80% over 60% of the visible wavelengths. In addition, the transmittance peaks evident in figures 9·8 and 9·7 were removed. Conventional thin film optics predicted no improvement with this three-layer design over the two-layer, so it is suggested here that the SiO_2 layer did act as a 'key' or 'seed' layer for the ITO. More importantly, it sealed the ITO on both sides, from leached sodium and other elements from the underlying KG3, and from atmospheric oxygen and contaminents from above. This prevented ingress of elements which could alter the ITO thickness and refractive index, and maintained the performance of the design at a level not possible with the two-layer system which was unprotected on the glass side.

9.5 Improving the electrical properties of ITO

Completion of the exercise into improvement of the transparency of the ITO on glass does not fulfil the requirement of a conducting, transparent coating. A coating with transmittance greater than 80% over 60% of the visible wavelengths is of little use in an aircraft canopy if the electrical conductivity is poor. Other workers in the ITO field have reported using hot substrates[8] or post-deposition annealing[9-11] as

Figure 9·8
Optical reflectance and transmittance of ITO/SiO_2 (125nm/85nm) stacks on KG3, compared with the uncoated substrate

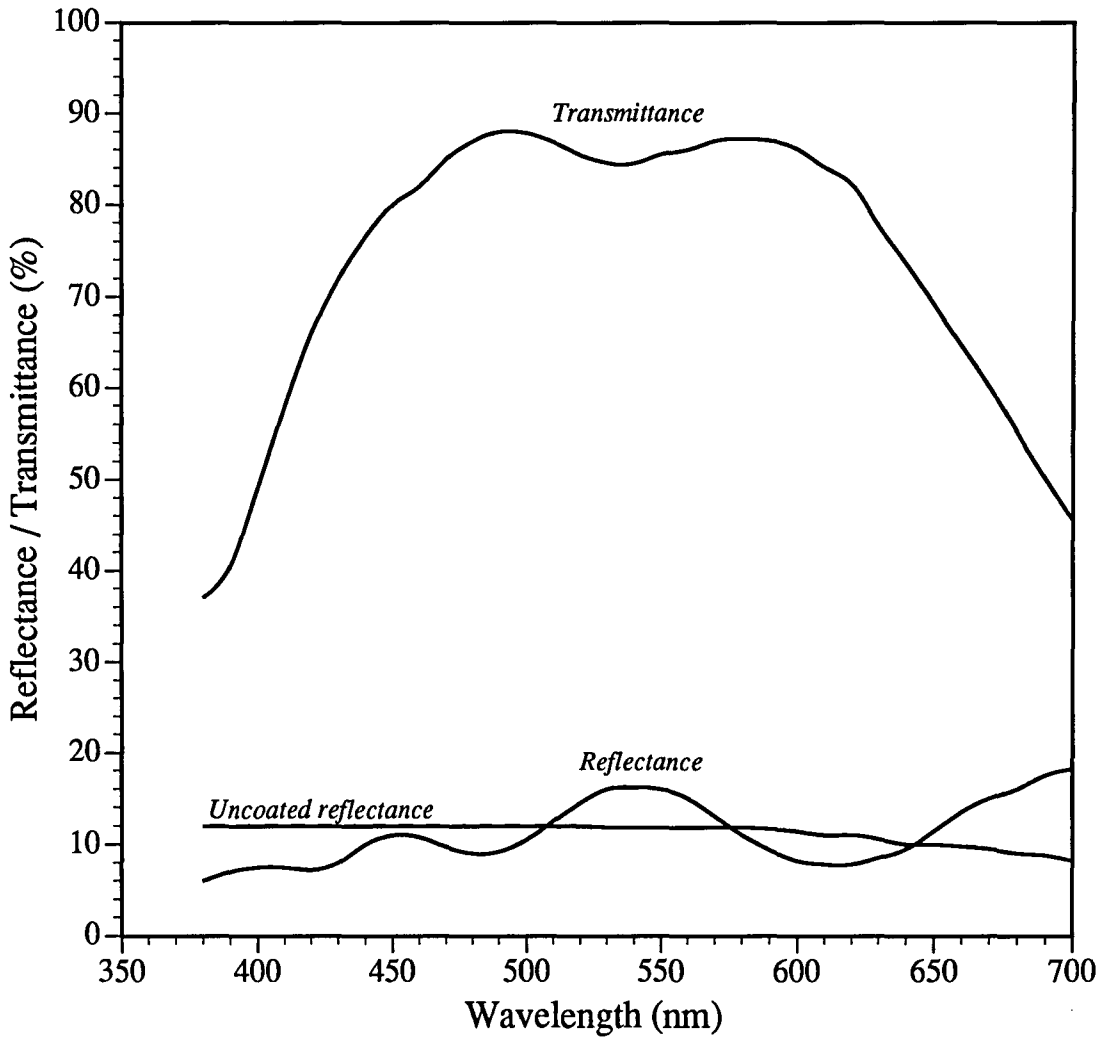

Figure 9·9
Optical reflectance and transmittance of SiO_2 /ITO/ SiO_2 (85nm/125nm/85nm) stacks on KG3, compared with the uncoated substrate.

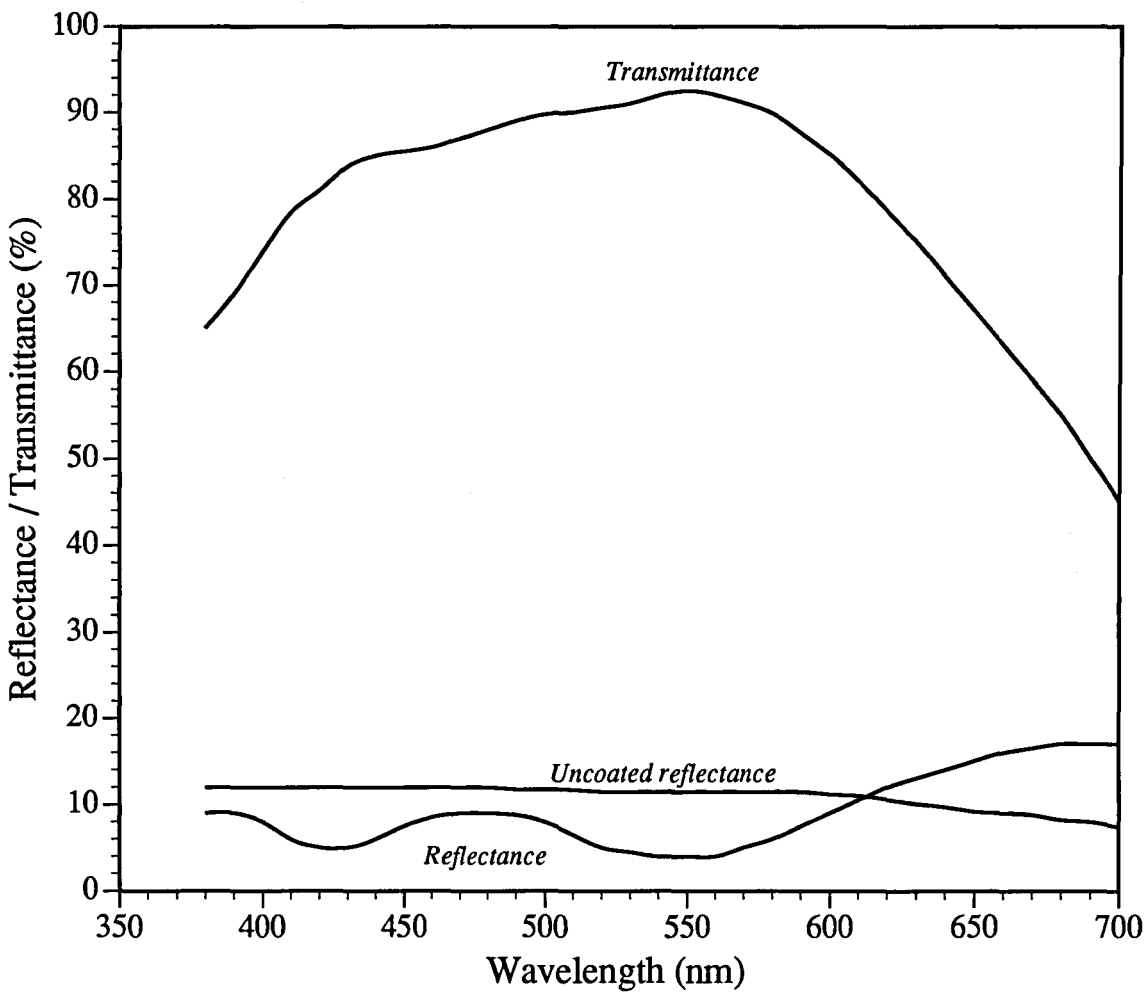

methods of improving electrical conductivity of the films. It has also been reported[12] that post-deposition annealing above 300°C in oxygen for oxygen deficient films, and in inert gas for oxygen rich films, reduces film resistivity. It was decided to determine the effect of post deposition annealing on film resistivity, and observe any concurrent effect on the optical transparency.

The effect of post-deposition annealing on the electrical and optical properties of both the ITO and SiO_2/ITO/SiO_2 highest transparency films was studied. No particular effort was made to produce samples with sheet resistances lower than 100 Ω/□ for these tests, so that any decrease in sheet resistance would be more readily apparent, but their thicknesses were comparable with the designs of the optical transmittance improvement experiments.

Both coating designs suffered increases in their sheet resistances following annealing in air at 200°C for two hours. Single layer ITO films more than doubled in sheet resistance from 74 Ω/□ to 165 Ω/□. Similarly the sheet resistances of SiO_2/ITO/SiO_2 films increased by a factor of 2.75 from 330 Ω/□ to 910 Ω/□. It was thought that the atmosphere within the oven was causing oxide ingression from either the surrounding air, or by depletion of the SiO_2. It is interesting that such observations were also made by Campet *et al*[13], who claimed the resistivity increase in air to be evidence that efficient n-type doping needs oxygen vacancies.

To determine the effect of air on the annealing process the next experiment involved the elimination of air from the samples during heating. An 'Ether Transitrol' type 990/13 furnace was acquired with a 40mm diameter bore through its centre. This permitted a glass tube to be passed through, into which the samples could be placed. Provision was made for a variable flow rate of argon through the tube; the gas entering through a pipe at one end, passing over the samples and then out at the far end. Argon exiting the tube was bubbled through liquid paraffin to prevent back-leaching of air or water vapour.The temperature was maintained by proportional control to a tolerance of 5°C. Two new samples were selected; single layer ITO with a sheet resistance of 2.6 kΩ/□ and SiO_2/ITO/SiO_2 with 33 Ω/□. They were annealed at 200°C for two hours in the furnace apparatus. Following the

heating, the ITO showed a significant reduction in sheet resistance to 333 Ω/□, but the SiO_2/ITO/SiO_2 sample showed no change. These resistances remained at these levels for a period of at least three months. The conclusion was that sheet resistance of ITO on KG3 with no protection can be significantly reduced towards the value achieved with deposition control in a protected film.

The same samples were used in the next experiment to determine if an increased temperature of 300°C for a duration of two hours (i) caused further decrease in the sheet resistance of ITO and (ii) initiated a decrease in that of SiO_2/ITO/SiO_2, which had been unaffected by lower temperatures. The ITO sample showed further reduction to 94 Ω/□ and SiO_2/ITO/SiO_2 also reduced to 46 Ω/□. The conclusion was now drawn that ITO continues to reduce in resistance at 300°C and SiO_2/ITO/SiO_2 begins to show reduced sheet resistance.

The experiment was repeated once more at 400°C for two hours with the same samples. A rise in sheet resistance was predicted due to leaching of sodium from the substrates, but both types of coating again showed a decrease; the ITO from 94 to 55 Ω/□, and the SiO_2/ITO/SiO_2 from 46 to 29 Ω/□. Having now concluded that successive annealing at 200°C, 300°C and 400°C for two hours each reduces the sheet resistance of ITO, and annealing at 300°C followed by 400°C reduces that of SiO_2/ITO/SiO_2 films, a final experiment was devised to to determine the time necessary for the effect to occur at a constant temperature of 400°C for the three-layer coating.

A temperature of 400°C was chosen because reductions in sheet resistance were shown to continue up to this level, but higher temperatures were considered likely to result in the opposite effect due to leaching of sodium. Three new SiO_2/ITO/SiO_2 samples, each of 165 Ω/□, were annealed at 400°C for two, four and six hours respectively to find the time beyond which no further sheet resistance reduction was observed. Examination of the samples following their individual annealing times showed their sheet resistances to be equal at 34 Ω/□, a reduction of 80% of the as-deposited values. This shows that at a constant annealing temperature of 400°C an annealing time of two hours is sufficient. Longer times yield no further decrease as the film properties are then approaching those of the bulk.

Assuming the ITO film thickness did not change during annealing, the change in resistivity resulting from the 'optimum' annealing conditions for both the single-layer and three-layer coatings are summarised in table 9.1 below:

Table 9.1: Effects of annealing at 400°C in argon for two hours on ITO resistivity, ρ

Coating	ρ, as-deposited (μΩ.m)	ρ, annealed (μΩ.m)	% ρ reduction
ITO	325	7	98
SiO_2/ITO/SiO_2	21	4	81

The optical effects of annealing were determined in parallel with the previous test. Each of the SiO_2/ITO/SiO_2 samples were analysed on the spectrophotometer before and after annealing. The results are shown in figure 9·10, and demonstrate that annealed films have a higher transmittance than as-deposited films, with an increase of 10% to 90% at 500nm. The mean transmittance across the visible following annealing had risen from 77% to 90%.

9.6 Reactive gas and deposition flux calculations

Table 9.2: Reactive gas and deposition flux transport parameters

Film	$\frac{n_i}{n_m}$	ε	$\frac{n_{gp}}{n_{gpp}}$	Necessary reactive gas partial pressure (mTorr)
In_2O_3	10.9	325	8×10^3	0.79

The energy per atom shown in the table is in excess of that necessary for bond formation, because of the order of magnitude difference between ion and metal atom numbers. As with the silicon oxides there are a factor of 10^3 more free oxygen molecules entering the system than are utilised by the film. The efficiency of oxygen utilisation could be increased by increasing the deposition rate or baffling the pumps.

Figure 9·10
Optical transmittance of SiO_2/ITO/SiO_2 layers
before and after annealing in argon at 400° C for two hours

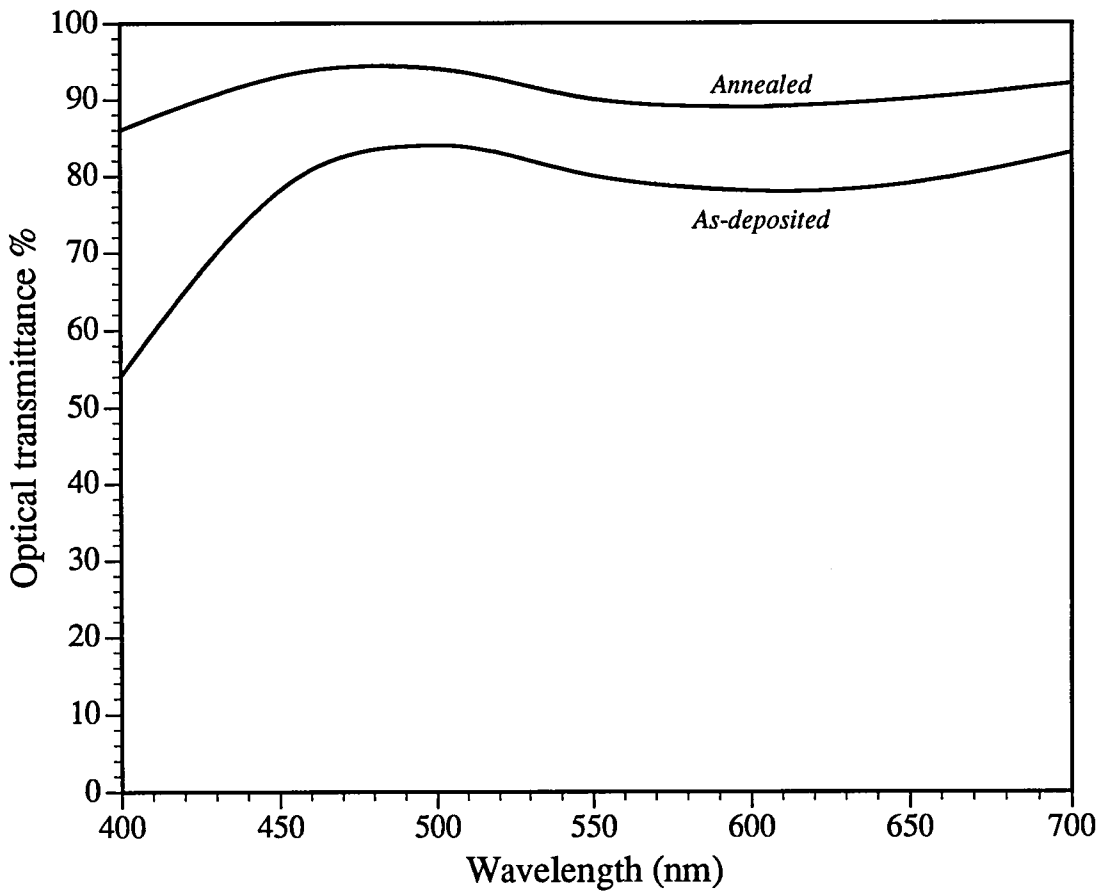

Finally, the predicted reactive gas partial pressure for stoichiometry of less than 1 mTorr is lower than that observed experimentally by a factor of ~2.5, allowing for the different sensitivity of the Pirani gauge to oxygen. It is suggested that this discrepancy is due to the assumptions made in the calculation. These did not take account of the effects of target poisoning, particularly with high reactive gas flow, and assumed that pumping speed was due to the vacuum pumps alone. It is also perhaps inaccurate to assume that the pumping speed of argon is equal to that of oxygen.

9.7 Chapter Summary

1: The previously unreported phenomenon of *increasing* indium emission signal with increasing oxygen flow rate during ITO film deposition was observed. This was attributed to changes in plasma density near the cathode.

2: Higher substrate bias enabled the resistivity minimum of ~3.6-3.8 μΩ.m to be achieved at a lower oxygen partial pressure, but the ITO deposition rate failed to show the expected associated increase.

3: Multilayers of ITO and SiO_2 of controlled optical thickness have been used to progressively improve and flatten the transmittance spectrum for such conducting film combinations.

4: An 85 nm thick 'seed' layer of SiO_2 improved the transmittance such that its peak was 93% at 550nm, and exceeded 80% over 60% of the visible wavelengths.

5: Optimum post-deposition annealing conditions of 400°C in argon for two hours, were established. These improved optical transmittance and increased film resistivity for both single-layer ITO and three-layer structures. Annealing in air results in increased resistivities.

6: The results of the post-deposition annealing work suggest that by using the technique on ITO coatings where substrates are sufficiently thermally insensitive reduces the need for such stringent process control in locating optimum films.

Chapter Nine References

1: A. Mukherjee., *Vacuum*, **39(6)**, (1989), 537-540

2: A. G. Spencer.,"High rate reactive magnetron sputtering", PhD Thesis, Loughborough University of Technology, U.K., (1988)

3: D. W. Hoffman., *J. Vac. Sci. Technol. A*, **3**, (1985), 561

4: S. M. Rossnagel.,*J. Vac. Sci. Technol. A*, **6**, (1988), 19

5: R. Lewin, R. P. Howson, C. A. Bishop & M. Ridge, *Vacuum*, **36**, (1986), 95

6: R. P. Howson, H. Barankova & A. G. Spencer, *Thin Solid Films*, **196**, (1991), 315-321

7: H. A. McLeod, "Thin film optical filters", (1986), Adam Hilger Ltd.

8: M. Mzuhashi., *Thin Solid Films*, **70**, (1980), 91

9: C. A. Bishop, R. P. Howson, J. Morris & M. I. Ridge, *J. Appl. Phys.*, **76**, (1980), 1860

10: S. Schiller, U. Heisig, Chr. Korndörfer, G. Beister, J. Reschke, K. Steinfelder & J. Strümpfel., Invited paper presented at Int. Conf. on Met. Coatings, San Diego, March 23-27 1987.

11: R. Tueta & M. Braguier, *Thin Solid Films*, **80**, (1981), 143

12: J. A. Thornton & V. L. Hedgecoth, *J. Vac. Sci. Technol.*, **13**, (1976), 117

13: G. Campet, C. Geoffroy, S. J. Wen, J. Portier, P. Keou, J. Salardenne & Z. W. Sun, *Active & Passive Elec. Comp.*, **14**, (1991), 151-161

Chapter Ten

Results and discussion - Doped Zinc Oxide

10.0 Experimental Particulars

There are two popular techniques used to introduce small concentrations of a dopant into depositing films. The first is to simultaneously sputter two magnetron cathodes[1], with one cathode operated at very low power compared with the host material, to provide the dopant. The alternative capitalises on the well documented property[2-5] of magnetron sputtering, that where a target is an alloy or composite of several materials, the film composition reflects that of the target, unlike thermal evaporation where the film composition varies throughout its thickness due to the different melting points of the evaporants.

Previous authors[6] have deposited ZnO:Ga and so the original intention was to reactively sputter ZnO:Ga and compare the electrical and optical properties with previous results. A Zn:Ga target was prepared by heating the gallium to 80°C on the zinc surface, ensuring that it was well 'wetted'. Different areas of the Zn surface could then be covered to achieve variable dopant concentrations. On inspection of the target following the addition of Ga, the latter had spread across inter-grain boundaries such that its original coverage of 5% area had increased to at

least 50% target coverage. Following a test sputtering of the target, the Ga diffusion was observed to have reached the rear surface of the target. It was obvious at this point that because it spread through the total zinc volume, not just on the surface where it was required, Ga was not a commercially viable dopant for ZnO.

The technique described above for applying the dopant material to the front surface of the zinc target was retained, but alternatives to Ga were now sought.

10.1 ZnO:Sn films

Strips of tin were cut to widths in increasing units of 5mm, and fixed across the horizontal diameter of the zinc target surface using an In:Sn alloy 'glue', melting at 114°C. A computer calculation gave the Sn target coverage as a percentage of the active Zn target area, allowing for centre pole masking and target utilisation, so a 10mm wide strip corresponded to a nominal area doping of ZnO:12%Sn, a 25 mm wide strip to ZnO:33%Sn and so on.

The Zn spectral emission line at 436nm was used as the input to the PEM loop, so that stable operation of the system was maintained as different oxygen flows were selected. The following discussion of electrical results refers to figure 10·1, which shows as-deposited sheet resistance as a function of oxygen flow rate for ZnO:Sn films deposited at 400W for 1 minute. Tin content is shown as a percentage area coverage of the Zn cathode, and the ordinate is plotted using a logarithmic scale because of the wide range in order of magnitude. The 12% coverage samples showed no resistance minimum as oxygen flow was increased, with the progression being made from opaque metal films up to 1 kΩ/□, through brown semi-transparent films to 7 kΩ/□, to transparent non-conducting oxides above 32 kΩ/□. When the dopant level was increased to 19% coverage, there is still no pronounced resistance minimum at any point, although there is a slight fall in the sheet resistance of the transparent oxides formed between 21 and 22 sccm oxygen. This may have been an indication that the dopant level was just sufficient to fill some energy levels in the ZnO band gap and hence increase conductivity, but the fall in sheet resistance was only

Figure 10·1
Sheet resistance as a function of oxygen flow
for zinc oxides doped with tin

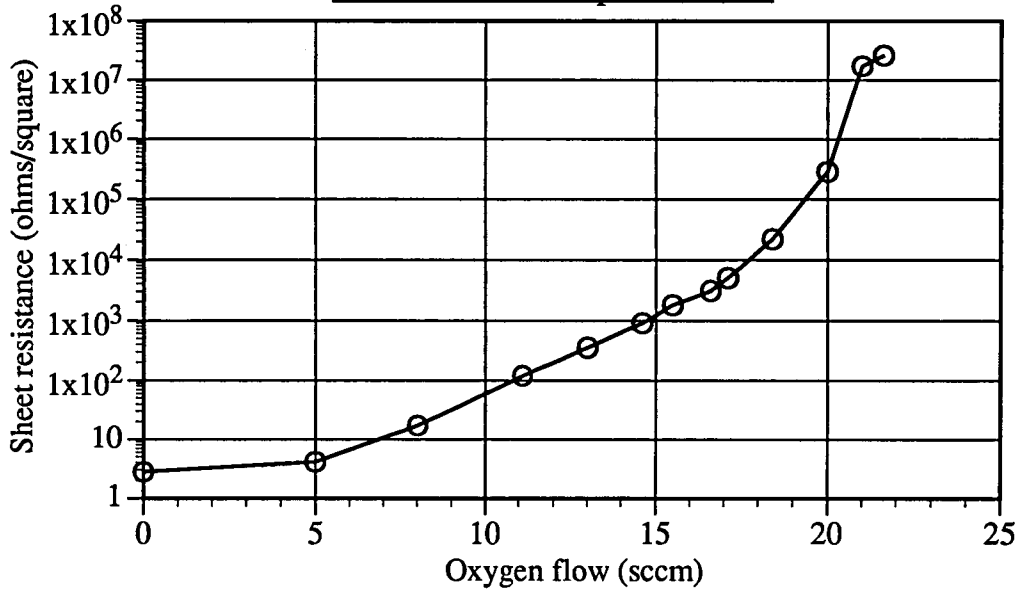

ZnO:12%Sn

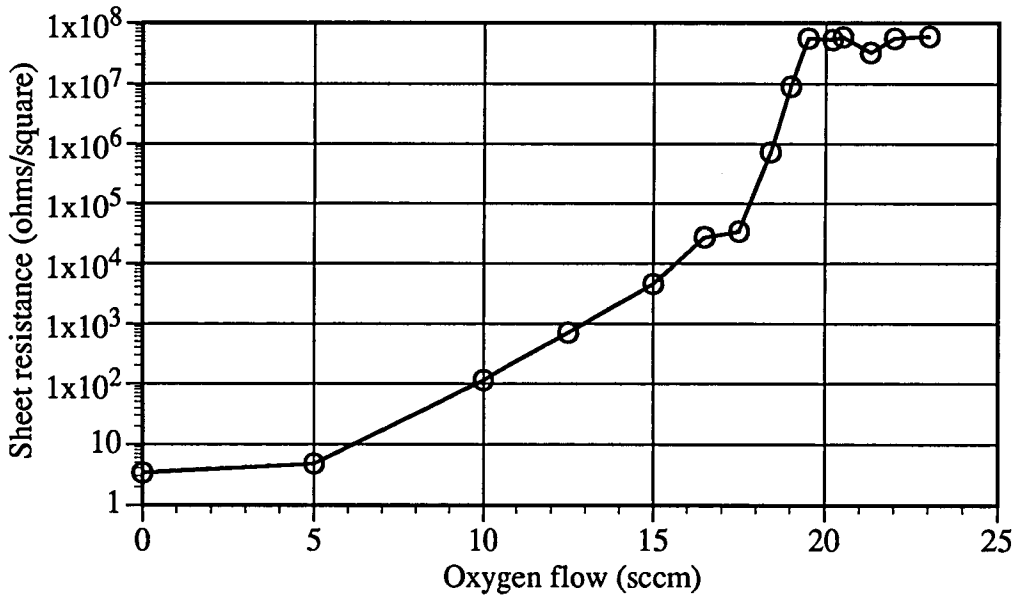

ZnO:19%Sn

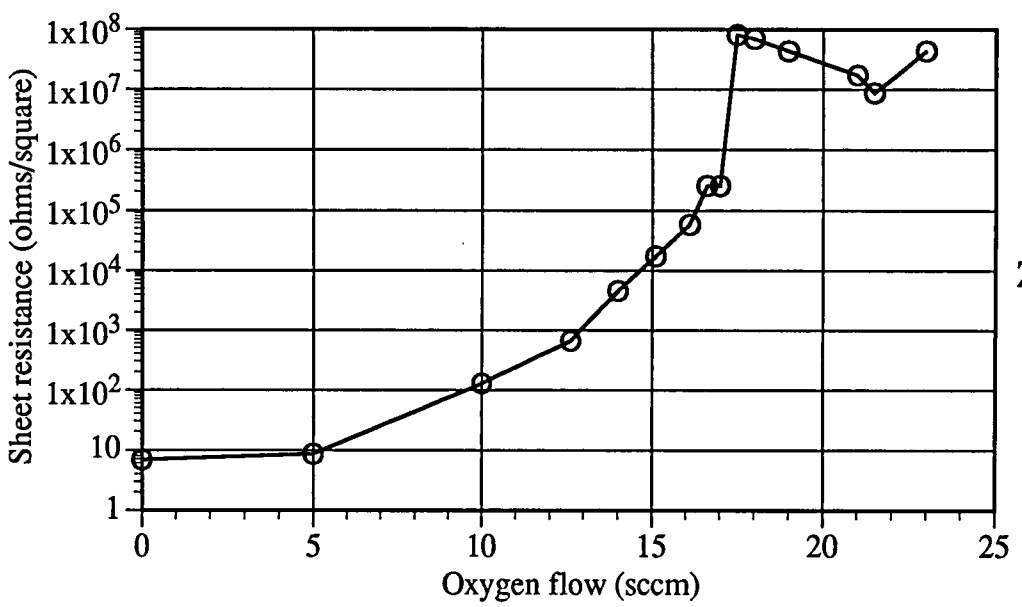

ZnO:33%Sn

from 58 MΩ/□ to 32 MΩ/□, and was not large enough to be considered conclusive. It was decided to increase the dopant level once more in the belief that additional donor levels could be introduced into the oxides, and the final part of figure 10·1 shows the effect. A greater degree of reduction in sheet resistance occurs, and at lower oxygen flows than with the lower dopant levels. The peak in sheet resistance of 70 MΩ/□ at 18 sccm falls to a minimum of 8.6 MΩ/□ at 21.5 sccm where the films are visibly transparent, but by 23 sccm the sheet resistance had again risen. The evidence was that the addition of tin had indeed introduced a resistance minimum into the otherwise insulating oxide films, but the minimum was not significantly useful for electrical conduction in the transparent films. Rather than continue to increase the tin coverage further, a new dopant material was selected using the following criteria: (i) The dopant should have a sputter yield approaching or exceeding that of tin so that its coverage of the zinc could afford to be lower. This would prevent any possibility of the extreme situation where the films became SnO:Zn because of the relative yields and area coverage. (ii) The dopant should be in a periodic group close to tin, to give similar bonding and provision of conduction electrons.

10.2 ZnO:In films.

Using the above criteria, indium was considered a suitable material because its sputter yield is 3.35 atoms per 500eV argon ion, compared with 2.7 for tin[7]. Zinc and indium form a co-sputtering target easily, so it was decided to investigate reactive dc sputtering of ZnO:In using a composite target similar to the Zn:Sn construction. Indium doping of the zinc target was achieved by applying different proportional areas of molten indium to the target surface, ensuring that the dopant was 'wetted', to give good thermal conductivity of the target for cooling purposes during deposition. The In strips were diametrically oriented; a 5mm wide strip corresponding to 6% area, and so on, as before.

Previous workers[8-10] on the preparation of doped ZnO have described the use of high substrate temperatures to assist the incorporation of the dopant into the matrix. For this work it was decided to investigate the differences between the properties of as deposited room temperature

films and the same films following post deposition annealing. Experience acquired during the annealing of ITO films (see section 9·5) suggested that an appropriate temperature for completion of dangling bonds was 400°C. Hence, the annealing conditions were maintained at this temperature for two hours in an argon atmosphere. Auger analysis was used to determine the actual Indium content of the films, to compare with the cathode area coverage.

Given the large number of samples produced in the iterative process to find a resistance minimum, with different degrees of stoichiometry for each dopant level, one sample had to be chosen from each dopant run so that common comparisons could be made. For the purposes of analysis, it was important to decide which sample to use from each dopant concentration for electrical and optical testing. Unlike the experiments with tin doping, all of the ZnO:In depositions showed the variation of sheet resistance with oxygen flow characteristic of transparent conducting oxides. Metallic films with low sheet resistance and low transmittance were deposited at low flow, with composition changing to a cermet as flow increased, then falling to the minimum resistance (R_s min), before rising to very high resistances in the oxide regime. Figure 10·2 shows this characteristic variation for undoped ZnO, 33% and 49% In coverage. For consistency it was decided to choose the film with R_s min for each dopant, and use these for electrical and optical comparison.

10.2.1 Electrical properties of ZnO:In films

From figure 10·2 it was observed that the oxygen flow necessary for R_s min decreased as the percentage coverage of indium increased. There was, however, no evidence to show that the magnitude of R_s min decreased with increasing indium coverage. Whilst undoped ZnO had R_s min=1680 Ω/□ , the value fell with increasing indium coverage so that the 33% indium coverage had R_s min=314 Ω/□ . This latter figure was the lowest sheet resistance exhibited by the as-deposited samples, the 49% coverage rising to an R_s min of 1450 Ω/□ .

The effect of post-deposition annealing was to reduce the sheet resistance of all samples except the undoped ZnO, which rose by a factor of 500 to 83 kΩ/□. This feature corresponds with the work of

Figure 10·2
Sheet resistance as a function of oxygen flow
for as-deposited ZnO:In

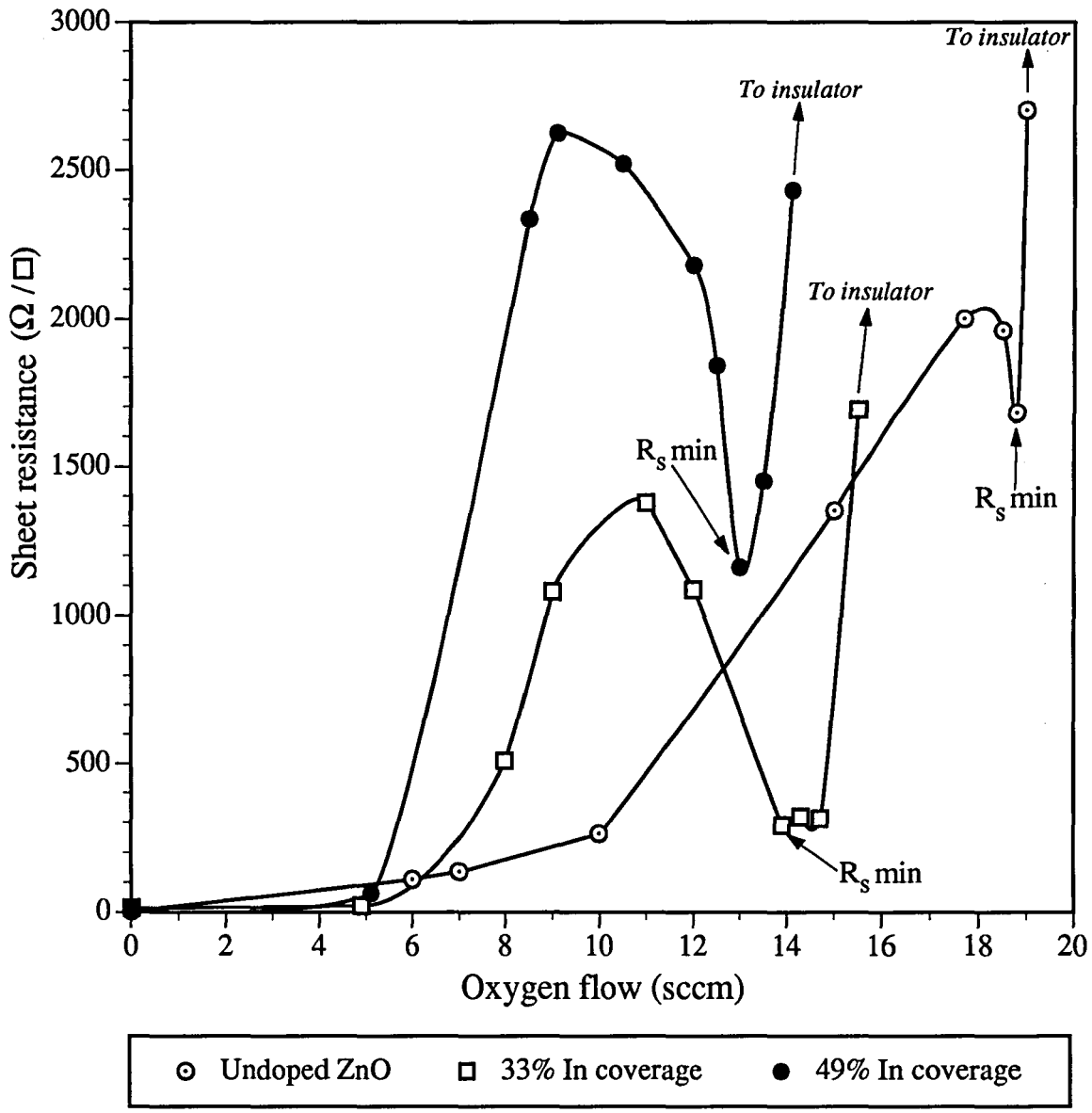

Minami *et al*[11], who quote a change in resistivity from 4 x10^{-4} Ωcm to 5 x 10^{-1} Ωcm for ZnO:Al, following post-deposition annealing in air for one hour above 200°C. All other dopant concentrations were reduced to around 300 Ω/□ following annealing, the decrease attributed to the completion of oxide dangling bonds, indium inclusion and film densification by the higher temperature inert atmosphere. An alternative explanation is the annealing removed free oxygen from the lattice to create the vacancies necessary for conduction.

The lowest initial resistivity, ρ, was 4.7x10^{-3} Ωcm for the 33% In coverage, but this rose slightly during annealing to 5.1x10^{-3} Ωcm. Because of its very high post anneal resistance the undoped sample resistivity rose to 0.9 Ωcm. The lowest ρ over all was the annealed 19% coverage sample, having 3.4 x10^{-3} Ωcm, a decrease of 60% of its as-deposited value. These results compare favourably with those of Jin and Granqvist[12], who quote resistivities of 6.3 x 10^{-3} Ωcm for rf sputtered ZnO. The same authors report a resistivity of 6.9 x 10^{-4} Ω.cm for ZnO:Al(2% wt.), which is an order of magnitude lower than the best annealed ZnO:In films prepared in this work. This confirms the observation of Harding *et al*[13], who state that resistivities of dc sputtered films are generally higher than those prepared by rf sputtering, presumably due to difficulties in guaranteeing correct as-deposited stoichiometry with the former technique.

10.2.2 Optical Properties

Figure 10·3 shows the variation of deposition rate and refractive index, n, with oxygen flow for the 'optimum' resistance minima of each dopant series. The refractive indices lie between 1.78 and 2.25, while the deposition rate increases with decreasing In, due to the increase of oxygen needed to produce R_s min in this direction. It is clear that tailoring of refractive index by selecting an oxygen flow is possible for a particular dopant concentration, but this would only be possible with disregard of the electrical properties of the material. Likewise, it is possible to tailor the resistivity of the sample, but control over the refractive index has to be sacrificed.

Figure 10·4 shows optical transmittance in the visible for as-deposited films. All dopants show absorption in the blue, with undoped ZnO having the lowest transmittance. This rises with indium coverage to a

Figure 10·3
Deposition rate and refractive index as a function of oxygen flow at the 'optimum' resistance points for ZnO:In

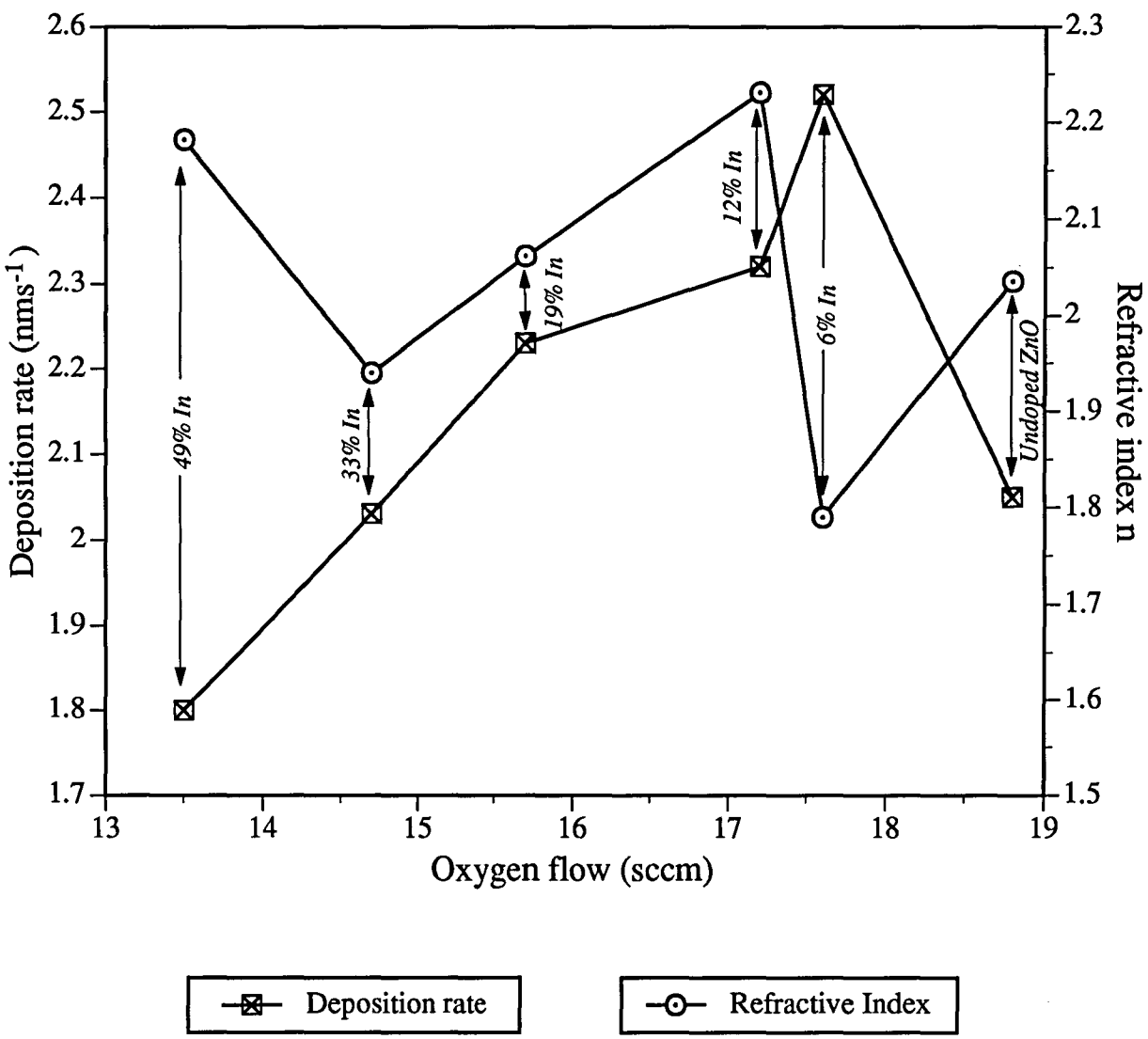

Figure 10·4
Optical transmittance of as-deposited ZnO:In

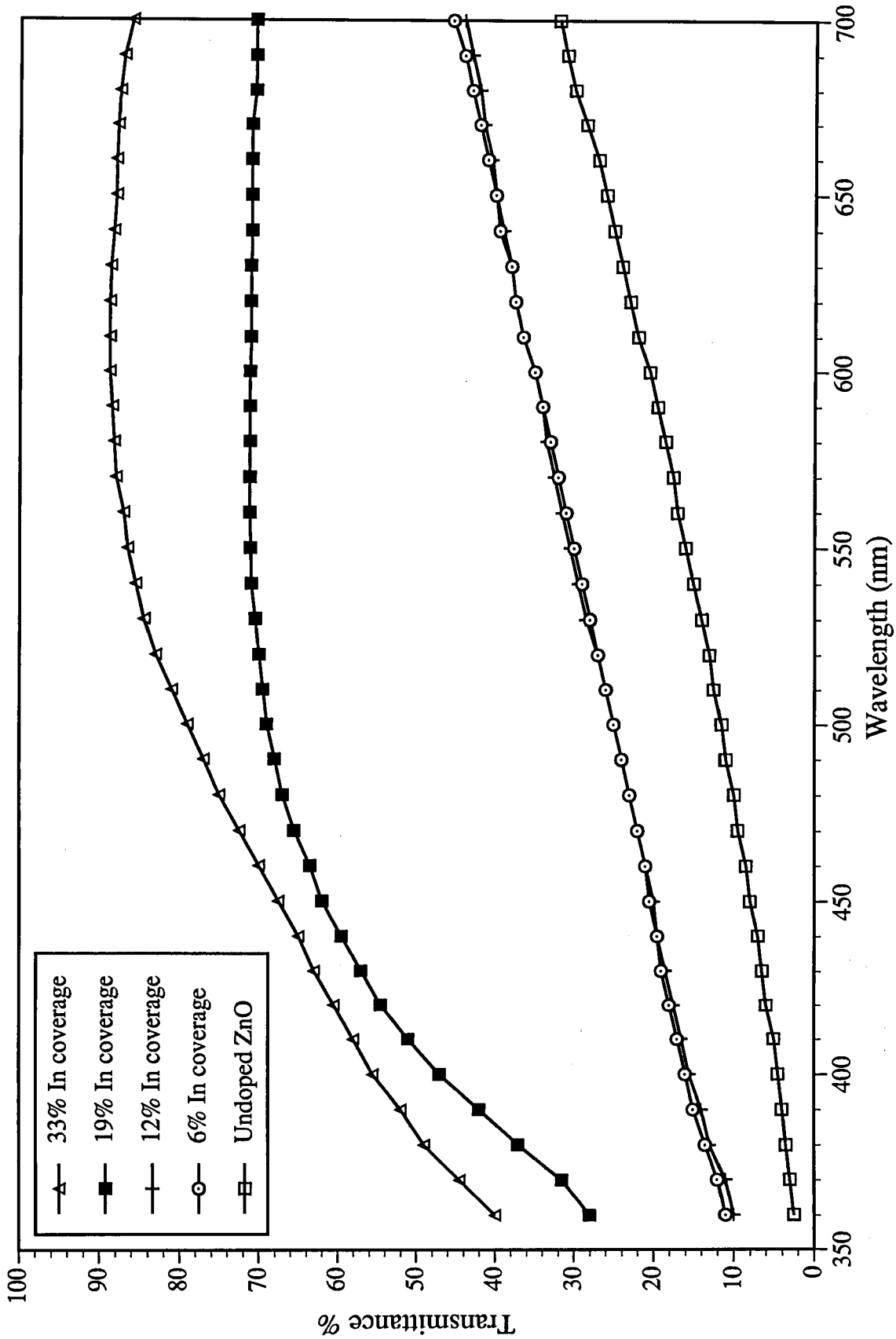

Figure 10·5
Optical transmittance of ZnO:In
following post deposition annealing at 400° C in argon for 2 hours

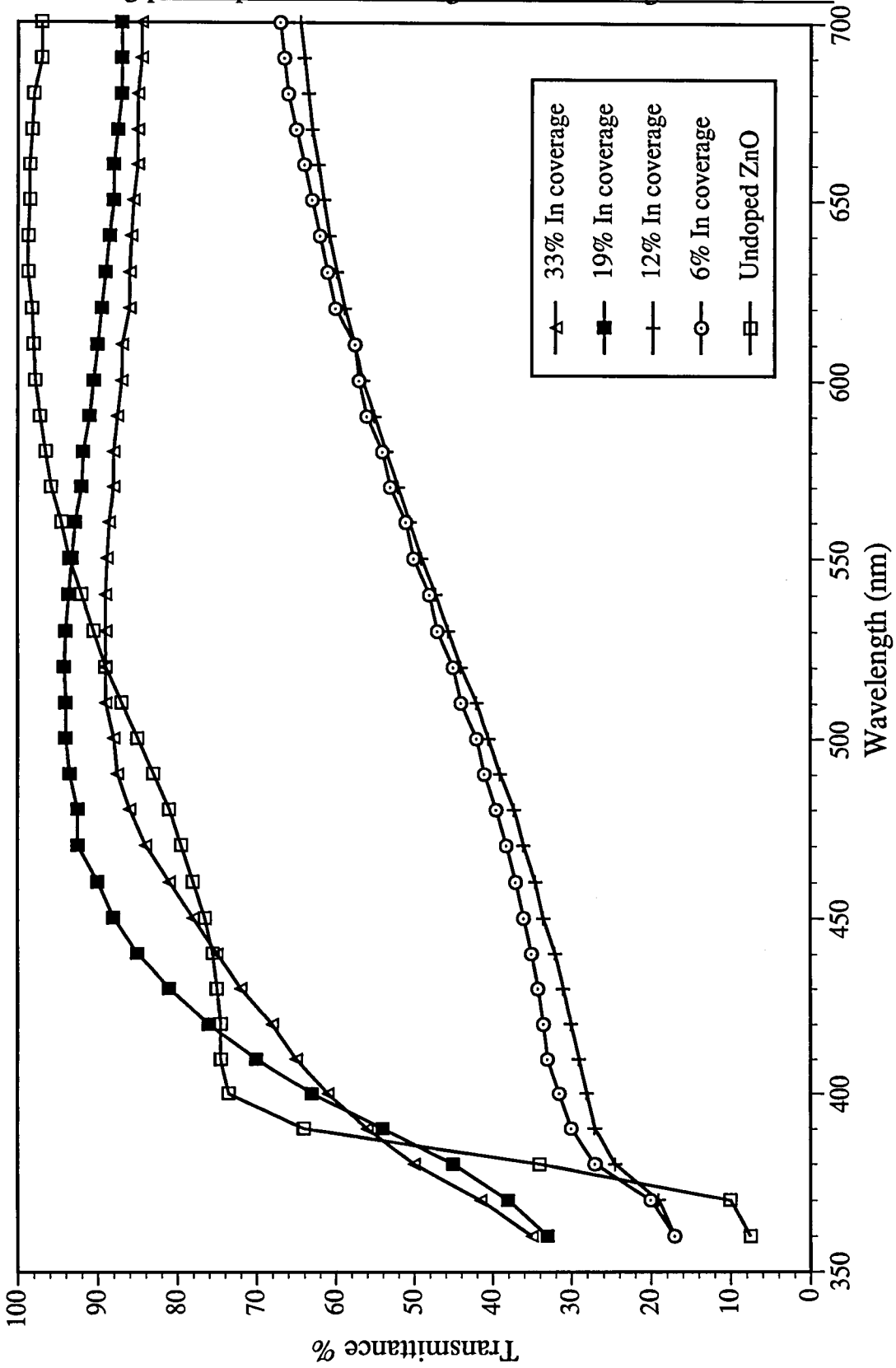

peak in the 33% sample of 89% transmittance at 600nm. Comparison with figure 10·5, the transmittance of annealed samples, shows that the undoped ZnO transmittance improved markedly over the whole wavelength range. The doped samples also show increases in transmittance of about 20%, and still the trend is that higher transmittance results from higher indium concentration. Disregarding the undoped sample, the highest post-deposition transmittance is 95% for the 19% coverage of indium. Hence it is concluded that annealing has resulted in this dopant concentration having the highest optical transmittance, and from the section above, the lowest electrical resistivity.

10.2.3 Auger analysis of R_s min. films for each doping concentration

Figures 10·6 and 10·7 show interpretations of the results of Auger analysis. The ratio of In:Zn does not correlate with the In coverage of the zinc target as it was expected to do, the increase in In coverage from 19% to 33% actually giving less dopant in the film. This apparent contradiction of the expected match between target and film composition was a feature also observed by Pratt[14] and Michalak[15], when sputtering from composite cathodes. It is suggested that although the PEM control system maintains the target as a whole in a stable operating regime, the lack of correlation in figure 10·6 is attributed to micro-instabilities over small areas of the target. The sputter yields of zinc and indium are 5.07 and 3.35 respectively, per 500eV argon ion[7], indicating different reactivities. It is concluded that differential target poisoning of the two elements occurs because PEM can only be tuned to one line, and hence percentage coverage of a zinc target by the dopant cannot be used as a direct indicator of the atomic ratio of the two elements in the sputtered film.

Figure 10·7 represents the film content of the process elements as determined by Auger analysis. These results justify the choice of R_s min as the comparison datum between dopant levels, because the measured elemental film contents follow the predicted pattern. As the In content in the films is increased from 0 to 3.3 at.%, the oxygen flow necessary for R_s min falls from from 18.8 sccm to 13.5 sccm because the higher In concentration completes a greater number of oxide dangling bonds. At the same time, Zn content is falling. Despite Zn having a higher

Figure 10·6
Indium:Zinc ratio in the films as a function of percentage area coverage of the zinc target by indium

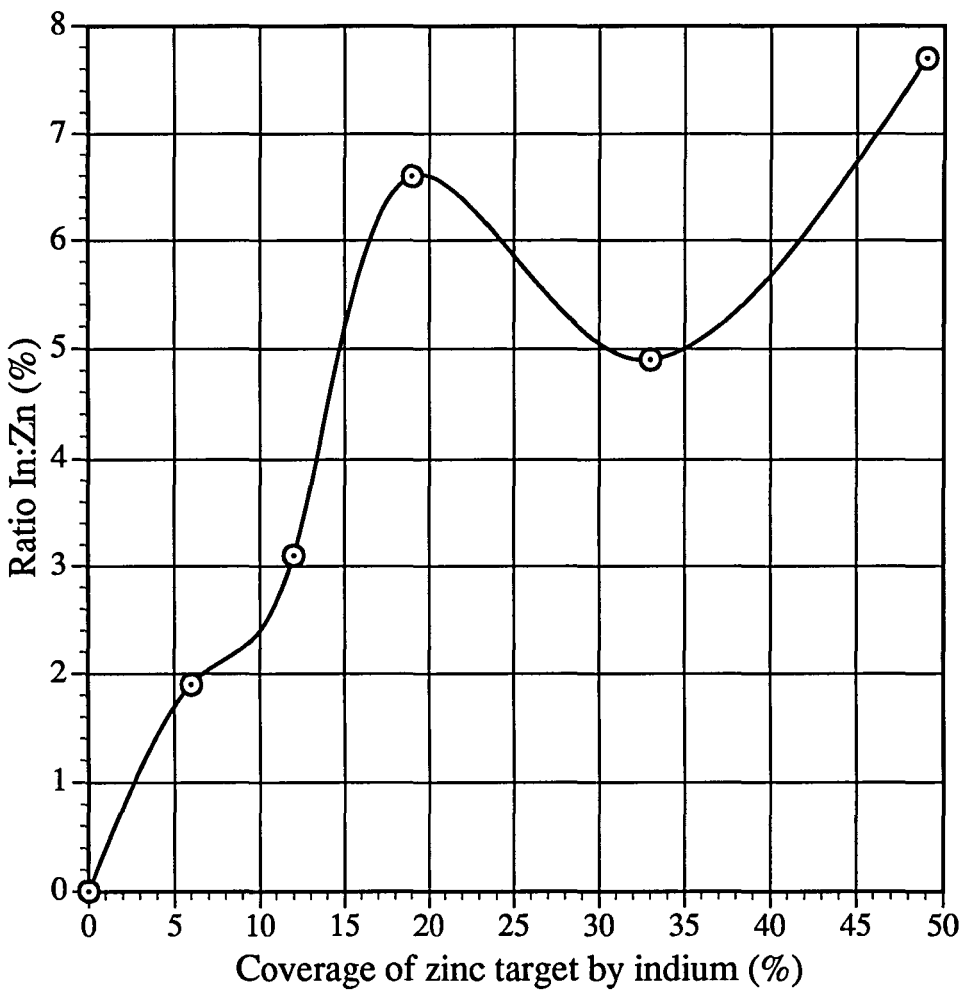

Elemental concentrations obtained by Auger analysis

Figure 10·7
The atomic percentage of zinc, oxygen and indium in the films as a function of the oxygen flow at the 'optimum' sheet resistance for each doping level

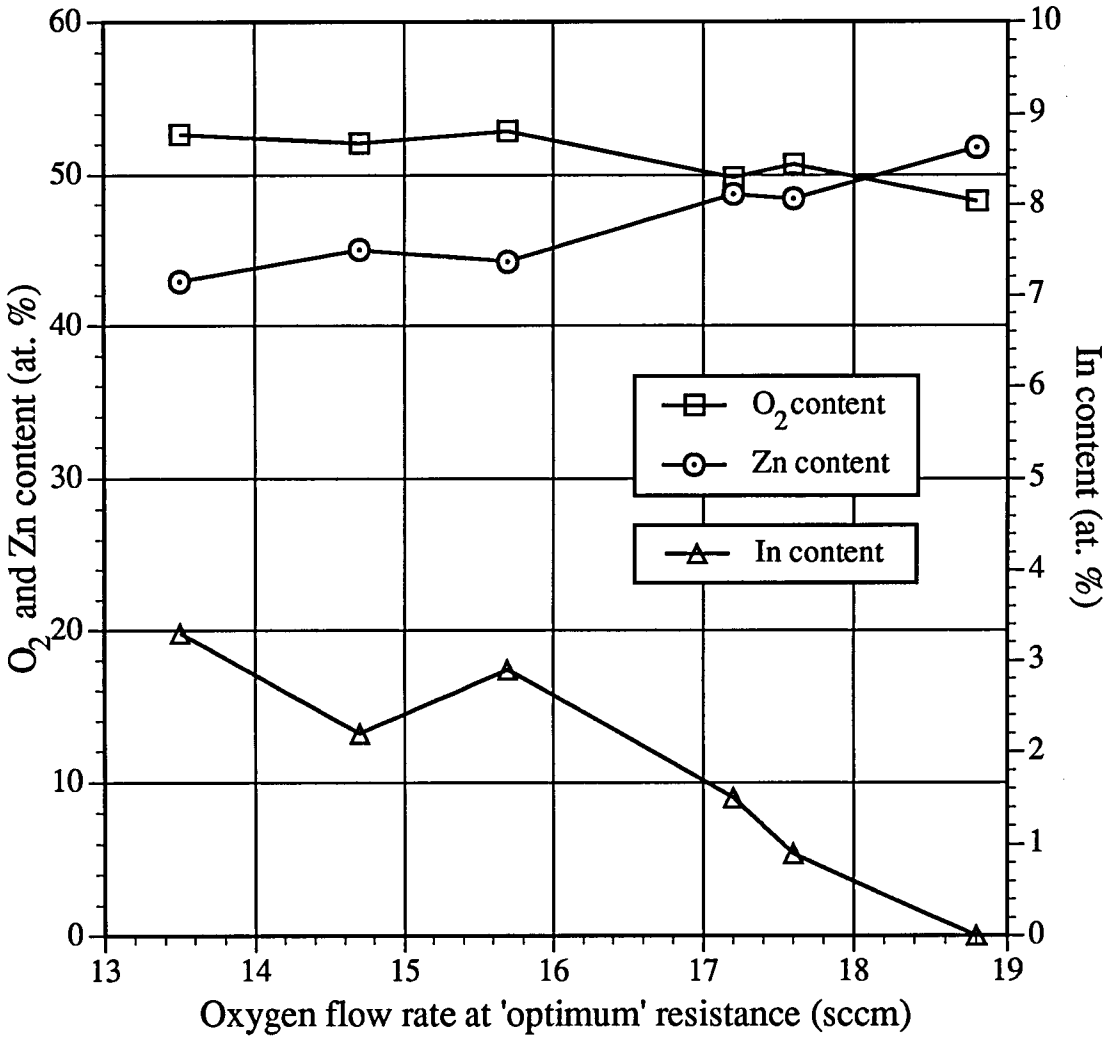

Elemental concentrations obtained using Auger analysis

sputter rate than indium, it appears that the target coverage by the latter has a greater effect on the film content. A possible explanation is that at low oxygen flows the poisoning rate of zinc is greater than that of indium, but as the oxygen flows increase the indium area becomes poisoned to a greater extent, resulting in proportionally higher levels of zinc in the film. With higher oxygen flows the oxygen content in the film is seen to fall from 53% to 48% as a result of higher consumption by the target surface and pumps than by the film.

10.3 Reactive gas and deposition flux calculations

Table 10.1: Reactive gas and deposition flux transport parameters

Film	$\frac{n_i}{n_m}$	ε	$\frac{n_{gp}}{n_{gpp}}$	Necessary reactive gas partial pressure (mTorr)
ZnO	3.08	92	5×10^3	0.62

Although the molecular contents of the dopants were established by Auger, their bonding into the ZnO matrix was unknown, and so the calculations of particle transport in table 10.1 were calculated only for undoped ZnO. There are only three incident ions for every zinc atom deposited for stoichiometric ZnO, leading to an ion energy of 92 eV per zinc atom. This is less than a third of the ion energy per indium atom calculated for In_2O_3 in section 9·6, and whilst it is sufficient energy to complete the chemical reaction at the substrate, it is suggested that the large excess of energy dissipated as heat in the In_2O_3 annealed the film, reducing it to a sub-stoichiometric state to create the oxygen vacancies necessary for conduction. The resistance minimum of undoped ZnO was fifty times higher than that of In_2O_3, and it is suggested from the data presented in table 10.1 that one reason for this is the lack of excess ion energy in the former case, reducing the probability of oxygen vacancies through in-situ annealing. Another possible explanation is that the increased absorptance seen with increasing doping concentration of ZnO creates a doping limit, presumably due to clusters of dopant not accommodated by the lattice. This doping limit is two to three times higher for In_2O_3 before absorptance becomes deleterious to

performance, and may explain the lower resistivity in the latter material.

This comparison has justified the calculation of those parameters in table 10.1, where the magnitudes of the parameters would not have been apparent from other observations of the material properties.

10.4 Chapter summary

The effects of indium doping on DC sputtered zinc oxide films of around 150nm thickness has been investigated, and the findings have shown that

1 The oxygen flow necessary for minimum sheet resistance decreases with increasing indium dopant.

2 Sheet resistance falls with increasing indium dopant, up to a critical value.

3 All doped samples show a decrease in resistance following annealing at 400°C in argon, but the resistance of undoped ZnO rises by a factor of 500.

4 Annealing reduces resistivity and increases transmittance. The lowest resistivity was with an annealed sample containing 2.9 atomic % indium. This had 95% transmittance at 500nm, compared with 68% prior to annealing.

5 Tailoring of refractive index or resistivity or optical transmittance is possible by selecting oxygen flow, but the first two of these parameters appear to be mutually exclusive.

6 The percentage of indium dopant in the sputtered films cannot be assumed proportional to the dopant coverage of the zinc target. This is attributed to differential poisoning of the two major elements in the target by the reactive gas.

Chapter Ten References

1: G. S. Anderson, G. V. Jorgenson & G. K. Wehner, Applied Science Division, Litton Annual Report on Sputtering, ONR Contract 1589(15), (1966)

2: B. L. Flur & J. Riseman, *J. Appl. Phys.*, **35**, (1964), 344

3: I. H. Khan & M. H. Francombe, *J. Appl. Phys.*, **36**, (1965), 1699

4: W. L. Patterson & G. A. Shirn, *J. Vac. Sci. Technol.*, **4**, (1967), 343

5: B. E. Sernelius, K. -F. Berggren, Z. -C. Jin, I. Hamberg & C. G. Granqvist, *Phys. Rev B*, **37(17)**, (1988), 10244

6: I. M. Song, *Thin Solid Films*, **193/194**, (1990), 712-720

7: M. P. Seah., *Thin Solid Films*, **81**, (1981), 279-287

8: W. S. Lau & S. J. Fonash, *J. Electron. Mat.*, **16**, (1987), 141

9: A. P. Roth & D. F. Williams, *J. Appl. Phys.*, **52**, (1981), 6685

10: F. S. Hickernell., Proc. 1st. Int. Symp. on ISSP, Tokyo, Volume, (1991), 57

11: T. Minami, K. Oohashi, S. Takata, T. Mouri and N. Ogawa, *Thin Solid Films*, **193/194**, (1990), 721-729

12: Z. C. Zin and C. G. Granqvist, SPIE Vol. 823 *Optical Materials Technology for Efficiency and Solar Energy Conversion VI* (1987), 28-35

13: G. L. Harding, B. Window and E. C. Horrigan, *Solar Energy Materials*, **22**, (1991), 69-91

14: R. H. Pratt., National Electronics Conf., (1964)

15: E. M. Michalak., Symposium on the Deposition of Thin Films by Sputtering, Univ. of Rochester, (1966)

Chapter Eleven

Results and discussion - Amorphous silicon

11.0 Experimental Particulars

The magnetron target was boron doped polycrystalline silicon constructed as described in section 7.1.2. Throughout this work the power supplied to it was maintained at 400W. Figure 11·1 shows the system geometry used for production of a-Si, and it is useful to cross-reference this figure with the side elevation shown in figure 6·1. Glass substrates were clamped to the end of the loading arm and loaded singly into the load lock, before being transferred to the main chamber. Once inside the main chamber, substrates located on the rotatable cage, so that they could be moved between the heating and deposition zones.

To ensure the formation of silicon hydride complexes rather than interstitial hydrogen atoms, and to increase photovoltaic efficiency, previous work[1,2] has identified the optimum deposition temperature. In the system of figure 11·1 the pre-deposition heating station is a halogen lamp which heats the substrate to 250°C before the substrate is rotated to the deposition zone in front of the silicon cathode. System geometry prevented both heating whilst the film was growing, and the in-situ

Figure 11·1:
The chamber arrangement for a-Si deposition

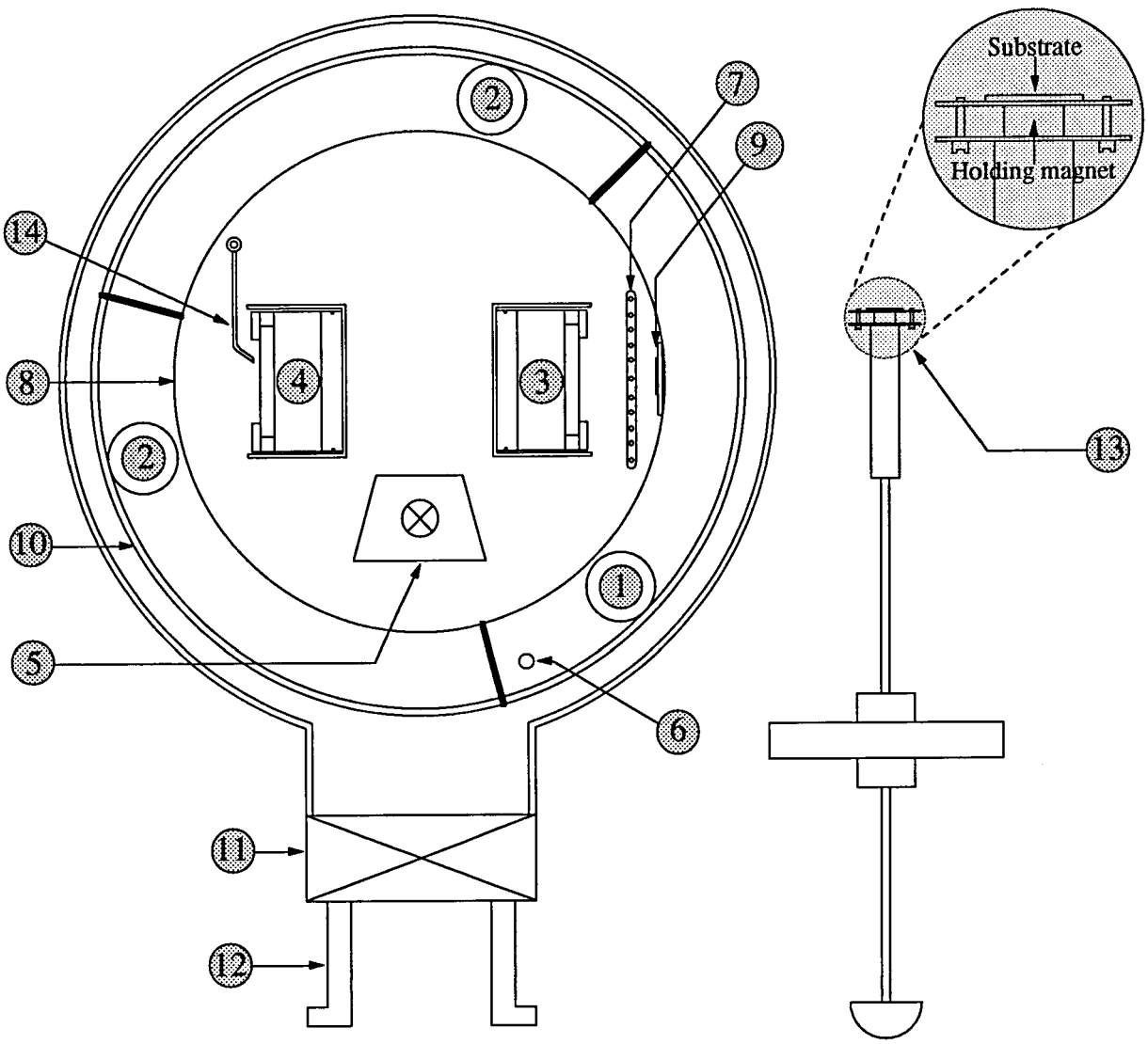

1: Drive wheel
2: Guide wheel
3: Silicon sputtering source
4: Dopant sputtering source
5: Pre-deposition heating station
6: Argon inlet
7: Reactive gas manifold
8: Cage
9: Substrate & holder in deposition zone
10: Rotating cage support
11: Gate valve
12: Separately pumped airlock
13: Substrate & holder on loading arm
14: Hydrogen injection line

monitoring of temperature, so in-vacuo calibration of the lamp at substrate-source distances was necessary prior to this section.

Chapter ten demonstrated one method of doping sputtered films, where the single sputtering source was a composite, constructed of different proportions of the two film constituents. Because the range of dopant concentrations was to be greater in the a-Si experiments, and the availability of silicon cathodes was prohibitive to preparing up to six cathodes, another technique of dopant incorporation was sought. The doping of silane deposited a-Si using phosphine or arsine is well documented, but for the d.c. sputtering technique, a safe, repeatable technique was sought which did not require elaborate extraction facilities for toxic gases. Following the work by Street[3], where molecular hydrogen was injected into a plasma before flowing downstream to the deposition zone, it was decided to use solid source doping. The aim was to allow molecular hydrogen to react with the dopant, forming volatile hydrides, which are etched from the surface to be transported to the growing film. The dopant source in figure 11·1 was either an indium or antimony target, sputtered concurrently with the deposition from the silicon source. A partial pressure of hydrogen was admitted through the injection line so that sputtered dopant atoms could either diffuse or be carried by the hydrogen to arrive at the substrate as silicon was being deposited on it.

Plate 11.1 is an overhead view of the internal layout of the chamber for deposition of amorphous silicon. The silicon source is at the bottom, with the dopant target in the magnetron at the top of the plate, whilst to the left is the halogen heating stage. Although the optical fibres are shown in the plate, they were not necessary for this stage of the work and are shown only to illustrate the compact design of the process components.

11.1 The difficulty of quantifying optical constants of thin film semiconductors

A key parameter for evaluating semiconducting materials with optical applications in general, and photonic conversion devices in particular, is the absorption coefficient, α. The conventional method for calculating α

Plate 11·1
System geometry for a-Si deposition - overhead internal view

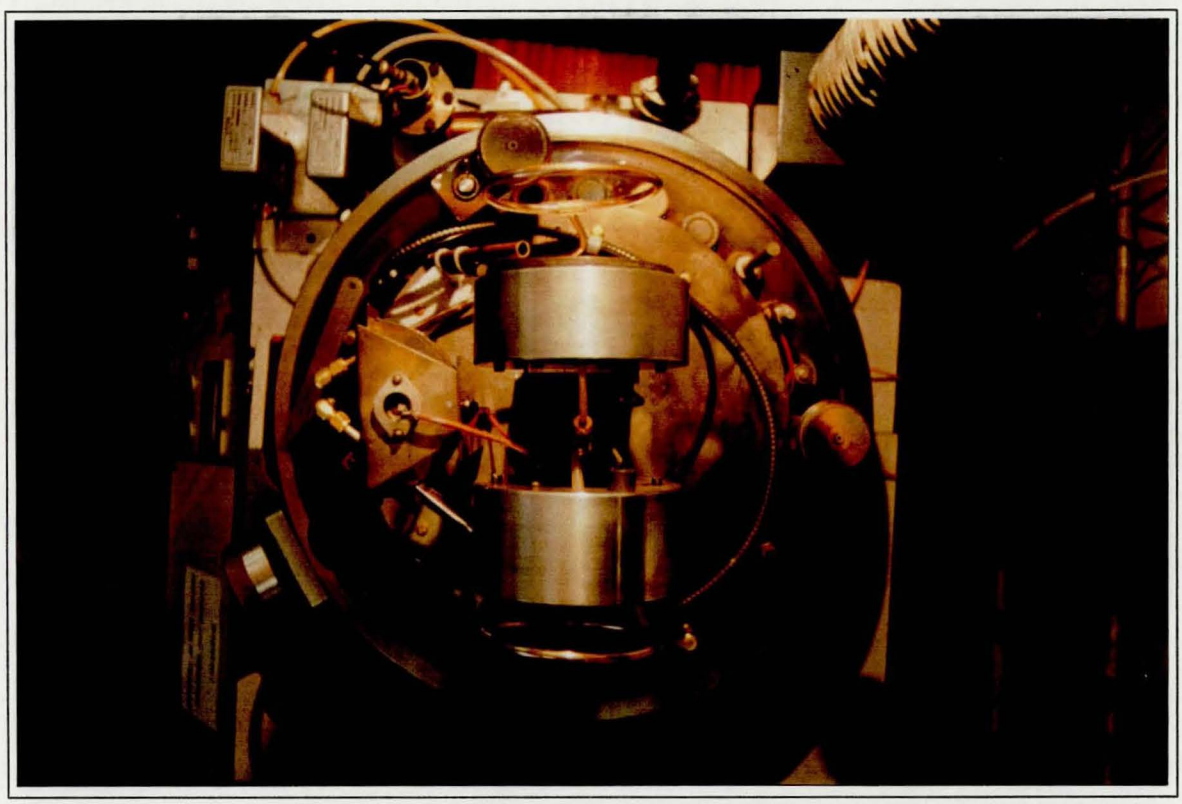

Heating station is centre left.
Silicon source is centre bottom.
Dopant source is centre top

Figure 11·2: Conventional interface parameters for incident light I_0

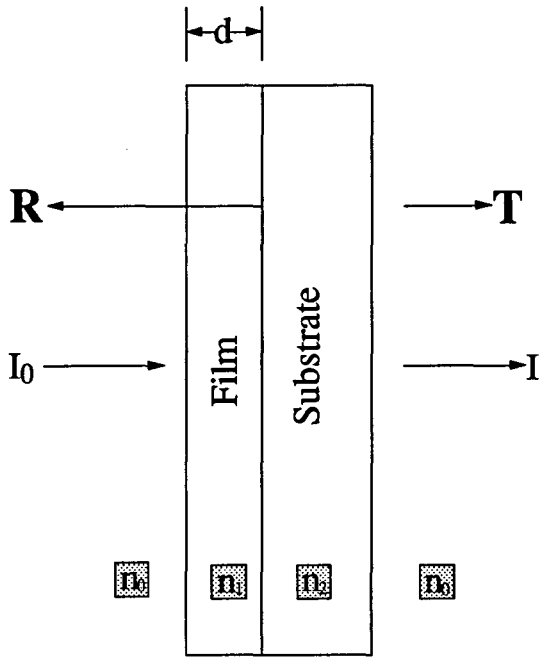

Measured parameters in bold type

Figure 11·3: Additional interface parameters used in the derivation of absorption coefficient

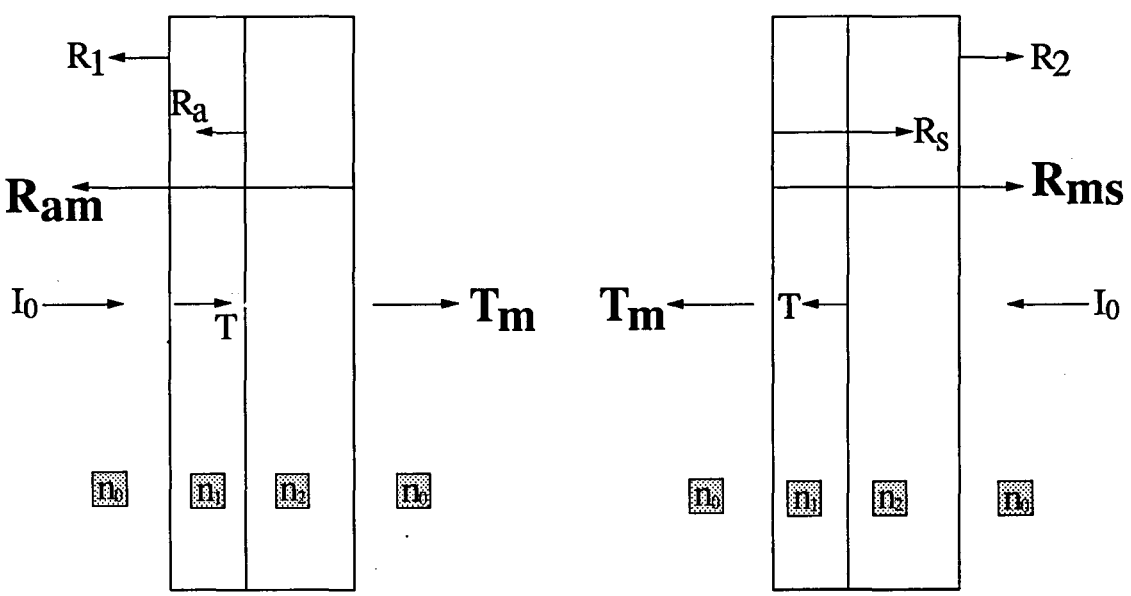

Film side illumination

Substrate side illumination

Measured parameters in bold type

Figure 11·4

(a): Optical transmittance, reflectance and absorptance of a-Si, quantified using conventional measurands.

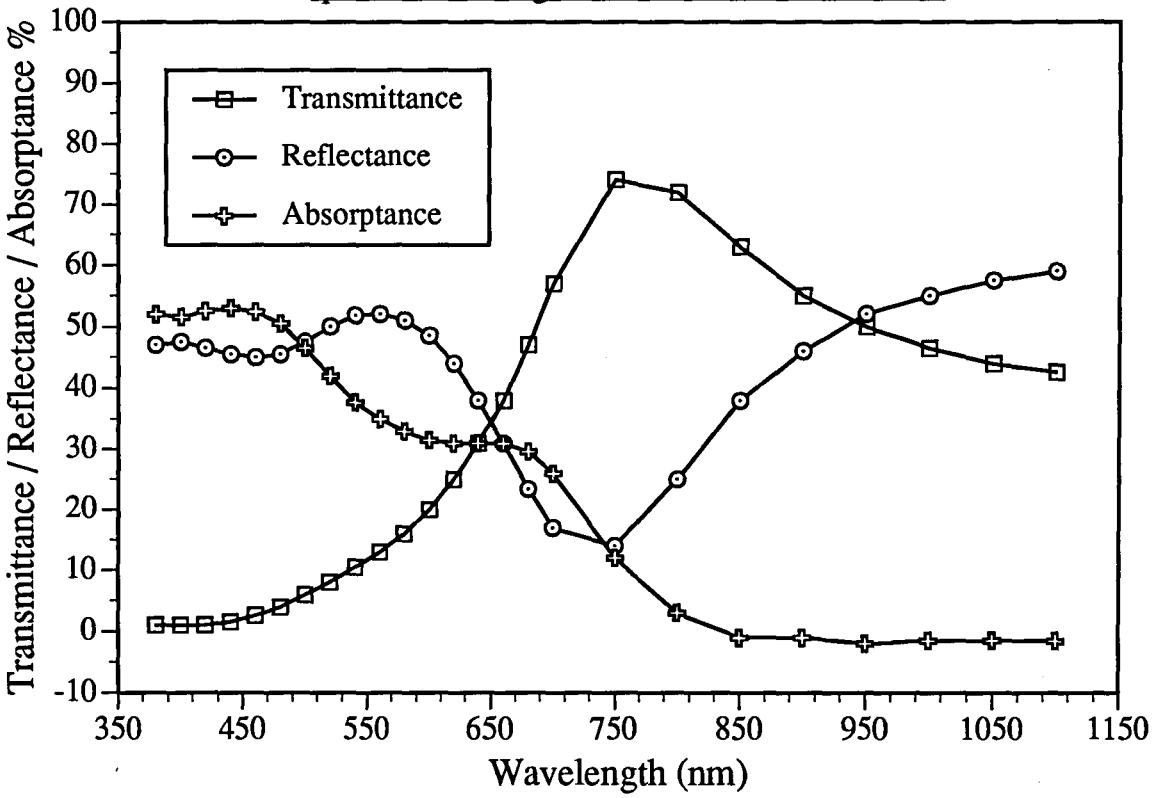

(b): Absorption coefficent calculation, making no allowance for interference in the film between 700nm and 800nm

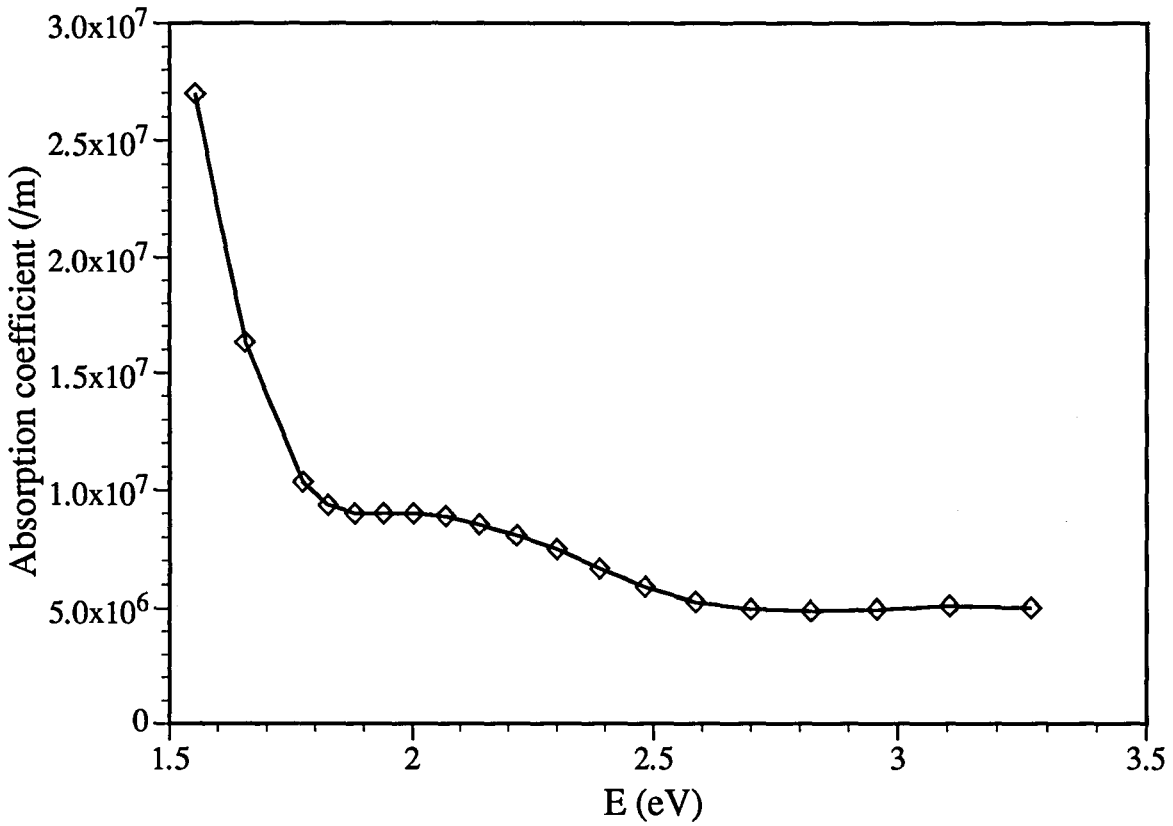

is to measure transmittance T and reflectance R as shown in figure 11·2, and calculate absorptance A from equation [6.6]. Absorption coefficient is then obtained from the standard attenuation equation:

$$I = I_0 \exp(-\alpha d) \qquad [11\cdot1]$$

where the symbols have the meanings shown in figure 11·2. The band gap of the film material can then be estimated by the extrapolated intercept of the $\sqrt{\alpha E}$ versus E plot, where E is wavelength converted to photon energy. This simple method, however, proved inaccurate for thin films showing interference, because the measured parameters are of the film+substrate combination, not of the film alone.

Figure 11·4(a) shows an example of the errors introduced by interference, for a 130nm thick a-Si film on a glass substrate. When the absorption coefficient is calculated from equation [11·1], figure 11·4(b) results. The effect of the interference in the film was to produce a 'mirror image' of the conventional appearance of such a plot, with no indication of the band gap. It was clear that for the film thicknesses involved in this work a new technique involving measurands of both substrate and film was necessary. The novel technique is derived with reference to figure 11·3.

Assume a film, thickness d, is deposited onto a much thicker substrate. The combination is illuminated by a spectrophotometer beam, firstly from the film side, then from the substrate side. Components of the incident radiation I_0, following its entry to the system, are...

T_m the measured transmittance through both film and substrate.

T the actual transmittance into the film.

R_1 interface reflectance between film and air.

R_2 interface reflectance between substrate and air.

R_{am} the measured reflectance (containing all components) from the film side.

R_{ms} the measured reflectance (containing all components) from the substrate side.

R_a the component of reflectance entering the film, with illumination from the film side.

R_s the component of reflectance entering the substrate, with illumination from the substrate side.

The expression for the transmittance of a film giving interference, attached to a thick substrate is[4]

$$T = \frac{n_2}{n_0} \cdot \frac{t_1^2 t_2^2 e^{-2\beta}}{1 - 2 r_1 r_2 e^{-2\beta} \cos 2\delta + r_1^2 r_2^2 e^{-4\beta}} \qquad [11\cdot2]$$

where multiple reflections are neglected, and t and r are the amplitude coefficients.

δ and β represent the real and imaginary parts of the phase change in the beam passing through the film.

$$\delta = \frac{2 \pi n_1 d_1}{\lambda} \qquad [11\cdot3]$$

and

$$\beta = \frac{2 \pi k d}{\lambda} = \frac{\alpha d}{2} \qquad [11\cdot4]$$

where k and α are the extinction coefficient and absorption coefficient respectively.

Rewriting [11·2] in terms of energy reflection coefficients gives

$$T = \frac{(1 - R_1)(1 - R_2) e^{-\alpha d}}{1 + 2\sqrt{R_1}\sqrt{R_2} e^{-\alpha d} \cos 2\delta + R_1 R_2 e^{-2\alpha d}} \qquad [11\cdot5]$$

The total energy reflection coefficient at the substrate-film interface, R_a is given by

$$R_a = \frac{r_2^2 - 2 r_1 r_2 e^{-2\beta} \cos 2\delta + r_1^2 e^{-4\beta}}{1 - 2 r_1 r_2 e^{-2\beta} \cos 2\delta + r_1^2 r_2^2 e^{-4\beta}} \qquad [11\cdot6]$$

Rewriting [11·6] in terms of energy reflection coefficients gives

$$R_a = \frac{R_1 + 2\sqrt{R_1}\sqrt{R_2}\, e^{-\alpha d} \cos 2\delta + R_2 e^{-2\alpha d}}{1 + 2\sqrt{R_1}\sqrt{R_2}\, e^{-\alpha d} \cos 2\delta + R_1 R_2 e^{-2\alpha d}} \qquad [11\cdot7]$$

Similarly, for illumination from the substrate side,

$$R_s = \frac{R_2 + 2\sqrt{R_1}\sqrt{R_2}\, e^{-\alpha d} \cos 2\delta + R_1 e^{-2\alpha d}}{1 + 2\sqrt{R_1}\sqrt{R_2}\, e^{-\alpha d} \cos 2\delta + R_1 R_2 e^{-2\alpha d}} \qquad [11\cdot8]$$

Although T is not directly measurable, it is related to measured transmittance, T_m, thus...

$$T_m = \left(\frac{1 - R_2}{1 - R_s R_2}\right) . T \qquad [11\cdot9]$$

The glass substrates used have uncoated reflectance coefficients of 0.04 per side, so rearranging [11·9] gives

$$T = \left(\frac{1 - 0.04R_s}{0.96}\right) . T_m \qquad [11\cdot10]$$

Similarly, R_{ms} is related to R_s by

$$R_{ms} = R_2 + \left\{\frac{(1 - R_2)^2 . R_s}{1 - R_2 R_s}\right\} \qquad [11\cdot11]$$

Rearranging for R_s and using $R_3 = 0.04$,

$$R_s = \frac{(R_{ms} - 0.04) . (1 - 0.04R_s)}{(0.96)^2} \qquad [11\cdot12]$$

If the error in R_{ms} is ≈1% then it can be assumed that

$$R_{ms} = R_s \qquad [11\cdot13]$$

This assumption will affect [11·12] little since the multiplier R_s is itself multiplied by 0.04. Hence [11·12] becomes

$$R_s = \frac{(R_{ms} - 0.04) . (1 - 0.04R_{ms})}{(0.96)^2} \qquad [11\cdot14]$$

and [11·10] becomes

$$T = \left(\frac{1 - 0.04R_{ms}}{0.96}\right) . T_m \qquad [11·15]$$

The measured reflectance from the film side, R_{am}, is given by

$$R_{am} = R_a + \left(\frac{T^2R_3}{1 - R_sR_3}\right) \qquad [11·16]$$

i.e.

$$R_a = R_{am} - \left(\frac{0.04T^2}{1 - 0.04R_s}\right) \qquad [11·17]$$

and since [11·14] yields R_s, R_a is easily determined.

In order to eliminate terms involving δ, and hence interference effects, take $R_a - R_s$, i.e. [11·7] -[11·8].

$$\Delta R = R_a - R_s = \frac{(R_1 - R_2) . (1 - e^{-2\alpha d})}{1 + 2\sqrt{R_1}\sqrt{R_2}\, e^{-\alpha d} \cos 2\delta + R_1R_2\, e^{-2\alpha d}} \qquad [11·18]$$

This still contains a term in δ, but if the operation $T/\Delta R$ is performed the denominator will cancel. Hence, from [11·5] and [11·18],

$$\frac{T}{\Delta R} = \frac{(1 - R_1) . (1 - R_2)}{(R_1 - R_2)} \cdot \frac{e^{-\alpha d}}{1 - e^{-2\alpha d}} \qquad [11·19]$$

For normal incidence on an isotropic medium, the reflection coefficients become[5]

$$R_1 = \left(\frac{n_0 - n_1}{n_0 + n_1}\right)^2 \qquad R_2 = \left(\frac{n_1 - n_2}{n_1 + n_2}\right)^2$$

Substituting for R_1 and R_2 in [11·19] gives measurable parameters of T (from [11·15]), ΔR, n_0, n_1, n_2 and d, leaving only α to be determined.

In order to evaluate [11·19], let

$$\Psi \equiv \frac{(1 - R_1).(1 - R_2)}{(R_1 - R_2)} \equiv \frac{\left(1 - \frac{\widehat{R_1}}{X}\right).\left(1 - \frac{\widehat{R_2}}{X}\right)}{\left(\frac{\widehat{R_1}}{X} - \frac{\widehat{R_2}}{X}\right)} \qquad [11\cdot20]$$

where X is the common factor $(n_1+n_2)^2.(n_0+n_1)^2$,

$$\widehat{R_1} = R_1X,$$

$$\widehat{R_2} = R_2X.$$

Simplifying [11·20] gives

$$\Psi = \frac{\left(X - \widehat{R_1}\right).\left(X - \widehat{R_2}\right)}{\left(\widehat{R_1} - \widehat{R_2}\right).X} \qquad [11\cdot21]$$

Using X as above and $R_1 = \left(\frac{n_0 - n_1}{n_0 + n_1}\right)^2$, $R_2 = \left(\frac{n_1 - n_2}{n_1 + n_2}\right)^2$ gives

$$\frac{\left[(n_1+n_2)^2.(n_0+n_1)^2 - (n_0+n_1)^2.(n_1+n_2)^2\right].\left[(n_1+n_2)^2.(n_0+n_1)^2 - (n_0-n_1)^2.(n_0+n_1)^2\right]}{\left[(n_1+n_2)^2.(n_0-n_1)^2 - (n_1-n_2)^2.(n_0+n_1)^2\right].[X]}$$

Expanding terms gives

$$\Psi = \frac{\left[4n_0n_1^3 + 8n_0n_1^2n_2 + 4n_0n_1n_2^2\right].\left[8n_0n_1^2n_2 + 4n_1^3n_2 + 4n_1n_0^2n_2\right]}{\left[-4n_0n_1^3 + 4n_1^3n_2 - 4n_0n_1n_2^2 + 4n_1n_0^2n_2\right].\left[(n_1 + n_2)^2.(n_0 + n_1)^2\right]}$$

Assuming the refractive index of air, $n_0 = 1$,

$$\Psi = \frac{\left[4n_1^3 + 8n_1^2n_2 + 4n_1n_2^2\right].\left[8n_1^2n_2 + 4n_1^3n_2 + 4n_1n_2\right]}{\left[-4n_1^3 + 4n_1^3n_2 - 4n_1n_2^2 + 4n_1n_2\right].\left[(n_1 + n_2)^2.(1 + n_1)^2\right]}$$

Taking out the common factor of 4 from both terms in the numerator, and the first term in the denominator,

$$\Psi = \frac{4\left(n_1^3 + 2n_1^2n_2 + n_1n_2^2\right).4\left(2n_1^2n_2 + n_1^3n_2 + n_1n_2\right)}{4\left(-n_1^3 + n_1^3n_2 - n_1n_2^2 + n_1n_2\right).(n_1 + n_2)^2.(1 + n_1)^2}$$

Now, taking out n_1 from the first terms in the numerator and denominator, and (n_1n_2) from the second term in the numerator,

$$\Psi = \frac{4n_1(n_1^2 + 2n_1n_2 + n_2^2) \,.\, 4n_1n_2(2n_1 + n_1^2 + 1)}{4n_1(-n_1^2 + n_1^2n_2 - n_2^2 + n_2) \,.\, (n_1 + n_2)^2 \,.\, (1 + n_1)^2} \qquad [11{\cdot}22]$$

Now,

$$(n_1{}^2 + 2n_1n_2 + n_2{}^2) = (n_1 + n_2)^2 \qquad [11{\cdot}23]$$

and

$$(2n_1 + n_1{}^2 + 1) = (1 + n_1)^2 \qquad [11{\cdot}24]$$

Substituting [11·23] and [11·24] into [11·22] above,

$$\frac{(1 - R_1) \,.\, (1 - R_2)}{(R_1 - R_2)} = \frac{4n_1n_2}{-n_1^2 + n_1^2n_2 - n_2^2 + n_2}$$

i.e.

$$\frac{(1 - R_1) \,.\, (1 - R_2)}{(R_1 - R_2)} = \frac{4n_1n_2}{(n_1^2 - n_2) \,.\, (n_2 - 1)} \qquad [11{\cdot}25]$$

For the glass substrates used, $n_2 = 1.5$, so combining [11·19] and [11.25],

$$\frac{T}{\Delta R} = \left(\frac{12\, n_1}{n_1^2 - 1.5}\right) \cdot \left(\frac{e^{-\alpha d}}{1 - e^{-2\alpha d}}\right) \qquad [11{\cdot}26]$$

For this calculation, assume that n_1 is constant. Then rearranging [11·26] gives

$$K = \frac{e^{-\alpha d}}{1 - e^{-2\alpha d}} \qquad [11{\cdot}27]$$

where K is the constant.

Now let $\gamma = e^{-\alpha d}$. Substituting for $e^{-\alpha d}$ in [11·27] gives

$$K = \frac{\gamma}{1 - \gamma^2} \qquad [11{\cdot}28]$$

This is in quadratic form, so solving for γ, and knowing d will enable α to be determined.

Rearranging [11·28],

$$\gamma^2 + \frac{\gamma}{K} - 1 = 0$$

The solutions are given by

$$\gamma = \frac{-\frac{1}{K} \pm \sqrt{\frac{1}{K^2} + 4}}{2} \qquad [11\cdot29]$$

The negative solutions are discarded because $e^{-\alpha d}$ cannot be negative, so

$$\gamma = e^{-\alpha d} = \frac{-\frac{1}{K} + \sqrt{\frac{1}{K^2} + 4}}{2} \qquad [11\cdot30]$$

The absorption coefficient α is then simply

$$\alpha = -\frac{\log_e \gamma}{d} \qquad [11\cdot31]$$

Despite the somewhat intimidating appearance of the derivation, the results show that from the simple measurement of the three film parameters of transmittance, and reflection from both sides of the substrate, values for the absorption coefficient can now be calculated over a wide spectral range.

11.2 Results obtained with the new technique

Figure 11·5 shows α calculated using this technique as a function of incident light energy E, for a-Si:H, where the hydrogen partial pressure was varied from 0 to 1 mTorr in 0.2 mTorr steps. The effect of increasing hydrogen dilution is to reduce α at constant energy (wavelength), and to increase the band gap E_g, since the extrapolation of $\sqrt{(\alpha E)}$ to low energies on a $\sqrt{(\alpha E)}$ v. E plot approximates the band gap. The demarcation between the tail and the remainder of the α versus E curves is well observed, and the ordinate covers seven decades. The estimation of E_g was made from extrapolation of this curve, because over such a range of ordinates the extrapolation will have the same degree of accuracy as with the $\sqrt{(\alpha E)}$ versus E curve. The increased

Figure 11·5
Absorption coefficient of undoped a-Si:H, varying hydrogen partial pressure

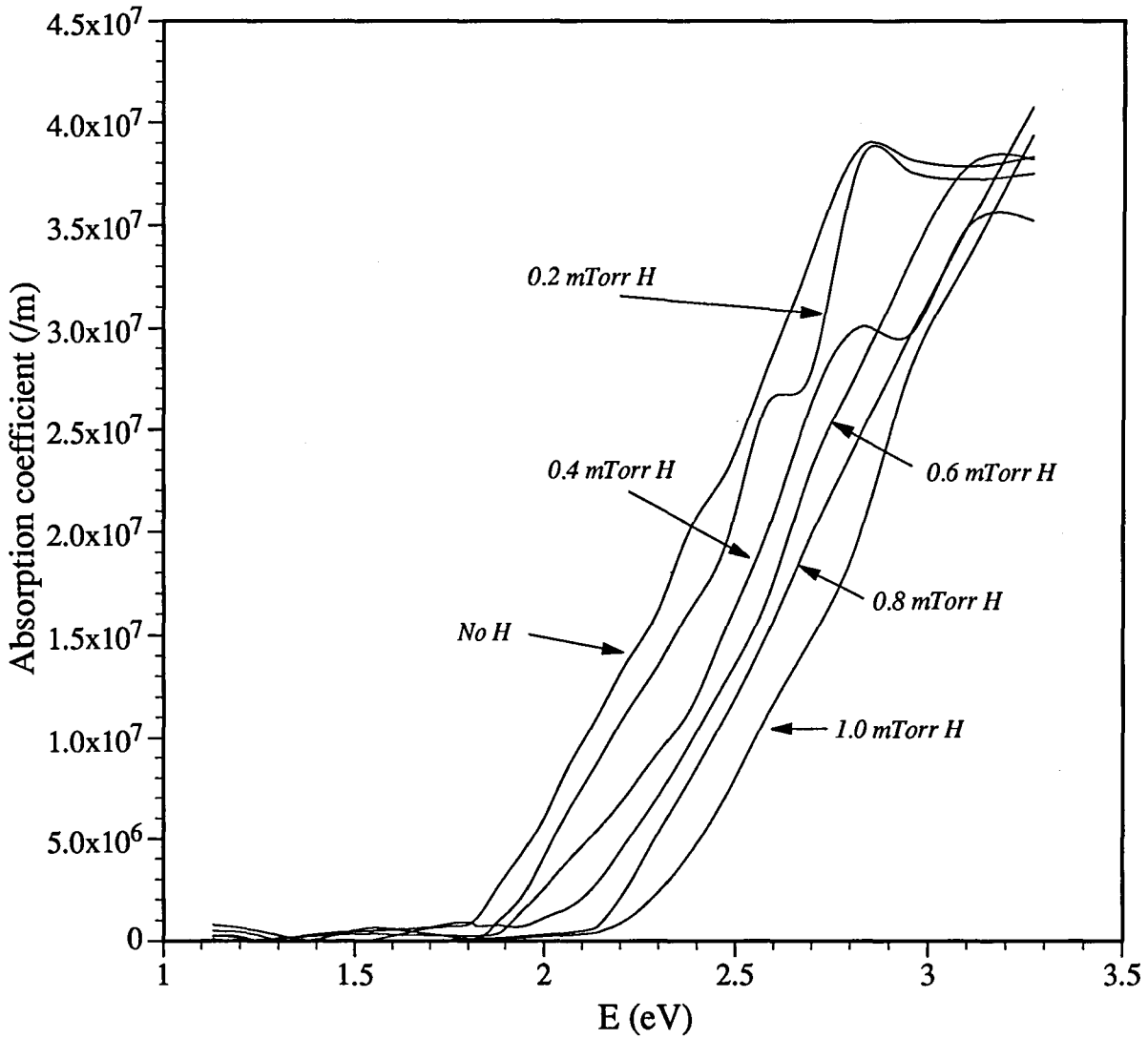

Footnote
The irregularities in the general form of the curves shown in this, and other similar figures to come, are attributed to erroneous data introduced by the older Hitachi spectrophotometer, particularly at range, and lamp change points. An alternative explanation could be that the effect is due to periodic interference maxima, but this would be expected to be more prevalent further into the infra-red. When this instrument was replaced by a computer controlled spectrophotometer to collect the data for figure 12·6, the irregularities do not appear, suggesting the former explanation is more likely.

band gap shown in the figure is thought[6] to be due to the elimination of electronic states at the top of the valence band. These results are in agreement with previous work of Shirafuji[7], Van Heuvel[8] and Pinarbasi[9].

Figure 11·6 shows the absorption coefficient for a-Si:H doped with indium. In this instance the indium source was run at 200W; half the power of the silicon source. As with figure 11·5, increasing the hydrogen content results in an increased band gap, but there is no significant difference between values of either α or E_g for undoped or indium doped a-Si. SIMS profiles showed the presence of indium in the films but it is suggested that because indium does not form a hydride, its incorporation is as interstitials. The hydrogen saturates dangling bonds as in the a-Si with no dopant, and the indium plays no beneficial role.

Unlike indium, antimony does form a hydride, so a-Si:H was deposited with varying hydrogen contents, firstly with the antimony source running at half the power of the silicon source (200W), then with it at twice the power (800W). Figures 11·7 and 11·8 show the absorption coefficient in the visible for the above antimony dopant source powers, respectively. Once again, the shift to higher band-gaps with increasing hydrogen contents is seen with both antimony source powers. The main difference between these two figures is in the values of α. As a reference, take a mid-range hydrogen partial pressure of 0.6 mTorr. At 2.5 eV, α is 5.2 x10^6 m^{-1} for the 800W antimony cathode, whilst for the 200W antimony source α is 1.2 x10^7 m^{-1}. This is in agreement with the work of Ellis *et al*[10], but contradicts the work of Schmid[11] who found α to *increase* with increasing hydrogen when using arsenic as a dopant. In heavily doped semiconductors such as ours (SIMS giving antimony concentrations of 1 x10^{19} cm^{-3}), valence band filling occurs and the drop in α at a given energy is due to the decrease in the number of available final states due to the Burstein-Moss shift.

Steeper absorption coefficient gradients at higher energies are seen in figure 11·8 compared with figure 11·7, in addition to less random variations in slope, and a movement of E_g to higher energies. Qualitatively, SIMS shows there to be less antimony in the 200W antimony doped a-Si samples, with approximately 1 x10^{19} antimony atoms.cm^{-3} in the 800W antimony sample produced at 0.6 mTorr

Figure 11·6
Absorption coefficient of a-Si:H doped with indium.
Indium cathode operated at 50% of the power of the silicon cathode.

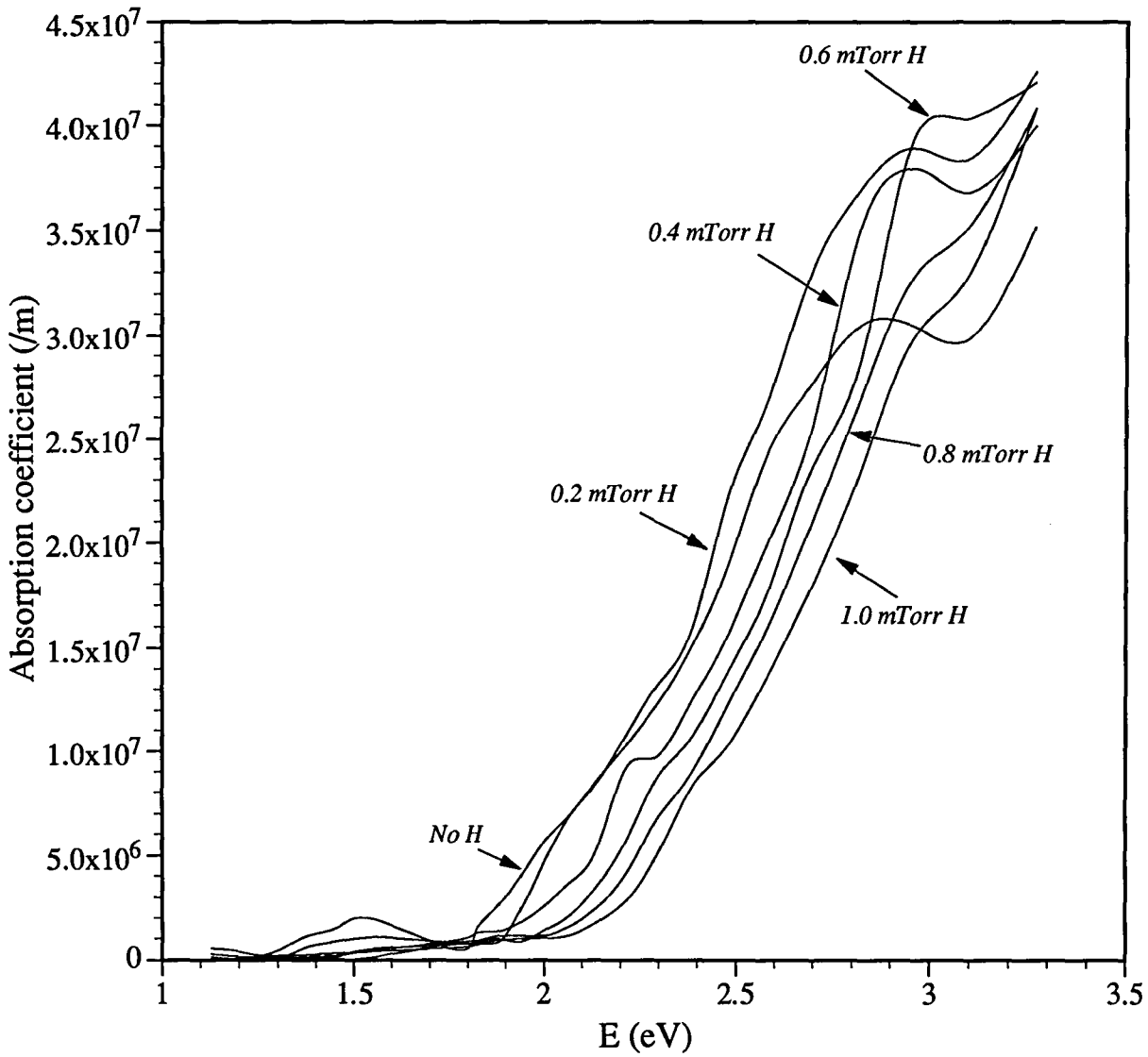

Figure 11·7
Absorption coefficient of a-Si:H doped with antimony.
Antimony cathode operated at 50% of the power of the silicon cathode.

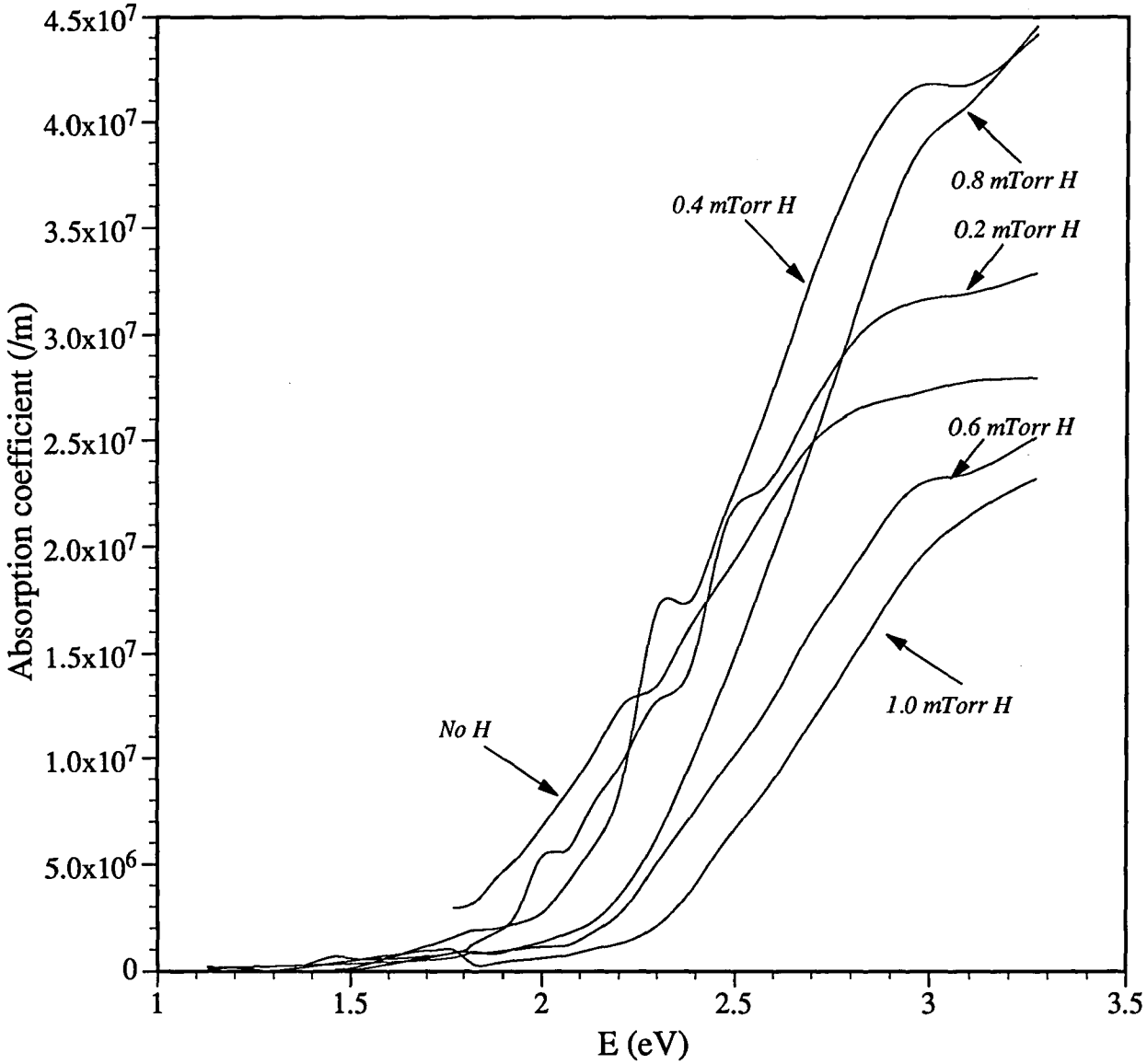

Figure 11·8
Absorption coefficient of a-Si:H doped with antimony.
Antimony cathode operated at twice the power of the silicon cathode.

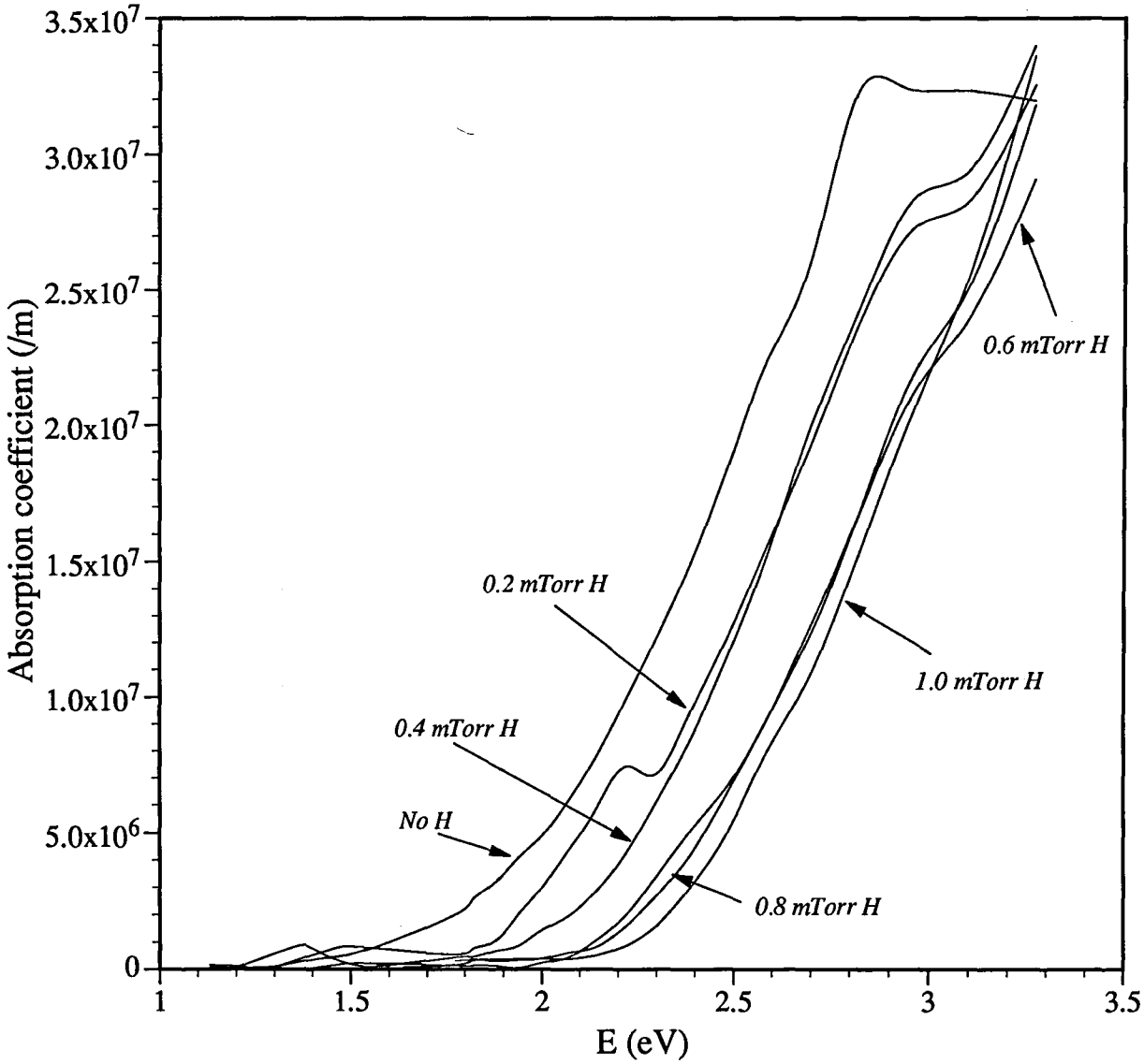

hydrogen partial pressure. Hence it is assumed that the increased antimony content of the a-Si is increasing α, steepening the slope, and widening the band gap of the material.

Room temperature conductivity measurements gave the results shown in Table 11.1. The hydrogen increases the conductivity from that of unhydrogenated sample, and the antimony doping increases it further. This conductivity of 9.7×10^{-5} $(\Omega.m)^{-1}$ is comparable with similar work of Street[3] but is lower than other workers' silane deposited[12] and RF sputtered[13] films. The two latter authors report conductivities of approximately 10^{-8} $(\Omega.cm)^{-1}$ at 280°C, whereas our conductivity measurements were at room temperature. The n-type antimony may have actually doped the a-Si more than is indicated above, because the silicon target material was itself boron doped. Hence a progression from p-type silicon through insulator would have to be overcome before n-type a-Si:Sb was reached.

Table 11.1: Dark Conductivity of a-Si, a-Si:H and a-Si:H:Sb.

SAMPLE	Hydrogen partial pressure (mTorr)	Sb target power (W)	Dark conductivity $(\Omega.m)^{-1}$
a-Si	-	-	4.5×10^{-5}
a-Si:H	0.6	-	8.9×10^{-5}
a-Si:H:Sb	0.6	800	9.7×10^{-5}

The combination of increased E_g with dopant, and lower conductivity than other similar work suggests that the antimony is assisting the process of hydrogenation more than acting as a conductivity enhancing dopant, *with the parameters used here.*

11.3 Chapter Summary

1 The energy gap of a-Si produced by reactive d.c. sputtering can be varied between 1.7 and 2.2 eV, by the addition of up to 1 mTorr of hydrogen during deposition.

2 Sputtering indium during deposition of a-Si has no measurable effect on the above optical parameters.

3 Incorporation of different antimony concentrations into a-Si:H has been achieved by sputtering such a target at different powers during deposition of a-Si.

4 The doping with antimony increased E_g further, and increased room temperature dark conductivity by a factor of 2 over a-Si without hydrogenation.

Chapter Eleven References

1: R. Sridhar, R. Venkattasubbiah, J. Majhi & R. Ramachandran, *Journal of Non-Crystalline Solids*, **119**, (1990), 331-341

2: J. M. Asensi *et al.*, 10th European Photovoltaic Solar Energy Conf. Book of Abstracts, (1991),1B09

3: R. A. Street, N. M. Johnson, J. Walker & K. Winer., *Philosophical Magazine Letters*, **60**, (1989), 177-182

4: R. P. Howson, *Journal de Physique*, **25**, (1964), 212-217

5: O. S. Heavens, "Optical Properties of Thin Films", Dover Publications, (1965)

6: B. von Roedern, L.ley & M. Cardona, *Phys. Rev. Lett.*, **39(24)**, (1977), 1576

7: T. Shirafuji *et al.*, *Solar Energy Mat.*, **23**, (1991), 256-264

8: J. C. Van den Heuvel *et al.*, *Solar Energy Mat.*, **22**, (1991), 185-194

9: M. Pinarbasi, M. J. Kushner & J. R. Abelson, *J. Vac. Sci. Technol. A.*, **8**(3), (1990), 1369-1373

10: F. B. Ellis Jr. & A. E. Delahoy, *Solar Energy Mat.*, **13**, (1986) 109-132

11: P. E. Schmid., *Physical Review B.*, **23**(10), (1981), 5531-5536

12: W. J. Varhue & H. Chao, *Thin Solid Films*, **169**, (1989), 179-186

13: M. C. Ozturk & M. G. Thompson, *Appl. Phys. Lett.*, **44**(9), (1984), 916-918

Chapter Twelve

Results and discussion - Low voltage sputtered amorphous silicon

12.0 The development of a low voltage magnetron

Encouraged by the disclosure of the benefits of low-voltage magnetron sputtering in reference 9, chapter three, a preliminary programme was begun in association with H. A. Ja'fer, also of the Department of Physics, Loughborough University, to investigate the possibility of adapting the existing magnetron geometry for low voltage sputtering. If the operating voltage can be reduced by some means to a level below that which usually results in sputtering of the cathode, the device ceases operation as a sputtering source, but becomes a 'plasma gun', the lower energy ions from which can be directed towards a target of source material.

Section 3.9 demonstrated that deposition at 200V was optimum for sputtered silicon films, in terms of ion-induced damage and sputtering efficiency. For this reason it was decided to attempt the low voltage preparation of a-Si:H in order to compare the optical properties of the material when deposited at 700V and 200V. A technique of electron injection into the plasma was sought, similar to that described by Cuomo and Rossnagel[1]. Their design incorporated a hollow cathode source, out

of the end of which electrons escaped, to be consumed by the discharge of a magnetron. These electrons have sufficient energy to ionise the background gas, and the increased ionisation forms a denser plasma than that produced by the magnetron alone. The plasma is characterised by a lower impedance, resulting in increased currents at constant voltage or decreased voltages at constant current.

12.0.1 The double low voltage magnetron deposition system

Rather than design and construct a hollow cathode source of electrons, a simple thermionic emitter was favoured for this work. A tungsten filament of the type used in thermal evaporation was attached to the centre of a magnetron, and mounted along the axis of the device. It was hoped that by allowing the filament to adopt cathode potential whilst passing a current of tens of amperes through it, a discharge could be maintained well below the sputtering threshold of the target due to the injected electrons. If the magnetron could be operated at, say, -50V rather than the normal operating potential, there would be no sputter flux from the cathode, effectively making the device an ion 'gun'. The intention was to direct this 'clean' plasma from the unbalanced magnetron 'gun' onto another unbalanced magnetron containing the silicon cathode, which was to be sputtered. If the silicon-based magnetron was independently biased at -200V, then the energy of impinging ions from the 'gun' would be ~200eV, and LVS of silicon would result.

Figure 12·1 illustrates the experimental arrangement for the initial LVS trials. The magnetron 'gun' contained a titanium cathode, chosen because its low sputter yield would help to guarantee a 'clean' plasma when the voltage was lowered by the electron injection. The figure shows the silicon 'target' magnetron at 45° to the axis of the 'gun', and although the unbalanced field is represented schematically for both magnetrons, the experimental separation was closer than shown in the figure, so that the magnetic fields could interact to trap the discharge in a closed 'bottle'. It was imperative for the magnetic arrangements of each magnetron to be exactly opposite in sign, so that the fields attracted each other to contain the discharge. The substrate position was parallel to the 'target' magnetron to ensure film uniformity, and out of the discharge 'bottle' to prevent ion damage. Plate 12·1 shows a head-on

view of the 'gun' magnetron, with the axial filament in the centre. The blue colouration is sputtered silicon which deposited on the face of the titanium cathode, evidence that the titanium sputter flux had indeed been suppressed. Plate 12·2 is an iron filing plot of the magnetic confinement provided by the attracting magnetic configurations, with the 'gun' to the left.

An evaluation of the viability of the arrangement shown in figure 12·1 as a deposition technique was made. Figure 12·2 shows the variation of the power in each magnetron with current through the filament, when the silicon source was maintained at -200V bias. At each of the two 'gun' biases the power in the titanium magnetron was always greater than that in the silicon 'target', and the ratio of power in each, Ti:Si, increased with filament current. It is seen that a higher power density can be achieved in the silicon target by increasing the bias on the titanium 'gun', but this increases the possibility of titanium contamination as the titanium sputtering threshold is approached. The maximum attainable power in the silicon target was 150W, at a filament current of 48A. Assuming the configuration gave, at best, the same deposition rate as the a-Si in chapter eleven, deposition times necessary for comparable film thicknesses would approach 8 minutes, and it was not thought feasible to pass 48A through the filament for this period, especially in a reactive atmosphere.

In order to increase the proportion of power in the silicon target, the bias to this magnetron was increased whilst maintaining the 'gun' at -50V. Figure 12·3 shows the effect on the power to each magnetron, again as a function of filament current. At silicon biases of -100V and -200V the power is higher in the 'gun', but when -400V is applied to the silicon the situation reverses, with twice the power of the titanium induced in the silicon. This appears to be the required effect, with 500W induced at a filament current of 50A, but when the filament was switched off, it was found that the discharge could be maintained by the magnetron alone. This showed that -400V was in fact in the regime of normal unbalanced magnetron cathode operation, and since the aim was to produce a-SI at -200V, no advantage was to be gained by using the -400V bias.

Figure 12·1
Power supply arrangement for low voltage sputtering of silicon from a filament-assisted magnetron 'gun'

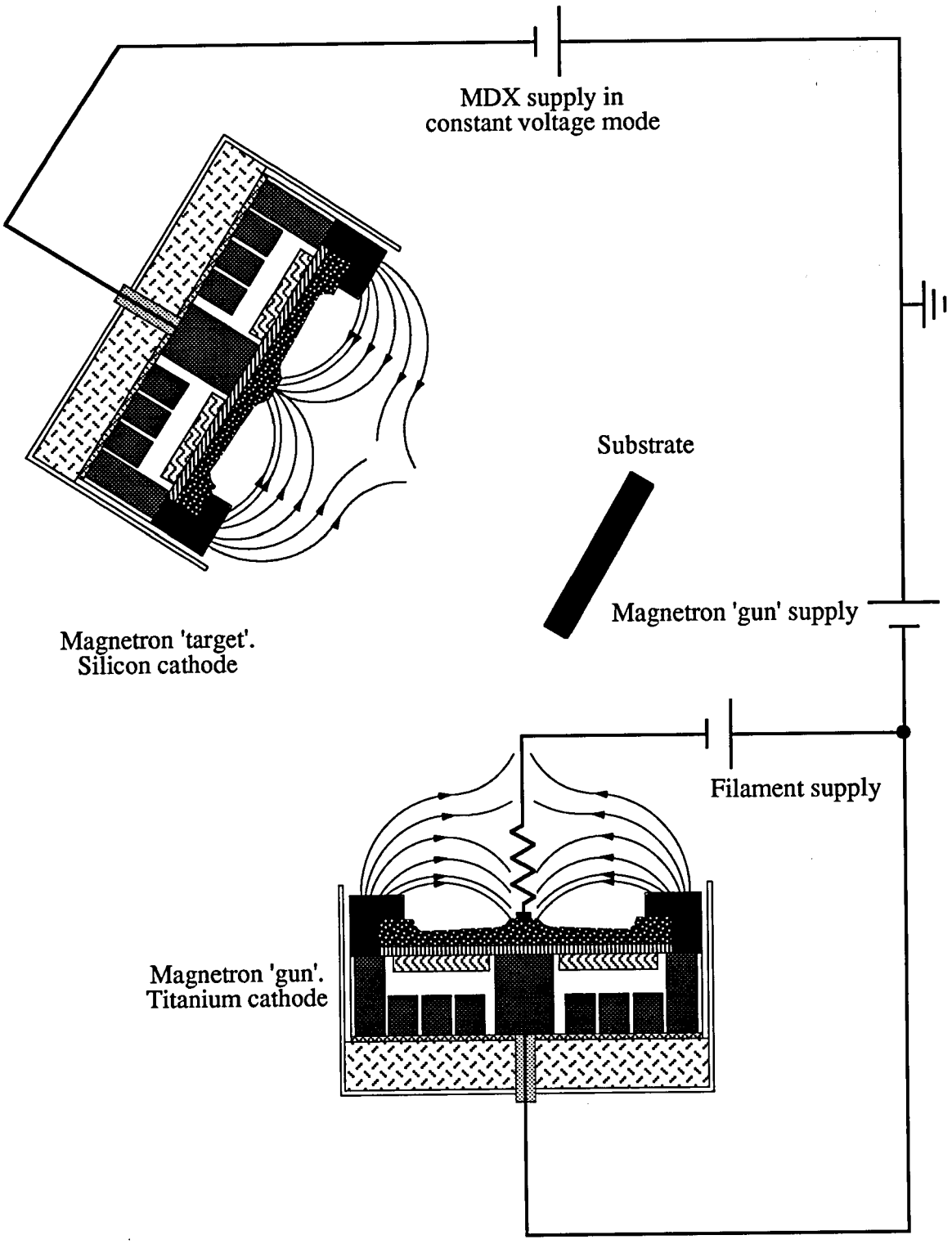

Magnetrons shown at greater separation than that used in practice, where the unbalanced fields interact

Plate 12·1
The axially oriented filament projecting from the Ti 'gun' magnetron

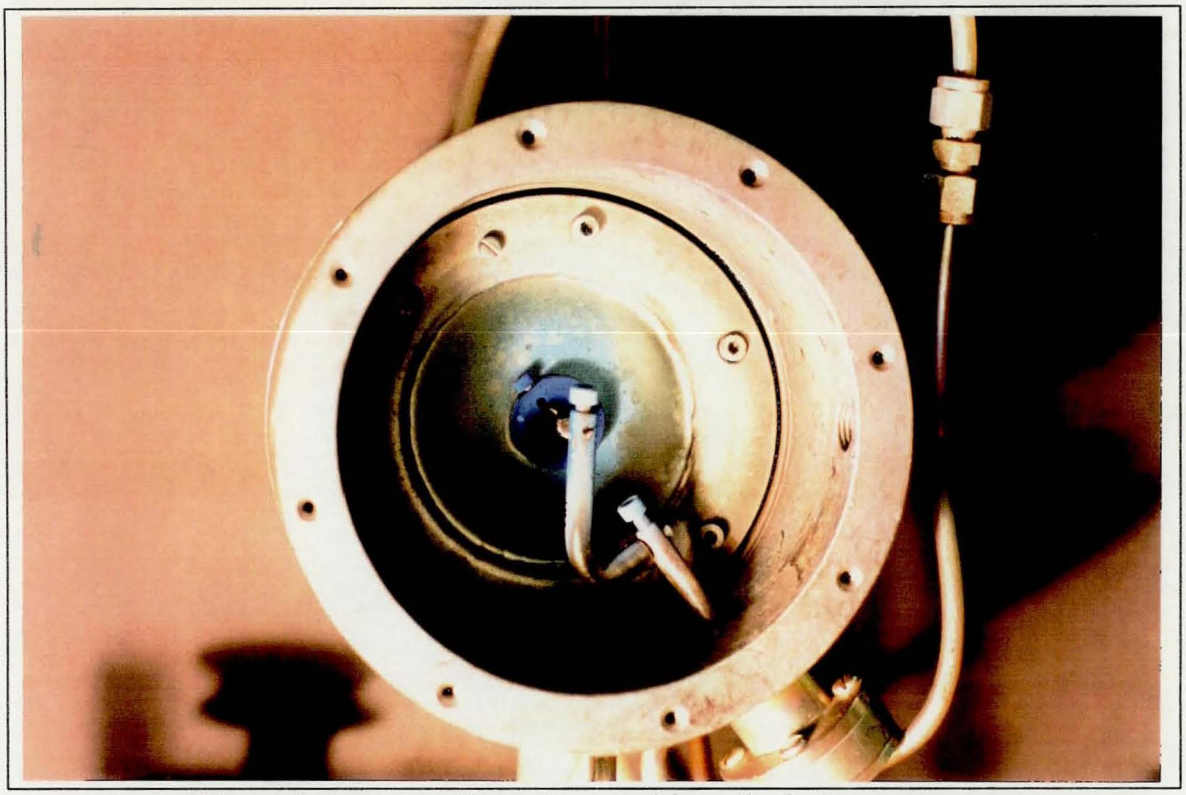

(Blue colouration is silicon deposited from the facing magnetron, onto the titanium 'gun' target operated below its sputtering threshold)

Plate 12·2
Flux lines of the magnetic 'bottle' between 'gun' and 'target' magnetrons

Figure 12·2
Relative induced operating powers for each magnetron using a bias of -200V for the Si 'target'

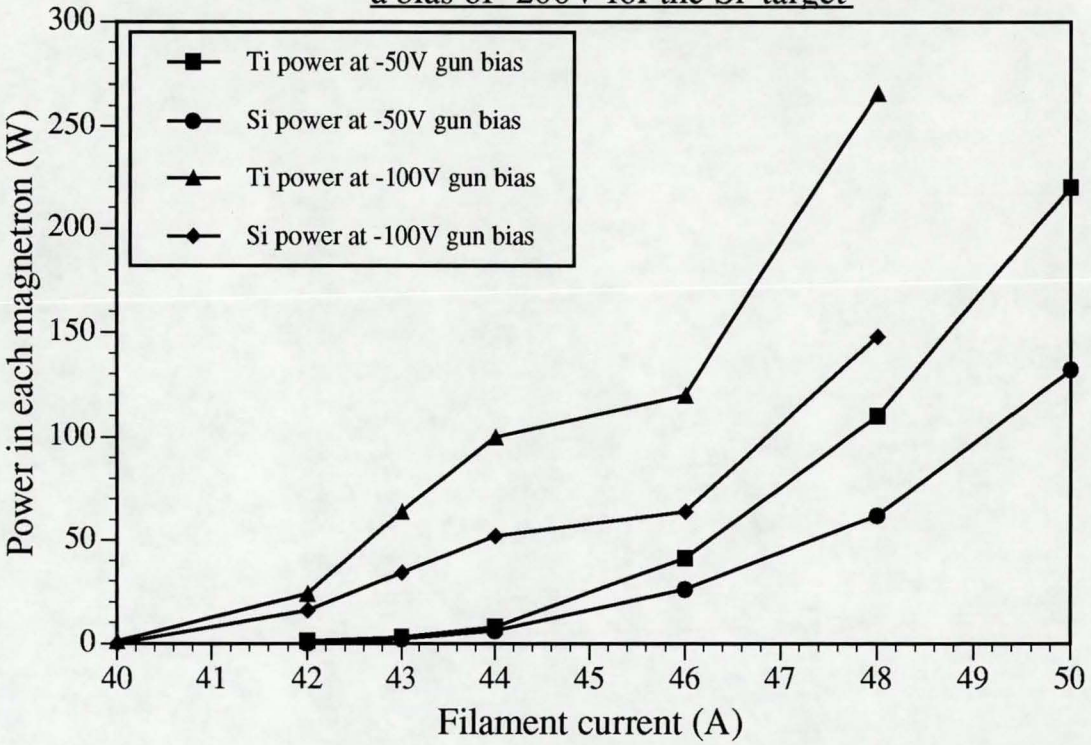

Figure 12·3
Relative induced operating powers for each magnetron using a bias of -50V for the Ti 'gun'

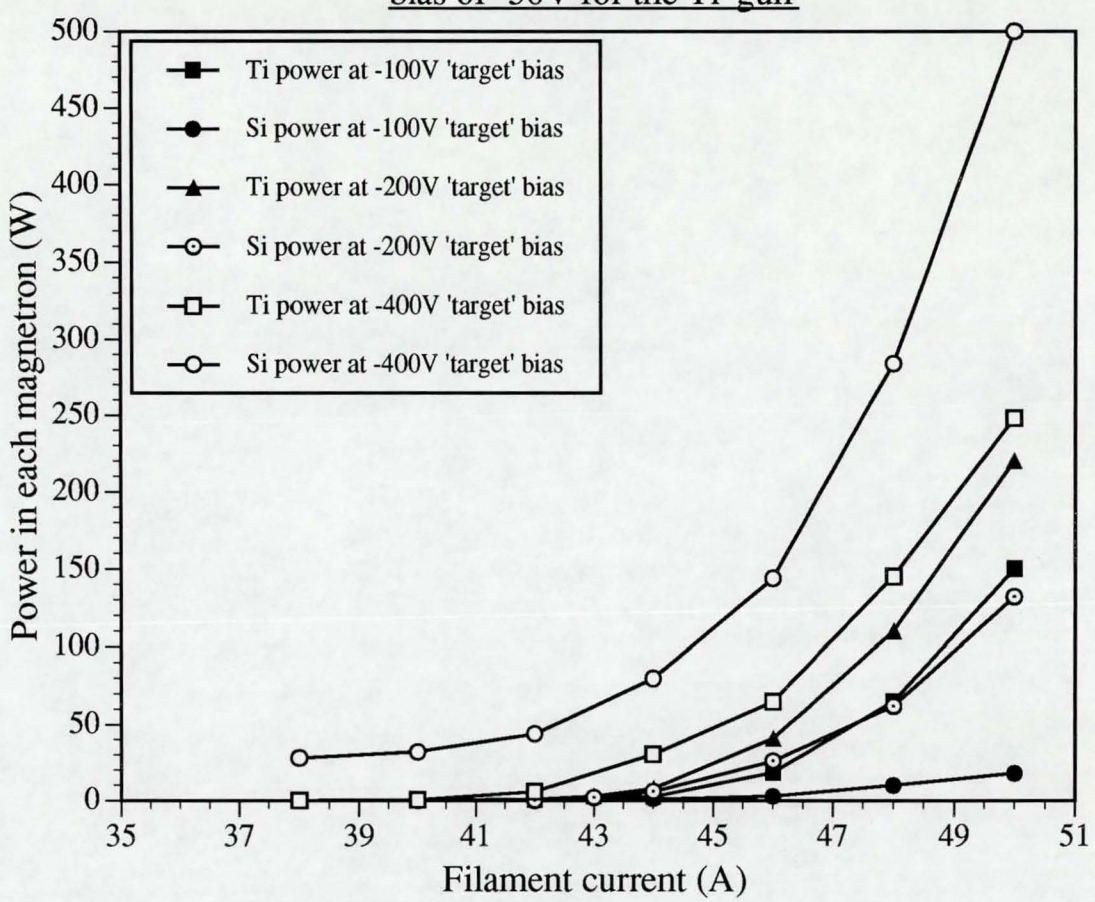

The problem of low power utilisation by the silicon target remained, and on examination of plates 12·2 and 12·3, the flux line plot and the plasma entrapment respectively, the reason becomes clear. The outer pole of the silicon magnetron attracts the discharge effectively, but because of the 45° incidence, the opposite side of the pole is further from the 'gun', has insufficient field strength to attract the plasma, and confinement is lost on this side. As a result, the electron injection enhances the dense plasma only near its origin, with highest induced operating power in the titanium. Incident plasma density is reduced and diffuse on reaching the inclined silicon 'target', with consequent low induced power. In order to ascertain the maximum power attainable in the silicon 'target', it was instructive to orient the magnetrons with zero incidence, head-on, and temporarily ignore the problem of substrate location. Plate 12·4 is a close-up view of the discharge confinement provided by the opposed magnetrons, with the axial electron emission supplied by the filament in the titanium cathode on the left. The confinement efficiency of the 'bottle' appears visually higher in plate 12·4 when compared with plate 12·3, with no diffuse regions or losses, and figure 12·4 confirms the observed effect. The power in each magnetron is shown as a function of the filament current for both the 45° incidence and head-on magnetron arrangements. In both cases the power to the titanium 'gun' is higher than that to the silicon 'target', and although the magnitude of power is no greater when using the head-on arrangement, similar values can be obtained at lower filament currents than that necessary at 45° incidence.

12.0.2 A single low voltage magnetron as a deposition source

The results had shown that although filament assisted LVS was achievable, the technique of using one magnetron below its sputtering threshold to behave as an ion 'gun', and magnetically directing the plasma to a silicon magnetron at -200V bias was not an efficient deposition arrangement. The most efficient utilisation of ion bombardment at -200V 'target' bias was achieved when the two magnetrons were head-on, and this arrangement precludes any suitable substrate location.

Extending the electron injection idea so that the 'gun' operated at -200V to give a sputter flux was the next development, with only one

Plate 12·3
Plasma confinement by the 'gun' and 'target' magnetrons at 45° incidence

(Filament is axially oriented in the 'gun' magnetron, to the left of plates 12·3 and 12·4)

Plate 12·4
Plasma confinement by the 'gun' & 'target' magnetrons at zero incidence

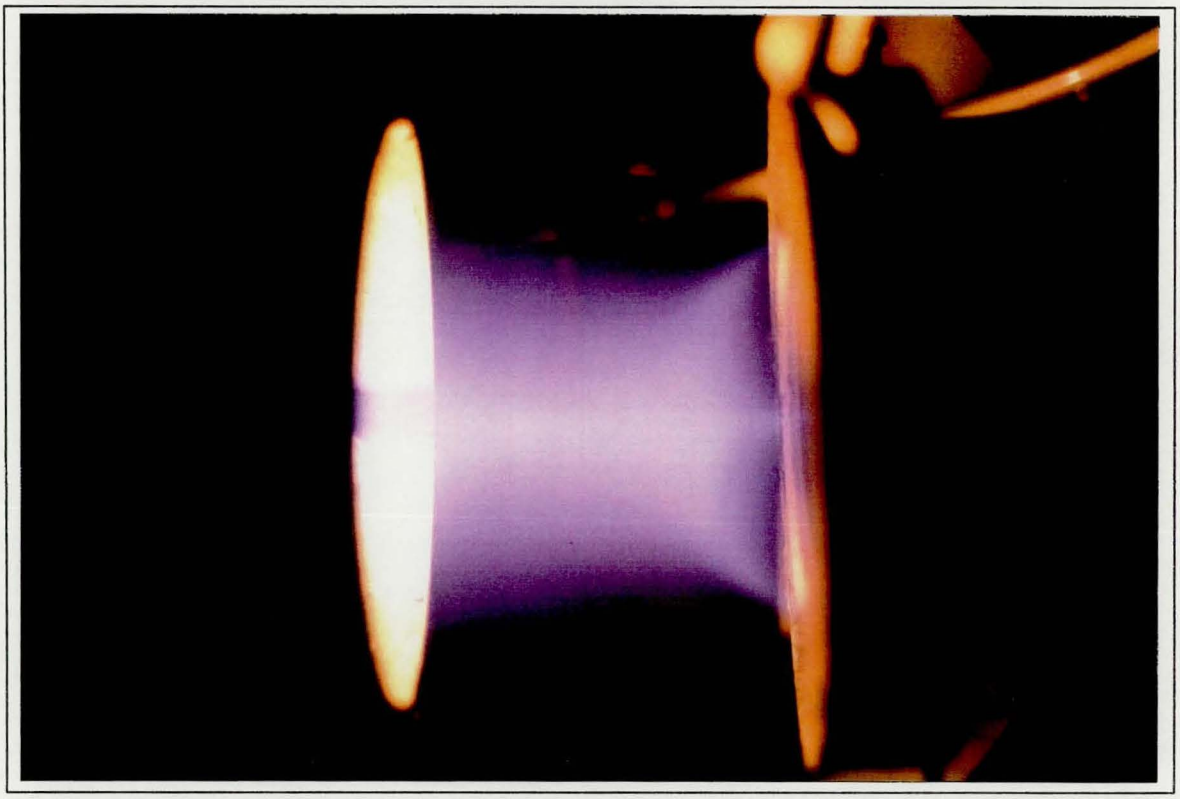

Figure 12·4
Comparison of power consumption by the 'gun' and 'target' magnetrons when at zero and 45° incidence to each other

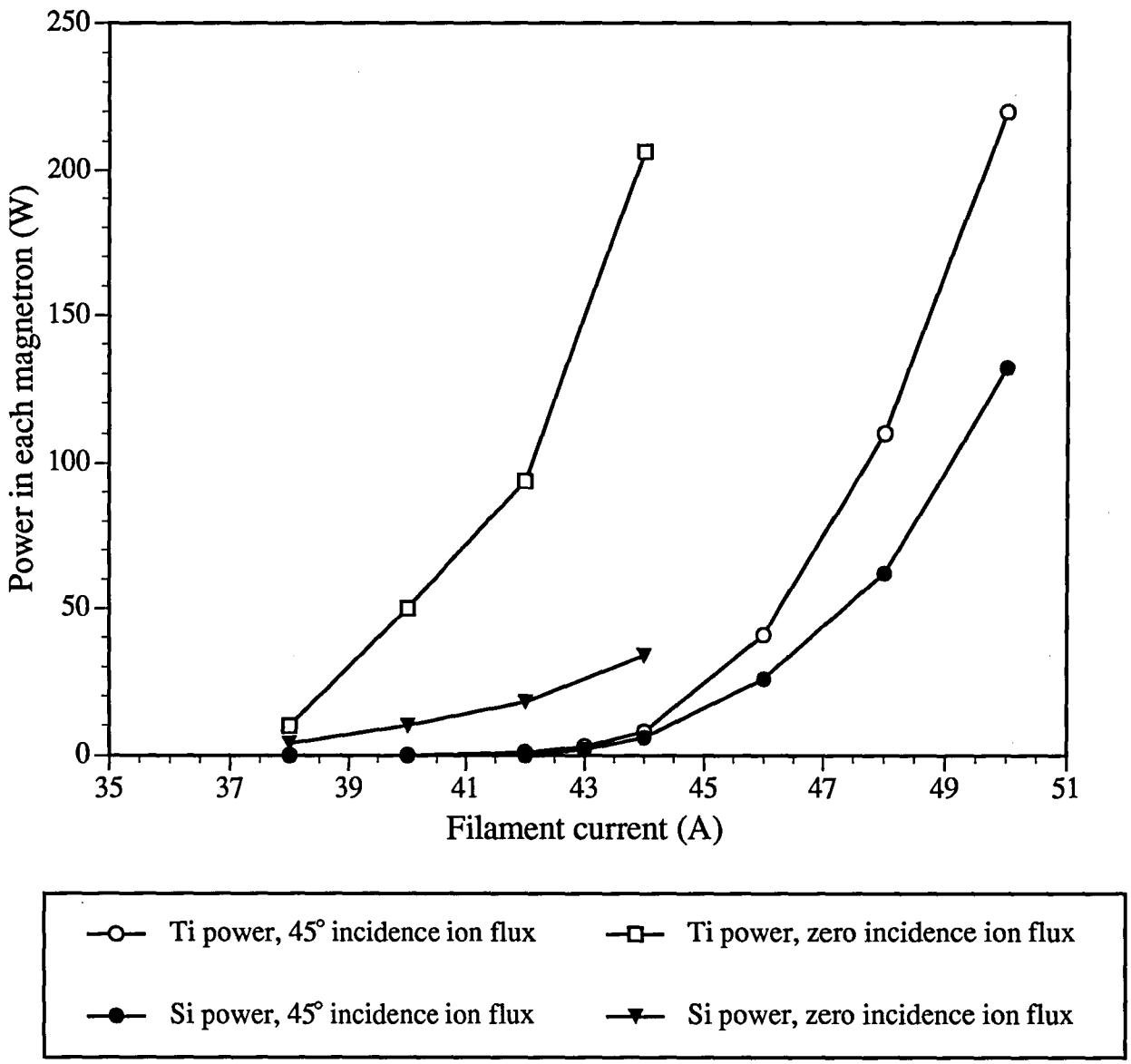

magnetron. The titanium target was replaced by silicon in the magnetron containing the filament, with the intent of using it as a deposition, rather than ion source. It was now found that by powering the device as in the previous experiment, and setting the MDX supply to constant power mode, the same applied power as that used in the conventional a-Si deposition could be achieved. This was made possible by adjusting the filament current so that the electron injection provided the necessary degree of ionisation in the plasma for the magnetron voltage to be maintained at -200V. Voltage regulation was typically ~5%. It appeared, then, that by using thermionic electron emission into the plasma of a single unbalanced magnetron, a constant operating power could be achieved at the desired cathode potential of -200V identified in figure 3·10. Now that a practical LVS device had been found, it was hoped that the factor of 3.75 lower ion damage imparted to the growing film by such a technique would result in a narrower band gap than that obtained for a-Si in chapter eleven.

12.1 Low voltage sputtered a-Si

The same technique of measurement developed in chapter eleven, involving five simple parameters, was used to calculate absorption coefficient α of the LVS a-Si films. The filament had an additional benefit to the process, in that it provided in-situ substrate heating, both prior to and during the deposition process. Calibration was achieved on a simple exposure time basis so that the substrates reached 200°C before the film deposition began.

An immediate advantage evident with LVS a-Si compared with normal unbalanced magnetron (UBM) deposition was the factor of seven higher deposition rate obtained with the former, when operated at a constant 400W. This effect has also been reported for a similar LVS system[2] in the case of copper deposition.

The initial comparison of LVS and conventional UBM was to be on the basis of the absorption coefficient of a-Si and a-Si:H films, where the hydrogen partial pressure in the latter was 1 mTorr. Since the UBM work in chapter eleven used an argon partial pressure of 3 mTorr, this pressure was selected for the LVS films. Both Cuomo and Rossnagel[1],

and Ja'fer and Howson[3] remark that electron enhanced magnetron sputtering enables operation at lower process pressures than normal UBM, so the limit of operation for the LVS system used in this work was evaluated. As expected, operation of the device could be achieved at 400W, 200V, even at 0.5 mTorr of argon. This is well below the operating threshold of 1.4 mTorr for the UBM, and implied advantages of the technique, even if beneficial film properties were not subsequently found. Certain reactive processing, such as the Si_3N_4 in chapter eight, requires particularly high reactive gas partial pressures, which may result in operation near to the stalling point of the pumping arrangement when added to the argon partial pressure. The above result suggests that the process may be moved away from the stalling point by using LVS to reduce the argon partial pressure by a factor of six.

Figure 12·5 shows the variation of absorption coefficient with photon energy for a-Si:H sputtered at 200V, at combinations of argon and hydrogen partial pressures. At both argon partial pressures, the effect of introducing 1 mTorr of hydrogen to the process is to decrease the absorption coefficient, although to a much lesser extent for the films prepared at 3 mTorr argon partial pressure. The reduction in α is agin attributed to completion of Si dangling bonds and the degree of α reduction to the proportions of Ar:H partial pressures; the greatest reduction seen when Ar:H is lower. Comparison of figures 11·5 and 12·6 immediately shows a difference between UBM and LVS absorption coefficients. As a constant reference point, 2.5 eV has been selected, and the calculated magnitudes of α shown in table 12.1 below:

Table 12.1: Absorption coefficient of a-Si at 2eV, produced at 3 mTorr argon partial pressure by UBM and LVS

	UBM		LVS	
	No H	1mTorr H	No H	1mTorr H
α (m^{-1})	2.5×10^7	8.0×10^6	5.0×10^6	4.3×10^6

These results show that LVS has reduced the absorption coefficient of the material in both hydrogenated and unhydrogenated states. It is

Figure 12·5
Absorption coefficient of LVS a-Si, deposited at different argon and hydrogen partial pressures

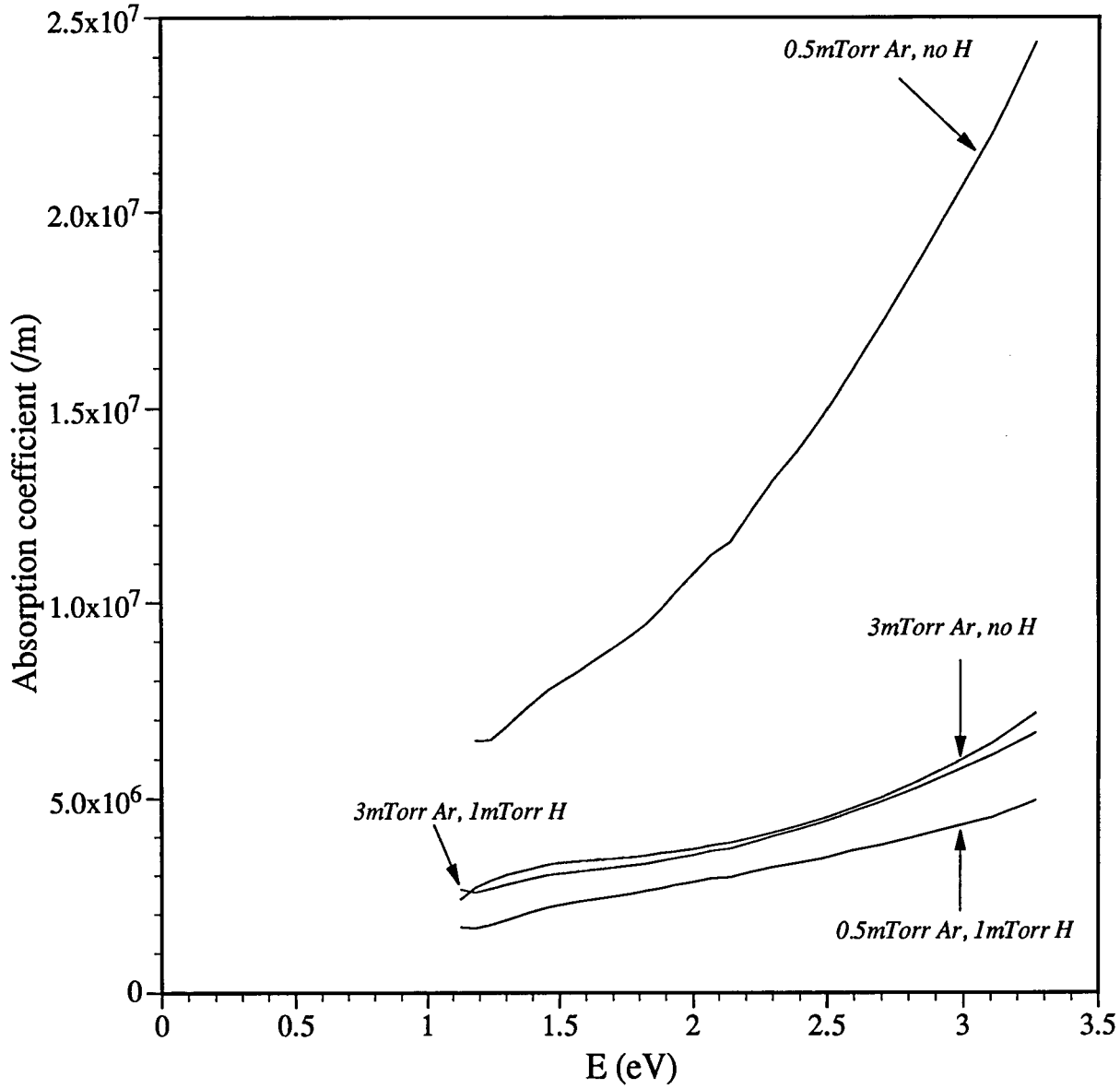

suggested that this is due to reduced ion damage, and hence lower specular reflection and scattering.

Figure 11·5 showed marked absorption tails for the UBM prepared a-Si:H films, which, combined with the large range over the abscissa meant that extrapolation of the so-called 'Tauc' plot of $\sqrt{(aE)}$ vs. E would not be necessary to estimate the band gap, E_g. The results of figure 12·5, however, do not show the same absorption tails, and so it was necessary to construct a 'Tauc' plot for this purpose. Figure 12·6 is the 'Tauc' plot for the four film types identified in figure 12·5, and the initial indication was that LVS had indeed narrowed the band gap as predicted at the beginning of this chapter. Closer inspection of the magnitudes of E_g showed that in all four cases it had been reduced to less than 0.5eV, and since E_g for crystalline silicon is ~1.1eV, these results suggested that contaminents were doping the a-Si to such an extent that E_g had been moved towards the regime of conductors.

As with the method reported by Posadowski[2], the design of the filament apparatus ensured efficient electron injection by placing the source as close to the cathode racetrack as possible, which unfortunately means that the filament and its water cooled support are located in the discharge. Because they are also at cathode potential, it is possible that some sputtering would occur from the filament and its support, so to establish if the contamination causing the band gap to narrow was from sputtered filament material, two further films were produced. The first was a-Si with the filament in place, but not powered, and the second was with the filament removed. Thus, the films were deposited under normal UBM conditions at 400W, at 3mTorr Ar partial pressure, and the effects of the two arrangements on the band gap shown in figure 12·6. The a-Si film produced with the filament removed from the apparatus showed the same absorption tail and band gap of ~1.7eV shown by the UBM film in chapter eleven. When the filament is left in the apparatus, but not powered, the absorption tail disappears and the band gap reverts to <0.5eV as with the other LVS films. This strongly suggested that either tungsten from the filament, or iron from its support was being sputtered even with the filament current switched off. Auger analysis at a depth of 80Å confirmed this suspicion, giving the film contaminent concentrations shown in table 12.2, along with those obtained by operating the filament in LVS mode at a current of 48A.

Figure 12·6
'Tauc' plot of LVS a-Si, deposited at various argon and hydrogen partial pressures

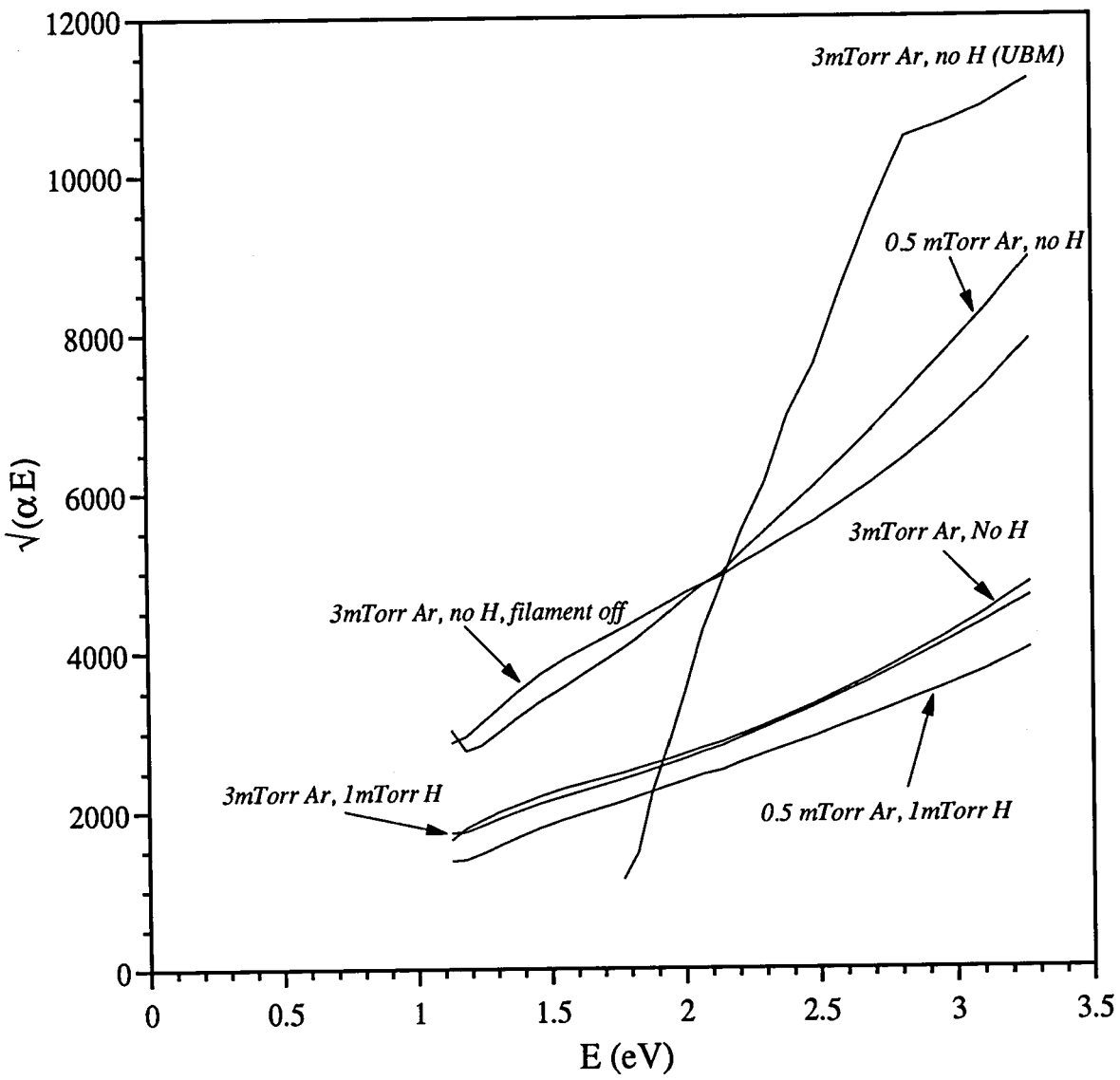

Table 12.2: Concentrations of W and Fe contamination in LVS a-Si

Sample	%W	%Fe
A-Si, filament removed	0.0	30.0
A-Si, filament present, not powered	0.6	29.0
A-Si, filament current = 48A	1.5	39.6

These results show clearly that the reason for the narrowed band gap obtained with LVS a-Si is the overwhelming contamination by Fe, and to a lesser extent, by W. When the filament is left unpowered, the W contamination drops by two-thirds, and the Fe by a quarter. On removal of the filament from the apparatus, W ceases to be a contaminent, but because the remaining support is still part of the power circuit, the Fe contamination level remains much the same. It is evident from plate 12·1 that the large, cooled stainless steel support for the filament was likely to be a major contamination source, but such a large percentage of Fe contamination was not expected. The potential advantages offered by LVS outweigh the existing problem of contamination, but time was not available to address the removal of Fe and W. Suggestions are made in the following chapter for possible solutions to the undesirable inclusion of these elements in the a-Si films.

12.2 Chapter Summary

Low voltage sputtering, LVS, of a-Si has been investigated with the aim of reducing ion damage to the growing film, during the course of which it has been found that

1 LVS is attractive because although sputter yield increases with operating potential, the lowest ion energies and most efficient sputtering occur at 200V for silicon.

2 A filament assisted 'gun' magnetron operated below the sputtering threshold voltage of its cathode, has been used to provide low energy ion bombardment of a silicon cathode in a separate biased magnetron. Low deposition rate and poor power consumption by the silicon cathode were the chief problems encountered.

3 Lower filament currents are required when the 'gun' and 'target' magnetrons are oriented 'head-on', but no significant gain in power consumption is seen, and substrate location becomes a complication.

4 A single, filament-assisted LVS silicon based magnetron has been successfully used as a deposition source, at a power of 400W and cathode potential of -200V. The device enables operation at argon partial pressures as low as 0.5 mTorr, well below the threshold for a normal magnetron.

5 LVS a-Si:H films show lower absorption coefficients than equivalent films produced at cathode potentials of 750V, but excessive Fe contamination levels were identified as the cause of band gap narrowing.

6 The advantages offered by LVS of higher deposition rate, low film damage, and semiconductor band gaps moved towards those of crystalline films should be used as an incentive to correct the overriding problem of contamination from the filament and its support.

Chapter Twelve References

1: J. J. Cuomo & S. M. Rossnagel, J. Vac. Sci. Technol. A, **4(3)**, May/Jun (1986), 393-396

2: W. M. Posadowski, "Multicomponent and Multilayered Thin Films for Advanced Microtechnologies: Techniques, Fundamentals and Devices", Kluwer Academic Publishers (1993), 109-113

3: H. A. Ja'fer & R. P. Howson, *Vacuum*, **44(3/4)**, (1993), 381-383

Chapter Thirteen

Concluding remarks and recommendations for future work

Each of the materials prepared in this work has been investigated with the aim of achieving reliable, repeatable control over its properties. The objective was not to examine the film properties in great detail, rather to observe and explain any material property distinctions which were either promoted, or hindered, by the process control invoked. To this end, the work has been successful in most respects, but as with all research, if there were no questions still remaining, nor capacity for further investigation at the conclusion of the study, it would have been doubtful whether the subject was worthy of examination from the outset. This final section will address some of those outstanding questions which remain.

Improvements made to the magnetron source highlighted and questioned some of the misconceptions of accepted theory of its operation, particularly the basic notion that the principle of secondary electron enhancement by the device is due to crossed electric and magnetic fields. This has, in fact, been shown to be due to $\mathbf{v} \times \mathbf{B}$ components, since the electric field has no significant effect above the cathode dark space. The development of the contamination free source with higher target utilisation was both interesting and useful, since meaningful film properties would not have been achieved otherwise. The manipulation

of magnetic field shape was, however, largely empirical, and it may prove beneficial for theoretical modelling of the field shape and its interaction with the electric field to be undertaken in order to provide further improvements to the magnetron design.

The process control complications introduced by the hysteresis effect inherent in reactive sputtering were overcome successfully for the preparation of oxides, nitrides and oxy-nitrides of silicon. No specific recommendations for further work are made for these materials, since the optical transmittance, refractive indices and film thicknesses were well controlled. The use of air as a reactive gas in order to increase sensitivity, could perhaps be extended to other compound films, particularly TiN alloys with Al, which have lately been shown to offer significant wear-resistance advantages over TiN, providing the stoichiometry can be finely controlled.

Once the peculiarities of PEM control of the ITO process had been identified and corrected, the controlled deposition of high conductivity, high transparency material was achieved. Annealing experiments in air and argon concluded that the latter was the preferred gas for ITO, but this may not be so for all semiconducting thin films. It would be interesting to investigate the optical and electrical effects resulting from vacuum annealing of the films. If further improvements in conductivity and transparency could be achieved with such a technique, the need for post-deposition annealing would be unnecessary, since the process could feasibly be in-situ, without the need to break vacuum.

First efforts in solid-source doping of semiconducting oxides were made with zinc oxide, and whilst film conductivity never approached that of ITO, positive effects were seen with indium dopant sputtered from the zinc cathode. The benefits of post-deposition annealing were also seen, and as with the ITO, it was shown that should the process control not have the reliability of that provided by PEM, poor film properties could be improved by using immersion in argon at 400°C, but only for *doped* ZnO. The conclusion that dopant concentration cannot necessarily be related directly to the proportion of the cathode covered by dopant source material was attributed to differential poisoning of the two elements. It is suggested that this problem may be solved by the use of two PEM control loops, with each optical fibre observing one element,

although it is recognised that sophisticated manifolds and gas metrology would be required for such a project. It would also be interesting to investigate the effects of other dopants, and concentrations, on both ITO and ZnO films, since both are the subject of great industrial drive towards finding the 'perfect' transparent conducting thin film.

It was successfully shown that the band gap of a-Si could be controllably varied between 1.7 and 2.2eV by the admission of up to 1mTorr of hydrogen during deposition. Although incorporation of indium had no measurable effect on the properties of the a-Si, use of antimony as a carrier for hydride species during the sputtering of the silicon cathode was shown to decrease the energy gap further, and to increase room temperature conductivity. The novel technique for calculation of absorption coefficient to eliminate spurious results due to the interference shown by the film thicknesses used, was considered reliable, and at the time of writing is being developed for automatic computer data acquisition and calculation.

The evaluation of a primitive system for low voltage magnetron sputtering was undertaken for a-Si film deposition. The potential advantages presented by this new development are encouraging for thin films of a higher quality than those currently produced by conventional magnetron processing. The problem of obtaining a high enough current density in the source magnetron was overcome by simplifying the original dual-magnetron arrangement whilst retaining the filament assistance. Two obstacles to further exploitation of the technique arose, and remain to be overcome. The first is the method of electron generation and injection, which was the cause of film contamination in chapter twelve. With the existing apparatus, the filament and its support are necessarily near to the racetrack and at cathode potential, and both inevitably sputter. A solution may lie in removing the electron generation source from the plasma, in a similar method to that described in section 12.1, where a remote hollow cathode was used. When this problem has been addressed, it is recommended that a means of protecting the filament (assuming thermionic injection is still favoured) from reactive gas during compound film deposition, since this is expected to reduce the lifetime of the filament considerably.

Appendix: Publication List

"DC reactive sputtering of silicon oxide, nitride and oxy-nitride", G. W. Hall & R. P. Howson, Proc. 8th Int. Conf. on Ion Asst. Techniques, CEP Consultants (1991), 128-133

"Ionicity and bonding in amorphous insulating silicon alloys", S. C. Bayliss, A. Singh, G. W. Hall, S. H. Baker & R. Bradley, Proc. 11th EPS CMD, Exeter, UK (1991), 304

"Direct current reactive sputtering of transparent conducting oxides of zinc doped with indium", R. P. Howson, G. W. Hall, G. W. Critchlow & D. E. Sykes, *Vacuum*, **43(1/2)**, (1992), 167-169

"Reactive unbalanced magnetron sputtering of hydrogenated amorphous silicon and silicon oxide", G. W. Hall, R. P. Howson & A. Chew, *Vacuum*, **44(3/4)**, (1993), 227-230

- THE END -